UNIVERSITÀ DEGLI STUDI DI MILANO

Dipartimento di Chimica

PhD in Industrial Chemistry – XXIX Cycle

Synthesis, characterization and rig tests of supported Fe and Co-based nanostructured catalysts active in the thermochemical BTL/CTL/GTL-FT processes

(S.S.D. ING-IND/25; CHIM/04)

Alberto Comazzi (R10487)

Tutor: Prof. Carlo Pirola

Co-Tutor: Prof. Claudia L. M. Bianchi

PhD program Coordinator: Prof. Maddalena Pizzotti

A.A. 2016/2017

“No one said this job was supposed to be easy”

“But nobody said it was supposed to be that hard neither!”

“Nessuno ha detto che sarebbe stato un lavoro facile”

“Ma nessuno ha detto che sarebbe stato così difficile!”

“The Hateful Eight”

Index

General Abstract

Introduction

During the recent years, the fossil fuel price is increasing, while the cost of renewable energies is decreasing, due to the greater availability of natural resources. In particular, the Annual Energy Outlook 2015 affirms that the extraction of natural gas, and the production of renewable energy is going to increase by 72% till 2040. The energy produced will be reached exploiting wind, hydrothermal and solar energies coupled with the use of biomasses and waste [1].

Beside to the direct production of electrical energy, it is required to develop and optimize chemical processes able to take advantages of all the potentiality that natural resources can offer. The three main non-crude oil based industrial processes for the production of chemicals are the biomass-to-liquid (BTL), coal-to-liquid (CTL) and gas-to-liquid (GTL) technologies [2,3]. In these three cases, syngas is produced from different raw materials: in the first one, the H_2/CO mixture is manufactured from biomass, in the second the production of syngas is obtained by the coal pyrolysis while in the last one, synthesis gas is produced via steam reforming of methane [4].

The conversion of the syngas into fuels is then done by Fischer-Tropsch (FT) synthesis, which is in the heart of the these processes [5]. In particular, FT is a well-known industrial reaction since a lot of decades, which produces hydrocarbons in the range C_1-C_{100}. The main target of FT is to produce olefins and paraffin with different molecular weights, limiting the formation of methane and CO_2. Moreover FT produces fuels with no content of sulfur and aromatics compounds [6].

The Fischer-Tropsch synthesis is an array of strongly exothermic reactions ($\Delta H \approx -200$ kJ·mol^{-1}). The main FT reactions are reported hereinafter (Eqs. A.1- A.5) [7]:

Production of alkanes:

$$(2n + 1)\ H_2 + n\ CO \rightarrow C_nH_{2n+2} + n\ H_2O \qquad \text{(Eq. A.1)}$$

Production of alkenes:

$$2n\ H_2 + n\ CO \rightarrow C_nH_{2n} + n\ H_2O \qquad \text{(Eq. A.2)}$$

Production of oxygenated compounds:

$$2n\ H_2 + n\ CO \rightarrow C_nH_{2n+2}O + (n\text{-}1)\ H_2O \qquad \text{(Eq. A.3)}$$

Boudouard equilibria:

$2\ CO \leftrightarrow CO_2 + C$ (Eq. A.4)

Water Gas Shift reaction (only with Fe-based catalysts):

$H_2O + CO \leftrightarrow H_2 + CO_2$ (Eq. A.5)

Industrial FT reaction requires catalysts based on massive iron or supported cobalt. Co is more catalytically active respect to iron and it has a greater selectivity to long and linear chain hydrocarbons [8]. On the other hand Fe is a metal active to the Water Gas Shift (WGS) reaction, which makes this kind of catalyst a suitable candidate for the catalytic reduction of CO in BTL plant where the syngas fed to the reactor has a low H_2/CO ratio, in fact even if H_2 poor bio-syngas is used, WGS is able to raise that ratio to 2 (the stoichiometry required for the FT reaction) by consuming CO and H_2O. Moreover, recent studies demonstrated that even supported Fe-based catalysts are suitable catalysts for FT synthesis; they offer several advantages (greater surface area, better dispersion of the heat developed by the reaction and better mechanical resistance) if compared to traditional massive iron catalysts [9].

Final Aims

The final aims of this PhD project have been the develop, synthesis, characterization by BET, TPR, SEM-EDX, TEM, ICP, CHN and XRD, and rig tests of three different catalytic systems. Moreover in some cases, the kinetic constants of FT reaction and WGS equilibria (when present) have been regressed starting from the experimental data obtained in the laboratory plant. This modeling work is useful to predict and confirm the catalytic results and for a primary evaluation of the performances of the catalysts in a whole BTL/CTL/GTL-FT process.

The three different catalytic systems studied were:

1- An impregnated synthesized Fe-based catalyst supported on SiO_2 and promoted with K and Cu (30 %wt of Fe, 2 %wt of K and 3.75 %wt of Cu) named $Fe_{30}K_2Cu_{3.75}$. In particular, potassium improves CO adsorption while Cu promotes the reduction of the iron oxides species [10,11]. The loading of active metal and promoters have been already determined elsewhere in recent studies, while a first evaluation of the catalytic performances is reported in the PhD thesis by A. Di Fronzo [12]. The catalyst has been tested at different temperatures in the range T= 220- 260 °C and with different H_2/CO ratios fed to the reactor ($1< H_2/CO< 2$). Moreover a primary series of experimental measurements of the light hydrocarbon fraction dissolved in the heavy products, carried out at different temperatures and H_2/CO ratios is proposed.

2- Three different Co-based catalysts synthesized by flame spray pyrolysis (FSP) and supported on SiO_2, and eventually promoted with Ru (5 %wt of Co; 10 %wt of Co; 10 %wt of Co and 0.4 %wt of Ru). The catalysts are named as 5Co, 10Co and 10Co-0.4Ru. Experimental tests have been performed at T= 220-275 °C and with a H_2/CO= 2. The results demonstrated the benefits of the FSP synthetic route, which produces highly dispersed supported materials with a great thermal stability. Moreover, FSP is not affected by traditional limitations respect to traditional preparation methods and it is a suitable technology even for the production of materials on large scale [7].

3- Three different Fe-based samples supported on SiO_2 and promoted with K and Cu, prepared with the use of ultrasound (US) (10 %wt of Fe; 30 %wt of Fe; 30 %wt of Fe, 2 %wt of K and 3.75 %wt of Cu). Catalysts are named as Fe_{10}US, Fe_{30}US and $Fe_{30}K_2Cu_{3.75}$US. The experimental runs have been performed in a limited range of temperatures, T= 250- 260 °C and with a H_2/CO= 2 in order to give a full comparison in terms of reactant conversion, products selectivity and heavy hydrocarbons composition respect to traditional synthesized catalysts. US proves a suitable method for the preparation of nanostructured catalysts due to the extreme effects of cavitation, where very high temperatures (T≈ 5000 K), pressure (P= 150 MPa) and cooling rates (≈ 10^9 °C/s) are reached [13].

Experimental

Catalysts synthesis

(1) Synthesis of $Fe_{30}K_2Cu_{3.75}$

The Fe-based sample was prepared in accordance with the traditional wet impregnation method [14], always using the same kind of commercially available silica support (Fluka product, BET surface area= 305 $m^2 \cdot g^{-1}$). Before the synthesis step, SiO_2 was first dried in air at T= 120 °C for 12 h, then impregnation was carried out with an aqueous solution of 1.67 M $Fe(NO_3)_3 \cdot 9H_2O$ (Riedel de Haen), 0.16 M KNO_3 (Merck), and 0.18 M $Cu(CH_3COO)_2 \cdot H_2O$ (Fluka). The catalyst was then placed in rotary evaporator at T= 40 °C at ω= 36 rpm for 24 h. At the end of the impregnation step, the sample was heated in air at T= 100 °C for 12 h, followed by calcination at T= 500 °C for 4 h [15].

(2) Synthesis of 5Co, 10Co and 10Co-0.4Ru

The catalysts were prepared according to the FSP method [16]. A burner was specifically designed for this application allowing the injection of 4.4 Nml·min^{-1} of an organic solution containing the catalysts precursors into a nozzle. The latter is co-fed with oxygen at high flow rate (5 NL min^{-1}). The mixture is ignited by external flamelets supported by feeding 0.5 NL·min^{-1} of CH_4 + 1NL·min^{-1} of O_2. The precursors solution was prepared by dissolving proper amounts of $Co(CH_3COO)_2{\cdot}4H_2O$ (Fluka) and $Si(OC_2H_5)_4$ (Sigma Aldrich) in a 1/1 mixture of CH_3CH_2COOH (Aldrich)/p-xylene(Aldrich) in order to obtain a molar concentration equal to 0.73 M. The pressure drop across the nozzle was adjusted to 0.7 bar, as optimized elsewhere [17]. The amount of metal present in the catalyst was easily varied by adjusting its concentration in the solution. Ru was added by wet impregnation using $Ru_3(CO)_{12}$ (Sigma Aldrich) as a precursor. A 0.003 M solution of Ru carbonyl in n-decane (Sigma Aldrich) was prepared and then added to the sample made by FSP. The catalyst was then placed in a rotary evaporator at T = 40 °C at ω= 36 rpm for 24 h. At the end of the impregnation step the sample was heated in air at T= 100 °C for 12 h and calcined at T= 200 °C for 4 h.

(3) Synthesis of $Fe_{10}US$, $Fe_{30}US$, $Fe_{30}K_2Cu_{3.75}US$

Sonochemical reactions for the samples synthesis were carried out in a glass reactor (V_{tot}= 15 mL) with rounded bottom; the distance from the US horn to the bottom of the reactor was 10 mm and it was equipped with 3 different inlet/outlet glass pipes which allowed the measurement of the temperature, the introduction of the reactants and maintenance of the solution under an inert gas (argon). The catalysts were prepared by decomposition of $Fe(CO)_5$ (Sigma-Aldrich) dissolved in n-decane (Sigma-Aldrich) in presence of dry silica (Fluka, BET surface area= 515 $m^2{\cdot}g^{-1}$) with US under Ar flow [18]; the support was dehydrated in air at T= 120 °C for 12 h. Before the US exposure, SiO_2 and solvent were added to ultrasonic reactor and all the atmospheric air was purged out with Ar flow for 15 minutes. The presence of air must be avoided inside the US reactor in order to evade the contact of oxygen with Fe^0 formed during the iron pentacarbonyl decomposition [19]; once the atmospheric air was eliminated from the reactor, $Fe(CO)_5$ was added. The US step has been carried out for a total ultrasound exposure time equal to 3 h with a duty cycle of 5/9 seconds at 20 kHz with an effective emitted power of 50 watt. During the preparation of all the three samples, the temperature inside the US reactor was maintained lower than T= 25 °C for the whole duration of the synthesis using a cooling bath. For the preparation of $Fe_{10}US$ sample the chosen precursor concentration was 0.08 M. The different loading of Fe was easily varied by changing the $Fe(CO)_5$ concentration in the n-decane solution. At the end of the US step, catalysts were oxidized flowing air over

the n-decane solution for t= 18 h (air flux= 0.5 $NL \cdot h^{-1}$) and then, filtered and washed with pentane (Sigma-Aldrich).

The promoted catalyst containing K and Cu was prepared using a previously optimized procedure in which an impregnation step on dry silica is added and comes before the sonochemical synthesis. The wet impregnation of the precursors has been carried out with an aqueous solution of 0.16 M KNO_3 (Sigma Aldrich) and 0.18 M $Cu(CH_3COO)_2 \cdot H_2O$ (Sigma Aldrich) in a rotary evaporator at T= 40 °C at ω= 36 rpm for t= 24 h. In a further step water was evaporated at T= 120 °C for t= 12 h and finally, calcined at T= 500 °C for t= 4 h [15].

Catalysts characterization

All the characterization analyses have been performed after the synthesis step, and before the activation procedure, which is carried out directly in the PBR reactor. In some cases, several analyses have also been made after the activation step or after the experimental test in order to give a better comparison with the starting material and to verify the effect of the experimental variables (activation and reaction temperatures, pressure, different times on stream). Moreover, for what concerns the US synthesized catalysts (3), part of the characterization work was carried out in the Frederick Seitz Materials Research Laboratory Central Research Facilities, University of Illinois.

The elementary composition of the samples were measured with a PerkinElmer-SCIEX ELAN DRCe ICP-MS and a PerkinElmer 2400 Series II CHN/O Elemental Analyzer. BET surface area, pore volumes and distributions were determined by low temperature (T= -196 °C) N_2 adsorption using a Tristar II 3020 Micromeritics apparatus. Before measurement, samples were outgassed at T= 200 °C for 1 h in a nitrogen flux. The morphology of the samples was investigated using a JEOL 7000F analytical SEM and a JEOL 2100 Cryo TEM. X-ray powder diffraction (XRPD) patterns were taken with a SIEMENS/BRUKER D-5000 using CuKα emission, operating at 40 kV and 20 mA, step scan 0.5 $° \cdot min^{-1}$, and in the 5- 80 2θ range at room temperature (T= 25 °C).

The Temperature Programmed Reduction analyses (TPR) were performed with a Thermoquest Mod. TPR/D/O 1100 (TCD detector). Samples were first pretreated with Ar flow at T= 200 °C for 30 minutes, then a reducing mixture (5.1 % on a volume basis of H_2 in Ar) was flowed in the samples (flux= 30 $mL \cdot min^{-1}$) while increasing the temperature from T= 50 °C to T= 800 °C with a rate of 8 $°C \cdot min^{-1}$.

Rig catalytic tests

The rig tests were carried out in a fixed bed reactor (internal diameter= 6 mm and total length of the catalytic bed= 70 mm) using 1 g of catalyst mixed with 1 g of α-Al_2O_3 (Fluka), which acts as diluent material in order to avoid the formation of hot-spots in the catalyst bed. The catalysts and the diluent material were pressed into pellets and then crushed and sieved into aggregates with dimensions in the range 105- 150 μm [20]. Before the experimental tests the catalysts were activated at different temperatures (Tact.) in situ, using different conditions as a function of the catalytic system and then tested at different temperatures. The chosen activation conditions and experimental parameters are reported hereinafter.

1- $Fe_{30}K_2Cu_{3.75}$:

   Activation step: flow of syngas (NL/h/g_{CAT}= 3.0) with a H_2/CO ratio equal to 2, at Tact.= 350 °C, P= 0.4 MPa, t= 4 h.

   Catalytic runs: flow of syngas (NL/h/g_{CAT}= 3.0) with a H_2/CO ratios equal to 2, 1.5, 1, P= 2.0 MPa and reaction temperatures in the range T= 220- 260 °C.

2- 5Co, 10Co, 10Co-0.4Ru:

   Activation step: flow of H_2 (NL/h/g_{CAT}= 5.5), at Tact.= 400 °C, P= 0.8 MPa, t= 4 h.

   Catalytic runs: flow of syngas (NL/h/g_{CAT}= 3.0) with a H_2/CO ratio equal to 2, P= 2.0 MPa and reaction temperatures in the range T= 220- 275 °C.

3- Fe_{10}US, Fe_{30}US, $Fe_{30}K_2Cu_{3.75}$US:

   Activation step: flow of syngas (NL/h/g_{CAT}= 3.0) with a H_2/CO ratio equal to 2, at Tact.= 350- 400 °C, P= 0.4 MPa, t= 4 h.

   Catalytic runs: flow of syngas (NL/h/g_{CAT}= 3.0) with a H_2/CO ratio equal to 2, P= 2.0 MPa and reaction temperatures in the range T= 250- 260 °C.

In all the experimental runs, the syngas mixture was mixed with 5.02 NmL·min^{-1} of an internal analytical standard (N_2).

The heavy organic phase (>C7 hydrocarbons) and H_2O condensed in a cold trap (which operates at T= 5 °C and at P= 20 bar) placed after the reactor. The heavy fraction was analyzed by a gas chromatograph (Fisons-8000 series) able to separate the C_7-C_{30} hydrocarbon fraction. The amount of carbonaceous species dissolved in water was determined with a total organic carbon analysis (TOC, Shimadzu 5000A).

The light hydrocarbons and the unreacted gas were analyzed with an online micro-gas chromatograph (Agilent 3000A) every 120 minutes. The analysis of the light

hydrocarbons dissolved in the heavy fraction was performed only for the sample $Fe_{30}K_2Cu_{3.75}$ (1) with the same instrument used for the analysis of the light fraction, keeping the same experimental conditions (columns temperatures and carrier pressure). The <C7 hydrocarbons were desorbed from the heavy hydrocarbons at low pressure and room temperature in a second trap placed after the cold trap. Before the desorption step, the aqueous phase was removed and atmospheric air was purged out.

Results

The results obtained during the experimental test in the FT bench-scale rig have been measured from the beginning of the test until the process reached the steady state. The experimental results are reported in terms of CO (%) conversion and selectivity (%) toward CO_2 and CH_4, which are undesired by-products of the process, light hydrocarbons (<C7 fraction), heavy hydrocarbons (>C7 fraction) and total yield of C_{2+}. When the results regarding the composition of >C7 fraction are presented, they are reported in different lumps, for example $C_{7\text{-}10}$, $C_{11\text{-}16}$, $C_{17\text{-}30}$ while the probability of chain growth has been calculated with the Anderson-Schulz-Flory (ASF) algorithm. For what concern the results regarding the light fraction dissolved in the heavy one, they are showed as the ratio of the molar composition of single component desorbed, respect to the molar composition of the same component in the light fraction flowing out from the reactor.

(1) $Fe_{30}K_2Cu_{3.75}$

The BET results show that the introduction of iron, potassium, and copper into SiO_2 reduces the surface area from 305 ± 2 to 133 ± 1 $m^2 \cdot g^{-1}$ without a significant change of the micropores percentage. This reduction in surface area may be due to the diluting effect of the metals [21]. The TPR profile highlights two different reduction steps: the first starting from hematite (Fe_2O_3) to magnetite (Fe_3O_4) at T= 230 °C and the second from magnetite to metallic iron (α-Fe) at T= 550- 750 °C [22]. The XRD diffractogram shows that iron is present on the support surface in form of hematite (2θ= 33°, 35°, 41°, 50°, 54°, 62°, 64°) [4]. SEM and TEM images reported in Figure A.1 presented Fe aggregates with dimension equal to 100 nm, uniformly distributed the bare silica surface.

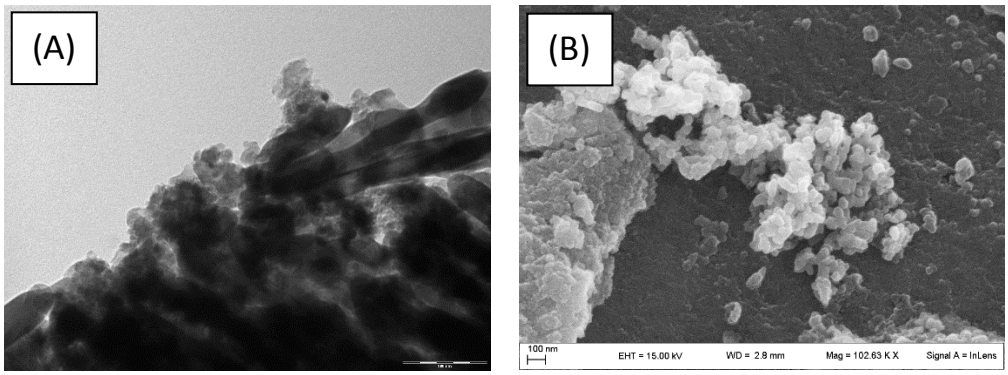

Figure A.1: TEM (A) and SEM (B) of $Fe_{30}K_2Cu_{3.75}$ catalyst.

For what concerns the catalytic results, $Fe_{30}K_2Cu_{3.75}$ showed a good stability in terms of CO conversion as a function of TOS (Figure A.2). Moreover, carbon monoxide consumption is strongly influenced by the H_2/CO reactor feed and reaches a stable value after 40 h from the start of the kinetic test; even the selectivity values are stable as a function of TOS and they presented constant results from the start of the kinetic test (Figure A.3). The selectivity towards the reaction products are independent of the H_2/CO ratio, remaining essentially unchanged in the range of syngas ratios tested.

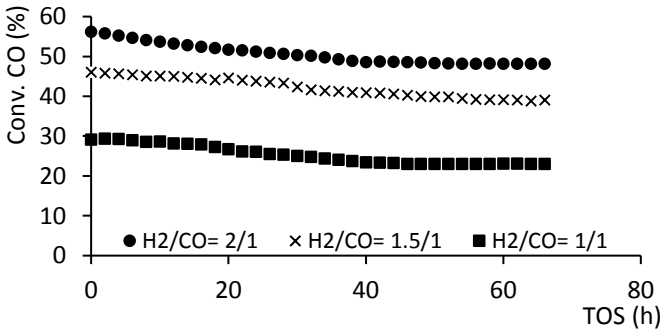

Figure A.2: CO conversion (%) as a function of TOS (h) at T= 250 °C and different H_2/CO ratios.

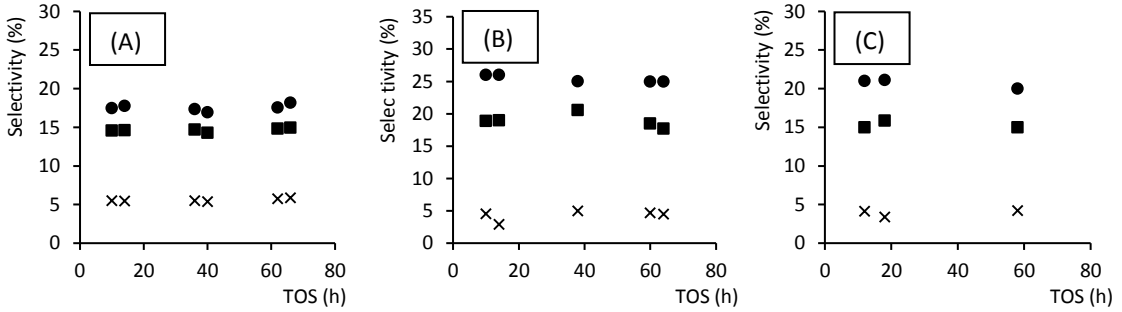

Figure A.3: Selectivity to (●) <C7; (▪) CO_2; (X) CH_4 at T= 250 °C and H_2/CO= 1 (A), 1.5 (B) and 2 (C).

The probability of chain growth (α) has been calculated with the Anderson-Schulz-Flory distribution. In Table A.1, the α values are reported for the catalyst at T= 250-260 °C and different H_2/CO ratios. This parameter remains unchanged in the range T= 250- 260 °C and 1 <H_2/CO< 2. The results of the GC analyses confirm that the molar distribution of the $C_{7\text{-}10}$, $C_{11\text{-}20}$, and $C_{20\text{-}30}$ lumps is not strongly influenced by the H_2/CO ratio; this trend is also confirmed at the different reaction temperatures tested [9].

H_2/CO	$\alpha_{C1\text{-}C30}$ T= 250 °C	$\alpha_{C1\text{-}C30}$ T= 260 °C
2/1	0.74	0.73
1.5/1	0.76	0.73
1/1	0.76	0.74

Table A.1: α values for the sample $Fe_{30}K_2Cu_{3,75}$ at T= 250-260 °C.

Moreover, the ratio of the molar composition of single component desorbed from the heavy fraction, respect to the molar composition of the same component in the light fraction has been calculated at different T and H_2/CO ratios. From the experimental results is evident that, as a general trend, higher is the number of carbon atoms in the molecule, higher is the ratio of the components. In particular, by increasing the reaction temperature this increase is more observable for runs performed with low H_2/CO ratio [23]. An example is reported in Figure A.4.

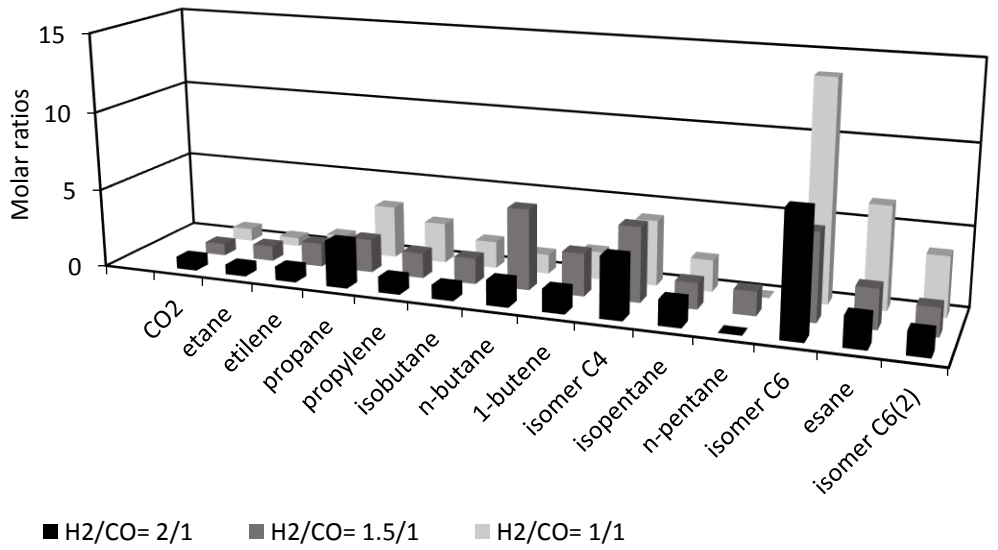

Figure A.4: Molar ratios between the molar fraction of the desorbed and light products at T= 250 °C and different H_2/CO ratios.

In addition to the experimental work, a kinetic model based on the co-presence of FT and WGS reaction on the catalyst is proposed, in order to allow the evaluation of the catalyst performances and to support the experimental test conducted at different conditions. The kinetic constants k_{FT} (for the Fischer-Tropsch reaction) and k_{WGS} (for the water gas shift equilibria) have been regressed by using the data obtained with the bench scale laboratory pilot plant at different temperatures and H_2/CO ratios. The two equations Eq. A.6 and Eq. A.7, suitable for fixed bed reactors with iron-based catalysts which express the rate of the FT and WGS reactions used for the regression are here reported [24].

$$r_{FT} = k_{FT}\frac{P_{H_2}P_{CO}}{P_{CO} + a_{FT}P_{H_2O} + b_{FT}P_{CO_2}} \qquad \text{(Eq. A.6)}$$

$$r_{WGS} = k_{WGS}\frac{P_{CO}P_{H_2} - \frac{P_{H_2}P_{CO_2}}{K_P}}{P_{CO} + a_{WGS}P_{H_2O} + b_{WGS}P_{CO_2}} \qquad \text{(Eq. A.7)}$$

The reaction rate is a function of the partial pressures of the reactants (CO, H_2, H_2O, and CO_2) and every kinetic constant is given using Arrhenius formula. A non-linear regression is therefore required, in order to optimize kinetic parameters inside the model. Parameters a_{FT}, a_{WGS}, b_{FT}, and b_{WGS} are not included, since they do affect the results significantly; moreover, the regression should optimize as few parameters as possible, in order to favour an efficient convergence. The regression of the parameter values $k_{0,i}$, was obtained with MATLAB (version. R2014b) using literature values for $k_{0,FT}$, $k_{0,WGS}$, a_{FT}, a_{WGS}, b_{FT}, and b_{WGS} for the first attempt [25]. The kinetic parameters have then been regressed by setting and minimizing an objective function here reported in Eq. A.8:

$$\min_{xo} \; fobj(xo) = \sum_{i=1}^{Nobs}\sum_{j=1}^{Nc}(y_{i,j}^{exp} - y_{i,j}^{sim})^2 \qquad \text{(Eq. A.8)}$$

Where xi are the molar fractions of each components measured experimentally and provided by the model. In Table A.2 are reported the regressed results which are in fully agreement with the ones founded in the recent literature.

Model	Parameter	Unit of measure	Regressed value
α	$k_{A,\,Ref}$	//	$1.45\cdot10^{-5}$
	$k_{B,\,Ref}$	bar	2.078
FT	k_{FT}^0	$mol\cdot g^{-1}\cdot s^{-1}\cdot bar^{-1}$	$3.365\cdot10^{3}$
	$E_{act,FT}$	$kJ\cdot mol^{-1}$	113.7
WGS	k_{wgs}^0	$mol\cdot g^{-1}\cdot s^{-1}\cdot bar^{-1}$	19.03
	$E_{act,WGS}$	$kJ\cdot mol^{-1}$	80.26

Table A.2: Regressed parameters.

In order to evaluate the model in terms of hydrocarbons productivity, the Anderson-Schulz-Flory product distribution calculated experimentally was compared with the modelled distribution given by the Lox and Froment correlation for iron-based catalysts [26]. The ASF diagrams obtained using the results predicted by the model at different temperatures and H_2/CO feed ratios confirm the good agreement of the constructed kinetic model with the measured experimental data. An example of a comparison between the experimental data and the simulated one, is reported in Figure A.5.

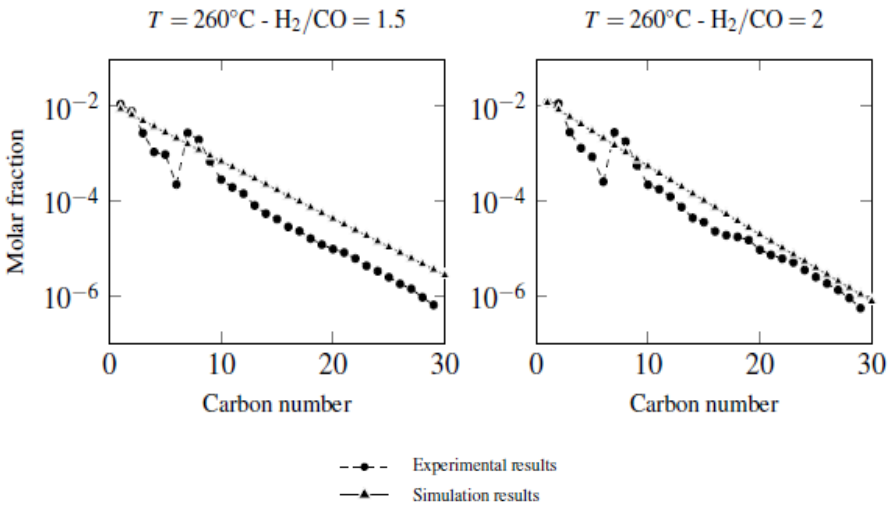

Figure A.5: ASF diagram of experimental data and simulated results at T= 260 °C and H_2/CO= 1.5/1- 2/1.

(2) 5Co, 10Co, 10Co-0.4Ru

The XRD patterns highlight that the active metal is present in its oxidized phase Co_3O_4 for both samples with 10 %wt of Co while XRD diffractogram of the sample 5Co did not reveal peaks related to cobalt oxides, due to the small size of the Co particles on the SiO_2 surface. The TPR profiles of the samples reported in Figure A.6 present two different reduction steps for samples 10Co and 10Co-0.4Ru. The first peak at T= 320-360°C was attributed to the reduction Co_3O_4 → CoO (A) and the second one at T= 700-800 °C was correlated to the reduction step CoO → Co (B) [27]. In the TPR profile of 5Co only a small peak is present at low reduction temperature (T= 350 °C), suggesting that almost all the metal is present of CoO or Co-silicates; as confirmed in the literature, the formation of metal-support phases is strongly influenced by the loading of the metal present in the samples [28], at low loadings (e.g., < 7 %wt), almost all of the cobalt is present as CoO strongly bounded to the support surface.

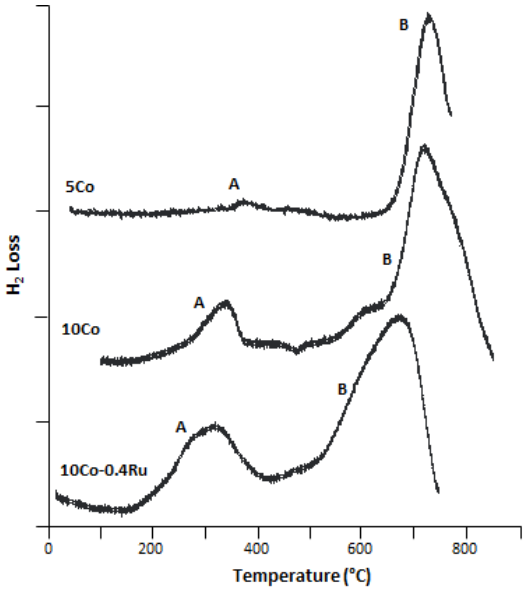

Figure A.6: TPR profiles of 5Co, 10Co and 10Co-0.4Ru.

The BET results reported in Table 2 show quite high surface area of the samples. The post-synthesis Ru deposition and calcination step almost unaffected the surface area of the promoted sample respect to the monometallic one [29].

Sample	BET S. A. ($m^2 \cdot g^{-1}$)	Pore Volume ($cm^3 \cdot g^{-1}$)	Average Pore Size (Å)
10Co	159 ± 1	0.35	100.9
10Co-0.4Ru	145 ± 1	0.33	113.4

Table A.3: BET results of 10Co and 10Co-0.4Ru.

The morphological analysis of the catalysts showed that cobalt is present in quite uniform spherical particles with diameters of 20- 40 nm, uniformly distributed on the SiO_2 grain. The calcination step performed at T= 200 °C during the synthesis of the Ru-promoted sample did not largely influence the size of the active metal particles and caused a little increase of about 1-5 nm.

For what concerns the catalytic activity in function of the metal loading, 5Co did not show any catalytic activity for the FT reaction. It presented nil CO conversion for the entire catalytic tests in the temperature range explored. This inactivity was attributed to unreducible Co oxide phases on the catalyst surface, as confirmed by TPR analysis.

The catalytic results of 10Co and 10Co-0.4Ru reached at different temperatures are reported in Figure A.7 and Table A.4; CO conversion increased by increasing reaction temperature for both catalysts. The promotion with 0.4 %wt of Ru greatly increased the catalyst activity in terms of reactant conversion. For example, at T= 245 °C, CO

conversion is equal to 23,4 % for the sample 10Co, while for 10Co-0.4Ru the conversion obtained is 94,5 % at the same temperature thanks to the greater reducibility achieved after Ru addition.

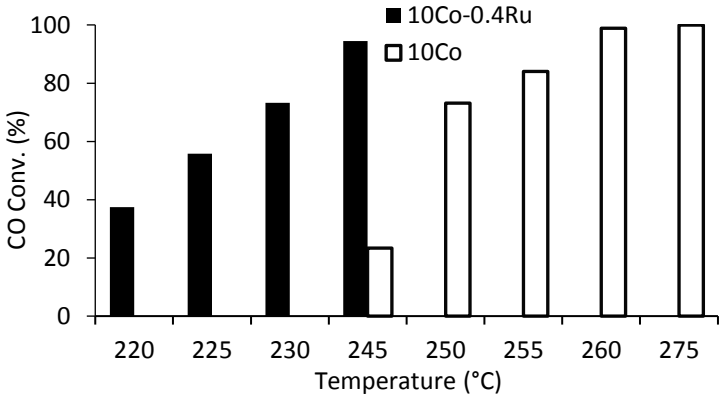

Figure A.7: CO conversion at different temperatures for the samples 10Co and 10Co-0.4Ru at TOS= 80 h.

Catalyst	T (°C)	C_{2+} Yield (%)	Selectivity (%)			
			CO_2	CH_4	$<C_7$	$>C_7$
10Co	245	20.4	1	12	10	77
	250	65.1	1	10	13	76
	255	73.1	2	11	13	74
	260	82.0	6	11	10	73
	275	80.9	7	12	8	73
10Co-0.4Ru	220	35.2	0	6	15	79
	225	50.2	1	9	18	72
	230	65.2	2	9	17	72
	245	77.5	6	12	14	68

Table A.4: Selectivity to the reaction products and C_{2+} yield at different temperatures and at TOS= 80 h.

The reaction temperature did not largely influence the selectivity toward the products for both catalysts, except for CO_2 formation in the case of un-promoted sample, which presents a variation from 1 % at T= 245 °C to 7 % at T= 275 °C. Ru promoted catalyst is more active in terms of C_{2+} yield at lower temperature if compared with the monometallic one, due to the higher CO conversion. Both samples showed low productivity toward the undesired byproducts (CO_2 and CH_4). Nevertheless, the un-promoted catalyst showed greater productivity to heavier products $>C_7$ with respect to the Ru-doped catalyst.

Moreover, a stability test has been carried out with the sample 10Co in a run performed at T= 250 °C in order to evaluate the catalyst stability in terms of CO conversion and selectivity toward the reaction products at high TOS (almost 200 h). Catalytic results over long TOS for 10Co reported in Figure A.8 highlight a great stability during time-on-stream; FSP synthesis proved a suitable synthesis way to produce materials characterized by a great stability for prolonged reaction time respect to the ones findable in literature prepared with different techniques [30,31].

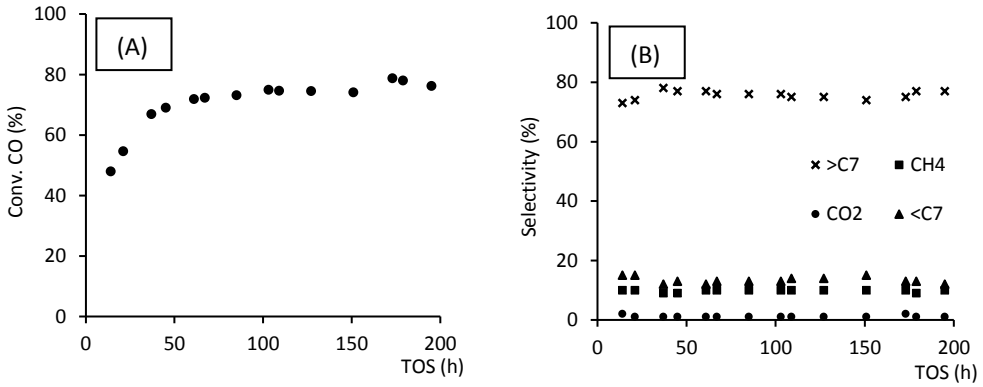

Figure A.8: CO conversion (A) and products selectivity (B) as a function of TOS at T= 250 °C

Moreover, a nonlinear parameter regression has been carried out in order to allow the simulation of the catalysts behaviour and to develop a suitable kinetic model with the use of FSP catalysts. In this case, only the FT reaction is active on the catalyst surface since Co is not active to the WGS synthesis.

The equation which express the FT reaction rate (Yates et al.) [32] is here reported in Eq. A.9:

$$-R_{CO} = \frac{aP_{CO}P_{H2}}{(1+bP_{CO})^2} \qquad \text{(Eq. A.9)}$$

While the probability of chain growth reported in Eq. 8.14 is given by (Vervloet et al.) [33]:

$$\alpha = \frac{1}{1+k_\alpha\left(\frac{C_{H2}}{C_{CO}}\right)^\beta \exp\left(\frac{\Delta E_\alpha}{R}\left(\frac{1}{493.15}-\frac{1}{T}\right)\right)} \qquad \text{(Eq. A.10)}$$

The regression procedure is achieved by minimizing Eq. A.8 using BzzMath libraries with C++ tool.

The minimization can be carried out with the regression of seven parameters: the ones regarding the FT reaction (a, b, E_a and E_b) and the ones related to the probability of chain growth (k_α, β and ΔE_α), or just the four FT reaction rate parameters.

The seven regressed parameters of 10Co-0.4Ru are reported in Table A.5.

Parameter	value	Unit of measure
a	$4.37 \cdot 10^{9}$	(-)
E_a	$9.28 \cdot 10^{4}$	$(J \cdot mol^{-1})$
b	$1.66 \cdot 10^{8}$	(-)
E_b	$1.71 \cdot 10^{5}$	$(J \cdot mol^{-1})$
k_α	0.216	(-)
ΔE_α	$1.25 \cdot 10^{5}$	$(J \cdot mol^{-1})$
β	0.8564	(-)

Table A.5: Regressed parameter of the sample 10Co-0.4Ru.

While the comparison among the experimental results and the simulated ones is reported in Figure A.9.

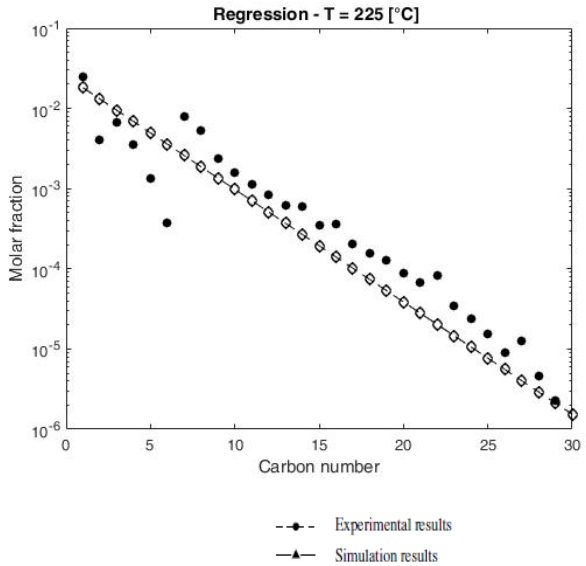

Figure A.9: ASF diagram of experimental data and simulated results at T= 225 °C for 10Co-0.4Ru

The results concerning the hydrocarbons distribution presented in Figure A.9, highlight that a nonlinear regression of the kinetic parameters allows a good reproduction of the experimental data obtained in the FT laboratory reactor.

(3) $Fe_{10}US$, $Fe_{30}US$, $Fe_{30}K_2Cu_{3.75}US$

ICP analysis allowed to evaluate the effective amounts of active metal and promoters, and the presence of Ti. Moreover the presence of C was determined by CHN analysis.

The results confirmed that the experimental amount of metals found in each samples is in good agreement with the theoretical one and they highlighted the presence of 0.009 ± 0.001 %wt of titanium and 1.5 ± 0.05 %wt of C in each sample; as reported in the recent literature, the presence of small amount of Ti does not affect FT catalysts performance [6], while the C contamination does not constitute a problem since iron carbide are active catalytic species for the FT synthesis [34].

BET analyses reported in Table A.6 showed that the greater the loading of metals present on the SiO_2, the lower the surface area of the catalysts; this result can be ascribed to the diluting effect of the metals [35]. Fe_{10}US and Fe_{10}IMP present the same surface area, while the other samples synthesized with the use of US present a bigger area if compared with traditional SiO_2 supported impregnated samples with the same metal loading.

Sample	BET s.a. ($m^2 \cdot g^{-1}$)	Pore volume ($cm^3 \cdot g^{-1}$)	Pore diameter (nm)
Fe_{10}US	362 ± 2	0.63	5.6
Fe_{30}US	314 ± 1	0.54	5.7
$Fe_{30}K_2Cu_{3.75}$US	216 ± 1	0.50	6.8
Fe_{10}IMP	362 ± 1		
Fe_{30}IMP	241 ± 2		
$Fe_{30}K_2Cu_{3.75}$IMP	133 ± 1	0.33	7.2

Table A.6: BET results of sonochemical and impregnated samples.

The XRD patterns of all the three sonochemical synthesized samples did not reveal peaks related to iron oxides, (Fe_2O_3 and Fe_3O_4) or to the presence of Fe-silicates. The lack of the typical iron oxides related peaks can be justified considering the formation of amorphous metal during the ultrasonic synthesis of supported or bulk materials [18,36].

TPR profiles highlighted that both Fe_{10}US and Fe_{30}US samples are characterized by the same reduction temperature regarding to the first peak at T= 350 °C ($Fe_2O_3 \rightarrow Fe_3O_4$). Moreover, there are not differences in the reduction temperature of the first step, respect to samples synthesized by impregnation. The effect of the Cu is visible in the TPR profiles of the promoted samples ($Fe_{30}K_2Cu_{3.75}$US and $Fe_{30}K_2Cu_{3.75}$IMP), in fact they present a left shift to lower reduction temperatures of both steps respect to the un-promoted samples [37].

TEM and SEM images reported in Figure A.10 highlight that ultrasonic samples present uniform and well dispersed iron nanoparticles with an average dimension less than 20 nm, without the presence of larger aggregates. SEM images show that the bare SiO_2 surface without the presence of metals is very smooth while, with an increase in the metal loading, Fe agglomerates are present on the support surface. In

the case of $Fe_{30}K_2Cu_{3,75}US$ the active metal and promoters agglomerates are better dispersed.

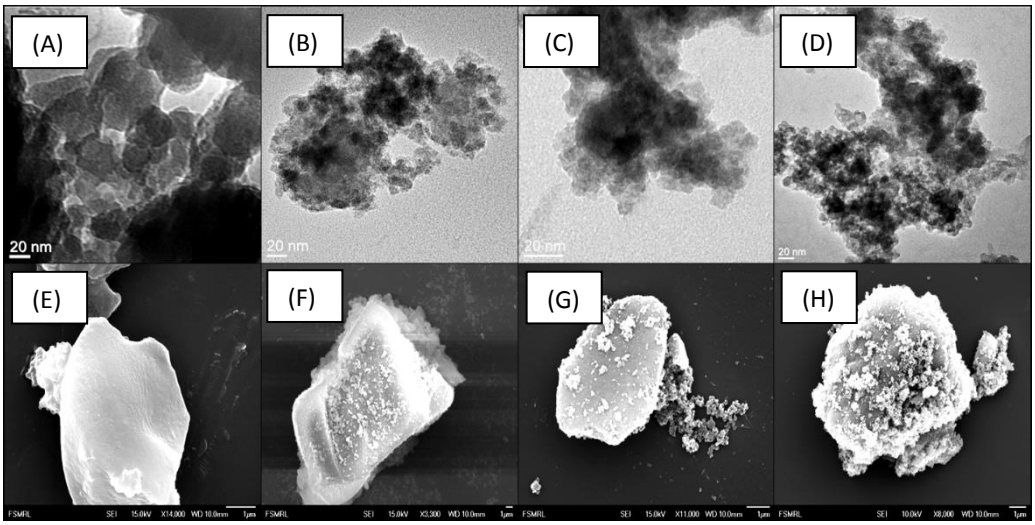

Figure A.10: TEM and SEM images of: SiO_2 (A, E); Fe_{10} (B, F); Fe_{30} (C, G); $Fe_{30}K_2Cu_{3.75}$ (D, H).

All the experimental runs have been performed testing two different activation temperature, Tact.= 350- 400 °C. The experimental results are reported in Figure A.11 and Table A.7. In particular, they showed that the CO conversion is faintly influenced by the temperature at which the samples are activated; during the experimental tests performed with $Fe_{10}US$, an increase of only 3% in CO conversion was detected by raising the activation temperature from Tact.= 350 °C to Tact.= 400 °C. The effect of an increase in the Tact. is more visible for $Fe_{30}US$ where the increase of the reactant conversion is almost equal to 13% by increasing the reduction temperature to Tact.= 400 °C. $Fe_{30}K_2Cu_{3.75}US$ did not show any catalytic result if reduced at Tact.= 400 °C, due to the high activity of this sample towards the Boudouard reaction which rapidly produces elementary carbon on the catalyst surface, resulting in a complete deactivation of the sample [38].

For what concerns the stability of the samples as a function of TOS, the CO conversion given by $Fe_{10}US$ and $Fe_{30}US$ was not decreasing during the whole duration of the tests, suggesting a great stability of the sonochemical samples, while a slight decrease in the reactant conversion provided by the promoted sample was recorded.

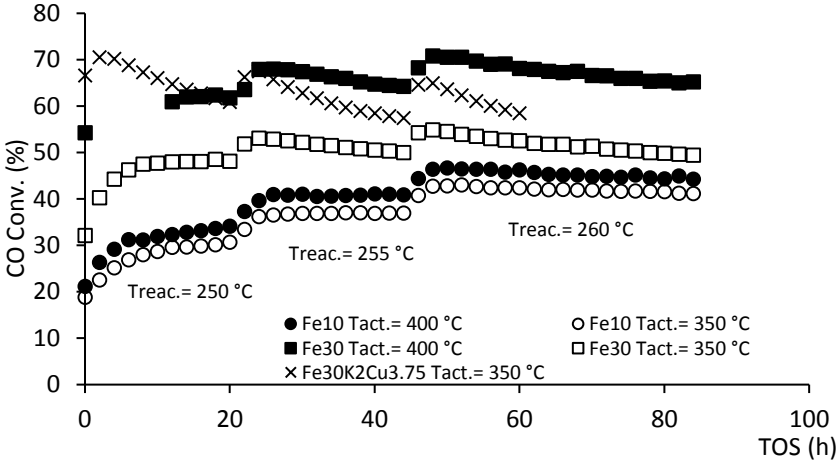

Figure A.11: CO conversion as a function of TOS and activation temperature for the samples $Fe_{10}US$, $Fe_{30}US$ and $Fe_{30}K_2Cu_{3.75}US$.

Sample	Tact. (°C)	Treac. (°C)	CO Conv. (%)	C_{2+} yield	Selectivity (%)			
					CH_4	CO_2	$<C_7$	$>C_7$
$Fe_{10}US$	400	250	33.6	30.2	5	5	18	72
		255	40.9	36.4	5	6	18	71
		260	44.3	39	5	7	18	70
	350	250	30.7	27.6	5	5	19	71
		255	37	32.9	5	6	19	70
		260	41.2	36.3	5	7	19	69
$Fe_{30}US$	400	250	62.4	54.3	4	9	17	70
		255	64.3	54	4	12	18	66
		260	65.2	54.8	4	12	17	67
	350	250	48.1	42.8	4	7	19	71
		255	50	44.0	4	8	19	70
		260	49.4	43.0	4	9	19	69
$Fe_{30}K_2Cu_{3.75}US$	350	250	60.9	48.1	3	18	14	65
		255	57.4	45.3	3	18	14	65
		260	58.5	45.1	3	20	14	63

Table A.7: C_{2+} yield and products selectivity of the sonochemical catalysts.

$Fe_{10}US$ presents the greatest selectivity to the heavy hydrocarbon fraction (72%) when tested with Tact.= 400 °C and a reaction temperature Treac.= 250 °C. The selectivity toward all the reaction products is not largely influenced by the reaction temperature and the activation temperature in the range of temperatures tested, only an increase in selectivity to CO_2 from 9 % to 12 % has been observed for the

sample $Fe_{30}US$ activated at Tact.= 400 °C instead of Tact.= 350 °C. Moreover, the selectivity value toward CH_4 is low (≈ 4 %) for all the samples. The K-Cu promoted sample showed the greater selectivity to CO_2 (20%) with respect to the other catalysts synthesized sonochemically.

If sonochemical catalysts are compared with traditional samples synthesized by impregnation with the same amount of active metal and promoters, they provide greater CO conversion if tested at the same temperatures, in particular an increase of about 5 times was observed for the sample $Fe_{10}US$ with respect to the impregnated one. All the samples sonochemically synthesized present lower selectivity to non-useful products (CH_4) in particular, $Fe_{10}US$ methane selectivity is 6 times lower while for $Fe_{30}US$ and $Fe_{30}K_2Cu_{3.75}US$ it decreased of about 50 % with respect to samples prepared with traditional impregnation [39]. The measured selectivity to CO_2 is lower for sonochemical $Fe_{10}US$ and $Fe_{30}US$ while $Fe_{30}K_2Cu_{3.75}US$ presents the highest value of selectivity towards carbon dioxide [40]. All the US synthesized catalysts showed higher selectivity to >C7 respect to the impregnated samples. A full comparison among US and impregnated catalysts is reported in Figures A.12 and A.13.

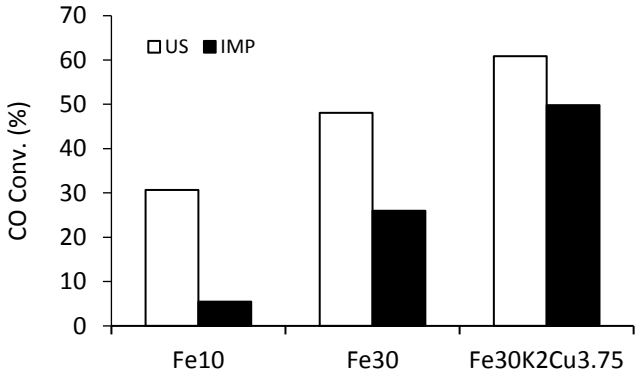

Figure A.12: Comparison between US and IMP samples in terms of CO conversion at Treac.= 250 °C.

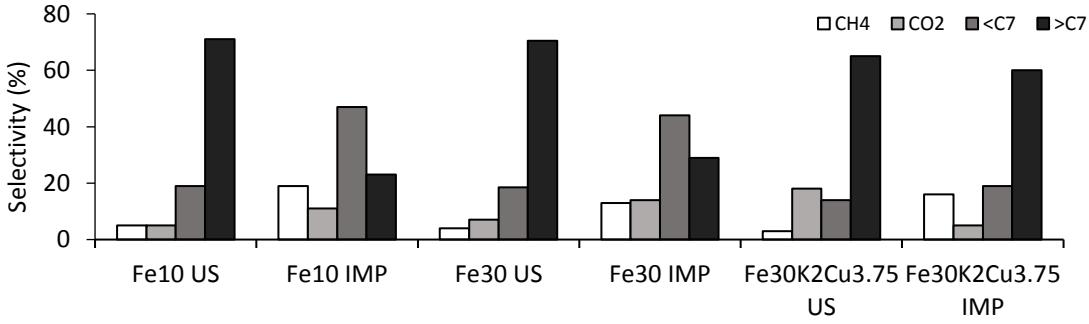

Figure A.13: Comparison between US and IMP samples in terms of products selectivity at Treac.= 250 °C.

Conclusions

Different Co-based and Fe-based catalysts supported on SiO_2 and active in the FT reaction have been synthesized with different techniques (impregnation, flame spray pyrolysis and ultrasonic synthesis) and then tested in a suitable FT laboratory bench scale rig using different experimental conditions. The main conclusions of the PhD have been separated as a function of the catalyst tested and are reported hereinafter.

(1) $Fe_{30}K_2Cu_{3.75}$

The study of the BET surface area confirms that the introduction of iron, potassium, and copper into the bare SiO_2 reduces the surface area from 305 to 133 $m^2 \cdot g^{-1}$. The tested sample is active for the FT conversion even if syngas with a H_2/CO ratio similar to the ratio of bio-syngas (H_2/CO= 1) is fed to the reactor. The catalyst presents a satisfactory stability as a function of TOS and shows a gradual drop of CO conversion from 49.8 % to 23.0 % at T= 250 °C when H_2/CO is lower than 2. Selectivity toward the reaction products remains essentially unchanged at different syngas ratios at the same temperature tested (about 60 % toward heavy products and 19 % toward light products at T= 250 °C and H_2/CO= 2/1). As it could be expected, the selectivity to >C7 decreases by increasing reaction temperature.

The probability of chain growth (α) remains unchanged in the range of temperature and H_2/CO ratios tested.

The developed kinetic model shows close agreement with the experimental data obtained at different H_2/CO ratios tested for both reactant conversion and product selectivity. The regressed kinetic parameters are in fully agreement with the ones fundable in the recent literature for iron-based catalysts tested in fixed bed FT reactor.

(2) 5Co, 10Co, 10Co-0.4Ru

SEM and TEM analyses showed nanometric particle size of the catalysts with a good metal dispersion. XRD and TPR analyses showed that cobalt oxide in form of Co_3O_4 was present in 10Co and 10Co-0.4Ru, whereas mostly Co_2O_3 was present after Ru addition, due to the post-impregnation calcination step. The 5Co sample revealed the presence of only CoO or, cobalt silicate.

10Co and 10Co-0.4Ru samples are active in the FT synthesis in the range of temperatures tested with an H_2/CO= 2 syngas fed to the reactor. 5Co did not show any activity to FT reaction in the experimental condition tested. 10Co sample showed

a great stability in function of TOS at T= 250 °C, reactants conversion and selectivity towards the reaction products were stable for the whole duration of the durability test (TOS= 200 h). The addition of 0.4 %wt of Ru improved significantly catalyst activity in terms of reactant conversion. Moreover, both catalysts showed good results in terms of products selectivity, which does not change in the range of temperatures tested. The nonlinear regression of the kinetic parameters allowed a good reproduction of the experimental data obtained in the FT laboratory reactor.

(3) $Fe_{10}US$, $Fe_{30}US$, $Fe_{30}K_2Cu_{3.75}US$

The BET analysis showed that $Fe_{30}US$ and $Fe_{30}K_2Cu_{3.75}US$ present a larger surface area if compared with traditional impregnated catalysts. The iron nanoparticles are well dispersed on the SiO_2 surface with dimensions of about 20 nm. TPR profiles showed that both $Fe_{10}US$ and $Fe_{30}US$ samples present the same reduction temperature (T= 350 °C) while the addition of 2.0 %wt of K and 3.75 %wt of Cu shifted the first reduction peak to lower temperatures of about 50 °C. All the US synthesized samples are suitable catalysts for the FT reaction at the different tested conditions and with a H_2/CO ratio equal to 2. Both $Fe_{10}US$ and $Fe_{30}US$ catalysts showed excellent stability as a function of TOS at all the tested reaction temperatures.

The sonochemically prepared catalysts showed good results in terms of selectivity toward the reaction products. Ultrasound synthesized catalysts provided higher steady state CO conversion and better selectivity to reaction products when compared to traditional impregnated catalysts.

References

[1] EIA, Annual Energy Outlook 2015, (2015) 154. doi:DOE/EIA-0383(2013).

[2] P.K. Swain, L.M. Das, S.N. Naik, Biomass to liquid: A prospective challenge to research and development in 21st century, Renew. Sustain. Energy Rev. 15 (2011) 4917–4933. doi:10.1016/j.rser.2011.07.061.

[3] S.S. Ail, S. Dasappa, Biomass to liquid transportation fuel via Fischer Tropsch synthesis – Technology review and current scenario, Renew. Sustain. Energy Rev. 58 (2016) 267–286. doi:10.1016/j.rser.2015.12.143.

[4] C. Pirola, A. Di Fronzo, F. Galli, C.L. Bianchi, A. Comazzi, F. Manenti, Biosyngas conversion by Fischer-Tropsch synthesis: Experimental results and multi-scale simulation of a pbr with high Fe loaded supported catalysts, Chem. Eng. Trans. 37 (2014) 595–600.

[5] W. Ma, G. Jacobs, D.E. Sparks, J.L.S. Klettlinger, C.H. Yen, B.H. Davis, Fischer–Tropsch synthesis and water gas shift kinetics for a precipitated iron catalyst, Catal. Today. (2016) -. doi:http://dx.doi.org/10.1016/j.cattod.2016.01.006.

[6] K. Shimura, T. Miyazawa, T. Hanaoka, S. Hirata, Fischer-Tropsch synthesis over alumina supported cobalt catalyst: Effect of promoter addition, Appl. Catal. A Gen. 494 (2015) 1–11. doi:10.1016/j.apcata.2015.01.017.

[7] A. Comazzi, C. Pirola, A. Di Michele, M. Compagnoni, F. Galli, I. Rossetti, et al., Flame Spray Pyrolysis as fine preparation technique for stable Co and Co/Ru based catalysts for FT process, Appl. Catal. A Gen. 520 (2016) 92–98. doi:10.1016/j.apcata.2016.04.010.

[8] B. Todic, L. Nowicki, N. Nikacevic, D.B. Bukur, Fischer-Tropsch synthesis product selectivity over an industrial iron-based catalyst: Effect of process conditions, Catal. Today. 261 (2016) 28–39. doi:10.1016/j.cattod.2015.09.005.

[9] S. Abelló, D. Montané, Exploring iron-based multifunctional catalysts for Fischer-Tropsch synthesis: A review, ChemSusChem. 4 (2011) 1538–1556. doi:10.1002/cssc.201100189.

[10] A.N. Pour, M.R. Housaindokht, S.F. Tayyari, J. Zarkesh, Kinetics of the water-gas shift reaction in Fischer-Tropsch synthesis over a nano-structured iron catalyst, J. Nat. Gas Chem. 19 (2010) 362–368. doi:10.1016/S1003-9953(09)60085-2.

[11] G.P. Van Der Laan, A.A.C.M. Beenackers, Kinetics and Selectivity of the Fischer–Tropsch Synthesis: A Literature Review, Catal. Rev. Sci. Eng. 41 (1999) 255–318. doi:10.1016/j.apcata.2013.10.061.

[12] A. Di Fronzo, Biomass to Liquid Process: new kind of cobalt and iron based catalysts for the Fischer-Tropsch Synthesis, (2013). https://air.unimi.it/retrieve/handle/2434/229549/297889/phd_unimi_R09037.pdf.

[13] J.H. Bang, K.S. Suslick, Applications of ultrasound to the synthesis of nanostructured materials, Adv. Mater. 22 (2010) 1039–1059. doi:10.1002/adma.200904093.

[14] L.T. Canham, M.R. Houlton, W.Y. Leong, C. Pickering, J.M. Keen, Atmospheric impregnation of porous silicon at room temperature, J. Appl. Phys. 70 (1991) 422–431. doi:10.1063/1.350293.

[15] A. Comazzi, C. Pirola, C.L. Bianchi, F. Galli, M. Longhi, F. Manenti, High-loaded Fe-supported catalyst for the thermochemical BTL-FT process: Experimental results and modelling, Can. J. Chem. Eng. 94 (2016) 696–702. doi:10.1002/cjce.22357.

[16] L. Mädler, H.K. Kammler, R. Mueller, S.E. Pratsinis, Controlled synthesis of nanostructured particles by flame spray pyrolysis, J. Aerosol Sci. 33 (2002) 369–389. doi:10.1016/S0021-8502(01)00159-8.

[17] G.L. Chiarello, I. Rossetti, L. Forni, Flame-spray pyrolysis preparation of perovskites for methane catalytic combustion, J. Catal. 236 (2005) 251–261. doi:10.1016/j.jcat.2005.10.003.

[18] K.S. Suslick, T. Hyeon, M. Fang, A.A. Cichowlas, Sonochemical synthesis of nanostructured catalysts, Mater. Sci. Eng. A. 204 (1995) 186 – 192.

[19] H. Xu, B.W. Zeiger, K.S. Suslick, Sonochemical synthesis of nanomaterials., Chem. Soc. Rev. 42 (2013) 2555–67. doi:10.1039/c2cs35282f.

[20] C.L. Bianchi, C. Pirola, V. Ragaini, Choosing the best diluent for a fixed catalytic bed: The case of CO hydrogenation, Catal. Commun. 7 (2006) 669–672. doi:10.1016/j.catcom.2006.02.004.

[21] C. Pirola, C.L. Bianchi, A. Di Michele, S. Vitali, V. Ragaini, Fischer Tropsch and Water Gas Shift chemical regimes on supported iron-based catalysts at high metal loading, Catal. Commun. 10 (2009) 823–827. doi:10.1016/j.catcom.2008.12.006.

[22] K.R.P. D. Bukur, K. Okabe, M. P. Rosynek, C. Li, D. Wang, G.P.H. M. Rao, Activation Studies with a Precipitated Iron Catalyst for Fischer-Tropsch Synthesis: I. Characterization Studies, (1995) 353–365.

[23] A.N. Pour, Y. Zamani, A. Tavasoli, S.M. Kamali Shahri, S.A. Taheri, Study on products distribution of iron and iron-zeolite catalysts in Fischer-Tropsch synthesis, Fuel. 87 (2008) 2004–2012. doi:10.1016/j.fuel.2007.10.014.

[24] Zimmerman, Bukur, Reaction kinetics over iron catalysts used for the Fischer-Tropsch synthesis, Can. J. Chem. Eng. 68 (1990) 292–301. doi:10.1002/cjce.5450680215.

[25] A. Rafiee, Optimal design issues of a gas-to-liquid process, (2012).

[26] E.S. Lox, G.F. Froment, Kinetics of the Fischer-Tropsch reaction on a precipitated promoted iron catalyst. 2. Kinetic modeling, Ind. Eng. Chem. Res. 32 (1993) 71–82. doi:10.1021/ie00013a010.

[27] H.Y. Lin, Y.W. Chen, The mechanism of reduction of cobalt by hydrogen, Mater. Chem. Phys. 85 (2004) 171–175. doi:10.1016/j.matchemphys.2003.12.028.

[28] J. Jansson, Low-Temperature CO Oxidation over Co3O4/Al2O3, J. Catal. 194 (2000) 55–60. doi:10.1006/jcat.2000.2924.

[29] S.E. Pratsinis, Flame aerosol synthesis of ceramic powders, Prog. Energy Combust. Sci. 24 (1998) 197–219. doi:10.1016/S0360-1285(97)00028-2.

[30] N. Fischer, E. Van Steen, M. Claeys, Structure sensitivity of the Fischer-Tropsch activity and selectivity on alumina supported cobalt catalysts, J. Catal. 299 (2013) 67–80. doi:10.1016/j.jcat.2012.11.013.

[31] K. Cheng, V. Subramanian, A. Carvalho, V. V. Ordomsky, Y. Wang, A.Y. Khodakov, The role of carbon pre-coating for the synthesis of highly efficient cobalt catalysts for Fischer-Tropsch synthesis, J. Catal. 337 (2016) 260–271. doi:10.1016/j.jcat.2016.02.019.

[32] I.C. Yates, C.N. Satterfield, Intrinsic Kinetics of the Fischer-Tropsch Synthesis on a Cobalt Catalyst, Energy & Fuels. 5 (1991) 168–173. doi:10.1021/ef00025a029.

[33] D. Vervloet, F. Kapteijn, J. Nijenhuis, J.R. van Ommen, Fischer–Tropsch reaction–diffusion in a cobalt catalyst particle: aspects of activity and selectivity for a variable chain growth probability, Catal. Sci. Technol. 2 (2012) 1221. doi:10.1039/c2cy20060k.

[34] M.K. Gnanamani, G. Jacobs, U.M. Graham, M.C. Ribeiro, F.B. Noronha, W.D. Shafer, et al., Influence of carbide formation on oxygenates selectivity during Fischer-Tropsch synthesis over Ce-containing Co catalysts, Catal. Today. 261 (2016) 40–47. doi:10.1016/j.cattod.2015.08.047.

[35] C. Pirola C, L. Bianchi, A. Di Michele, P. Diodati, S. Vitali, V. Ragaini, High loading Fe-supported fischer-tropsch catalysts: Optimization of the catalyst performance, Catal. Letters. 131 (2009) 294–304. doi:10.1007/s10562-009-0060-6.

[36] K.S. Suslick, T. Hyeon, M. Fang, Nanostructured Materials Generated by High-Intensity Ultrasound: Sonochemical Synthesis and Catalytic Studies, Chem. Mater. 8 (1996) 2172–2179. doi:10.1021/cm960056l.

[37] Y. Jin, A.K. Datye, Phase Transformations in Iron Fischer–Tropsch Catalysts during Temperature-Programmed Reduction, J. Catal. 196 (2000) 8–17. doi:http://dx.doi.org/10.1006/jcat.2000.3024.

[38] S. Li, S. Krishnamoorthy, A. Li, G.D. Meitzner, E. Iglesia, Promoted Iron-Based Catalysts for the Fischer–Tropsch Synthesis: Design, Synthesis, Site Densities, and Catalytic Properties, J. Catal. 206 (2002) 202–217. doi:10.1006/jcat.2001.3506.

[39] K. Cheng, V.V. Ordomsky, M. Virginie, B. Legras, P. a. Chernavskii, V.O. Kazak, et al., Support effects in high temperature Fischer-Tropsch synthesis on iron catalysts, Appl. Catal. A Gen. 488 (2014) 66–77. doi:10.1016/j.apcata.2014.09.033.

[40] K. Keyvanloo, W.C. Hecker, B.F. Woodfield, C.H. Bartholomew, Highly active and stable supported iron Fischer-Tropsch catalysts: Effects of support properties and SiO2 stabilizer on catalyst performance, J. Catal. 319 (2014) 220–231. doi:10.1016/j.jcat.2014.08.015.

1 Introduction

The world energy demand is increasing quickly during the recent decades due to the growing of the earth population and to the exponential growth of industries, which will result in greater volumes of emitted pollutant [1]. For these reasons it is necessity to develop chemical and thermochemical processes able to exploit natural sources and to valorize waste and by-products produced by the other industries.

In particular, the Annual Energy Outlook 2015 [2] indicated that the energy demand will increase by an average value equal to 0.3 % per year from now to 2040 and the strongest energy consumption will be given by the industrial sector with a demand increase equal to 0.7 % per year through 2040. This increase in the global energy demand will result in an increase of the price and the extraction rate of the crude oil but, on the other and it will stimulate the renewable energy production which will growth by 72 % to 2040 in order to meet much of the growth in electricity demand. In particular the electrical energy can be produced exploiting different ways beside traditional renewable as nuclear, natural gas, coal and biomass.

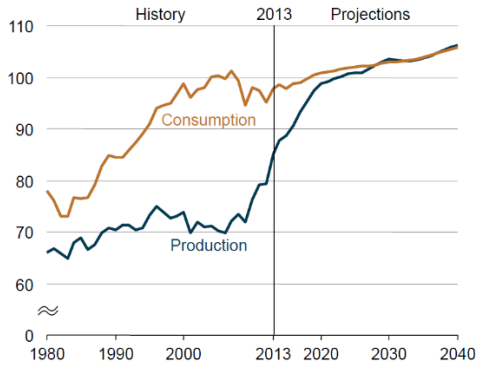

Figure 1.1: Projections of production and consumption of energy through 2040 (quadrillion of BTU) [2].

During the upcoming decade, it will be required to develop and optimize chemical processes able to take advantages of all the potentiality that natural resources can offer for example, due to the content of chemical compounds based on carbon and hydrogen, coal, natural gas and biomasses can be used in several processes for the conversion of these feedstocks into fuels. These three different raw materials can be converted into syngas, i.e. a mixture of H_2 and CO, with different technologies and then finally converted into fuels via Fischer-Tropsch (FT) synthesis [3]. Syngas can be

used not only as a reactant mixture for fuels, but also as a starting material for the production of a wide range of chemical compound.

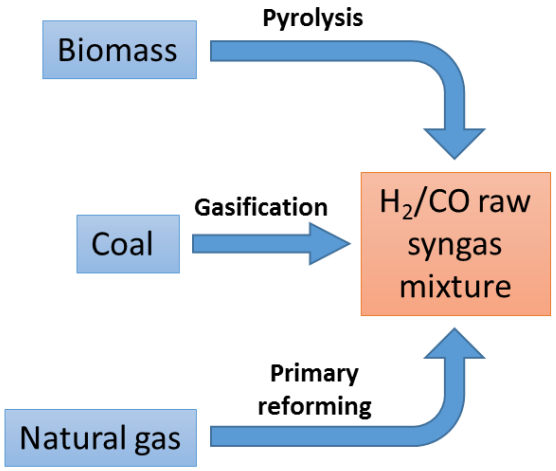

Figure 1.2: Syngas production from biomass, coal and natural gas.

Depending on the type of feedstock, syngas can be produced exploiting different chemical or thermochemical reaction. The type of the raw material used as a source of syngas is dependent of its availability, for example Russia is the greatest natural gas producer in the world, USA have the biggest coal reserves while for South America is the first producer of biomass in the world.

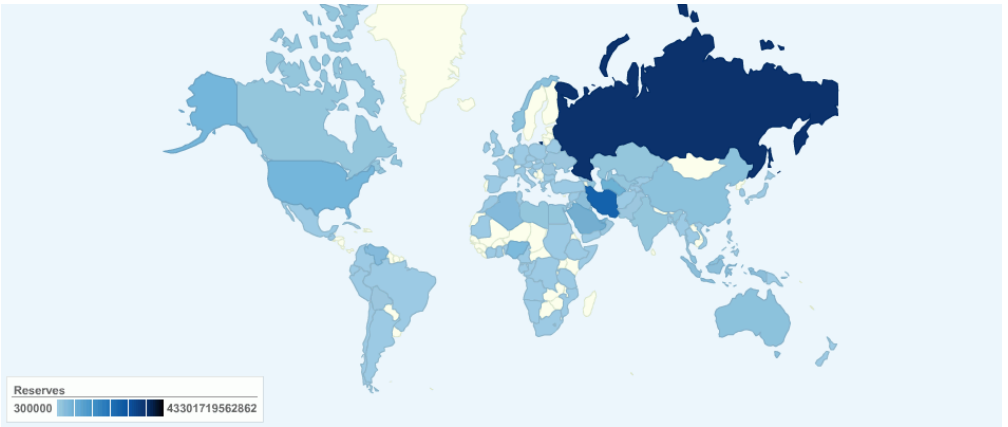

Figure 1.3: Natural gas reserves in the world (m^3) [ChartsBin statistics collector team, Current Worldwide Natural Gas reserves].

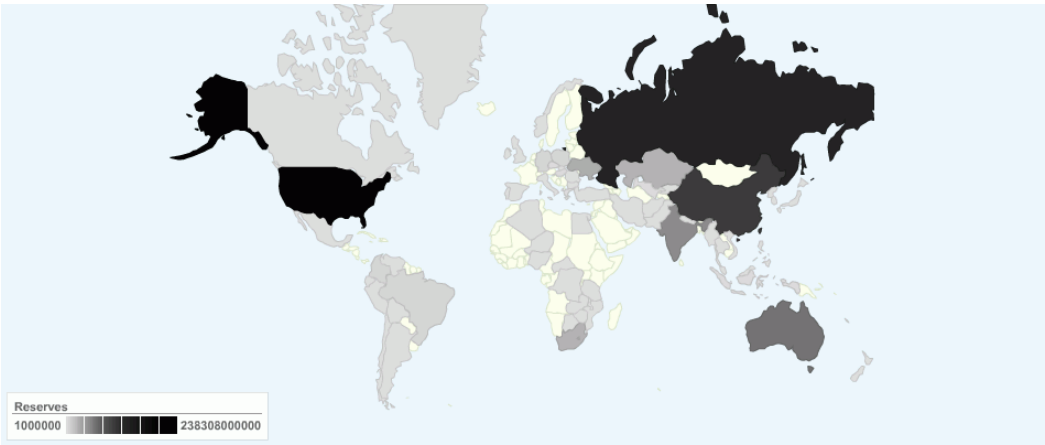

Figure 1.4: Coal reserves in the world (tons) [ChartsBin statistics collector team, Current Worldwide coal reserves].

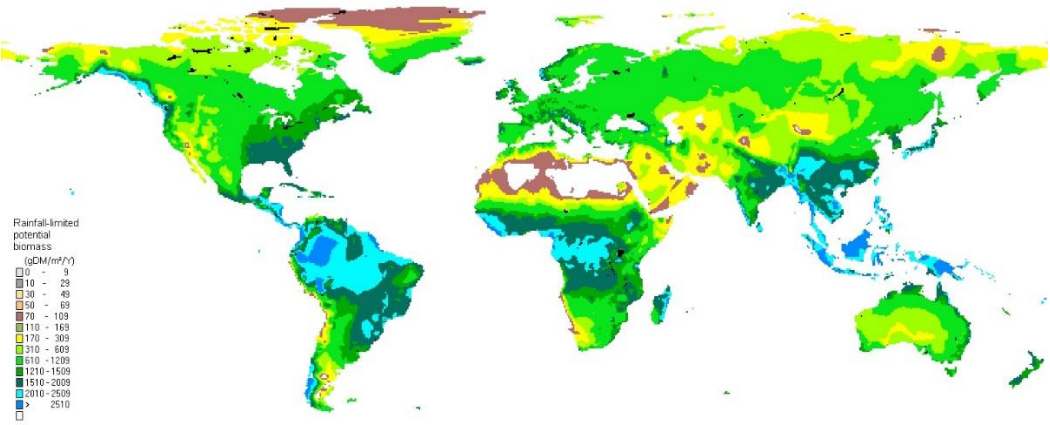

Figure 1.5: World biomass resources [4].

Once that the syngas mixture is produced, it must be purified due to the content of impurities and by products. For example, biomass derived syngas even called bio-syngas, contains CO_2, CH_4, N_2, HCl, H_2S and NH_3 in various portions [5]. The cleaning process is necessary in order to meet the reaction specifications, such as a good H_2/CO ratio.

After these first steps, the hydrogen/carbon monoxide gas mixture is ready to be converted in different chemicals compounds with catalytic processes. The most important products that can be obtained from syngas are aldehydes and alcohols like ethanol and methanol; in particular this latter opens a wide range of ways for the production of important molecules such as acetic acid, olefins, MTBE and DME.

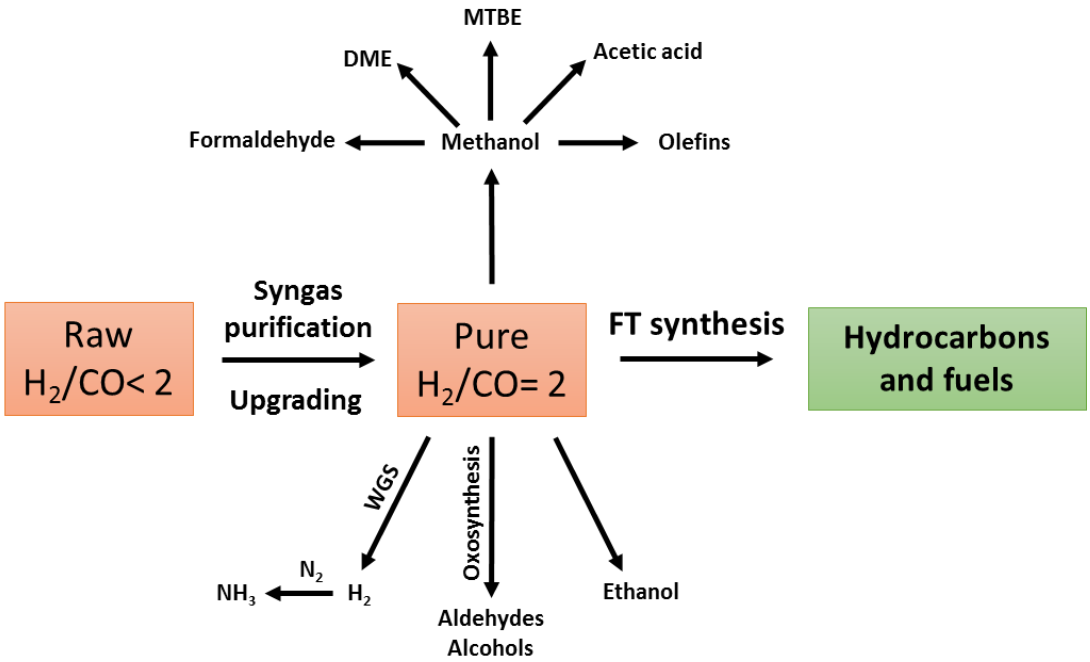

Figure 1.6: Example scheme of chemical products obtainable from syngas.

The FT reaction is in the heart of the conversion of the syngas into liquids products as hydrocarbons and fuels. In particular the FT synthesis is an array of strong exothermic irreversible reactions ($\Delta H \approx$ -200 kJ·mol$_{CO converted}^{-1}$) [6]. The main target of the FT synthesis is to produce linear and branched paraffins and olefins in the range C_1-C_{100} while limiting the synthesis of CH_4 and CO_2 which are undesired products of the reaction.

The main FT reactions and equilibria are reported hereinafter (Eqs 1.1- 1.5) [7]:

Alkanes production:

$$(2n+1)\ H_2 + n\ CO \rightarrow C_nH_{2n+2} + n\ H_2O \qquad \text{(Eq. 1.1)}$$

Alkenes production:

$$2n\ H_2 + n\ CO \rightarrow C_nH_{2n} + n\ H_2O \qquad \text{(Eq. 1.2)}$$

Production of oxygenated compounds:

$$2n\ H_2 + n\ CO \rightarrow C_nH_{2n+2}O + (n-1)\ H_2O \qquad \text{(Eq. 1.3)}$$

Boudouard equilibria:

$$2\ CO \leftrightarrow CO_2 + C \qquad \text{(Eq. 1.4)}$$

WGS synthesis:

$H_2O + CO \leftrightarrow H_2 + CO_2$ (Eq. 1.5)

FT requires catalysts based on iron or cobalt, Co is more expansive but it guarantees greater yield and better selectivity to long chain hydrocarbons. On the other hand, iron is less active but it is suitable even if syngas with low H_2/CO molar ratio due to the activity to the WGS equilibria which can raise the H_2/CO ratio to 2, which is the stoichiometry required by the FT reaction. This feature makes iron a good candidate as an active metal for the conversion of biomass derived syngas.

Depending on the source of raw syngas that will be then converted in liquid products via FT synthesis, the whole process will be called in different ways. If biomasses are used as starting compound, it is called biomass-to-liquid Fischer-Tropsch process (BTL-FT), if coal is converted into hydrogen and carbon monoxide, coal-to-liquid Fischer-Tropsch process (CTL-FT), while if natural gas is used as a source of syngas the name is gas-to-liquid Fischer-Tropsch process (GTL-FT).

1.1 The biomass-to-liquid (BTL) process

The biomasses are playing a key role in the future energy scenario because they are the only natural and renewable energy sources with carbon content. A wide range of biomasses can be directly burned or used in thermal processes for the direct conversion into liquid products like bio-ethanol [8].

For example, wood is constituted of about 80 % of volatile compounds and close to only 20 % char can be converted to gaseous fuels. The BTL process offers a good route for the reduction of the use of fossil fuels and a positive key in order to reduce the emission of carbon dioxide in the atmosphere, in fact a 15 % loss in CO_2 emission is expected just by replacing fossil fuels. Moreover, BTL allows a closed loop of the CO_2 produced [9].

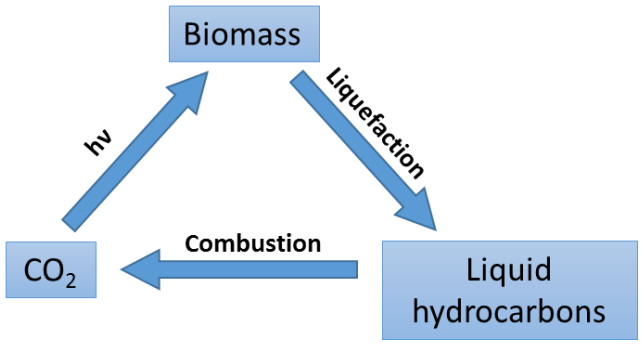

Figure 1.7: CO_2 closed loop achievable in the BTL process.

Biomasses can be divided into three big different sectors, agricultural biomasses, forestry and waste. Each one of them result in a different end-use. The most common biomass types with the relative use, are summarized in Table 1.1.

Sector	Biomass type	End-use
Agriculture	Sugar, starch and oil crops lignocellulosic biomass	Bio-fuel Hydrogen production
	Energy maize	Combustion
	Dry and liquid manure	Downstream electricity production
	Olive pits	Combustion
	Pruning and straw/stubble	Combustion
Forestry	Stemwood	Electricity production, hydrogen production
	Logging residue and landscape care	Biomass gasification, bio-syngas production
	Woodchips, pellets, sawdust and black liquor	Biomass gasification, bio-syngas production
Waste	Biodegradable waste	Cogeneration and electric generation
	Other waste	Cogeneration and gasification

Table 1.1: Most common biomass types and their use [10].

Nowadays there are several chemical processes able to achieve the production of fuel derived from biomass that have been already studied and developed; these processes are fast pyrolysis (FP), direct liquefaction of biomass, transesterification of vegetable oils, agricultural crops derived bio-ethanol, production of bio-oil from algae, and the FT process for the conversion of biomass derived syngas (bio-syngas) into hydrocarbons.

In the fast pyrolysis of biomass the raw material is treated at high temperatures, T= 450- 500 °C in inert atmosphere, with very high heating rates (≈ 10^4 K/s) [11]. Even if the fast pyrolysis process guarantees high yield of total product (≈ 65- 70 %wt) [12] it presents some problems due to the energy efficiency and to the industrial scale of the process. Moreover, FP produces pyrolytic oils with an high content of oxygen and water which makes FP products low-quality fuels if compared with the one obtainable with other technologies [13,14].

The direct liquefaction is a catalytic process which involves the reaction of dry biomass with hydrogen at very high pressure, P= 150- 200 bar and T= 300- 370 °C. The general reaction of the direct liquefaction process is [15]:

$CH_{1.4}O_{0.7} \rightarrow -CH_2-$ (Eq. 1.6)

The most common industrial direct liquefaction process is the hydrothermal upgrading (HTU), which is carried out with high water biomass ratio, H_2O/biomass= 3/1- 10/1 and residence time equal to 4- 10 minutes [16]. The direct liquefaction usually requires catalysts based on iron, but the literature is full of different example where the process is carried out with Mo, Co and Ru based catalysts. The large presence of oxygen in the produced fuels, the difficult separation of liquids and solids products and the high demand of hydrogen as a reactant make the direct liquefaction of biomass a difficult scalable process to commercial volumes.

The transesterification of vegetable oils is carried out using MeOH with NaOH or KOH, used as homogeneous catalysts dissolved in the reactant [17]. The process is simple and produces methyl esters-based bio-diesel which has equal characteristics to the conventional fuels. The vegetable oils can be produced from palms (palm oil), coconut and jatropha. The main drawbacks of this process are the big amount of by-products and wastewaters produced and the purifications procedures of the main product, coupled with the cleaning process required by the catalyst [18]. In order to make the transesterification of vegetable oil a feasible process for bio-fuels production a good recovery of the useless products (proteins and glycerin) must be taken into account in the overall production.

During the recent years a lot of research efforts have been directed towards the production of bio-fuels from algae. Despite this kind of technology is only in its emergent step, the first experimental results achieved are really encouraging thanks to the high yield reachable in the production of algae bio-diesel which are almost 10-20 times higher respect to the conventional vegetable oil bio-fuels [19]. In particular, the oil level per gram of dry biomass can be close to 80 % in the case of algae, while this percentage is equal to 20- 50 % for traditional vegetable oils. On the other hand, the production of algae is extremely expansive if compared with oil crops. The microalgae are grown in photo-reactor and they need an adequate supply of nutrients, pure water and CO_2; moreover, the growth of the biomass is strongly influenced by the environmental factors such as temperature and exposure to sunlight [20]. These reasons make the bio-fuel production from microalgae a challenging research topic for the upcoming years, but at the moment the high cost for the production of the starting material is an unfavorable point for the industrial scale up of this technology.

1.1.1 The BTL-FT process

Differently from the other biomass liquefaction process, the BTL-Fischer-Tropsch involves three main steps, the first one is the bio-syngas production from biomass, the second one is the bio-syngas cleaning/upgrading and the last one is the final FT reaction which converts the bio-syngas into bio-fuels [21]. Depending on the type of biomass used, several types of pretreatment could be carried out.

Biomass derived syngas usually contains CO, H_2, CO_2, CH_4, and N_2 in different quantity [6]. The composition of the bio-syngas is strongly influenced by the type of biomass gasified.

Component	Wood gas (air)	Charcoal gas (air)	Bio-syngas (N_2 free)
N_2	50- 60	55- 65	0
CO	14- 25	28- 32	28- 36
CO_2	9- 15	1- 3	22- 32
H_2	10- 20	4- 10	21- 30
CH_4	2- 6	0- 2	8- 11
C_2H_4	n/a	n/a	2- 4
BTX	n/a	n/a	0.84- 0.96
C_2H_5	n/a	n/a	0.16- 0.22
Tar	n/a	n/a	0.15- 0.24
Others	n/a	n/a	< 0.021

Table 1.2: composition of bio-syngas using charcoal and wood as raw biomass, and an example of N_2 free bio-syngas [22].

In addition to the content of impurities with respect to traditional syngas, the bio-syngas has a lower H_2/CO ratio (≈ 1- 1.5). For this reason the choice of the catalytic system for the FT step plays a crucial role in the overall feasibility of the whole process. In particular, if after the cleaning process bio-syngas is directly fed to the Fischer-Tropsch unit, the reaction must be catalyzed by an Fe-based catalyst, because iron is a metal active in the WGS synthesis therefore it can increase the H_2/CO ratio to the value of 2. Otherwise, if the FT reaction is carried out with a Co-based catalyst, a WGS reactor must be included before the FT unit in order to raise the hydrogen/carbon monoxide ratio to the stoichiometry required by the Fischer-Tropsch reaction. A general scheme of a BTL-FT process carried out with both Fe or Co catalysts is reported in Figure 1.8.

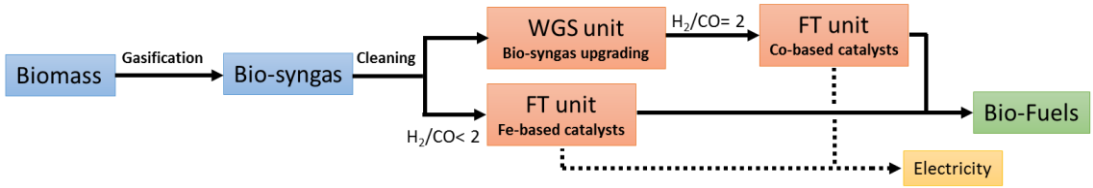

Figure 1.8: General scheme of a BTL-FT plant.

1.1.1.1 Biomass gasification

The gasification process involves several reactions that convert carbonaceous feedstocks, such as wood and agricultural wastes, into the bio-syngas mixture. Generally, if the biomass used for the gasification step is a clean biomass, like wood produced from dedicated plantations, even the produced bio-synthesis gas will be clean [23].

In order to achieve a good gasification yield, it is very important that the biomass has an uniform and optimized size (20- 80 mm), for this reasons several pre-treatment technologies could be carried out before the gasification step. The most important pretreatment technologies are torrefaction, drying and pelletization.

The drying pre-treatment can improve the whole efficiency of gasification because it reduces the water content of the biomass feedstock to 10- 15%. On the other hand, it also reduces the H_2 in the gas product, forming a bio-syngas with a low H_2/CO ratio [24].

The torrefaction is a thermal treatment which provides a very high efficiency, close to 94 %. It is carried out at T= 250- 300 °C in inert atmosphere with the aim to produce a uniform solid biomass product with a low H_2O content.

The pelletization is a mechanical pre-treatment useful to lower the size of the pellet of biomass with the result to increase the volumetric energy density. This process can be described as drying and compressing biomass to produce cylindrical pieces.

Once that biomass has the right water content a size, it is ready to be gasified. The general gasification reaction is (Eq. 1.7) [22]:

$$\text{Biomass} + O_2/H_2O \rightarrow CO + CO_2 + H_2 + H_2O + CH_4 + C_mH_n + \text{tar/char/ash} \quad \text{(Eq. 1.7)}$$

The first step of the gasification process is thermochemical where cellulose, hemicelluloses and lignin compounds are decomposed into tar, after that several equilibria reactions start. The detailed description of the gasification reactions is reported hereinafter (Eqs. 1.8- 1.16) [22]:

$$C_nH_mO_x \rightarrow CO + CO_2 + H_2 + H_2O + CH_4 + (C_2\text{- }C_5) \quad \text{(Eq. 1.8)}$$

$C + O_2 \rightarrow CO_2$ (Eq. 1.9)

$C + ½\ O_2 \rightarrow H_2O$ (Eq. 1.10)

$C + H_2O \rightarrow CO + H_2$ (Eq. 1.11)

$C + 2\ H_2O \rightarrow CO_2 + 2\ H_2$ (Eq. 1.12)

$C + CO_2 \rightarrow 2\ CO$ (Eq. 1.13)

$C + 2\ H_2 \rightarrow CH_4$ (Eq. 1.14)

$CO + 3\ H_2 \rightarrow CH_4 + H_2O$ (Eq. 1.15)

$C + H_2O \rightarrow ½\ CH_4 + ½\ CO_2$ (Eq. 1.16)

Even though the chemical reactions involved in the gasification step are known, it is very difficult to predict the final composition of the bio-syngas. It is influenced by different factors, first of all the type of biomass, the gasifier agent, the operating parameters (temperature and pressure) and then by the geometry of the gasifier [24]. Several types of industrial biomass gasifier are available nowadays, in order to guarantee a good hydrodynamic using different gasifier agents, and conditions. The most important are the updraft fixed bed gasifiers, downdraft fixed bed gasifiers, fluidized-bed gasifiers, and entrained flow gasifiers.

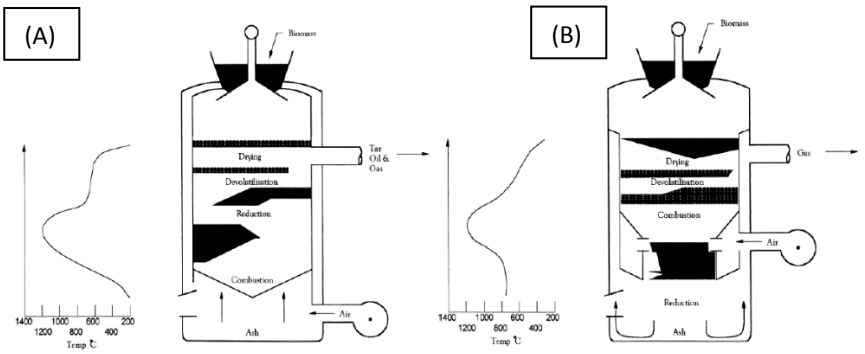

Figure 1.9: Scheme of a downdraft gasifier (A) and an updraft one (B) [24].

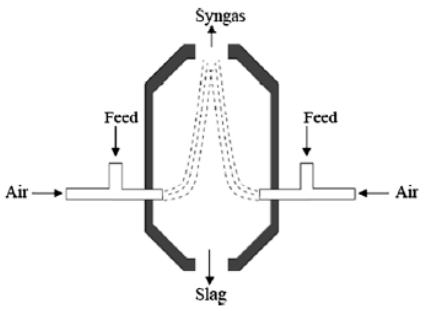

Figure 1.10: Scheme of an entrained flow gasifier [24].

In the updraft configuration the reactant feed is introduced from the top and goes down while the gasifying agent (O_2 or stream) pass from the bottom to the top. The combustion area is placed in the bottom of the bed at T= 500 °C. In the downdraft gasifier both biomass feed and gasifying agent move downward, at a T= 800 °C.

If the gasification process needs higher temperatures (T= 1000 °C) an entrained flow gasifier is required. In this configuration, the mass feed and air are introduced co-currently and the reactions happen at high pressures (P= 20- 70 bar). Due to the high temperature this kind of gasifier can process even coal feedstock but it requires very small dimensions feeds with respect to the other gasifier. The advantages and disadvantages of the most common gasifier are reported in Table 1.3 [22].

Gasifier type	Advantages	Disadvantages
Updraft	- Simple, inexpensive process - Exit gas temperature about T= 250 °C - Operates satisfactorily under pressure - High carbon conversion efficiency - Low dust levels in gas - High thermal efficiency	- Large tar production - Potential channeling - Potential bridging - Small feed size - Potential clinkering
Downdraft	- Simple process - Only traces of tar in gas product	- Minimum feed size - Limited ash content allowable in feed - Limits to scale up capacity
Fluidized bed	- Flexible feed rate and composition - High ash fuels acceptable - Able to pressurize - High CH_4 in gas product - High volumetric capacity - Easy temperature control	- Operating temperature limited by ash clinkering - High gas product temperature - High tar and fines content in gas - Possibility of high C content in fly ash
Entrained bed	- Very low in tar and CO_2 - Flexible to feedstock - Exit gas temperature	- Low in CH_4 - Feed size reduction required - Complex operational control

Table 1.3: Advantages and disadvantages of the most common gasifiers.

1.1.1.2 Bio-syngas cleaning process

Even if the gasification process is carried out under optimized conditions, the produced bio-syngas usually contains impurities which make it not meeting the FT requirements. These impurities can decrease the activity of the FT catalyst resulting in a lower efficiency of the whole process. The syngas FT requirements are summarized in Table 1.4.

Impurity	Specification
$H_2S + COS + CS_2$	< 1 ppmv
NH_3 + HCN	< 1 ppmv
HCl + HBr + HF	< 10 ppbv
Alkali metals (Na + K)	< 10 ppbv
Particles (soot, ash)	"almost removed"
Organic components (tar)	below dew point
Hetero-organic components (S, N, O)	< 1 ppmv

Table 1.4: Syngas specifications to meet the FT requirements (ppmv= part per million per volume; ppbv = part per billion per volume) [22].

The impurities in bio-syngas are usually divided into three types [22]:

- 1: Organic impurities (tars, Benzene, Toluene, and Xylenes)

There are two types of tar cracking methods in order to decrease the content of organic impurities: thermal cracking and catalytic cracking. The catalytic process results in a tar conversion over 99 % by using Ni based catalysts [25].

- 2: inorganic impurities (O_2, NH_3, HCN, H_2S, COS, and HCl)

The O_2 level is decreased by using deoxidizers reactor packed with Pd/Al_2O_3 while ammonia is removed by aqueous scrubber or by decomposition process.

- 3: other impurities (dust and soot)

Dust, soot and other impurities can be removed by using cyclones, metal filters, moving beds, candle filters, bag filters, and special soot scrubber.

1.1.1.3 Fischer Tropsch unit

The Fischer-Tropsch step which follows the bio-syngas cleaning one, will be fully explained in Chapter 2 of this thesis.

1.1.1.4 Example of an economical evaluation of the BTL-FT process

In order to meet the European bio-fuels targets within 2020, a Fischer-Tropsch diesel production capacity of 785 PJ is required. The number of the BTL-FT processes necessary to satisfy the energy demand are strongly influenced by the capacity of every single plant. If only small-scale plants are considered, almost one thousand 50 MW_{th} BTL plants should be in operation in 2020, this number corresponds to an average of forty plants per European country, which is just a fictitious scenario due to insufficient suitable locations, different countries legislations and in some countries insufficient biomass resources. Otherwise, if only large plants would be available, only six plants of 8,500 MW_{th} would be required.

From a realistic point of view, it is possible to expect that ten to fifty plants with a capacity of 1000- 5000 MW_{th} is an optimal scenario, considering that in Europe there are almost one hundred of oil refinery plants, it means that a BTL plant has to be built on every third refinery. Moreover, large scale plants are required in order to limit the total costs of the plant. Operating a smaller BTL plant might be advantageous when cheap local biomasses are available.

In order to understand which will be the perfect scale of a BTL-FT plant that guarantees a satisfactory economic assessment, all the information about the entire production chain, from the biomass to the sell bio-fuel must be available.

Due to the presence of consolidated industrial processes, information regarding the cost of biomass, transportation and pre-treatments technologies are available, however for what concern data regarding the operating costs of a BTL process they are hard fundable, and the only results present in the public literature are academic examples.

H. Boerrigter [26] gave an example of a simplified estimation of an integrated BTL-FT plant, which can be represented as the one reported in Figure 1.8.

The proposed model is based on some assumption regarding the costs (i.e. biomass cost, transportation cost) which are summarized in Table 1.5.

The results obtained highlight that the overall cost of the process is highly influenced by the capacity of the plant. In particular production costs decrease from 30 €/GJ_{FT} for a 50 MW_{th} plant to just above 15 €/GJ_{FT} at a scale of 9,100 MW_{th}.

If the total cost is divided into costs due to transportation, biomass, pre-treatment and conversion (i.e. annual CAPEX and OPEX) is easy to observe that the capacity of the plant is almost irrelevant for the cost of the first three points. On the other hand, CAPEX and OPEX are the dominant cost factor when the capacity of the plant is below 2000 MW_{th}.

Even though the costs of the biomass does not vary as a function of the size of the plant, it adds 7.3 €/GJ to the FT diesel fuel costs. The cost of the energy produced from the FT plant is calculates with a total efficiency of the BTL-FT plant equal to 56 %.

The assumption and the results are reported hereinafter.

Parameter	Unit	Value
BIOMASS		
Forest fraction of land	[%]	38
Exploitable fraction of forest	[%]	50
Biomass production	[ton_{ds}/ha/year]	10
Biomass bulk density	[kg/m^3]	202
Biomass calorific value [LHV_{ar}]	[MJ/kg]	16.2
TRANSPORT		
Loading in forest	[€/m^3]	0.073
Biomass transport costs (truck) - fixed	[€/ton]	2.0
Biomass transport costs (truck) - variable	[€/ton/km]	0.08
Road distance efficiency	[-]	1.2
Storage costs at BTL plant (one week)	[€/m^3/year]	5.3
EFFICIENCIES		
Efficiency pre-treatment (chips to torrefied biomass)	[%]	97
Efficiency gasifier (torrefied biomass-to-biosyngas)	[%]	80
Efficiency fuel synthesis (bio-syngas to FT C_{5+} liquids)	[%]	71
Plant availability	[h/year]	8,000
ECONOMY		
Biomass costs (as received in forest: 7% moisture wood chips)	[€/GJ_{bm}]	4.0
Costs pre-treatment by torrefaction (fixed)	[€/GJ_{ptt}]	1.5
Required IRR	[%]	12
Depreciation period (linear)	[year]	15
Operation and Maintenance (O&M) costs	[% of annual investment]	5
Scale-up factor (constant)	[-]	0.7

Table 1.5: Input parameters for the economic assessment of production costs of BTL diesel fuel.

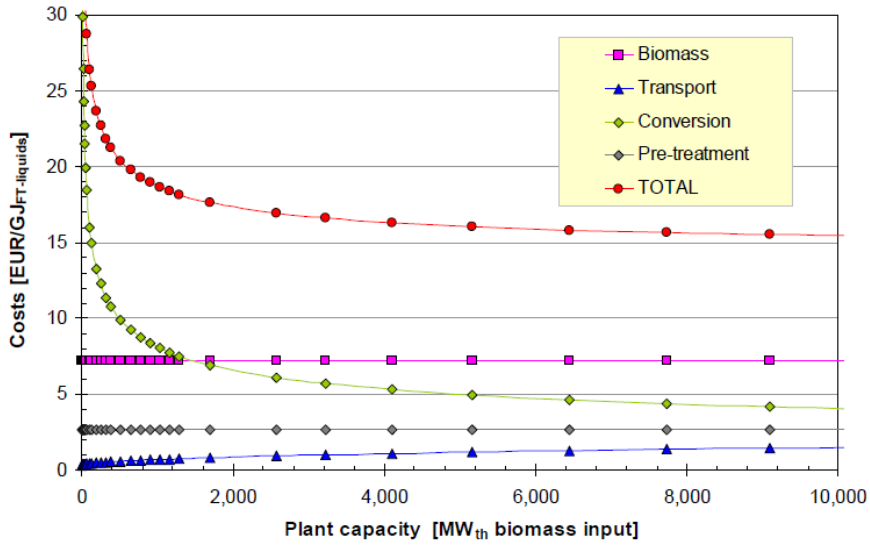

Figure 1.11: Scale dependency of Fischer-Tropsch diesel fuel production costs, including contributions of biomass feedstock costs, transport and storage, pre-treatment, and the conversion of the biomass into fuel [26].

From the results of the study that has been carried out, the main statements and findings are that the total capital investments (TIC) is higher of about 60 % with respect to a traditional GTL plant with the actual biomass costs, a large scale BTL-FT produces energy with a cost of 15 $/GJ, which means a fuel cost of approximately 0.55 $/L.

Whit the collected results, it is possible to affirm that the BTL-FT bio-diesel is competitive with the traditional crude-oil based fuels when the oil price is around 70 $/barrel. Therefore, based on economic considerations, it is advisable to direct technology development towards large BTL facilities.

1.2 The coal-to-liquid (CTL) process

Differently from biomass based technologies, the fuel production using coal as a feedstock is a quite old process developed in the beginning of the 20th century but, the recent emission problems and poor availability of crude oil, recently attached more attention on this kind of process [27]. From an historical point of view, CTL processes provided almost 90 % of fuels demand during the two world wars.

The development of this technology over the decades, made it suitable to handle a big quantity of different types of carbon but at the moment, the average conversion rates to liquid fuels are not very high. Depending on the type of coal used, and the

type of liquefaction process, a production rate between 1 or 2 barrels per ton of coal is expected. This fact puts very strict limitation regarding the use of coal as a world primary source for fuels production; however several CTL plants could be a good route to supply the fuels demand if coupled with other strategies, in those countries where coal and CTL technologies are highly available.

The most common types of coal are lignite (or brown coal) which is not suitable for liquefaction and it is directly used as a source of electricity; sub-bituminous coal, which has huge content of aromatics compound; bituminous coal which is a dense black/dark brown sedimentary rock and its primary use in the electricity production and to make coke; steam coal, used in vapor-powered train; anthracite, a hard and black coal which has the highest rank; graphite, the hardest coal to burn and it is usually not used as a fuel or source of fuels.

The coal can be divided into different categories, based on the different chemical composition.

Type	Volatiles (%wt)	C (%wt)	H (%wt)	O (%wt)	S (%wt)
Lignite	45- 65	60- 75	6- 5.8	34- 17	0.5- 3
Flame coal	40- 45	75- 82	6- 5.8	> 9.8	≈ 1
Gas flame coal	35- 40	82- 85	5.8- 5.6	9.8- 7.3	≈ 1
Gas coal	28- 35	85- 87.5	5.6- 5	7.3- 4.5	≈ 1
Fat coal	19- 28	87.5- 89.5	5- 4.5	4.5- 3.2	≈ 1
Forge coal	14- 19	89.5- 90.5	4.5- 4	3.2 2.8	≈ 1
Nonbaking coal	10- 14	90.5- 91.5	4- 3.75	2.8- 3.5	≈ 1
Anthracite	7- 12	> 91.5	< 3.75	< 2.5	≈ 1

Table 1.6: Elementary composition of different types of coal [28].

Similarly to the use of biomasses, even the use of coal imply a purification process in order to remove the sulfur compounds and other impurities which are present in the order of ppm, like mercury, arsenic and selenium.

The production of liquid fuels from coal can follow two different routes, the first one is the direct liquefaction (DCL) which produces fuels directly from coal, while the second one is an indirect liquefaction (ICL) which add another step before the final fuel production. This intermediate step is the gasification of the coal in order to produce syngas, followed by the syngas conversion via FT synthesis.

The two most important processes for the direct liquefaction of coal are the pyrolysis, the oldest one, and the Bergius process. Pyrolysis does not have high yield and the technological scale up lead very high costs. The liquefaction procedure is carried out by heating the coal up to T= 950 °C in a closed reactor. This high temperature favor the thermal decomposition of the coal and at the same time the volatile compounds produced are purged out; as a result, the carbon content is increased. Pyrolysis could

be also carried out at lower temperatures around T= 450- 650 °C in order to maximize the production of char and coke. This technique has been applied for the upgrading of low-rank coal rather than a fuels production process. Mid-temperature pyrolysis has greater yields respect to the high-temperature one, but with a maximum of ≈ 20 % [27].

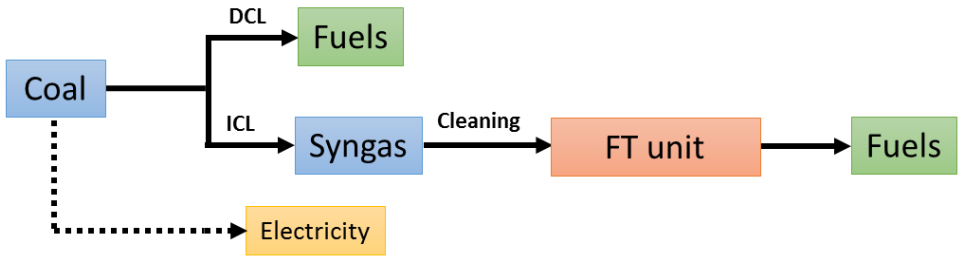

Figure 1.12: General scheme of a CTL process

The second way to produce liquid hydrocarbons via direct liquefaction, is the Bergius catalytic process; the main reaction is (Eq. 1.17):

$$n\,C + (n+1)\,H_2 \rightarrow C_nH_{2n+2} \qquad \text{(Eq. 1.17)}$$

The reaction splits the carbonaceous matrix into lower hydrocarbons with the addition of hydrogen. Basically, the Bergius synthesis is an hydro-cracking reaction carried out at high temperatures and pressures. This kind of process requires catalysts based on transition metals, the most commons are iron, cobalt or ruthenium.

The Bergius DCL process provides higher yields (≈ 70 %) if compared with pyrolysis and moreover the fuels produced have better quality. However, even though this kind of liquefaction presents these good factors, the produced hydrocarbons require several refining treatments before they can be used or commercialized.

Anyhow, DCL processes are affected by some drawbacks, for example the reactor designs are optimized for a type of coal, so if the quality or the chemical composition of the coal fed is different than the one expected it can cause several problems. In particular, even the cracking of the coal can cause some hydrodynamic problems because when smaller grains and agglomerates are formed, they can plug the gas outlet resulting in pressure drops. Moreover, the coke residue in the channels can burn if some air or oxygen are present, causing some damages at the unit [29].

1.2.1 The CTL-FT process

The indirect coal liquefaction implies a complete breakdown of the coal feed. Once the syngas mixture is produced, a large class of derivate can be synthesized. In particular, if olefins and paraffins hydrocarbons are formed via Fischer-Tropsch

synthesis, the process is named as CTL-FT. At the moment one of the biggest ICL plant is owned by SASOL company in South Africa [30].

Both DCL and ICL processes provide fuels which have better characteristics with respect to the petroleum derived ones. For example they are free of nitrogen, sulfur and aromatics which make them more environmental compatible fuels with lower emissions levels. Moreover the almost total absence of sulfur compounds in the products helps to avoid the catalysts poisoning if further reactions are required.

The general flowsheet of a CTL-FT process is not so different if compared with a BTL-FT one except for the source of syngas. Even in the coal-to-liquid FT process a gasification unit is present, followed by a cleaning process and then the FT unit.

The catalytic system that will be adopted in the FT reactor is a function of the type of coal used and the syngas produced. However, the coal derived H_2/CO mixture can be modulated and adjusted in order to meet the optimized catalyst parameter [30].

1.2.1.1 Coal gasification

The gasification of coal is an irreversible thermochemical process carried out in presence of oxygen, water or both of them. It is very important to optimize the size and the geometry of both coal ashes and gasifier in order to maximize the production of syngas instead of other by-products like CO_2. The main reactions are here reported (Eqs. 1.18- 1.20) [29]:

$$2\ C + O_2 \rightarrow 2\ CO \qquad \text{(Eq. 1.18)}$$

$$C + H_2O \rightarrow CO + H_2 \qquad \text{(Eq. 1.19)}$$

$$3\ C + O_2 + H_2O \rightarrow 3\ CO + H_2 \qquad \text{(Eq. 1.20)}$$

The gasifier type usually used in coal gasification processes are similar to the one to achieve the biomass gasification. There are several industrial gasifier types, but they can be divided into three different categories.

1 - Entrained flow gasifiers: in this unit, coal particles concurrently react at high speed with steam and oxygen or air in a suspension mode called entrained fluid flow. They work at high temperatures (T> 1000 °C) and high pressures (P= 20- 80 bar). This technology allows short contact times, in the order of seconds, but it requires a pulverized coal. At the moment, entrained flow gasifier is the most used gasification technology.

2 - Fluidized bed gasifiers: this type of thermo-reactor operates at T= 900- 1050 °C. It does not require particular coal pre-treatments since the coal particles must have

dimensions in the range 0.5- 5 mm. The contact times are in the order of 10- 100 seconds, but sometimes they could be greater.

3 - Fixed bed gasifier: This gasifier type works at higher temperatures with respect to the other types (T= 1500- 1800 °C) and at P= 30 bar. This kind of unit requires quite big coal particles with diameter between 5- 80 mm which result in long contact time (15- 60 minutes) or in some cases, even several hours are required.

The main advantages and disadvantages of these type of gasifiers are reported in Table 1.3.

The different features of the gasifier types result in different type of syngas produced. In particular, an example of a coal derived syngas produced with these three kind of apparatus is reported in Table 1.7.

Compounds (%mol)	Gasifier type		
	Fixed bed	Fluidized bed	Entrained bed
Ar	Trace	0.7	0.9
CH_4	3.3	4.6	-
C_2H_4	0.1	-	-
C_2H_6	0.2	-	-
CO	5.8	33.1	43.8
CO_2	11.8	15.5	4.6
COS	Trace	-	0.1
H_2	16.1	28.3	21.1
H_2O	61.8	16.8	27.5
H_2S	0.5	0.2	1.1
N_2	0.1	0.6	0.9
NH_3 + HCN	0.3	0.1	-

Table 1.7: Compositions of coal derived syngas [31].

As is possible to observe from Table 1.7, the syngas mixture produced from coal, can have different H_2/CO ratios in the range 0.5- 3 as a function of the type of coal gasified and the type of the gasifier used, besides a wide range of other hydrocarbons and by-products.

1.2.1.2 Coal derived syngas cleaning process

The gaseous mixture which quit the gasification unit is not suitable to be converted directly into hydrocarbons and it requires to be purified. The main FT syngas requirements are reported in Table 1.4.

Once the gaseous mixture is produced, the types of cleaning treatments are completely the same as the ones used in the purification process of biomass derived syngas.

1.2.1.3 Fischer Tropsch unit

The Fischer-Tropsch step which follows the gas cleaning process, will be fully explained in Chapter 2 of this thesis.

1.2.1.4 Comparison between DCL and ICL technologies

Some studies report a comparison between DCL and ICL processes [30,32,33], however it is not easy to give a full comparison about which one is the best, this because they have to be analyzed by several points of view.

DCL is a more efficiency process, compared to ICL, due to the complete coal breakdown required in the indirect coal liquefaction. The overall estimated system efficiency for a DCL plant has been estimated around 70 % while the theoretical one calculated for ICL is no more than 60 %.

DCL and ICL require almost the same amount of water, in particular DCL consumes more hydrogen respect to the ICL due to the Bergius reaction, but on the other hand ICL process requires further treatments like gas cooling and different separation stages before that the syngas mixture can be fed to the FT reactor.

Both DCL and ICL provide fuels with better properties respect to the ones based on crude oil. DCL products are usually rich in aromatic polycyclic compounds, and due for the recent restriction in the use of fuel even with a low level of aromatics, ICL is a little bit advantaged. The main characteristic of DCL and ICL fuels are reported in Table 1.8.

Another difference between the two kind of fuels is the diesel cetane number which is higher for ICL due to the presence of several straight chain hydrocarbons.

The estimated production cost of DCL and ICL fuels is highly influenced by the total size production of the plant. However, these processes are competitive when the price of the extracted crude oil is around 55 $ per barrel, which makes at the moment the CTL process more competitive with respect to the BTL one.

Features	DCL	ICL
Distillate product mix	65 % Diesel 35 % Naphtha	80 % Diesel 20 % Naphtha
Diesel cetane number	42- 47	70- 75
Diesel sulfur content	< 5 ppm	< 1 ppm
Diesel aromatics	4.8 %	< 4 %

Diesel specific gravity	0.865	0.780
Naphtha octane number	> 100	45- 75
Naphtha sulfur content	< 0.5 ppm	Nil
Naphtha aromatics	5 %	2 %
Naphtha specific gravity	0.764	0.673

Table 1.8: Properties of DCL and ICL final products [30] *(ppm= part per million).*

1.3 The gas-to-liquid (GTL) process

The gas-to-liquid (GTL) process uses natural gas (CH_4) as a primary source for the production of liquid hydrocarbons. Its importance has raised during the last thirty years due to the continuous raising of the energy demand, coupled with the attractive alternative for gas monetization. For these reasons the exploration of new natural gas reserves has been accelerated as well in the last decade [34].

Similarly to the BTL and CTL processes, the GTL one offers a different way beside crude oil to produce liquid hydrocarbons and then, after further chemical manipulation, a wide array of chemical compounds which are essential for the all-day life.

The GTL technology was initially developed during the second world war, as the CTL one, in order to supply the demand of liquid fuels during the war period. Differently to CTL and BTL, the gas-to-liquid is an already industrially established process. The GTL process is based on the conversion of methane into syngas, and even if the H_2/CO mixture opens a lot of ways to produce liquid hydrocarbons and fuels, most of the capital investment in GTL remains focused on the Fischer-Tropsch technologies [34].

Shell commissioned what it is claimed as the first commercial GTL plant in Malaysia, with a capacity of 12500 barrels per day. Nowadays Shell company is owing the biggest GTL plant in the world called “Pearl” in Qatar. This huge GTL plant started to run in 2012 and at the moment it is consuming 1.6 billion cubic feet of gas per day in order to produce around 260000 barrel of hydrocarbons per day (140000 of liquid hydrocarbons and 120000 of LPG, ethane and other condensate) [35].

Figure 1.13: The "Pearl", the biggest GTL plant the world (Qatar) owned by Shell.

Sasol developed an integrated GTL process which is an evolution of a CTL one in 1980, in South Africa, and then a some different other GTL processes in Qatar, Nigeria with an overall production of around 30000 barrels per day in each plant. In the recent years it is planning to develop GTL plants in Uzbekistan, Canada and USA [36].

1.3.1 The GTL-FT process

The gas-to-liquid Fischer-Tropsch process converts the natural gas in H_2 and CO, as all the common GTL processes, but then it produces hydrocarbons via FT synthesis. In this way, a wide range of products like oils and waxes, naphtha and specialty chemicals can be produced.

By using optimized conditions in the FT unit, the mixture of products can be changed, for this reason GTL-FT can target a part of the high-value product markets that at the moment are mostly produced from crude oil and refinery. A simple flowsheet of a GTL-FT process is reported in Figure 1.14.

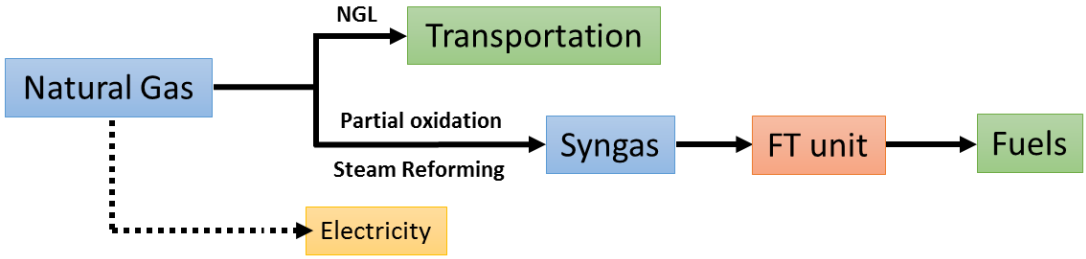

Figure 1.14: GTL-FT scheme.

1.3.1.1 Methane to syngas conversion

The syngas mixture obtained from methane can be basically produced in two different ways, the first one is a thermal exothermic reaction which is called partial oxidation, while the second is an endothermic catalytic process called steam reforming (Eqs. 1.21- 1.22) [34].

$CH_4 + ½\ O_2 \rightarrow CO + 2\ H_2$ (Eq. 1.21)

$CH_4 + H_2O \rightarrow CO + 3\ H_2$ (Eq. 1.22)

Moreover, two different equilibria can occur (Eqs. 1.23- 1.24).

$CO + H_2O \leftrightarrow CO_2 + H_2$ (Eq. 1.23)

$CH_4 + CO_2 \leftrightarrow 2\ CO + 2\ H_2$ (Eq. 1.24)

The partial oxidation process requires an air separation unit in order to eliminate the nitrogen and have an oxygen enriched air. Beside the air separation unit, this approach is usually composed by two main operation steps, the first one in a combustion chamber at high temperatures (T= 1200- 1500 °C) and then a carbon black removal unit achieved by water scrubbing and an extraction with naphtha. It is very important to optimize the process parameters and design in order to minimize the formation of carbon by methane decomposition [37].

The steam reforming process is not only used in GTL-FT process but also in the petrochemical industry for the production of hydrogen used in the hydro-crackers. It is usually carried out with nickel based supported catalysts at temperatures of T= 850-950 °C and pressure equal to P= 30 bar [37].

Both processes can be run separately or together in an integrated process called autothermic synthesis gas production process. In this configuration the heat produced by the partial oxidation unit is recovered in the steam reforming one and the gaseous products from the oxidation burner are mixed with steam and then fed to the catalytic steam reforming reactor [35].

The syngas mixture produced from CH_4 usually does not require a particular cleaning process like the one produced from biomass and coal. Only the H_2/CO ration must be adjusted to meet the required one for the FT reaction.

1.3.1.2 Fischer Tropsch unit

The Fischer-Tropsch step which follows the partial oxidation/steam reforming one, will be fully explained in Chapter 2 of this thesis.

1.3.1.3 Comparison and economical evaluation between GTL-FT and crude oil based products

The reachable yield of a GTL-FT plant is higher than the one obtainable from the crude oil refining processes. Typically gas-to-liquid FT yield are in the order of 70 % while the petroleum based industry reach only 40 %. This latter value is dependent from the type of crude oil processed because its quality highly influences the overall yield of the process.

Despite a comparison between GTL-FT and crude oil based products is easy from a chemical point of view, an economical evaluation would be more difficult due to the presence of several factors which can influence the costs and the efficiency of the plants, moreover the cost for some of these factors could change overtime.

The commerciality of a GTL-FT plant with respect to a refinery is sensitive to the cost of the feedstocks and the crude oil, the capital and operating costs, the GTL plant efficiency and the costs related to the transportation.

A. Wood reported that the cost of GTL-FT plant is much more influenced by the crude oil price and capital costs instead of natural gas cost. If these costs are kept substantially low, a GTL-FT plant could be competitive with an oil price of around 40 $/barrel [34].

2 The Fischer-Tropsch synthesis

2.1 Historical background of the FT reaction

The Fischer-Tropsch (FT) synthesis has a story which looks back in the past of around seventy years. The FT reaction gives the access to the industrial organic chemistry starting from two simple inorganic gaseous molecules, H_2 and CO.

The reaction was developed by two German scientist, Franz Fischer (1877- 1947) and Hans Tropsch (1889- 1935), during the World wars period and it was patented in 1925 using iron or cobalt based catalyst and operating at pressures in the range P= 10- 20 bar. The first FT plant on a laboratory scale started to operate in 1934 while the first one on an industrial scale began to produce hydrocarbons and fuels in 1936 [38].

Figure 2.1: Franz Fischer (on the left) and Hans Tropsch (on the right).

During those years the raising of the fuels demand for war equipment made the German scientist to focus their attention on the development of a process which was able to achieve the production of a large range of hydrocarbons without the use of crude oil. In the decades after the second World war, the growth of the crude oil extraction, and the develop of chemical industrial processes for the crude oil refining decreased the interest in the FT process from both academic and industrial side, except in South Africa where the oil embargo during the apartheid period has caused the develop of a FT plant by Sasol company. However, during the recent years several economic factors, like the raising of petroleum price, the growing of the energy consumption and strict environmental policies such as CO_2 emissions, turned on again the interest for this reaction.

FT synthesis proved to be a suitable way for the production of fuels with better features with respect to the crude-oil based ones, the main characteristic of FT fuels, also called green diesel, are the low content of sulfur and aromatics compounds. Moreover FT products provide better flash point and higher cetane number.

For these reasons, academic and industrial research groups are spending several efforts to develop and test innovative FT catalysts, or reactor designs in order to better the overall performances of the process. The number of academic publications regarding the FT synthesis increased in the last years and it is still growing.

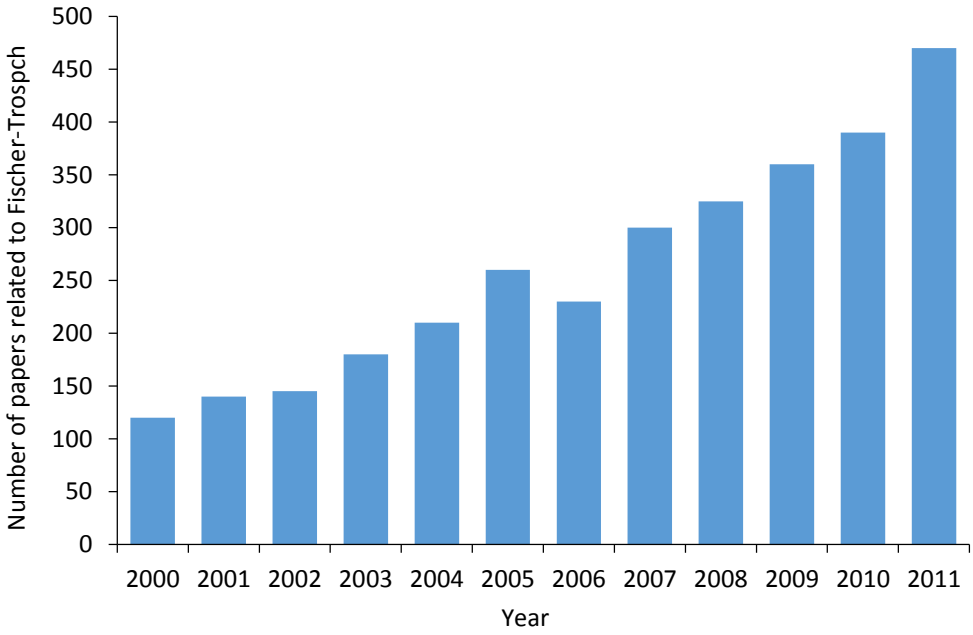

Figure 2.2: Academic papers regarding the FT reaction published in the period 2000- 2011 [39].

The renewed interest in the FT synthesis has had also the effect to increase the number and the capacity of the Fischer-Tropsch plant worldwide. At the moment the biggest company involved in the production of FT derived fuels and hydrocarbons are Shell and Sasol, but also a wide amount of smaller companies, especially where feedstocks resources as biomass, coal and natural gas are available, are working on this field.

Figure 2.3: Industrial worldwide FT plants [40].

The capacity of an industrial FT plant can vary from dozens of barrel per day for pilot plants, like the one owned by ENI in Italy and hundreds of thousands as the Pearl by Shell in Qatar or the Sasol FT plant in South Africa [41].

Company	Country	Capacity (bpd)	Raw material
Sasol	South Africa	150.000	Coal
	Australia	30.000	Natural gas
	Nigeria	34.000	
	Qatar	34.000	
Shell	Malaysia	14.700	Natural gas
	Qatar	140.000	
	Indonesia	75.000	
	Egypt	75.000	
	Argentina	75.000	
	Australia	75.000	
Shell Choren	Germany	300	Biomass
Mossgas	South Africa	22.500	Natural gas
EniTechnologie	Italy	20	Natural gas
BP	USA	300	Natural gas
Rentech	USA	1.000	Natural gas
	South Africa	10.000	
	Bolivia	10.000	
Rentech pertamina	Indonesia	15.000	Natural gas

Syntroleum	Australia	11.500	Natural gas
	Chile	10.000	
	Peru	5.000	
Syntrol.-Tyson Foods	USA	5.000	Biomass
Gazprom syntroleum	Russia	13.500	Natural gas
Repsol-YPF	Bolivia	13.500	Natural gas
Syntroleum	Bolivia	90.000	
Conoco	Qatar	60.000	Natural gas
	USA	400	
Bioliq	Germany	—	Biomass

Table 2.1: Operating industrial FT plants and their feedstocks.

2.2 The chemistry of the Fischer-Tropsch reaction

The Fischer-Tropsch synthesis is an array of strongly exothermic catalytic reactions which gives an overall variation of enthalpy $\Delta H \approx -200$ kJ·mol$_{CO converted}^{-1}$. The main target of the FT synthesis is to produce hydrocarbons in the range C_1-C_{100} starting from syngas while limiting the formation of methane (CH_4) and carbon dioxide (CO_2) which are undesired products of the FT reaction. The main FT reactions are reported hereinafter (Eqs. 2.1- 2.7) [42]:

- *Irreversible reactions*

Olefins production:

$$1n\ CO + 2n\ H_2 \rightarrow C_nH_{2n} + n\ H_2O \quad \text{(Eq. 2.1)}$$

$$2n\ CO + n\ H_2 \rightarrow C_nH_{2n} + n\ CO_2 \quad \text{(Eq. 2.2)}$$

Paraffins production:

$$2n\ CO + (1+2n)\ H_2 \rightarrow C_nH_{(2n+2)} + n\ H_2O \quad \text{(Eq. 2.3)}$$

Alcohols production:

$$n\ CO + 2n\ H_2 \rightarrow C_nH_{(2n+1)}OH + (n-1)\ H_2O \quad \text{(Eq. 2.4)}$$

- *Equilibria reactions:*

Water-gas-shift (WGS):

$$CO + H_2O \leftrightarrow CO_2 + H_2 \quad \text{(Eq. 2.5)}$$

Methanation:

$$CO + 3\ H_2 \leftrightarrow CH_4 + H_2O \quad \text{(Eq. 2.6)}$$

Boudouard equilibrium:

$$2\ CO \leftrightarrow C + CO_2 \qquad \text{(Eq. 2.7)}$$

Nevertheless the FT system is composed by several reactions, it can be simplified with only the main FT reactions and the WGS equilibria [6].

2.2.1 Reaction mechanism

Due to the production of lots of different chemical compounds and to the different catalysts that can be used to catalyze the reaction, it is very difficult to define a unique mechanism for the FT reaction. In the literature, the growth of the hydrocarbons chain is described with the activation of a CO molecule and the insertion of a C_1 unit in the already formed chain. Three different mechanisms are proposed and discussed in the literature [43,44].

- The carbide mechanism (direct CO dissociation):

In this type of mechanism, the formation of the hydrocarbon chain starts with the dissociation of a molecule of CO and H_2 on the catalyst surface, which reacts in order to form a unit of $-CH_2-$. Then, the formed methylene unit reacts with an another dissociated molecule of CO to increase the chain length. The reaction ends when a termination step occurs, that could be a hydrogen addition, which produces paraffin, or on the other hand, a hydrogen abstraction, that forms an olefin molecule. The carbide mechanism does not take into account the formation of alcoholic molecules, that may be formed through a reaction between the adsorbed molecule and oxygen. The scheme of the direct CO hydrogenation mechanism is reported in Figure 2.4.

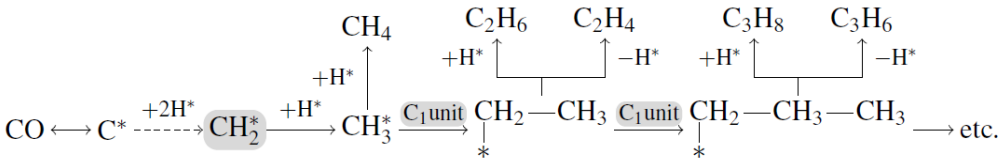

Figure 2.4: Carbide mechanism.

- The enolic mechanism (H-assisted CO dissociation):

Differently from the previous mechanism, in this case the CO molecule adsorbs on the catalyst surface without dissociating. Thus it reacts with an hydrogen molecule to form the C_1 unit which is similar to formaldehyde. The enolic mechanism contemplate two different termination steps, in the first one a molecule of H_2O is lost in order to form an hydrocarbon, in the second a H_2 is added to form an alcohol molecule.

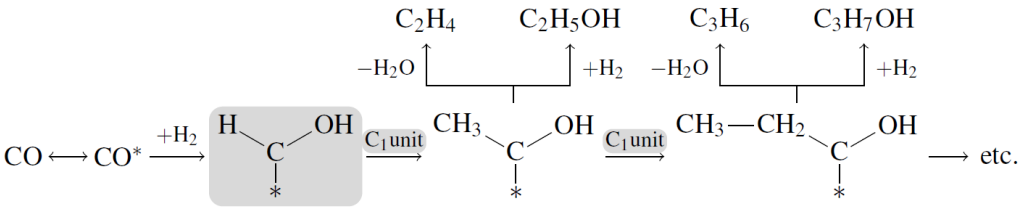

Figure 2.5: Enolic mechanism.

- The insertion mechanism (direct CO hydrogenation):

In this last mechanism proposed in the literature, the CO is the main unit for the chain growth. The carbon monoxide molecule is directly inserted in between of an active site and the specie adsorbed on the catalyst surface. The termination step takes place in the same way described in the enolic mechanism.

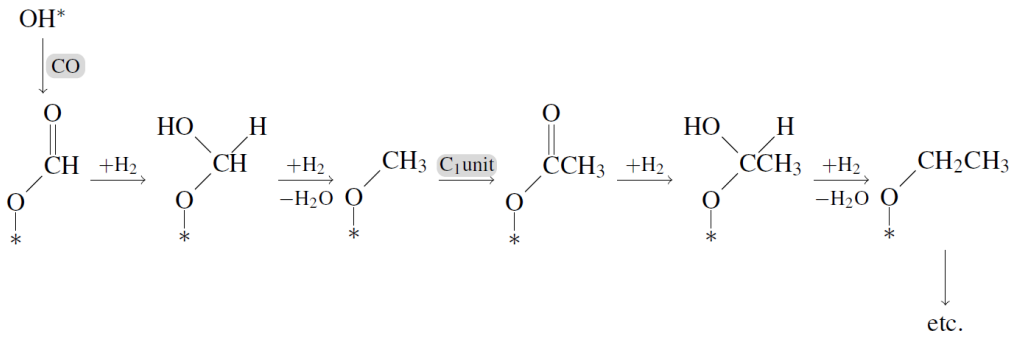

Figure 2.6: Insertion mechanism.

Nevertheless these are the three main mechanisms proposed by several authors in the literature it is difficult to say which one is correct, probably in the reality the mechanism which takes part during the reaction is a combination of the three. However, the carbide mechanism is considered the predominant one.

2.2.2 Thermodynamic aspects of FT synthesis

As previously reported, the FT synthesis is a strong exothermic reaction which gives a contribution in terms of enthalpy almost equal to 200 $kJ \cdot mol_{COconverted}^{-1}$.

The formation of paraffin, olefins, and oxygenated compounds starting from syngas is energetically favorable, which means that the ΔG^0 of the reaction is lower than 0.

For example, the free Gibbs energy for the formation of methane, ethane and butylene at T= 225 °C normalized by the number of carbon atoms (n) are -110, -72 and -40 $kJ \cdot n^{-1} \cdot mol_{COconverted}^{-1}$ respectively.

From the Gibbs energy reported in Figure 2.7 it is possible to observe that methane formation is favored with respect to longer chain hydrocarbons or alcohols; in addition to this, paraffinic hydrocarbons formation is favorable from an energetic point of view if compared to olefins and oxygenated compounds.

The high exothermicity of the FT synthesis suggests that the formation of hydrocarbons via FT synthesis is not favored at high temperature, however the FT reactions involve a reduction in the total number of moles of the systems, which means that high pressures can higher the conversion of the process, even if the ΔG^0 is close to 0.

If the free Gibbs energy of compounds with the same number of carbon atoms is compared, it is possible to observe that saturated hydrocarbons are favored respect to olefins and molecules with hydroxyl groups.

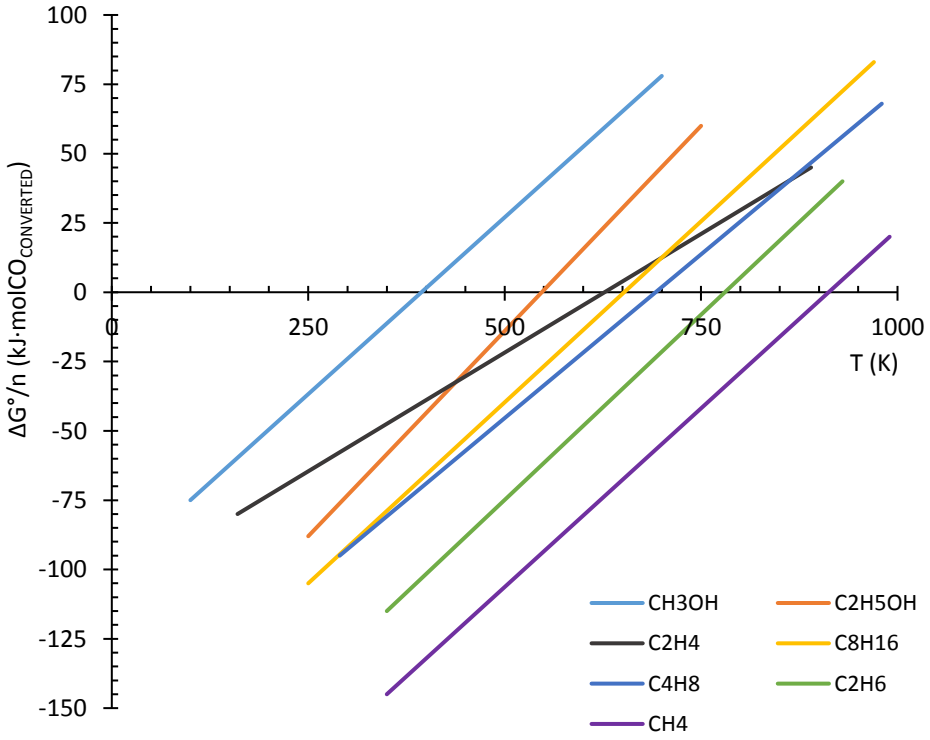

Figure 2.7: Normalized Gibbs energy formation of some Fischer-Tropsch products.

Figure 2.7 shows that a wide range of hydrocarbons, with different length and structures can be formed in the range T= 400- 500 °C, but the selectivity to each product is determined by the catalyst used in the FT reactor.

In addition to the main FT reactions, even other secondary reaction are thermodynamically possible under FT process conditions. These reaction may be the hydrogenation of olefins and dehydration of alcohols, beside the incorporation of H_2 and CO in an already formed organic molecule which acts as a unit in the reaction mechanism. The incorporation is not the predominant mechanism of the FT process, but it could be possible when a short chain molecule (CH_4) reacts with syngas to create a longer paraffin.

2.2.3 The kinetic of the FT reaction

Because to the very complex mechanism of the FT reactions that makes impossible to determine which is the rate limiting step, it is very difficult to describe the system with a unique kinetic equation which take into accounts all the variables of the process. Over the years several authors published their works regarding the study of the rate of H_2 and CO consumption. However, it is needful to specify that the empirical equations elaborated are fully suitable if used in the system in which they have been studied, due to the difference of the reaction parameters (temperature, pressure, contact time, H_2/CO ratio), the catalysts (Co or Fe based catalysts, massive or supported samples, presence or not of promoters) and the type of reactor (PFR, slurry, trickle bed).

In addition to the empirical equations, also Langmuir-Hinshelwood-Hougen-Watson (LHHW) and Eley-Rideal type of rate equations have been applied.

Generally, during the kinetic rates consumption of CO and H_2, the system is simplified as a combination of only FT reaction and WGS equilibria. This assumption may be considered valid when iron based catalysts are used since Fe is a metal active to the WGS synthesis resulting in the develop of different equation sets as a function of the active metal used to achieve the synthesis of the hydrocarbons. The reaction rate can be described as a function of the rate of overall consumption of syngas (independent to the presence or not of WGS), the rate of CO consumption for the FT reaction (dependent by the WGS) or the rate of syngas consumption just for the FT step. The three equations (Eqs. 2.8- 2.10) are reported hereinafter.

Overall syngas consumption:

$$- R_{H2+CO} = -R_{CO} - R_{H2} \qquad \text{(Eq. 2.8)}$$

CO consumption for the FT reaction:

$$R_{FT} = - R_{CO} - R_{WGS} \qquad \text{(Eq. 2.9)}$$

Syngas consumption for the FT reaction (m, n= stoichiometry coefficients):

$-R_{H2+CO} = (2 + m/2n)\ R_{FT}$ (Eq. 2.10)

The main kinetic equations which describes the rate of overall syngas consumption, CO consumption and CO_2 consumption (WGS rate) that have been studied and elaborated are reported in Table 2.2 [43,44] (Eqs. 2.11- 2.22).

Intrinsic kinetic expression	Catalyst	
$-R_{H2+CO} = \frac{aP_{H2}^2}{P_{CO}}$	Co/MgO/ThO_2/kieselguhr	(Eq. 2.11)
$-R_{H2+CO} = \frac{aP_{H2}^2 P_{CO}}{(1 + bP_{H2}^2 P_{CO})}$	Co/ThO_2/kieselguhr	(Eq. 2.12)
$-R_{H2+CO} = \frac{aP_{H2}^2}{P_{CO}^{0.5}}$	Co/CuO/Al_2O_3	(Eq. 2.13)
$-R_{H2+CO} = \frac{aP_{H2}^{0.55}}{P_{CO}^{0.33}}$	Co/La_2O_3/Al_2O_3	(Eq. 2.14)
$-R_{CO} = \frac{aP_{H2}P_{CO}^{0.5}}{(1 + bP_{CO}^{0.5})^3}$	Co/Al_2O_3	(Eq. 2.15)
$-R_{CO} = \frac{aP_{H2}^{0.5}P_{CO}^{0.5}}{(1 + bP_{CO}^{0.5} + cP_{H2}^{0.5} + dP_{CO})^2}$	Co/kieselguhr	(Eq. 2.16)
$-R_{CO} = \frac{aP_{H2}^{0.5}P_{CO}}{(1 + bP_{CO} + cP_{H2}^{0.5})^2}$	Co/kieselguhr	(Eq. 2.17)
$-R_{CO} = \frac{aP_{H2}P_{CO}}{(1 + bP_{CO})^2}$	Co/MgO/SiO_2	(Eq. 2.18)
$-R_{H2+CO} = \frac{aP_{H2}P_{CO}}{P_{CO} + bP_{H2O}}$	Fused Fe/K	(Eq. 2.19)
$-R_{H2+CO} = \frac{aP_{H2}^2 P_{CO}}{P_{CO}P_{H2} + bP_{H2O}}$	Precipitated Fe	(Eq. 2.20)
$-R_{CO} = \frac{P_{H2}P_{CO}}{P_{CO} + aP_{H2O} + bP_{CO2}}$	Supported Fe	(Eq. 2.21)
$-R_{CO2} = \frac{P_{H2O}P_{CO} - \frac{P_{H2}P_{CO2}}{Kp}}{P_{CO} + aP_{H2O} + bP_{CO2}}$	Supported Fe	(Eq. 2.22)

Table 2.2: Kinetic equations for overall syngas consumption, CO consumption and WGS rate.

Where:

P"i"= Partial pressure of "i" specie;

Kp= Equilibrium constant;
a, b, c, d= constants dependent by the catalytic system adopted, calculated using an Arrhenius form equation.

The equations reported above express the rate of the reactions as a function of the partial pressures of the species which are involved in the reaction mechanism. The equations suitable for Co-based catalysts take into account the pressure of only H_2 and CO while the one referred to the rate of reaction in presence of Fe-based catalysts report the reaction rate as a function of partial pressure of H_2O and CO_2 due to the presence of the WGS equilibria. However, even if carbon dioxide and water are both present on the catalyst surface, CO_2 inhibition is not as strong as water inhibition due to the large difference in adsorption coefficients [45].

2.2.4 Products selectivity and influence of the process conditions

Even though several reaction mechanisms have been proposed to describe the FT synthesis, it is universally accepted that the hydrocarbons production can be considered as an oligomerization reaction in gaseous phase where the chain grow through the addition of a C_1 block. The probability that this unit is added to the chain is defined as (Eq. 2.23):

$$\alpha = \frac{r_{propagation}}{r_{propagation} + r_{termination}} \qquad \text{(Eq. 2.23)}$$

Where $r_{propagation}$ is the rate at which the chain is growing, $r_{termination}$ is the termination rate of the hydrocarbons chain and α is the chain growth probability.

The probability of chain growth is also defined with the Anderson-Schulz-Flory (ASF) theory [46], with the assumption that this parameter is independent by the length of the chain.

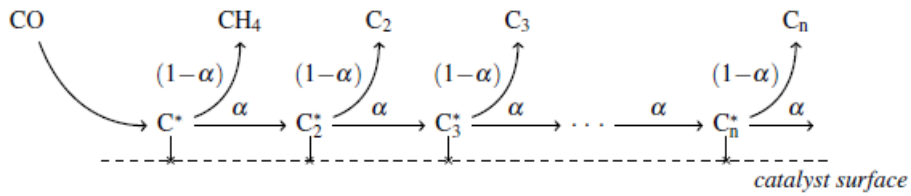

Figure 2.8: ASF mechanism.

The product distribution by the ASF model, referred to the mass fraction of products is then defined as (Eq 2.24) [47]:

$$\frac{W_n}{n} = (1-\alpha)^2 \alpha^{n-1} \qquad \text{(Eq. 2.24)}$$

Where n is the number of carbon atoms in the product, W_n is the weight fraction of product containing n carbon atoms.

The α can be estimated by a least-squares linear regression of the logarithmic form of Eq. 2.24. α is then given by the slope and intercept values.

$$\ln\left(W_n/n\right) = ln(1-\alpha)^2 + (n-1)\ln(\alpha) \qquad \text{(Eq. 2.25)}$$

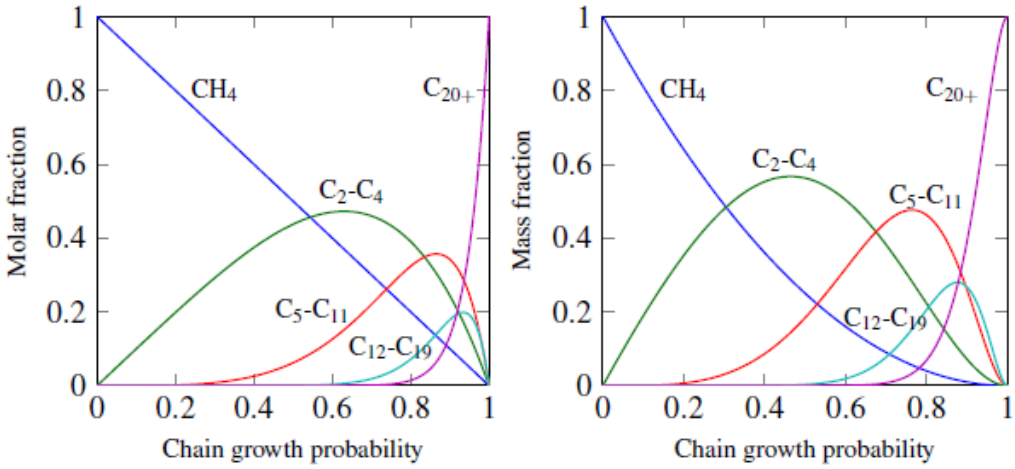

Figure 2.9: Ideal Anderson-Schulz-Flory distribution on a molar and mass basis.

The chain growth probability defines the spectra of the products, the greater is, the longer the hydrocarbon chain is; α is dependent of several factors, such as the type of the catalyst and the process conditions (H_2/CO ratio, temperature, pressure) adopted. For example, Ru promoted Co based catalysts give higher α values with respect to massive iron catalysts.

The presented ASF algorithm is not able to distinguish the type of products generated, but just the molar or mass composition of a defined fraction, as C_2, C_3, C_4 and so on. As know, FT reaction proved to synthesize paraffin, alpha and beta olefins and oxygenated compounds. Since ASF equation was developed, further investigations have been made in order to better the algorithm and predict a more defined products variety. In particular it was noted that the alcohols productivity is similar to the one of (n + 1) hydrocarbons fraction, for example, if C_4 hydrocarbons fraction is the predominant one, C_3H_7OH is the major oxygenated product. An improvement has been made by Anderson with the introduction of the chain branching into the product distribution model by the insertion of a C_1 unit beside the beta carbon atom of a growing chain [48]. More recently, a kinetic model called non trivial surface polymerization was developed by Schultz et al. [48] in which chain branching rate

constants have been regressed with the assumption of an exponential decrease by increase the carbon number.

Even though the ASF equation gives a primary approximation of the products distribution, it is not suitable for a detailed result. This drawback is due by the deviations of the algorithm. There are three main type of ASF deviations:

- *Methane selectivity*: usually CH_4 selectivity predicted by ASF model is lower than the one measure experimentally. Several mechanism have been elaborated to explain this behavior. Sarup et al. [49] estimated that the termination probability is about 5- 20 times higher than a paraffin termination probability. Other works [38,48] reported the assumption of the presence of specific methanation catalytic sites on the catalyst surface. Other possible reaction mechanisms involved that favor methane productivity reported in the literature [50] may be secondary hydrogenolysis by demethylation and secondary spillover/support reaction path. Even heat/mass transfer phenomena and catalyst hot spot could be attributable to the enhancement of the selectivity to methane, because they can generate local area on the catalysts surface when the partial H_2 pressure is higher than the average value, resulting in an higher methane productivity.
- *Anomalies of ethane and ethylene*: the predicted selectivity to C_2 fraction by the ASF is supposed to be close to 30 %wt, while experimentally that values reach only 18 %wt. This deviation could be due from different reasons, the most accredited is the incorporation or the hydrogenolysis of ethylene [6].
- *Not constant α*: in the ASF algorithm the chain growth probability is considered as a constant value. From an experimental point of view, it has been demonstrated that the slope of the hydrocarbons semi logarithmic mole fractions versus the number of carbon atoms increase when the hydrocarbon chain contains 10 or more carbon atoms due to the presence of different catalytic sites or different chain termination reactions on the catalyst surface [49,51].

For what concerns the influence of the process conditions, such as temperature, pressure, H_2/CO ratio, space velocity and the conversion given by the catalyst, they play a key role in the selectivity control of the FT reaction. In particular, with an increase in the temperature, the selectivity turns to lighter products while the CO conversion increases. An high H_2/CO ratio results in an higher H_2 partial pressure which favors the production of light hydrocarbons and decreases the olefins productivity; on the other hand, an high CO partial pressure inhibits reactions as hydroformilation, isomerization, oligomerization and hydrogenation [52]. Low contact time (high space velocity) proved to increase the olefin/paraffin ratio while a decrease in the space velocity results in a lower methane selectivity due to the greater presence of secondary reactions [6]. The effect of the time on stream (TOS) is directly

correlated with the stability of the catalyst, especially if this latter is an iron based one. Long TOS lead to the formation of carbonaceous species on the catalyst surface resulting in a lower availability of active catalytic sites. The effect of CO conversion is conducible to the CO partial pressure one, since high CO conversion values result in a low P_{CO}. The low CO partial pressure favors secondary hydrogenation reactions which decrease the olefin/paraffin ratio.

The effects on the catalyst efficiency and selectivity of all the variables are summarized in Table 2.3.

Parameter	Chain length	Chain branching	Olefin selectivity	Alcohol selectivity	Carbon deposition	Methane selectivity
Temperature	↓	↑	x	↓	↑	↑
Pressure	↑	↓	x	↑	x	↓
H_2/CO	↓	↑	↓	↓	↓	↑
CO conv.	x	x	↓	↑	x	↑
Space Velocity	↑	↓	↑	↑	↑	↑

Table 2.3: Effects of the process variables on the products selectivity, ↑: direct dependency, ↓: inverse dependency; x: difficult correlation.

2.3 Industrial FT reactors

From an industrial point of view, reactors suitable for the FT synthesis can be divided in two types, the first ones are fixed bed reactors, while the seconds are two/three phases reactors. Even though they implies different technologies and features, the main problem in the industrial FT synthesis is to efficiently remove the heat generated while the reaction is carried out [53].

In what it is called High Temperature Fischer-Tropsch (HTFT), only the first kind of reactor is adopted since only light hydrocarbons are produced and a liquid phase is not present in the reaction media. Typical set up conditions for HTFT are T= 330- 350 °C in presence of iron based catalysts. Fixed multi-tubular reactors and fluidized bed reactor are suitable too under HTFT conditions. Multi-tubular reactors are composed with a series of pipes where the catalysts is packed, the temperature is controlled by reducing the tubes diameters but pressure drop phenomena can occurs if the catalyst granulometry is not adequate. The pressure drop may result in a not homogeneous H_2/CO ratios over the catalyst surface which leads to an un-optimal control of the selectivity. Fluidized bed reactors are projected to avoid the problems of fixed bed reactors, they does not need a strict defined catalyst dimension and they can work with smaller particles therefore there are no intra-phase resistances affecting the catalyst selectivity. The presence of a liquid phase, usually a wax mixture, helps to

better control the reaction temperature but requires additional equipment for the catalyst recovery [53].

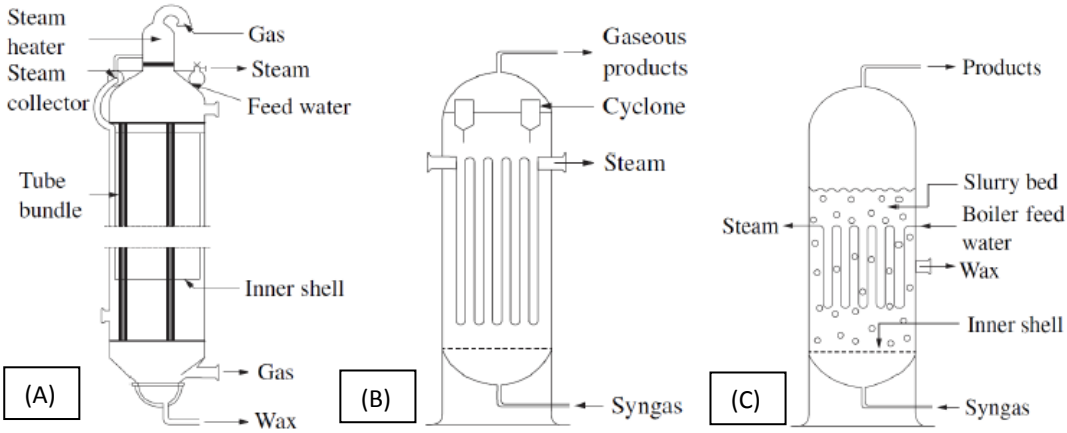

Figure 2.10: FTS reactors, A: multi-tubular; B: fluidized bed; C: slurry bubble column [43].

The Low Temperature Fischer-Tropsch (LTFT) works in milder conditions with respect to HTFT, the average temperature range is T= 220-260 °C. In LTFT the reaction system is usually composed by three different phases, the gaseous feeding mixture and light products, the liquid heavy hydrocarbons, and the solid catalyst.

In this case, the PFR reactor becomes a trickle bed one due to the presence of a liquid phase which better removes the heat generated during the reaction and helps to keep the reactor temperature constant; nevertheless it presents a drawback due to the contact between the liquid and the solid catalyst that increases the inter-phase resistances. Slurry type reactor are suitable too for the LTFT, they presents the same advantages and disadvantages of fluidized bed reactors.

During the recent years other types of reactors are being studied, like membrane reactors which can help to remove the water produced with the use of membranes and microchannel reactors which are composed by series of very small pipes with diameters in the range of 0.5-1 mm which provide a good heat exchange efficiency [54].

3 Fischer-Tropsch catalysts and novelty of the PhD project

3.1 Typical Fischer-Tropsch catalysts

The active metals able to catalyze the FT synthesis are VIII and IX group metals (iron, cobalt and ruthenium). From an industrial point of view, even though it is less active, Fe is preferred to Co and Ru due to the lower price and the activity toward the WGS equilibria which makes it a suitable candidate for an integrated BTL-FT plant [41].

Cobalt is more expansive than iron, but it provides longer lifetime and better activity and selectivity to linear and longer chain hydrocarbons; Co usually catalyze FT reactions in GTL process where syngas with stoichiometry H_2/CO ratio is fed to the FT unit. Ru is very active in terms of reactant conversion, but it is no more used as a FT catalyst by itself due to the very high price of the metal and the high selectivity to methane [3]; even Ni is a suitable catalyst for FT synthesis, but it presents the same trend of ruthenium based ones.

Iron is used in its massive form, but some recent studies demonstrated the activity of inorganic supported iron based catalyst, even with the use of alkali promoters. Co is used as a supported catalyst, eventually promoted with Ru, Re, Pt and Pd [55].

SASOL company tried to develop Cr and Mo catalysts for FT synthesis, but the project has been shelved since both metals didn't show satisfactory activity toward this reaction.

Metal	Price ratio
Fe	1.0
Ni	250
Co	1.000
Ru	48.000

Table 3.1: Price ratios of the most common active metals for FT synthesis.

Schulz [38] reported in his work a comparison among the common characteristic of active metals for FT synthesis, in particular he found that:

- They are active for hydrogenation reactions and capable to produce metal carbonyls;

- The experimental conditions i.e. temperature and pressure adopted in the FT reactors are close to the thermodynamics that would allow the formation of metal carbonyls, this confirms the importance of the presence of carbonyls in the hydrocarbons production process.

A primary comparison between Fe and Co FT catalyst is reported in Table 3.2.

Parameter	Cobalt catalyst	Iron Catalyst
Cost	More expensive	Less expensive
Lifetime	Resistant to deactivation	Less resistant to deactivation (coking, carbon deposit, iron carbide)
Activity at low conversion	comparable	
Productivity at high conversion	Higher; less significant effect of water on the rate of CO conversion	Lower; strong negative effect of water on the rate of CO conversion
Maximal chain growth probability	0.94	0.95
Water gas shift reaction	Not very significant; more noticeable at high conversion	Significant
Maximal sulfur content	< 0.1 ppm	< 0.2 ppm
Flexibility (temperature and pressure)	Less flexible; significant influence of temperature and pressure on hydrocarbon selectivity	Flexible; CH_4 selectivity is relatively low even at 340°C
H_2/CO ratio	2	0.5-2.5
Attrition resistance	Good (always supported)	Not very resistant if not supported

Table 3.2: Properties comparison between industrial Fe and Co catalyst for FT synthesis.

3.1.1 Chemical state of the active phase

3.1.1.1 Cobalt catalysts

Metallic Co^0 is present in two different crystalline forms, fcc and hcp. In the case of cobalt, the hcp phase is more stable at lower temperatures. However, due to the complexity of the FT synthesis and the unknown exact reaction mechanism, it is impossible to establish which one is the predominant crystalline form in a FT catalyst; anyway, the reactant atmosphere does not influence the hcp/fcc ratio. Some works reported that hcp phase of Co^0 is more active to FT reaction with respect fcc from a

CO conversion point of view, but the selectivity toward reaction products is not influenced by this factor [56].

There are two possible proposed mechanism for the catalyst deactivation, without considering poisoning damages. The first one is the deposition of carbon on the catalyst surface which reduces the total number of active sites, while the second is the presence of cobalt carbides (Co_2C) which diminish the activity toward the FT synthesis. The two mechanism are in competition among them, because carbon deposition is favored by using the catalyst over long time on stream, but on the other hand prolonged TOS lead to the decomposition of Co_2C into Co^0 with the result to increase the reactant conversion and the selectivity to high hydrocarbons [39].

The formation of cobalt carbides is favored if the catalyst pretreatment step, before the FT synthesis, is carried out in pure CO. However a study by Jiao et al. [57] demonstrated that if La_2O_3 is added to a 15 wt% Co supported on an activated carbon, the selectivity to alcohols in the range C_2- C_{18} was increased and the same result was recorder for CO conversion. At the same time, the selectivity to heavy hydrocarbon was decreased of about ≈ 13 %. This behavior was attributed to the fact that the presence of La_2O_3 promotes the formation of cobalt carbide, and the co-presence of Co_2C and Co^0 fcc enhance the selectivity to mixed alcohols.

3.1.1.2 Iron Catalysts

It is well known that FT reaction conditions promote the formation of iron carbides (general formula Fe-C) if Fe-based catalysts are used. This is due to the fact that CO hydrogenation and formation of Fe-C have almost the same activation energy. A wide range of iron carbides may be formed: Fe_2C, $Fe_{2.2}C$, Fe_7C_3, Fe_5C_2, Fe_3C. However, even though all these carbides have been observed during FT synthesis, the real active species under working conditions remains still unknown. Anyway, every type of iron carbides is very sensitive to passivation even with small exposure to air [39].

It has been noted that both massive or supported iron-based catalyst can be easily reduced into α-Fe if treated with pure H_2 at T= 350 °C and then the metallic iron is easily converted into Fe_3C if the catalyst is tested under typical FT conditions. If pretreatment step is carried out with a H_2/CO mixture Fe_2C_5 and fcc phase Iron (γ-Fe) are both formed. The co-presence of Fe_2C_5 and γ-Fe provides a better FT activity in terms of CO conversion and heavy hydrocarbons productivity, suggesting that the presence or formation of Fe_3C could be responsible for the catalysts deactivation mechanism. Moreover, further studies demonstrated the presence of amorphous iron carbides (Fe_XC) if the pretreatment is carried out in presence of both H_2 and CO, but only magnetite (Fe_3O_4) is formed if the activation is done with the presence of only carbon monoxide. An high CO_2 productivity has been recorded if the catalyst with

Fe_3O_4 was tested under FT conditions, suggesting that magnetite is an active specie for WGS equilibria [58].

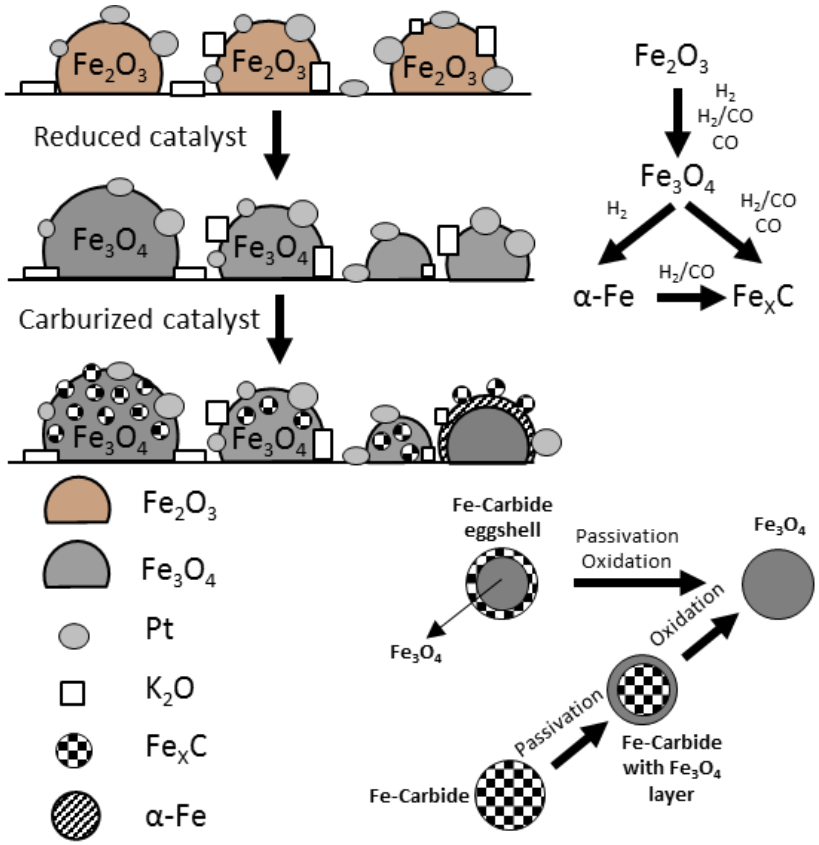

Figure 3.1: Formation of Fe carbides scheme.

3.1.2 Size of the active phase

The size of the active metal particles play a key role in heterogeneous catalysis; in the studies regarding Co-based catalysts, Iglesia reported that the turn over frequency (TOF) i.e. the amount of CO converted on the Co surface per second, is not dependent by the size of the active phase in ranges 10- 200 nm [39]. The main question is if the FT synthesis is a structure-insensitive reaction in all the Co dimensions range. Several studies have been carried out regarding the dependence of the FT activity as a function of Co particles size. Bezemer et al. [59] reported that Fischer-Tropsch is structure sensitive for Co particles with dimensions less than 10 nm (critical point), and a series of further works with different Co-based catalysts confirmed his results [39]. If the FT performances given by Co particles with dimensions between 1 and 10

nm are compared, the general trend is that the TOF and the yield to C_{5+} increase with the dimensions of the Co nanoparticles, while the selectivity to CH_4 is reduced.

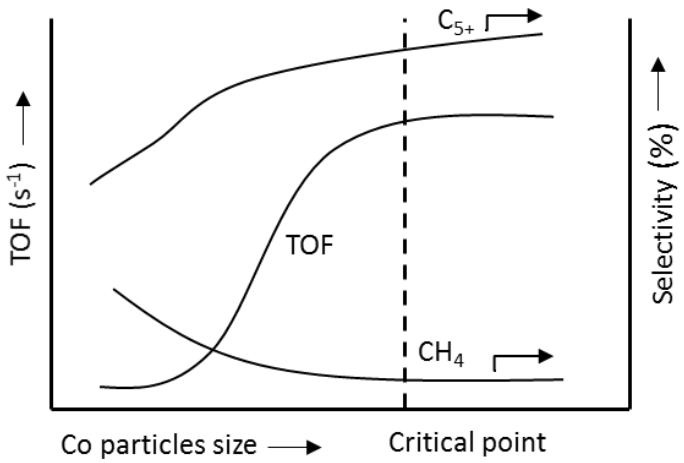

Figure 3.2: General behavior of Co-based catalysts for FT reaction as a function of Co particles size.

Differently from size-dependence studies for Co-based catalysts, the one regarding Fe-based ones are less present in the literature, and only a few works are available. The two main work about the effects of Fe particles dimensions on the FT activity are from Park et al. [60] and Sun et al. [61]. The Authors proposed opposite results, in particular, Park observed the same trend of Co particles, greater TOF and C_{5+} yield, and lower CH_4 selectivity if the dimensions of the Fe nanoparticles was increased from 2.4 to 6.2 nm, and then no more variations till dimensions equal to 12 nm. On the other hand, Sun highlighted a decrease in the CO conversion ranging the dimensions of the particles from 8.3 to 22 nm and the productivity of long chain hydrocarbons, at the expense of CH_4 selectivity, was favored with smaller particles.

3.1.3 Effect of the promoters

Promoters play an important role in the catalysts systems for FT synthesis, especially for Fe-based catalyst. The phase contact among the promoter/s and the active metals is crucial in order to reach an optimized effects [39].

Since Co is already more active with respect to Fe, promoters are not playing a crucial role in the Co-catalyzed FT reactors. However, typical Co-promoters are metals like Ru, Re, Pt or Pd. The real effect and the mechanism with which the promoter works with the active metal is highly influenced by the type of synthetic method adopted for the catalyst preparation. In general, noble metals can increase the dispersion over the

bare support and they can favor the H_2 adsorption thus increasing catalyst reducibility. A less expensive promoter for cobalt based catalysts is manganese. Some works reported the benefits in the use of Mn which decreased the selectivity to CH_4 and increased the yield to the heavy hydrocarbons fraction [39,62].

The promoters effects become much more important when iron based catalysts are taken into account. Alkali metal proved to be great promoter by suppressing the selectivity to CH_4 and increasing the C_{5+} fraction productivity. The addition of alkali metal could also enhance CO conversion and the production of light olefins in the range C_2-C_4. A lot of works have been carried out regarding the alkali metal promotions, the accepted effect is that the contact between Fe and alkali atom increases the heat of adsorption of a CO molecule on the catalyst surface thanks to the electronic promoting effect, with the result to wake the C-O bond and favor the CO dissociation [39].

It is important to highlight that, as has been reported previously, metallic iron is not stable under FT conditions, thus iron carbides are formed. For this reason it is important to know the effects of the promoters not only on metallic iron, but even on the Fe-carbides. Ribeiro et al. [63], thanks to a detailed X-ray study, showed that alkali metals lead to the formation of iron carbides. In particular, the rate of carbides formation increases in the order reported hereinafter:

Un-promoted< Li< Na< K= Rb= Cs.

Further studies reported that Mn could be a suitable promoter even for Fe-based FT catalysts since it increases the CO conversion and it improves the selectivity to C_{5+} and light olefin fraction. It has been demonstrated that Mn is incorporated in the octahedral sites of the magnetite structure and forms a mixed oxide with the structure $(Fe_{1-x}Mn_x)_3O_4$. This Fe-Mn oxide may promotes the formation of amorphous iron carbides (Fe_xC) with the result to increase the rate of CO hydrogenation. However, it has been noted an increase in the CO_2 selectivity provided by Mn-promoted Fe-based catalysts. This drawback could be due to the fact that Mn favor the conversion from metallic Fe species to Fe_5C_2, and then from this latter to Fe_3O_4 which increases the activity towards the WGS equilibria [39].

3.1.4 Effect of the support

The most common inorganic supports adopted in the preparation of industrial FT catalysts are silica, alumina, titania, magnesia and zirconia. SiO_2 has been identified as the best support in terms of activity and heavy fraction production while Al_2O_3 is an interesting support too, thanks to the activity towards the isomerization reaction due

to its amphoteric form. Titania has proved to be a good support for hydrogenation catalysts [64].

Anyway, during the recent years a wide range of innovative supports like zeolites, hydrotalcites and carbon nanotubes have been applied to the synthesis of Fischer-Tropsch catalysts.

The support dramatically influences the catalyst performances, in particular Bartholomew [65] reported a study where different Co-based catalysts with 10 %wt of active metal and supported on different inorganic support were tested at the same conditions (P= 1 bar, T= 225 °C, H_2/CO= 2). The author found out a variation of three orders of magnitude regarding the samples activity depending on the nature of the support which followed this order:

$Co/MgO < Co/C < Co/SiO_2 < Co/Al_2O_3 < Co/TiO_2$

On the other hand, a study carried out by Iglesia et al. [66] at higher pressure (P> 5 bar, T= 200 °C, H_2/CO= 2) demonstrated that the type of support has no influences on the catalyst activity and products selectivity. As reported in this work, the FT synthesis is a structure insensitive reaction and the differences in the catalysts performances are not due to the differences in the surface properties but rather from physical effects that affects transportation phenomena. For example, the chain growth probability should be greater in catalysts with an high percentage of micropores since the contact time is higher and diffusions limitations have a minor effect.

There are four different mechanisms with which the support can interacts with the active metals [65]:

- Decoration of the metal with inorganic support species by creating new active site that may act as promoters or inhibitors.
- Interactions metal/support that could modify the electronic properties of the active metal due to the acid or basic nature of the inorganic support.
- Formations of mixed oxides, like cobalt aluminate ($CoAl_2O4$) or cobalt silicate (Co_2SiO_4) which are very difficult, or impossible, to be reduced at suitable temperature for an industrial plant. These hard reducible species are completely inactive to FT reaction and they affect negatively the catalysts performances. The presence of low metal loadings (< 10 %wt) favors the formation of metal/support mixed oxides.
- The metal/support interactions have much more effect when metal loadings are relatively low and/or very high dispersions due to the presence of mixed oxides. For example, the type of support has almost no influence in catalyst when high metal loadings (> 10 %wt) and with a great fraction of active metal reducible (>

70 %wt) are synthesized. In this way, the different results obtained by Bartholomew and Iglesia are explained.

3.2 Novelty of the PhD project

The final aims of this PhD research work have been the synthesis, characterization and experimental tests in a suitable laboratory scale rig of innovative SiO_2 supported Fe and Co-based nanostructured catalysts active in the FT reaction. The use of supported catalysts, instead of massive ones, provides greater surface area, better dispersion of generated heat, and better mechanical resistance [67].

The kind of catalysts, the amount of active metals and promoters, and the type of preparation methods have been chosen in order to propose new materials and to optimize the one already existing in the FT literature.

In particular, two different synthetic techniques have been used to prepare nanostructured FT catalysts: flame spray pyrolysis (FSP) and synthesis by sonochemical decomposition (US). These two particular preparation techniques have been already largely applied for the synthesis of materials with special peculiarities but their use in the FT field is still very limited [68].

The recent literature is full of exhaustive examples of a wide rage application of nanostructured materials as develop of magnetic devices, photoelectronic equipment as semi-conductors, and then heterogeneous catalysts. These nanostructured materials have different surface and chemical-physical properties, i.e. higher surface area, better metal dispersion and better catalytic activity, if compared with bulks material synthesized traditionally. FSP and US are not the only two techniques for the synthesis on nano-supported catalysts, other established preparation procedure are gas-phase techniques (decomposition of volatile organometallic compounds), liquid-phase methods (reduction of metal halides), and mixed-phase approaches (metal atom vapor deposition into cryogenic liquids) [55].

Three different catalysts sets with different amounts of metal and promoters have been prepared and tested. The list of the samples synthesized is reported hereinafter; every number indicates the %wt of active metal or promoter in the catalysts:

1- An impregnated synthesized Fe-based catalyst and promoted with K and Cu (30 %wt of Fe, 2 %wt of K and 3.75 %wt of Cu) named $Fe_{30}K_2Cu_{3.75}$. The optimal loading of active metal and promoters have been already determined elsewhere in recent studies [69] while a first evaluation of the catalytic performances in reported in the PhD thesis by A. Di Fronzo [70].

2- Three different Co-based catalysts synthesized by flame spray pyrolysis (FSP), and eventually promoted with Ru (5 %wt of Co; 10 %wt of Co; 10 %wt of Co and 0.4 %wt of Ru). The catalysts are named as 5Co, 10Co and 10Co-0.4Ru.

3- Three different Fe-based samples eventually promoted with K and Cu, prepared with the use of ultrasound (US) (10 %wt of Fe; 30 %wt of Fe; 30 %wt of Fe, 2 %wt of K and 3.75 %wt of Cu); catalysts are named as Fe_{10}US, Fe_{30}US and $Fe_{30}K_2Cu_{3.75}$US.

Characterization analyses have been done on the catalysts after the synthesis step, after the activation pretreatment and, in some cases, even after the whole catalytic run, in order to justify, correlate and compare the experimental results with the catalysts physical-chemical and surface properties. The synthesized samples have been then characterized with ICP and CHN in order to verify the exact weight composition and the possible presence of impurities, with TPR in order to determine the optimal activation conditions, with TEM and SEM/EDX to verify the dispersion of the active metal and the dimensions of the nanoparticles on the bare support, with BET to measure the surface area of the catalysts and with XRPD in order to determine the presence and the phase of metal oxides.

The catalysts have been then tested using different conditions (activation temperatures, reaction temperatures, TOS, and H_2/CO ratios) in a suitable bench scale FT rig. The experimental plant used for the catalytic tests will be fully explained in Chapter 4 of this thesis. Moreover in some cases, the kinetic constants of FT reaction and WGS equilibria (when present) have been regressed starting from the experimental data obtained in the laboratory plant. This modeling work is useful to predict and confirm the catalytic results and for a primary evaluation of the performances of the catalysts in a whole BTL/CTL/GTL-FT process.

The detailed research work done with each catalysts set is explained in the upcoming paragraphs.

3.2.1 $Fe_{30}K_2Cu_{3.75}$

This sample was prepared with the traditional wet impregnation technique. The optimized synthesis procedure, activation conditions, and loading of active metal and promoters have been determined in previous works by Pirola et al. [69] and Di Fronzo et al. [70]. The experimental set up conditions adopted with this catalyst are reported here:

$Fe_{30}K_2Cu_{3.75}$: 30 %wt of Fe, 2.0 %wt of K and 3.75 %wt of Cu.

Activation step: flow of syngas (NL/h/g_{CAT}= 3.0) with a H_2/CO ratio equal to 2, at Tact.= 350 °C, P= 0.4 MPa, t= 4 h.

Catalytic runs: flow of syngas (NL/h/g_{CAT}= 3.0) with a H_2/CO ratios equal to 2, 1.5, 1, P= 2.0 MPa and reaction temperatures in the range T= 220- 260 °C.

In this part of the PhD research activity, a detailed study concerning the surface properties of the sample, such as BET surface area and the difference of the pore volume and pore area between the support without iron and the catalyst $Fe_{30}K_2Cu_{3.75}$ has been carried out in order to evaluate the effect of a high loading of iron on the bare SiO_2 surface.

The sample has been tested at different temperatures in order to understand the effect of this parameter on the catalyst activity, products selectivity and sample stability over TOS. Moreover the H_2/CO ratio has been varied between 1- 2 in order to evaluate the catalyst performances when a flow of syngas with a composition similar to the one of bio syngas is fed to the FT unit. Moreover a new part of the FT bench scale rig has been ideated to allow a primary series of experimental measurements of the composition of the light hydrocarbon fraction dissolved in the heavy products produced during the catalytic runs at different temperatures and H_2/CO ratios. These results will be useful in a further development of a kinetic model for slurry FT reactors which takes into account the diffusional limitations between the solid phase (catalyst), liquid medium (waxes) and gases (reactants and products).

The experimental results obtained in the FT rig have been then used to carry out a non-linear regression in order to regress the kinetic constants of FT reaction and WGS equilibria, which are both present on the catalysts surface. The regressed data can be used in a further work to develop a reactor model which can be included into a multi scale simulation of a whole BTL-FT plant with the relative economic analysis.

3.2.2 5Co, 10Co, 10Co-0.4Ru

Flame spray pyrolysis is an innovative synthetic technique which offers several advantages with respect to traditional methods. First of all, common catalysts preparation way commonly used both in research and industrial laboratories involves several steps and sometimes this result is a time-consuming process; moreover, even if one of these steps is not carried out correctly it can influence the final product with variations and alterations of the physical chemical properties resulting in a different material behavior [71].

Differently from the traditional synthesis ways, FSP does not present the same limitations and it is suitable for the production of catalytic materials on an industrial scale [72]. Flame spray pyrolysis has been also applied for the synthesis of high-

temperature stable materials thanks to the thermal resistance imparted by the flash calcination where very high temperatures (T> 1300 °C) are reached [68]. Moreover, this particular technique has been already applied in the synthesis of thermally stable well dispersed Ni-based catalysts for ethanol and glycerol steam reforming [73] and for the production of vanadium-based catalysts active in the oxidative dehydrogenation of paraffin to olefins [74]. Similarly with FT catalysts, both cited applications share non-negligible issue of coking. It has been demonstrated that small metal particle size can inhibit the growth of carbon on the catalyst surface; moreover. it was also showed that the flame spray pyrolysis method was able to improve the interactions between the metal and the bare support with the result to improve the metal dispersion and to stabilize the metal nanoparticles avoiding sintering over prolonged operation at high temperatures [75].

FSP has been successfully applied in a wide range of different application fields, as extensively reviewed by many authors [72,76,77] but it has been studied in a very limited way in the field of Fischer-Tropsch synthesis at the moment. Minnermann et al. [78] used this preparation approach to prepare an Al_2O_3 supported 10 %wt Co-based catalyst. The cited work reports a deep study on the influence of different parameters used during the FSP synthesis, but only few FT activity tests were carried out.

The formation of the catalyst via FSP method can be divided into four different steps which are carried out almost simultaneously in the flame:

- Drops evaporation: the organic solution which contains the solvent, the precursors and an organic liquid which, with the presence of methane, improves the combustion process. This mixture is then pumped into a capillary ending in a coaxial nozzle and mixed with O_2 in order to obtain an aerosol;

- Nucleation: the support and active metal precursors start the pyrolysis process and the organic part of the molecules starts to burn. In this way the first nuclei of the catalysts are formed;

- Condensation: the formed solid nucleus start to collide and they condensate each other while forming bigger catalysts agglomerate;

- Agglomeration: this steps takes part at the end of the flame and the smaller catalyst agglomerates collapse together and form agglomerates with bigger dimensions.

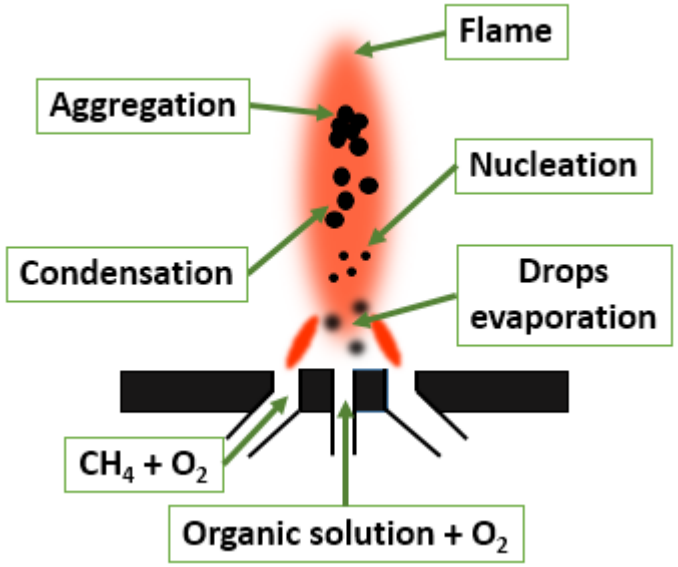

Figure 3.3: Mechanism of flame spray pyrolysis.

In this part of the work the attention has been focused on the optimization of the active metal loading during the FSP preparation of SiO_2 supported Co based FT catalysts in order to optimize the samples performances such as activity, selectivity and above all the samples stability over prolonged TOS. In particular three different samples have been synthesized using FSP, two monometallic catalysts and a bimetallic Ru-promoted one. The addition of ruthenium allows to improve the reduction of the Co oxide species, from Co_3O_4 to CoO and further to metallic Co [68].

The type of catalysts tested and experimental set up conditions adopted with this catalysts set are reported here:

5Co: 5 %wt of Co.

10Co: 10 %wt of Co.

10Co-0.4Ru: 10 %wt of Co and 0.4 %wt of Ru.

Activation step: flow of H_2 (NL/h/g_{CAT}= 5.5), at Tact.= 400 °C, P= 0.8 MPa, t= 4 h.

Catalytic runs: flow of syngas (NL/h/g_{CAT}= 3.0) with a H_2/CO ratio equal to 2, P= 2.0 MPa and reaction temperatures in the range T= 220- 275 °C.

The experimental data allow a comparison among the monometallic and bimetallic catalysts, moreover the benefits of the FSP technique with respect to other traditional synthetic methods are showed.

Even with FSP catalysts, a regression of the main kinetic parameters of the FT reaction has been carried out in order to simulate the performances of 10Co and 10Co-Ru. The regressed parameters can then be used to simulate an industrial FT reactor integrated in a BTL-FT plant.

3.2.3 $Fe_{10}US$, $Fe_{30}US$ and $Fe_{30}K_2Cu_{3.75}US$

Ultrasound (US) have been deeply investigated in the last two decades [79]. The power of US is originated from the physical phenomena of the acoustic cavitation, i.e. the formation, growth and implosion of bubbles in a liquid. The implosive collapse of the bubbles generates extreme conditions in which very high temperatures (T≈ 5000 K), cooling rates (10^9 K·s^{-1}) and pressures (P≈ 150 MPa) are locally reached [80]. These specific and particular conditions can be used in several ways as medicine, extraction processes and the production of bulk and nanostructured materials.

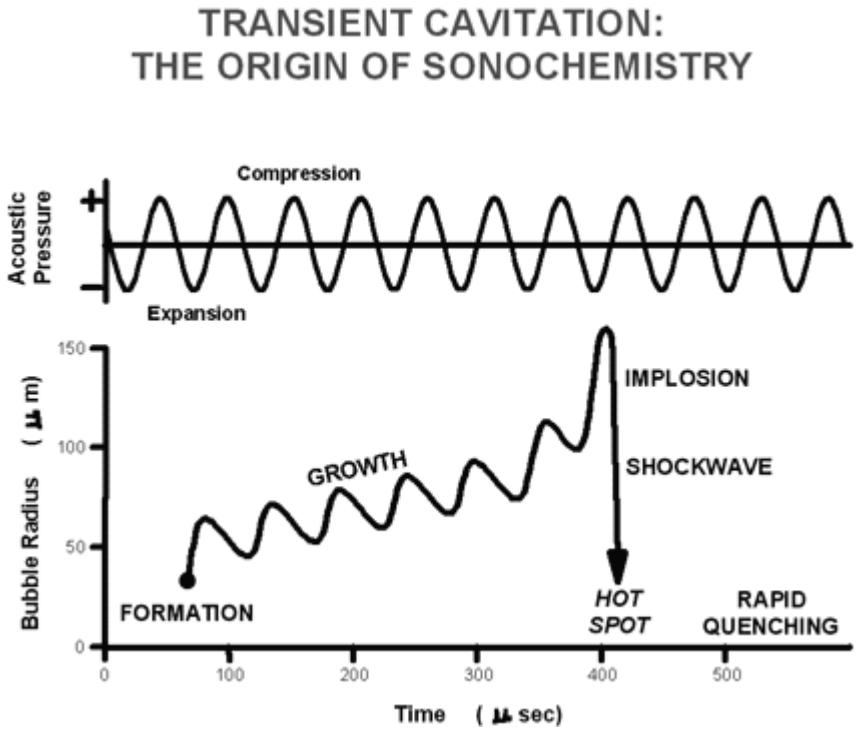

Figure 3.4: Mechanism of the acoustic cavitation od a gas into a liquid [80].

The use of US have been already tested in the production of several nanostructured materials and devices [55]. One possible US assisted synthesis of heterogeneous catalysts is the coupling of traditional preparation methods as wetness impregnation with ultrasound, in order to optimize the dispersion of the inorganic precursor on the support surface [81]. Another approach to achieve the synthesis of catalysts made

with the use of US is the sonochemical decomposition of volatile organometallic precursors like metal carbonyl in high boiling solvents in presence of an inorganic support as silica, alumina or titania. The exposure of the metal carbonyls like $Fe(CO)_5$ and/or $Co_2(CO)_8$ to ultrasound produces amorphous metallic nanoparticles with the oxidation state equal to 0, on the support surface [80].

The power, the frequency and the sonication length are not the only key parameter in the ultrasonic cavitation process, also the vapor pressure of the carbonyl reactants and the solvent used during the US synthesis are crucial parameters for the preparation of this kind of materials. The precursors have to be volatile because the sonochemical reaction starts in the vapor bubble while the solvent should have an high boiling temperature. Otherwise, the presence of the solvent in the collapsing bubble would reduce the efficiency of the sonication process. If compared to the already cited traditional synthetic ways, this method offers the same advantages of FSP such as nanostructured catalysts with more uniform size distribution, greater surface area and a more controlled phase composition [80].

Catalysts sonochemically prepared can be also exploited in the Fischer-Tropsch synthesis. In particular, different SiO_2 supported iron-based samples synthesized with traditional wetness impregnation and with the use of US have been already studied during the recent years in several works by Suslick et al. [80,82] and Pirola et al. [81]. Suslick synthesized a Fe-based sample with 10 %wt of active metal by US decomposition of $Fe(CO)_5$ and then he tested the FT activity of the catalyst at different temperatures and low pressure (100 kPa) without oxidizing the Fe^0 produced by the iron carbonyl decomposition present on the SiO_2 surface before the FT runs. In the work presented by Pirola, different iron-based samples with different loadings of Fe and promoters were synthesized by US assisted wetness impregnation, this technique consists into sonicate an aqueous solution where the inorganic precursors are dissolved. Furthermore he then tested the catalysts at high pressure (2.0 MPa) and different temperatures.

In this PhD project, three different iron based samples supported on SiO_2 with different amount of Fe and promoters are synthesized sonochemically by decomposing $Fe(CO)_5$ and a simpler way to oxidize the catalysts after the synthesis is proposed.

The type of catalysts tested and experimental set up conditions adopted with this catalysts set are reported here:

Fe_{10}US: 10 %wt of Fe.

Fe_{30}US: 30 %wt of Fe.

$Fe_{30}K_2Cu_{3.75}$US: 30 %wt of Fe, 2 %wt of K and 3.75 %wt of Cu.

Activation step: flow of syngas (NL/h/g_{CAT}= 3.0) with a H_2/CO ratio equal to 2, at Tact.= 350- 400 °C, P= 0.4 MPa, t= 4 h.

Catalytic runs: flow of syngas (NL/h/g_{CAT}= 3.0) with a H_2/CO ratio equal to 2, P= 2.0 MPa and reaction temperatures in the range T= 250- 260 °C.

With the experimental data collected and the characterization analyses, a deep evaluation of the benefits of the US synthesis with respect the traditional synthesis techniques is proposed.

4 Experimental: Fischer-Tropsch rig and analytical methods

All the catalytic tests were carried out in the same FT bench scale fixed bed reactor with an internal diameter of 6 mm and a length of the catalytic bed equal to 70 mm, always keeping the same experimental procedure and analytical set up with each run.

The catalyst (mass= 1 g) was mixed with α-Al_2O_3 (mass= 1 g) which is completely inert in terms of catalytic activity toward the FT reaction and acts as a diluting material in order to avoid the formation of hot spots in the catalytic bed, due to the heat generated during the reaction [83]. The catalysts and the diluent material have been pressed in pellets shape and then crushed and sieved into aggregates with dimensions in the range 105- 150 μm. Before the experimental tests the catalysts were activated in situ using the experimental conditions already reported in paragraph 3.2.

The feeding gas mixture (CO, H_2 and N_2 used as internal standard) was prepared in situ by mixing three different flow of pure CO, pure H_2 and pure N_2 using three different flowmeters and the pressure was set to P= 20 bar during each run. The total gaseous volume was measured before and after the FT catalytic reactor using two different gas totalizer.

After that the gaseous mixture was fed thought the fixed bed reactor, it passed into a cold trap which operates at the same pressure of the reactor and at T= 5 °C. This trap allows the condensation of the aqueous phase and the heavy hydrocarbons fraction (C_7-C_{30}). The amount of carbonaceous species dissolved in H_2O was determined at the end of each run with a TOC (Shimadzu 5000A) while the composition of the heavy fraction was measured using a gas chromatograph (Fisons-8000 series) equipped with a Porapack Q column.

The light gaseous fraction (CO, H_2, CO_2, CH_4 and light hydrocarbons) was on-line analyzed with a micro-gas chromatograph (Agilent® 3000A) every 120 minutes.

The analytic set-up used for each analytical instrument will be reported in the following paragraphs.

All the experimental runs had a whole duration of almost t= 80 h. The time zero is assumed to be the time at which all the process variables are set at the set-up values.

Using all the experimental data, a carbon balance with a maximum error of ±5 % on a molar basis was measured for each run.

4.1 FT laboratory plant

The general flowsheet of the FT laboratory rig used for the catalytic runs is reported in Figure 4.1.

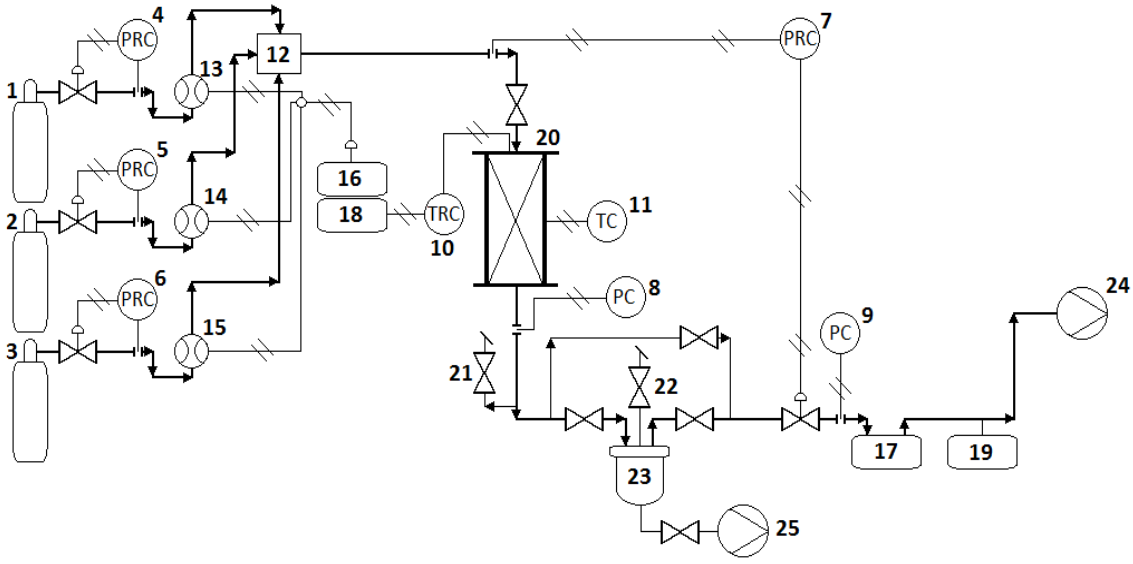

Figure 4.1: FT rig flowsheet.

The key explanation of every plant part is reported hereinafter:

- 1, 2, 3: H_2, N_2 and CO gas cylinders;

- 4, 5, 6, 7: Pressure regulators and controllers;

-8, 9: Pressure controllers;

- 10: Temperature regulator and controller;

- 11: Temperature controller;

- 12: Gas mixer;

- 13, 14, 15: Volumetric flowmeters;

- 16, 17: Volumetric flowmeters controllers and gas totalizers;

- 18: Reactor temperature controller and regulator;

- 19: Micro-GC;

- 20: FT fixed-bed reactor;

- 21, 22: Vent to air;

- 23: Cold trap;

- 24: Vent in the hood

- 25: Connection with the desorption system (paragraph 4.2).

A picture of the FT rig is reported in Figure 4.2 hereinafter:

Figure 4.2: Picture of the FT rig.

4.1.1 Flowmeters and equipment for pressure and temperature regulation

FT laboratory plant pressure is controlled by an electronic controller (Brooks®); this controller directly acts on an automatic valve placed after the cold trap. This vale works thanks to a pneumatic actuator and is able to work in a pressure range P= 0- 25 bar. This system can control the plant pressure with a care of 0.1 bar respect the set up and the valve temperature is kept at T= 110 °C in order to avoid the condensation of some heavy hydrocarbons residues which have not been condensed in the cold trap. For the same reason, even the pipe lines after the reactor are heated at T= 220 °C. The heating system of the pressure valve and the pipe lines is regulated by two electrical cables, both with a resistance of 7 Ω/m (Ascon®).

Figure 4.3: Pressure valve.

The fixed bed reactor temperature is regulated by a heating oven (Renato Brignole) and the CO, H_2 and N_2 flows are regulated by a series volumetric flowmeters (Brooks® 5850TR). The picture and the main characteristics of the flowmeters are reported in Figure 4.4 and Table 4.1.

Figure 4.4: Volumetric flowmeters for the regulation of CO, H_2 and N_2 flow.

Component	Range ($Nml \cdot min^{-1}$)	I/O signal (vdc)	Max Pressure (Bar)
H_2	0- 50	0- 5	100
CO	0- 50	0- 5	100
N_2	0- 20	0- 5	100

Table 4.1: Characteristics of the flowmeters.

4.1.2 FT reactor

The FT fixed bed reactor has been produced by Renato Brignole® Company. The tubular reactor allows to locate the catalyst vertically. The reactor is made of AISI 316 stainless steel and in the internal surface of the reactor where the catalyst is packed is made by a copper tube (thickness= 1 mm) in order to prevent some catalytic activities given by the steel and to help to keep the reactor temperature uniform as much as it is possible.

The gaseous mixture is fed from the top of the reactor and it goes to the bottom while passing thought the catalytic bed. The catalyst mixture is placed inside the reactor from the top and it is unloaded from the bottom. The FT reactor is equipped with an upper and a lower flanges which are connected with four screws each. The opening and closing operations require attention from the operator in order to avoid gas leaks and mechanical damages. The reactor picture is showed in Figure 4.5.

Figure 4.5: FT tubular reactor (left) and upper flange (right).

The catalytic bed temperature inside the reactor is monitored by two thermocouples: the first one is vertical and it is in direct contact with the catalyst while the second one is horizontal and it is in contact with the copper pipe placed inside the reactor. The temperature values measured showed only a small difference (≈ 2 °C).

The main characteristics of the FT reactor are summarized in Table 4.2.

Volume (cm^3)	Max. operating pressure (bar)	Max. operating temperature (°C)	Internal diameter (mm)	Height (mm)
17	100	400	6	560

Table 4.2: Characteristics of the FT reactor.

4.1.3 Cold trap

The condensation of the heavy hydrocarbon fraction (>C_7) and the aqueous phase is obtained in the cold trap. This trap is placed after the FT reactor and before the pressure control valve; this allows to the trap to work at the same pressure of the reactor (P= 20 bar) and at T= 5 °C. The volume, height and width of the cold trap are, respectively, 125 ml, 100 mm and 40 mm.

The temperature of the cold trap is maintained constant by an external system in which circulates cold water from a thermocriostat (Crioterm® 190 isco). The scheme of the cold trap is reported in Figure 4.6.

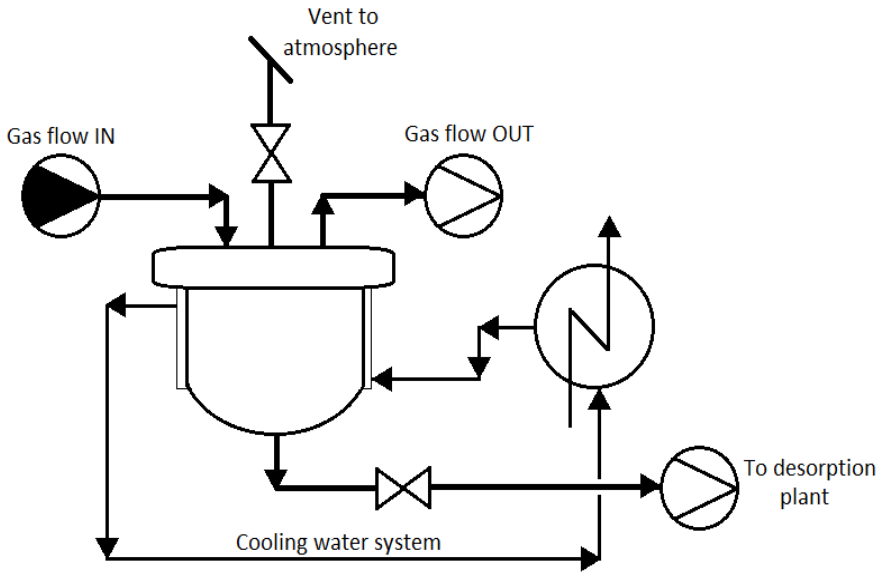

Figure 4.6: Flowsheet of the cold trap.

The cold trap can be opened only at the end of the catalytic test in order to don't compromise the process equilibria and stability. Since is not possible to withdraw liquid samples during the test, the one that will be found at the end of the run represents an average value of the whole TOS. The cold trap is opened by an upper

flange fixed with four screws. once the trap is open, the two different phases are extracted and weighted; after it, the cold trap is well washed with acetone.

4.1.4 Volumetric flow totalizer

In order to calculate all the products selectivity and to do an accurate measurement of the total carbon molar balance it is needed to know the total gas volume, and to monitor the exact volumetric flowrate which flow out from the plant. The incoming flow of the reactant mixture and nitrogen is totalized by the same flowmeters that regulate the volumetric flow (Brooks® Instruments) before the gas mixer, while the out coming flow which contains the unreacted H_2 and CO, the light hydrocarbons and the by-products (CO_2 and CH_4) is totalized by a Ritter® mod. TG01-5 instrument which is reported in Figure 4.7.

Figure 4.7: Flow totalizer Ritter® mod. TG01-5.

4.2 Novelty made in the FT rig during this PhD project: the desorption system

Part of the PhD work has been focused on the development of a desorption system directly connected to the FT rig in order to desorb the light fraction of hydrocarbons, C_1-C_6 which is dissolved in the heavy organic phase. The desorption of a gas into a liquid is favored at high temperature and low pressures, Since the light hydrocarbon fraction produced has a very high vapor pressure, it is not needed an heated

equipment, since just a vacuum pump is enough to obtain the complete desorption of the products. The pump used to decrease the pressure till the value of P≈ 10 torr is a Leroy-Somer® 63 ER.

The average mass of heavy fraction produced during a typical FT runs is around ≈ 5- 7 g, so it is understandable that the light hydrocarbons dissolved into it are just a few millimoles. For this reason it is important to adopt a performing system for the products desorption which is able to separate the aqueous fraction from the organic one before the desorption and to evade the presence of air in the desorption vessel since it can dilute the light hydrocarbons gaseous mixture produced. The water fraction is separated by the organic one using a transparent sampling pipe (8) and a three ways valve (V3) which can be seen in Figure 4.8. Once the water is eliminated only the $>C_7$ mixture is present in the cold trap and it is then flowed into the desorption vessel (V= 100 ml). It is very important to avoid a direct contact between the cold trap and the desorption vessel for two reasons: the first one is that a part of the light hydrocarbons present in the pipe lines of the plant can flow into the desorption plant and the second is because a very high difference of pressure between the trap and the vessel (ΔP≈ 21 bar) can create serious damages to the mechanical equipment and the operator. After that the vacuum is applied, the produced gaseous mixture is analyzed by the same micro-GC already described using the same analytical conditions. Once the desorption process is done, the atmospheric air is inserted again in the vessel by opening the head valve and the heavy hydrocarbons fraction in the vessel are flowed out from the bottom. The flowsheet of the desorption system adopted is showed in Figure 4.8.

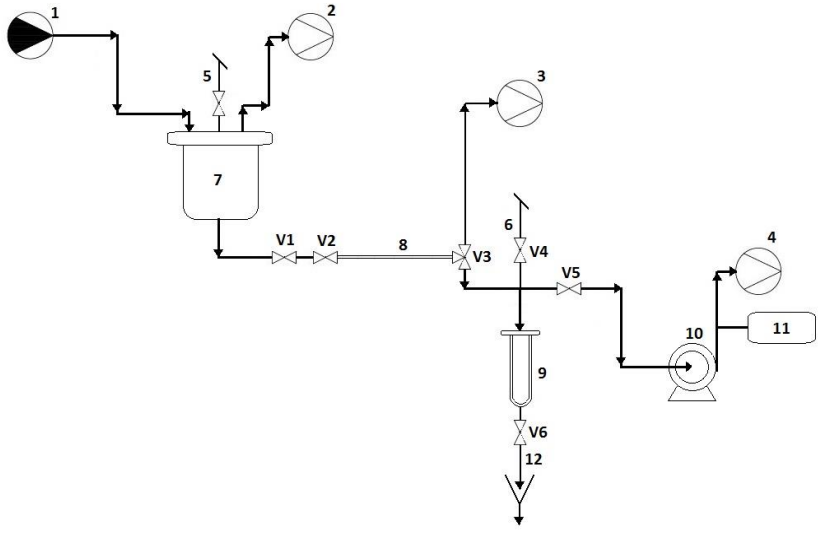

Figure 4.8: Flowsheet of the desorption system.

The key part of the system are explained hereinafter:

- 1: Inlet gas in the cold trap;

- 2: Outlet gas from the cold trap;

- 3: Drain pipe line of the water phase;

- 4, 5, 6: Vent in the hood;

- 7: Cold trap;

- 8: Sampling pipe line;

- 9: Desorption vessel;

- 10: Vacuum pump;

- 11: Micro-GC;

- 12: Drain of the heavy hydrocarbon phase.

While the complete list of the relevant valves for the desorption process is here reported:

- V1: Cold trap valve;

- V2: Inlet sampling pipe valve;

- V3: Outlet three ways sampling pipe valve;

- V4: Head vessel valve;

- V5: Vacuum pump valve;

- V6: Bottom drain valve.

4.2.1 Desorption system procedure

As already explained, the desorption system must be used in a completely standardized procedure in order to achieve a perfect success of the analysis and to avoid any type of damage.

The desorption procedure can be divided in four parts:

- *Elimination of the atmospheric air*: in order to eliminate all the air present in the plant before the desorption process it is important to keep V1, V6 and V4 completely closed and then to set the three ways valve V3 in order to connect the desorption vessel with the sampling pipe line. At the same time V2 and V5 must be opened. Once that all the valves are set, it is possible to turn on the vacuum pump and to wait ≈ 25-30 mins in order to be sure that all the air present is evaded.

- *Separation of the aqueous/organic phases*: first of all, V3 must be closed (no connection between sampling pipe line and drain/desorption vessel). At this point V1 must be opened in order to allow the water to flow in the sampling pipe line. H_2O is the first component which flows out since it has the greater density and the sampling pipe line is connected to the bottom part of the cold trap. Once the sampling pipe is full of liquid water, V1 and V2 must be closed and V3 tuned on the drain side in order to eliminate the water present. It is very important to keep V1 and V2 closed while water is drained otherwise all the liquid products in the cold trap would be pushed out due to the great pressure difference. In order to eliminate all the water present it is just needed to repeat this point procedure till the organic phase does appear in the sampling pipe line. It is very easy to understand the difference between the organic phase and the water one because they have different colors and the sampling line is a transparent pipe.

- *Desorption process*: in this step the sampling tube is filled with the organic phase, so it is necessary to repeat the same procedure but to tune the V3 valve on the desorption vessel. So, close V3, open V1 and V2 and fill the sampling pipe line, close V1 and V2 again and open V3 on the vessel side than repeat this procedure till all the organic phase is flowed in the vessel (again, it is important to don't open V1, V2 and V3 contemporaneously and it's easy to determine the end of the organic phase just by observing the sampling pipe line). When all the organic phase is in the vessel it is possible to close V3 and to leave the system into static vacuum for some minutes in order to allow the light gases desorption. After this time, it is possible to open V5 and start the micro-GC analysis.

- *End of the desorption process and vessel cleaning*: at the end of the procedure, when the analysis on the desorbed gases has been done, it is just necessary to keep V1 closed and V5 opened, to turn off the vacuum pump and then to open V4 in order to flow atmospheric air inside the plant and increase the pressure to the atmospheric value. At this point the heavy products that are still in the vessel can be drained from the bottom by opening V6. At the end of this procedure the vessel can be opened by the upper flange and washed with acetone.

4.3 Analytical apparatus

4.3.1 Micro-GC

In order to quantify the amount of produced and unreacted gases, the mixture is on-line analyzed every 120 minutes during the whole test with a micro-GC Agilent® 3000A.

In this instrument the analyzed sample is divided in two different modules and analyzed at the same time. The first one has a chromatographic column filled with molecular sieves (molsieve) which is able to separate the molecule as a function of their size, in particular it can separate He (used as carrier), He, H_2, Ne, Ar, O_2, N_2, CH_4 and CO; the second one is a OV-1 module filled with polydimethylsiloxane by which it is possible to separate CO_2 and all the hydrocarbons in the range C_2-C_6. Even if the two modules can work with different carriers, helium has been chosen as carrier for both of them. Moreover each module is equipped with a thermo-conductibility detector (TCD) which guarantee a sensibility limit of the analyses of about 50 ppm for each compound.

The adopted analytical set-up was a carrier pressure of 100 kPa and a column temperature of T= 100 °C for the first module and a pressure of 241 kPa and a T= 45 °C in the second one.

The micro-GC scheme and an example of an analysis are reported in Figure 4.9 and Figure 4.10.

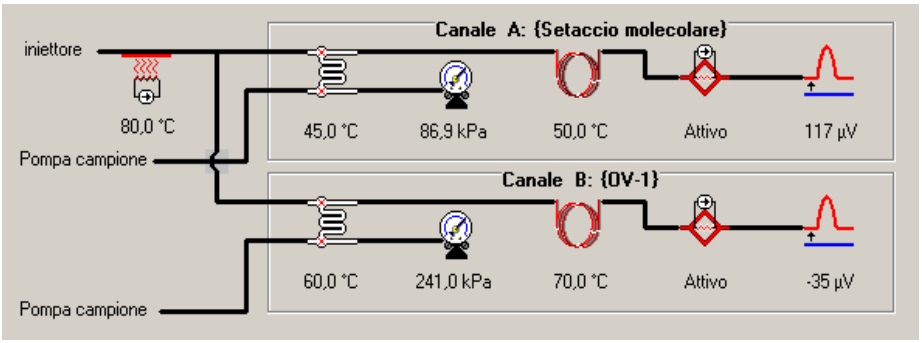

Figure 4.9: Micro-GC scheme.

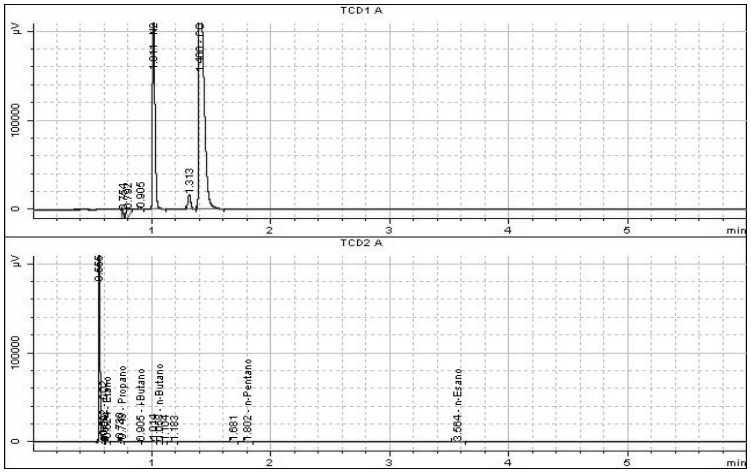

Figure 4.10: Example of a GC analysis made with Agilent® 3000A.

4.3.2 Gas chromatograph

The determination of the molar composition of the heavy organic phase was carried out with a Fision Carlo Erba® 8000 series GC equipped with a Varian VF-1ms column filled with polydimethylsiloxane with a length equal to 25 m and a FID detector. This instrument is able to separate the C_7-C_{30} fraction with a sensibility limit of about 100 ppm for each compound. The analysis starts with a column temperature of T= 60 °C for 3 mins, and then it is heated up to T= 260 °C with a rate of 8 °C·min^{-1}. At the end of the analysis a regeneration process at T= 300 °C for 90 mins is necessary in order to clean the column. A typical chromatograph of the analysis is reported in Figure 4.11.

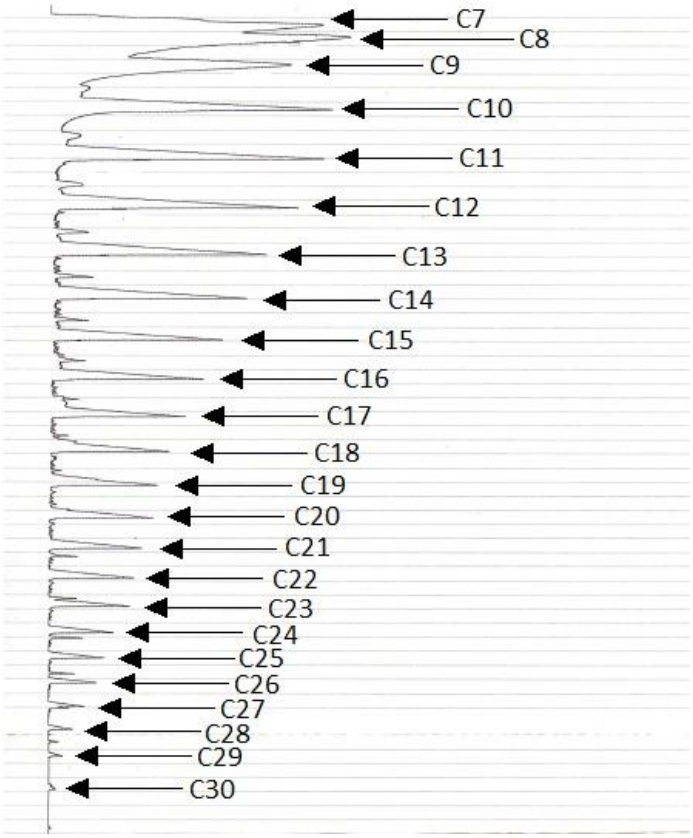

Figure 4.11: Example of a chromatograph of an heavy organic phase.

4.3.3 Total organic carbon (TOC)

In order to exactly determine the carbon molar balance for each runs, it is necessary to quantify the amount of carbonaceous species (short chain alcohols) dissolved in the water produced during the FT reaction.

This analysis is carried out with a Shimadzu® TOC 5000A. This instrument is able to oxidize all the organic carbon present in the sample by flowing the vaporized sample through an oxidation reactor filled with a Pt-based catalyst at high temperature (T= 700 °C). In this way all the carbon present in the sample is converted into CO_2 and quantified by an IR detector.

4.4 Analytical instruments calibration

4.4.1 Flowmeters calibration

The flowmeters calibration was carried out directly by the production company Brooks®. The obtained calibration results for all the three flowmeters are reported hereinafter in Table 4.3- 4.5.

- H_2 flowmeter:

Set Flow ($Nml \cdot min^{-1}$)	Measured flow ($Nml \cdot min^{-1}$)	Error (%)	Error limit (±%)
5	5.085	1.70	20
10	10.09	0.9	10
25	25.11	0.44	4
50	50.18	0.36	2
75	75.3	0.4	1.33
100	100.5	0.5	1

Table 4.3: Calibration of H_2 flowmeter.

- CO flowmeter:

Set Flow ($Nml \cdot min^{-1}$)	Measured flow ($Nml \cdot min^{-1}$)	Error (%)	Error limit (±%)
2.5	2.47	-1.2	4.70
5	4.96	-0.8	2.70
12.5	12.42	-0.64	1.50
25	24.86	-0.56	1.10
37.5	37.32	-0.47	0.97
50	49.88	-0.24	0.9

Table 4.4: Calibration of CO flowmeter.

- N_2 flowmeter:

Set Flow ($Nml \cdot min^{-1}$)	Measured flow ($Nml \cdot min^{-1}$)	Error (%)	Error limit (±%)
1	1.18	18	20
2	2.21	10.5	10
5	5.19	3.8	4
10	10.17	1.7	2
15	15.18	1.2	1.33
20	20.04	0.2	1

Table 4.5: Calibration of N_2 flowmeter.

In the set point conditions adopted in the FT plant the error given by the flowmeters is always lower than the maximum error limit allowed.

4.4.2 micro-GC calibration

The calibration of the micro-GC was made using the analysis parameters already optimized. These parameters for each module are reported in Table 4.6.

Parameter	Module 1 (molsieves)	Module 2 (OV-1)
Sample Injector temperature (°C)	80	80
Column Injector temperature (°C)	50	60
Column temperature (°C)	100	45
Sampling time (s)	60	60
Injection time (ms)	30	30
Analysis time (s)	360	360
Post-analysis time (s)	0	0
Column pressure (kPa)	100	241
Detector sensibility	standard	standard

Table 4.6: Optimized parameters for the FT micro-GC analysis.

The calibration has been carried out by using two different gas mixtures and has been made in the laboratory of "SRA Instruments Italia". This company is a Agilent Technologies Premier Solution Partner, directly present in Italy and France, and it is constantly engaged in research and development of solutions based on portable and ultra-fast micro-GC.

Anyway, a further calibration for the quantification of the CO flow has been then carried out in the laboratory where the FT rig is present.

The compositions of the gas mixtures used during the calibration process are reported in Table 4.7 and 4.8.

Standard Mix 1	
Compound	Quantity (%mol)
CH_4	96.65
N-hexane	0.03
Iso-pentane	0.03
N-pentane	0.03
N-butane	0.03
Iso-butane	0.03
Propane	0.10
Ethane	0.10
CO_2	1.00
N_2	2.00

Table 4.7: Composition of the standard mix 1.

Standard Mix 2	
Compound	Quantity (%mol)
H_2	0.0976
N_2	1.960
CO	1.030
CH_4	96.910

Table 4.8: Composition of the standard mix 2.

Since the micro-GC is equipped with an automatic injection system and the volume injected in the GC columns is always the same, it is possible to calibrate directly CO_2 and light hydrocarbon with a direct calibration without the use of an internal standard. The chromatographic area is directly correlated with the concentration of the compound in the mixture, so the calibration factors have been determined with Eq. 4.1.

$$calibration\ factor = \frac{chromatographic\ area}{compound\ concentration} \quad \text{(Eq. 4.1)}$$

Once that all the calibration factors are calculated using the standard mixtures provided by SRA company, it is easy to figure out how to calculate the concentration of a "i" compound during a typical FT run. The equations used are here reported (Eqs. 4.2- 4.4):

$$\%v_{"i"} = \frac{area_{"i"}}{calibraction\ factor_{"i"}} \quad \text{(Eq. 4.2)}$$

However, it is important to remember that in the FT plant a flow of N_2 has been always used in all the runs as an analytical standard for the CO quantification. Since N_2 is not a FT gas (reactant or product) Eq. 4.2 must be rearranged into Eq. 4.3:

$$\%v_{"i"} = \frac{area_{"i"}}{calibraction\ factor_{"i"}} \cdot \frac{Flow_{Total}}{Flow_{FT}} \quad \text{(Eq. 4.3)}$$

Where:

$$Flow_{FT} = Flow_{Total} - Flow_{N2} \quad \text{(Eq. 4.4)}$$

In order to better understand this issue, an example is here reported; if during a run a FT flow equal to 20 Nml·min^{-1} is measured, and a concentration of 2 % of CO_2 is detected, it means that a flow of 0.4 Nml·min^{-1} of CO_2 is passing thought the plant. However, if N_2 flow is set to 10 Nml·min^{-1} it means that the total flow will be 30 Nml·min^{-1} (20 Nml·min^{-1} + 10 Nml·min^{-1}). If the % of CO_2 is calculated just by using the total flow, the result would be:

$$\%v_{"CO2"} = \frac{Flow_{CO2}}{Flow_{Total}} \cdot 100 = \frac{0.4\ Nml \cdot min^{-1}}{30\ Nml \cdot min^{-1}} \cdot 100 = 1.33\ \% \quad \text{(Eq. 4.5)}$$

Which is a wrong result. However if the concentration of CO_2 is calculated with the correction made in Eq. 4.3, the result will be:

$$\%v_{"CO2"} = \frac{Flow_{CO2}}{Flow_{Total}} \cdot 100 \cdot \frac{Flow_{Total}}{Flow_{FT}} = \frac{0.4\ Nml \cdot min^{-1}}{30\ Nml \cdot min^{-1}} \cdot 100 \cdot \frac{30\ Nml \cdot min^{-1}}{20\ Nml \cdot min^{-1}} = 2\ \% \quad \text{(Eq. 4.6)}$$

Which is the right result.

This method is useful for the quantification of all the light hydrocarbons C_1-C_6, and the CO_2 and all the calibration factors calculated with the standard mixtures are reported in Table 4.9.

Module	Compound	Retention time (min)	Calibration factor
Molsieves	N_2	1.007	35119
	CH_4	1.203	27027
	CO	1.402	//
OV-1	CO_2	0.592	16722
	Ethane	0.624	19230
	Propane	0.745	25706
	I-butane	0.918	28248
	N-butane	1.061	27027
	I-pentane	1.556	32051
	N-pentane	1.808	32326
	N-hexane	3.578	33670

Table 4.9: Calibration factors and retention times of the light fraction.

As reported before, the only component that is not directly determined with the calibration reported above, is the CO which is quantified using the internal standard (N_2). Nitrogen is not involved in FT reaction so it pass through the FT rig without any chemical modification and the inlet N_2 flow is the same as the outlet N_2 flow.

Even if CO can be determined directly with the previous calibration method, it is preferable to develop a method with the use of an internal analytical standard in order to measure with more precision the outlet CO flow since it determines the CO conversion value and all the products selectivity.

In this method, the ratio between the chromatograph areas of CO and N_2 is linearly correlated with the ratio between their flowrates. The calibration has been carried out using the typical FT conditions (T= 250 °C, P= 20 bar), without the catalyst and by varying the CO and N_2 flows.

The experimental results obtained during the calibration of the CO-N_2 system are reported in Table 4.10.

Flow CO (Nml·min^{-1})	Flow N_2 (Nml·min^{-1})	Flow CO / Flow N_2	Area CO	Area N_2	Area CO / Area N_2
15.6	5.02	3.1076	309212	127456	2.4260
15.6	10.04	1.5538	255448	212938	1.1996
10.4	5.02	2.0717	279949	181124	1.5456

Table 4.10: CO calibration of the micro-GC.

The calibration factor of the carbon monoxide is easily calculated by calculating the slope of the straight line obtained by plotting the chromatograph area ratios of CO and N_2 and the ratio between their flowrates, presented in Figure 4.12.

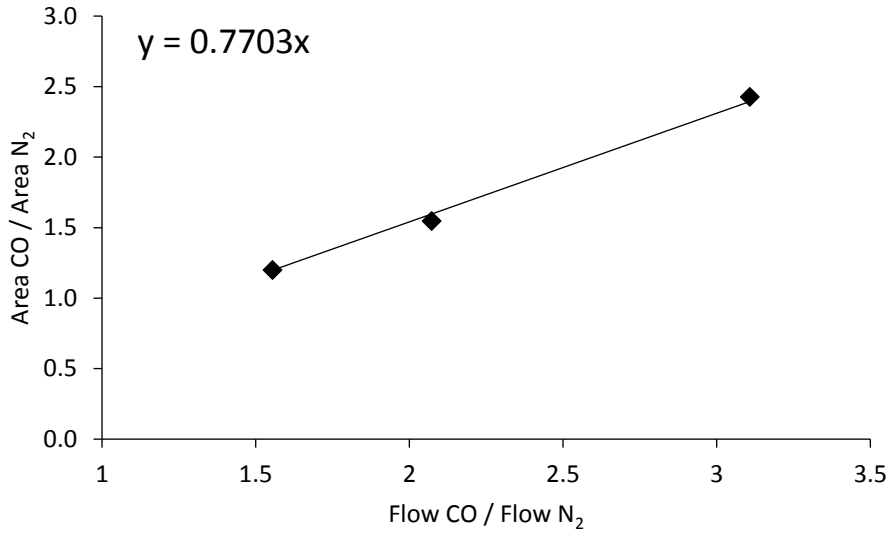

Figure 4.12: Calibration graph.

From the graph reported in Figure 4.12, it is evident that the obtained calibration factor is 0.7703.

The correlation between the reported ratios is reported in Eq. 4.7:

$$\frac{Area_{CO}}{Area_{N2}} = 0.7703 \cdot \frac{Flow_{CO}}{Flow_{N2}} \quad \text{(Eq. 4.7)}$$

During an experimental run, where the areas of both CO and N_2 are given by the micro-GC and the N_2 flow in known, the outlet flow of CO is easily calculated as reported in Eq. 4.8:

$$Flow_{CO} = \frac{Area_{CO} \cdot Flow_{N2}}{Area_{N2} \cdot 0.7703} \quad \text{(Eq. 4.8)}$$

Finally, the CO conversion can be calculated as follows in Eq. 4.9:

$$CO_{conversion} = \frac{Flow\ CO_{IN} - Flow\ CO_{OUT}}{Flow\ CO_{IN}} \cdot 100 \quad \text{(Eq. 4.9)}$$

4.4.3 Gas chromatograph calibration

As reported in the previous paragraphs, this instrument is used to analyze and quantify the hydrocarbons fractions in the range C_7-C_{30}, which is the heavy organic phase collected in the cold trap.

Even in this case it is necessary to identify a standard by which it is possible to calculate all the calibration factors for each fraction, the calibration equation will be presented in Eq. 4.10:

$$\frac{Area_{"i"}}{\%\ mol._{"i"}} \cdot f_{"i"} = \frac{Area_{"j"}}{\%\ mol._{"j"}} \cdot f_{"j"} \quad \text{(Eq. 4.10)}$$

Where "i" and "j" are the component of the mixture, Area "i" and Area "j" are the GC areas obtained in the analysis and % mol. "i" and % mol. "j" are the molar fractions of the two component in the mixture.

This calibration method used is called "internal standard method" since one of the analyzed compound is defined as a standard and not external standards are needed. Usually the calibration factor of the chosen internal standard is set equal to 1. In this analysis it has been decided to use n-heptane as internal standard since is if a FT product, moreover it usually has a great and well determinable composition in the heavy organic phase and it is always all condensed in the trap.

Eq. 4.10 can be rearranged in Eq. 4.11 as follows:

$$f_{"i"} = f_{n-heptane} \cdot \frac{Area_{n-heptane}}{\%mol_{n-heptane}} \cdot \frac{\%\ mol._{"i"}}{Area_{"i"}} \quad \text{(Eq. 4.11)}$$

Where the calibration factor of n-heptane is equal to 1. In this way all the other calibration factors are easily determinable just by preparing a standard mixture of n-heptane and the other heavy hydrocarbons. If all the hydrocarbons in the range C_7-C_{30}

are not available it is possible to use some of them in the standard mixture and then calculate by extrapolation all the other factors. Before that the standard mixture was analyzed, is has been diluted 1/1 on a weight basis with carbon disulfide (CS_2).

The composition of the standard mixture used for the calibration is reported in Table 4.11.

Compound	PM ($g \cdot mol^{-1}$)	Mass (g)	% mol.	Area
n-heptane (C7)	100.2	0.1839	0.326294847	57951830
Undecane (C11)	156.31	0.1724	0.196086054	69138380
Dodecane (C12)	170.33	0.1184	0.123582439	48818840
Tetradecane (C14)	198.4	0.1439	0.128948215	56681360
Pentadecane (C15)	212.41	0.1276	0.106800165	51430420
Hexadecane (C16)	240.48	0.0799	0.059069599	30647300
Nctadecane (C18)	254.494	0.0443	0.030947273	15579240
Nonadecane (C19)	268.52	0.0427	0.028271408	16618320

Table 4.11: Standard mixture used for the calibration.

The standard mixture reported in Table 4.11 is an example of a typical one, several reproducibility tests have been made with different standard mixtures. The average calculated calibration factors from all the standard mixtures analyzed are reported in Figure 4.13.

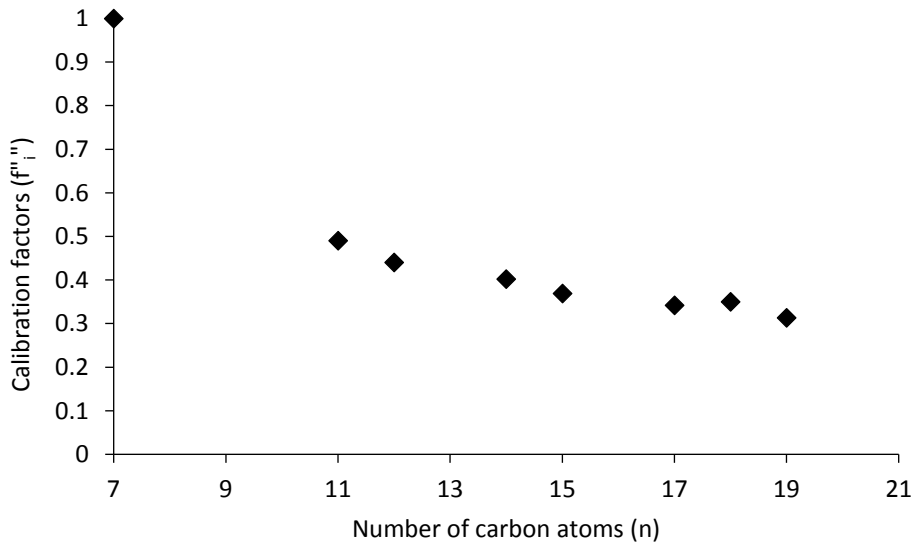

Figure 4.13: Calculated calibration factors for the GC analysis.

From the calibration factors founded and presented in Figure 4.13 is possible to elaborate a trend line which will allow the calculation of the factors of each component in the range C_7-C_{30}.

The trend line which allows the interpolation of the data is reported in Eq. 4.12:

$$f_{"i"} = -0.1134 + \frac{7.4192}{n} \qquad \text{(Eq. 4.12)}$$

Where f"i" is the calibration factor of the i-component and n is the number of carbon atom in the "i" molecule. With Eq. 4.12 is then possible to calculate all the calibration factors for each component. The results of the interpolation are reported in Table 4.12.

Number of C atoms in the molecule	Calibration factor
7	0.946486
8	0.814
9	0.710956
10	0.62852
11	0.561073
12	0.504867
13	0.457308
14	0.416543
15	0.381213
16	0.3503
17	0.323024
18	0.298778
19	0.277084
20	0.25756
21	0.239895
22	0.223836
23	0.209174
24	0.195733
25	0.183368
26	0.171954
27	0.161385
28	0.151571
29	0.142434
30	0.133907

Table 4.12: Interpolated calibration factors of the GC analysis.

Moreover, the GC allows a qualitative evaluation of the components which are present in the heavy organic phase since each of them has its retention time, in particular, greater is the number of carbon atoms higher is the retention time in the column. The retention times of all the fractions as a function of the number of C atoms are reported in Figure 4.14.

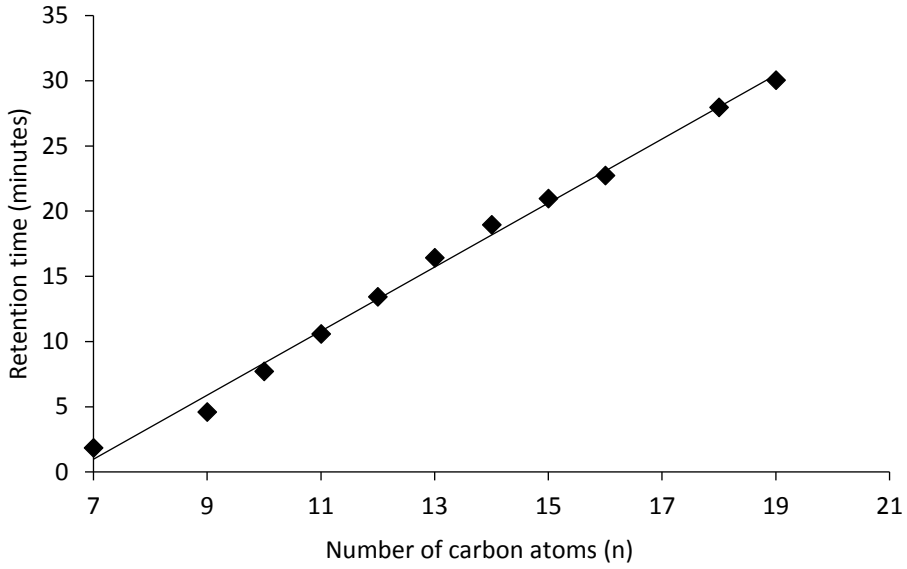

Figure 4.14: Retention time of the components present in the heavy fraction.

4.4.4 Total organic carbon (TOC) calibration

The Shimadzu® TOC 5000A allows to carry out a quantitative determination of the carbonaceous species dissolved in the aqueous phase but it is not possible to determine the type of molecules. For this reason it is possible to perform the calibration procedure with a solution which contains a standardized amount of carbon.

The best standard molecules for the TOC calibration are stable, well water soluble and non-volatile compounds like the potassium hydrogen phthalate.

The calibration is possible since there is a linear correlation between the amount of C dissolved and the areas given by the instrument. The TOC calibration line is reported in Figure 4.15.

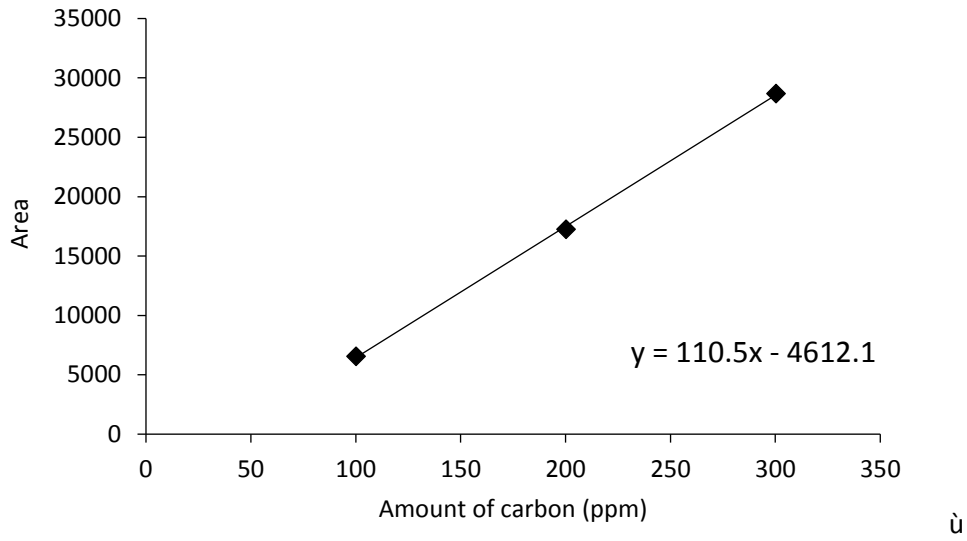

Figure 4.15: TOC calibration.

4.5 FT rig laboratory procedure

Every FT runs reported have been carried out in a precise an well-defined procedure in order to make all comparable data, since a difference in the experimental conditions can cause a loss of reproducibility of the data. This procedure can be divided into different steps here presented in order of time:

- Catalyst/diluent mixture preparation and loading into the FT fixed bed reactor;

- Sample activation and FT catalytic test;

- End of the run, cold trap opening and recover of the aqueous and organic phases;

- Reactor and analytical apparatus cleaning step.

4.5.1 Catalyst/diluent mixture preparation and loading into the FT fixed bed reactor

The catalyst preparation is a standard procedure and it is the same for every kind of samples tested in the FT reactor. In particular, as previously explained, the catalyst is pressed into pellets and big aggregates, and then crushed and sieved in the range between 105 and 150 micron. The same operation is required with the diluting material (α-Al_2O_3) provided by Fluka. Once the sieves operation are done, both catalyst and alumina must be placed into an oven at T= 120 °C for almost 12 hours in

order to eliminate all the water and moisture present on the powders. Once that 12 hours passed it is possible to mix the catalyst and the alumina with a ration 1/1 on a weight basis. Since a mass equal to 1 g of catalysts has been used in all the experimental runs, 1 g of dry α-Al_2O_3 was needed before each run. The main characteristic of α-Al_2O_3 are summarized in Table 4.13.

Surface area ($m^2 \cdot g^{-1}$)	Density ($g \cdot cm^{-3}$)	Composition (%)	Moisture (%)
0,7- 1,3	1,72	99,6 Al_2O_3 < 0,05 SiO_2 0,1 FeO < 0,01 TiO_2	26

Table 4.13: Main characteristic of the Al_2O_3 used as diluent material.

Once the mixture is prepared, it is possible to load it into the reactor. It is important to charge the catalyst in the middle of the reactor because only in the middle the temperature inside the reactor pipe is constant.

The catalysts/diluent mixture is immobilized by a piece of quartz wood placed on the lower and upper side of the catalytic bed. It is preferable to load and press only a small amount of mixture per time in order to avoid the formation of preferential paths and to make all the catalytic bed as more uniform as possible. A schematic representation of the catalytic bed is reported in Figure 4.16.

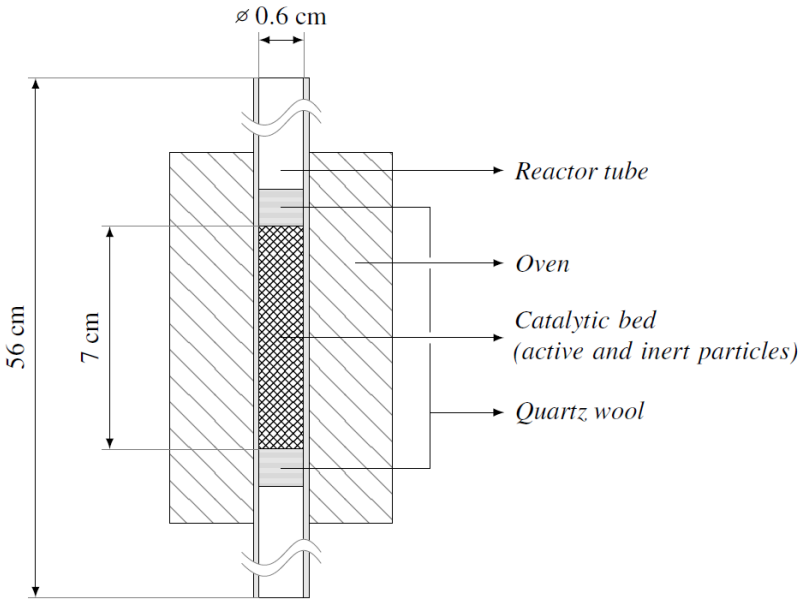

Figure 4.16: Scheme of the catalytic bed.

When all the mixture is completely loaded it is possible to close the upper and lower reactor flanges and to start the experimental test.

4.5.2 Sample activation and FT catalytic test

Before every FT test, the catalyst requires an activation (reduction) procedure either with Co or Fe-based ones. The activation parameters have been already reported in the previous paragraphs. However it is important to raise the pressure using the proper reducing gas or gas mixture to the set-up value (P= 8 bar for Co-based catalysts and P= 4 bar for Fe-based catalysts). Once the plant reaches the set up pressure it is advisable to close the valve before the reactor and check if the pressure remains constant since some leaks could be present. If the pressure values does not decrease, it is possible to increase the temperature to the optimized value to perform the activation step.

Usually, the set activation time is 4 hours, but in some cases longer activation steps could have been performed. When the activation step is done, the pressure must be increased till the P= 20 bar (standard operating condition) and the temperature must be set to desired value to perform the test. When both P and T values are reached the in and out gas totalizer must be reset to 0 and the on-line micro-GC analyses have to be set. Moreover it is important to turn on the cold trap cryostat and the pipe lines heating system in order to condense the water and the heavy hydrocarbons in the trap instead of the pipes of the plant.

The FT tests usually have a duration of 90 hours, which means a non-stop run from Monday afternoon till Friday morning of the same week. Sometime longer runs (TOS≈ 200 h) have been carried out in order to evaluate the catalysts long term stability.

4.5.3 End of the run, cold trap opening and recover of the aqueous and organic phases

When the catalytic run is ended, the P must be set to 0 bar (atmospheric pressure) and the heating oven turned off. The use of compressed air connected to a disposed pipe in the reactor will faster up the cooling process.

When the pressure reaches the atmospheric value it is possible to disconnect the cold trap and to open it to recover liquids products. The two phases are then separated, weighted and analyzed. The aqueous is analyzed by TOC and the heavy organic fraction by GC analysis.

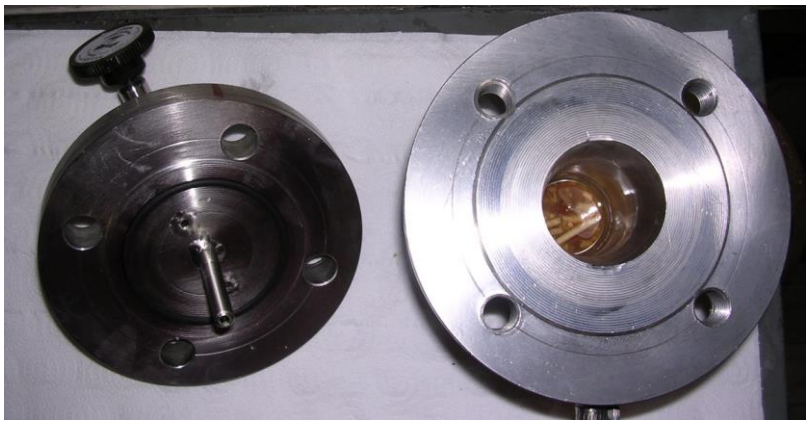

Figure 4.17: Opened cold trap with heavy hydrocarbon phase (yellow liquid).

At this point, it is also possible to turn off the cryostat and the automatic analysis system of the micro-GC.

4.5.4 Reactor and analytical apparatus cleaning step

After that the automatic on-line analysis system is off, it is possible to regenerate both modules of the micro-GC. The regeneration method is already present in the micro-GC methods list and it is easily changeable from the instrument software. This method increases the pressure and the temperature in the columns in order to clean them from the eventual presence of compounds traces that are still adsorbed on the stationary phase. At the end of the regeneration process it is possible to turn off the TCD filament (with a preponed method) an then to shut down the instrument.

The FT reactor has to be disconnected from the plan pipe lines and both upper and lower flanges have to be opened. The catalyst can be unloaded by breaking the catalytic bed with a conical ending pipe from the bottom of the rector. Catalyst can be recovered into a vial if post-test characterizations analyses are needed.

Hazard note: when the catalyst is unloaded, the metal is in an oxidation state equal to 0, which means that it could be pyrophoric when it comes in contact with air and moisture.

The FT reactor is then cleaned with water and acetone for several times. After this, a new FT test could be carried out.

4.6 FT data elaboration

With the analytical apparatus integrated in the FT plant, it is possible to measure:

- The temperature and pressure;

- The inlet flowrates of each gas (CO, H_2 and N_2) and the total outlet flowrate. Moreover, at the end of the experimental test, the measure of the total volume of gas that entered and left the FT plant is available;

- The composition of the light hydrocarbons fraction (made by micro-GC)

- The weight of the organic and aqueous phase collected in the cold trap at the end of the run;

- The composition of the heavy organic phase (GC) and the amount of C-content species dissolved in the water.

All the collected data have been elaborated with the use of Microsoft Excel software. After the experimental elaboration it is possible to calculate:

- The conversion of CO;

- The molar flowrates of all the light hydrocarbons and of each fraction of the heavy organic phase (range C_7-C_{30});

- The selectivity and the molar productivities of CH_4, CO_2, the light fraction and the heavy fraction;

- The composition of the light hydrocarbons dissolved in the liquid organic phase;

- The carbon and oxygen balances;

- The probability of chain growth given by the ASF algorithm.

4.6.1 Equations concerning the CO conversion, the mixture composition, the molar flowrates and productivities of the light fraction

$$Flow_{FT} = Flow_{Total} - Flow_{N2} \quad \text{(Eq. 4.13)}$$

$$CO_{conversion} = \frac{Flow\ CO_{IN} - Flow\ CO_{OUT}}{Flow\ CO_{IN}} \cdot 100 \quad \text{(Eq. 4.14)}$$

$$\%\ CO = \frac{Flow\ CO_{OUT}}{Flow_{FT}} \cdot 100 \quad \text{(Eq. 4.15)}$$

$$\%"i,n" = \frac{area_{"i"}}{calibraction\ factor_{"i"}} \cdot \frac{Flow_{Total}}{Flow_{FT}} \quad \text{(Eq. 4.16)}$$

Where:

- “i”: is a generic light product with n carbon atoms;

- %CO: is the molar fraction of CO;

- %"i,n": is the molar fraction of the i,n molecule;

- $Flow_{FT}$: is the out coming volumetric flowrate (Nml·min^{-1});

- $Area_{"i,n"}$: is the chromatographic area given by the micro-GC;

- Calibration factor: is the factor (one for each component) determined by the micro-GC calibration which correlates the area and the composition.

$$"i,n"_{molar\ flowrate} = \frac{Flow_{FT} \cdot 0.001 \cdot \%"i,n"}{22.414} \quad \text{(Eq. 4.17)}$$

$$C_{molar\ flowrate\ of\ "i,n"} = "i,n"_{molar\ flowrate} \cdot nc \quad \text{(Eq. 4.18)}$$

$$CO_{IN\ molar\ flowrate} = \frac{Flow\ CO_{IN}}{22.414} \cdot 0.001 \quad \text{(Eq. 4.19)}$$

$$CO_{OUT\ molar\ flowrate} = \frac{Flow\ CO_{OUT}}{22.414} \cdot 0.001 \quad \text{(Eq. 4.20)}$$

$$Total\ C_{OUT\ molar\ flowrate} = CO_{OUT\ molar\ flowrate} + \sum_{n=1}^{n=6} C_{molar\ flowrate\ of\ "i"} \quad \text{(Eq. 4.21)}$$

Where:

- $i,n_{molar\ flowrate}$: is the outlet molar flowrate of i,n component;

- $C_{molar\ flowrate\ of\ "i,n"}$: is the outlet molar flowrate referred to the moles of C in the i,n compound;

- $CO_{IN\ molar\ flowrate}$: is the inlet molar flowrate of CO;

- $CO_{OUT\ molar\ flowrate}$: is the outlet molar flowrate of CO;

- Total $C_{OUT\ molar\ flowrate}$: are all the moles of carbon that left the plant in gas phase;

- 0.001: is the conversion factor from Nml·min^{-1} to NL·min^{-1};

- 22.414: is the volume expressed in L which has a mole of gas in standard conditions;

- nc: is the number of carbon atom in the "i,n" molecule.

4.6.2 Equations concerning the heavy phase composition and productivity

The heavy fraction is assumed to be a series of -CH_2-, thus the total number of moles of the organic phase are calculated as reported in Eq. 4.22:

$$moles\ of(-CH_2-) = \frac{Weight_{>C7}}{14} \quad \text{(Eq. 4.22)}$$

Where:

- moles of (-CH_2-): is the total number of methylene units in the heavy phase;

- $Weight_{>C7}$: is the mass of the heavy organic phase collected in the cold trap;

- 14: is the molecular weight of the -CH_2- unit.

$$\%\text{"j,n"} = \frac{Area_{\text{"j,n"}} \cdot fc}{Area_{TOTAL}} \cdot 100 \quad \text{(Eq. 4.23)}$$

$$moles\ of\ \text{"j,n"} = \%\text{"j,n"} \cdot\ moles\ of(-CH_2-) \quad \text{(Eq. 4.24)}$$

$$\text{"}j,n\text{"}_{molar\ flowrate} = \frac{moles\ of\ \text{"j,n"}}{TOS} \quad \text{(Eq. 4.25)}$$

$$C_{molar\ flowrate\ of\ \text{"}j,n\text{"}} = \text{"j,n"}_{molar\ flowrate} \cdot nc \quad \text{(Eq. 4.26)}$$

Where:

- "j,n": is a generic heavy product with n carbon atoms;

- "j,n" molar flowrate: is the molar flowrate of the j,n compound;

- $C_{\text{molar flowrate of "j,n"}}$: is the outlet molar flowrate referred to the moles of C in the j,n compound;

- nc: is the number of carbon atoms in the j molecule;

- $Area_{\text{"j,n"}}$: is the chromatographic area given by the GC;

- $Area_{TOTAL}$: is the sum of all the chromatographic areas given by the GC in the range C_7-C_{30};

- fc: is the calibration factor determined by the GC calibration;

- TOS: is the time on stream measured at the end of the run expressed in hours.

4.6.3 Equations concerning the selectivity and the C_{2+} yield

$$S_{\text{"}CO2\text{"}} = \frac{CO_2\ molar\ flowrate}{CO_{IN\ molar\ flowrate} - CO_{OUT\ molar\ flowrate}} \cdot 100 \quad \text{(Eq. 4.27)}$$

$$S_{\text{"}CH4\text{"}} = \frac{CH_4\ molar\ flowrate}{CO_{IN\ molar\ flowrate} - CO_{OUT\ molar\ flowrate}} \cdot 100 \quad \text{(Eq. 4.28)}$$

$$S_{\text{"}i,n\text{"}} = \frac{C_{molar\ flowrate\ of\ \text{"}i,n\text{"}}}{CO_{IN\ molar\ flowrate} - CO_{OUT\ molar\ flowrate}} \cdot 100 \quad \text{(Eq. 4.29)}$$

$$S_{<C7} = \sum_{n=1}^{n=6} S_{\text{"}i,n\text{"}} \quad \text{(Eq. 4.30)}$$

Where:

- S_{CO2}: is the selectivity to CO_2;

- S_{CH4}: is the selectivity to CH_4;

- $S_{"i,n"}$: is the selectivity to the generic light "i,n" product;

- $S_{<C7}$: is the selectivity to the light products phase.

$$S_{"j,n"} = \frac{C_{molar\ flowrate\ of\ "j,n"}}{CO_{IN\ molar\ flowrate} - CO_{OUT\ molar\ flowrate}} \cdot 100 \quad \text{(Eq. 4.31)}$$

$$S_{>C7} = \sum_{n=7}^{n=30} S_{"j,n"} \quad \text{(Eq. 4.32)}$$

Where:

- $S_{"j,n"}$: is the selectivity to the generic heavy "j,n" product;

- $S_{>C7}$: is the selectivity to the heavy products phase.

However, the selectivity toward the heavy phase can be calculated even as reported in Eq. 4.33:

$$S_{>C7} = 100 - S_{"CO2"} - S_{"CH4"} - S_{<C7} \quad \text{(Eq. 4.33)}$$

The C_{2+}yield is given by Eq. 4.34:

$$C_{2+}yield: CO_{Conversion} \cdot \frac{(>C7_{Selectivity} + <C7_{Selectivity})}{100} \quad \text{(Eq. 4.34)}$$

4.6.4 Equations concerning the carbon and oxygen molar balances

$$\%C = \left(\frac{mol,C_{IN} - mol,C_{OUT\ (CO,\ CO2,\ CH4)} - mol,C_{OUT\ (<C7)} - mol,C_{OUT\ (>C7)} - mol,C_{OUT\ (H2O)}}{mol,C_{IN}} \cdot 100\right) \quad \text{(Eq. 4.35)}$$

$$\%O = \left(\frac{mol,O_{IN} - mol,O_{OUT\ (CO,\ CO2,\ H2O)}}{mol,O_{IN}} \cdot 100\right) \quad \text{(Eq. 4.36)}$$

Where:

- mol, C_{IN}: total number of C moles IN;

- mol, $C_{OUT(CO, CO2, CH4)}$: total number of C moles OUT from unreacted CO, produced CO_2 and CH_4;

- mol, $C_{OUT(<C7)}$: total number of C moles OUT from light products (<C7);

- mol, $C_{OUT(>C7)}$: total number of C moles OUT from heavy products (>C7);

- mol, $C_{OUT(H2O)}$: total number of C moles OUT from carbonaceous species dissolved in H_2O;

- mol, O_{IN}: total number of O moles IN;

- mol, $C_{OUT(CO,\ CO2,\ H2O)}$: total number of O moles OUT from unreacted CO, produced CO_2 and water;

4.6.5 Equations concerning the calculation of α and ASF algorithm

As already explained in paragraph 2.2.4 the probability of chain growth can be estimated with the use of the ASF algorithm by a least-squares linear regression of Eq. 4.37:

$$\ln\left(\frac{\mathrm{Wn,j}}{nc}\right) = ln(1-\alpha)^2 + (nc-1)\ln(\alpha) \qquad \text{(Eq. 4.37)}$$

Where:

- Wn,j/nc: is the weight fraction of j-product with n carbon atom number.

- α: is the probability of chain growth

- nc: is the number of carbon atoms in the j molecule.

From the experimental data Wn/n is calculable with the following Eqs. 4.38- 4.42:

$$moles\ of\ C\ in\ \mathrm{j,n} = C_{molar\ flowrate\ of\ "j,n"} \cdot TOS \qquad \text{(Eq. 4.38)}$$

$$weight\ of\ C\ in\ \mathrm{j,n} = moles\ of\ C\ in\ \mathrm{j,n} \cdot 14 \qquad \text{(Eq. 4.39)}$$

$$total\ weight\ of\ C\ = \sum_{n=7}^{n=30} weight\ of\ C\ in\ \mathrm{j}\ ,n \qquad \text{(Eq. 4.40)}$$

$$Wn,j = \frac{weight\ of\ C\ in\ \mathrm{j,n}}{total\ weight\ of\ C} \qquad \text{(Eq. 4.41)}$$

$$\frac{Wn,j}{n} = \frac{Wn,j}{n\ of\ C\ atoms\ in\ j} \qquad \text{(Eq. 4.42)}$$

Where:

- moles of C in j,n: is the total number of moles of -CH_2- in the j,n compound;

- weight of C in j,n: is the weight of the -CH_2- units in the j,n molecule;

- total weight of C: is the total weight of the -CH_2- units in the heavy phase;

- $W_{n,j}$: is the weight fraction referred to the j,n compound;

The probability of chain growth is calculated by making a diagram where -log(Wn,j/n) is reported versus the number of C atoms in the molecules. An example of this graph is reported in Figure 4.18.

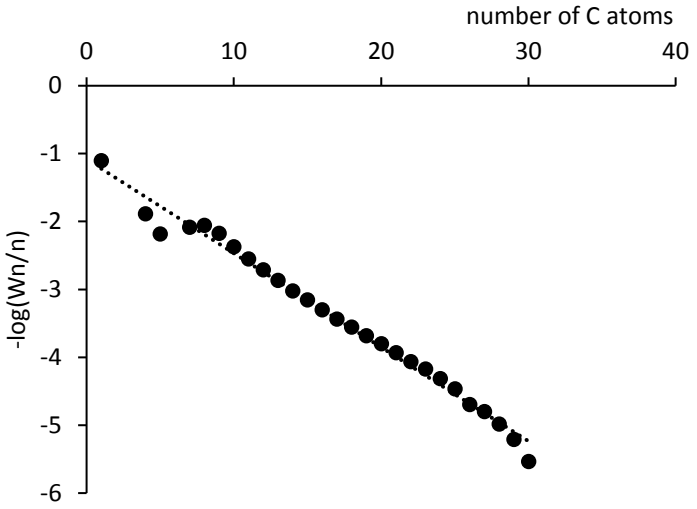

Figure 4.18: Experimental ASF diagram obtained with a 10 %wt Co-based catalyst tested at T= 245 °C.

4.6.6 Equations concerning the calculation of the light products dissolved in the heavy organic phase

The average weight of heavy organic phase collected at the end of the experimental runs is around ≈ 5- 7 g thus, the amount of the light hydrocarbons dissolved in the heavy phase are few Nml. For this reason it is hard to directly measure the exact volume of the light products that are desorbed from the organic liquid.

A possible calculation that can give a first idea of which light hydrocarbons are dissolved and their affinity with the heavy organic phase is to calculate the ratio between the corrected molar fraction of the "i,n" compound calculated by the micro-GC analysis when the desorbed fraction is analyzed and the one calculated when a normal analysis of the light hydrocarbons which left the reactor is carried out. The ratios are calculated as follows in Eqs. 4.43- 4.45:

$$Corrected\ area_{"i,n"} = \frac{Area_{"i,n"}}{calibraction\ factor_{"i,n"}} \quad \text{(Eq. 4.43)}$$

$$\%"i,n"_{DESORBED} = \frac{Area_{"i,n"}}{Area_{TOTAL}} \quad \text{(Eq. 4.44)}$$

$$Ratio"i,n" = \frac{\%"i,n"_{DESORBED}}{\%"i,n"_{LIGHT}} \quad \text{(Eq. 4.45)}$$

Where:

- Corrected area$_{"i,n"}$: is the area given by the micro-GC of the i,n light product with n carbon atoms divided by its calibration factor;

- %"i,n"$_{DESORBED}$: is the molar fraction of the i,n component calculated by dividing its corrected area with the sum of all the corrected areas;

- Ratio"i,n": is the ratio of the mola fraction of the i,n$_{DESORBED}$ component divided by the molar fraction of the i,n$_{LIGHT}$ compound (same molecule) given by a normal analysis of the light phase performed during the same experimental run, in the same conditions.

5 Catalysts synthesis

The samples have been synthesized using different preparation methods and reactants. All the catalysts are supported on SiO_2, in particular the type of silica used to support the impregnated sample and the samples synthesized with the use of US has different characteristics; at the same time tetraethyl orthosilicate has been used as a support precursor in the preparation of FSP synthesized catalysts. The list of all the reactants used for the samples preparation will be reported in the following paragraph.

All the catalysts synthesized, characterized and tested during this PhD research work contain different amounts of active metal (Fe and Co) and eventually promoters (Ru, K, and Cu). The complete summary of the samples is reported hereinafter in Table 5.1; each number indicates the %wt of active metal and/or promoters present in the catalysts.

Synthesis technique	Catalyst	%wt of active metal and promoters				
		Co	Ru	Fe	K	Cu
Impregnation	$Fe_{30}K_2Cu_{3.75}$	//	//	30	2	3.75
FSP	5Co	5	//	//	//	//
	10Co	10	//	//	//	//
	10Co-0.4Ru	10	0.4	//	//	//
US	$Fe_{10}US$	//	//	10	//	//
	$Fe_{30}US$	//	//	30	//	//
	$Fe_{30}K_2Cu_{3.75}US$	//	//	30	2	3.75

Table 5.1: Catalysts tested during this PhD research work.

5.1 Synthesis of $Fe_{30}K_2Cu_{3.75}$

The sample $Fe_{30}K_2Cu_{3.75}$ has been synthesized according to the traditional wetness impregnation method [69]. The impregnation procedure starts with the preparation of an aqueous solution of the active metal and promoters precursors. The summary and the main characteristics of the support and all the precursors are reported in Table 5.2.

	Reagent	Features
Support	SiO_2	Company: Fluka Molecular weight: 60,086 $g \cdot mol^{-1}$ Purity: > 99 % Superficial area: 305 $m^2 \cdot g^{-1}$
Precursors	$Fe(NO_3)_3 \cdot 9H_2O$	Company: Riedel de Hean Molecular weight: 403,85 $g \cdot mol^{-1}$ Purity: 98 %
	KNO_3	Company: Merk Molecular weight: 101,11 $g \cdot mol^{-1}$ Purity: > 99 %
	$Cu(CH_3COO)_2 \cdot H_2O$	Company: Fluka Molecular weight: 199,65 $g \cdot mol^{-1}$ Purity: 99 %

Table 5.2: Features of precursors and support used for the synthesis of $Fe_{30}K_2Cu_{3.75}$.

The chosen amount of active metal (Fe, 30 %wt) and promoters (K, 2 %wt and Cu, 3.75 %wt) have been decided on the basis of the results of a previous work carried out by Pirola [84] where different Fe-based supported catalysts with different amounts of Fe (10 %wt, 30 %wt and 50 %wt), K (2 %wt, 5.65 %wt) and Cu (3.75 %wt) have been synthesized. The author characterized and tested all the samples using different experimental conditions such as activation temperature, reaction temperatures, reactor pressure and different syngas compositions.

Pirola indicated that $Fe_{30}K_2Cu_{3.75}$ was the most promising sample in terms of catalytic activity, stability and selectivity. In particular, thanks to the effects of the promoters, K enhance the electron transfer to the iron and inhibits hydrogen adsorption with the result to increase the electron density and the CO adsorption while decreasing the selectivity to methane. At the same time Cu promotes the reduction from Fe_2O_3 (hematite) to Fe_3O_4 (magnetite) and then from the latter to metallic iron or iron carbides; a probable mechanism for the copper promotion is the migration of atomic hydrogen from reduced Cu to the iron oxides. Even though the promoters have a benefic effect to the catalytic properties an excess of K could increase the selectivity toward CO_2 and an excess of Cu is dangerous because this element is not directly active to the Fischer-Tropsch reaction.

5.1.1 Experimental preparation procedure

The detailed preparation procedure steps adopted for the synthesis of $Fe_{30}K_2Cu_{3.75}$ are reported hereinafter:

- Drying step of SiO_2 support into the oven at T= 120 °C overnight;

- Weigh of the exact amount of $Fe(NO_3)_3 \cdot 9H_2O$, KNO_3 and $Cu(CH_3COO)_2 \cdot H_2O$;

- Dissolution of all the precursors into a 250 ml flask by adding 25 ml of ultra-pure H_2O;

- Add the correct amount of dry SiO_2 (1 g per 5 ml of water used);

- Connect the flask to a rotary evaporator at 36 rpm, T= 40 °C, and atmospheric pressure for 24 hours;

- After the impregnation step, evaporation of the solvent at T= 80 °C under vacuum;

- Drying step of the catalyst powder into the oven at T= 120 °C for 4 hours;

- Calcination step at T= 500 °C in air for 4 hours;

Once the calcination step is done; the catalyst is ready to be sieved and then used in the FT plant.

Figure 5.1: Rotary evaporator used for the synthesis of $Fe_{30}K_2Cu_{3.75}$.

5.1.2 Calculation of the amount of active metal and promoters precursors

The right amounts of iron and promoters are calculated using the following Eq. 5.1-5.3:

$$\%wt_{Fe} = \frac{g_{Fe}}{g_{Fe}+g_K+g_{Cu}+g_{SiO2}} \qquad \text{(Eq. 5.1)}$$

$$\%wt_K = \frac{g_K}{g_{Fe}+g_K+g_{Cu}+g_{SiO2}} \quad \text{(Eq. 5.2)}$$

$$\%wt_{Cu} = \frac{g_{Cu}}{g_{Fe}+g_K+g_{Cu}+g_{SiO2}} \quad \text{(Eq. 5.3)}$$

Where:

- $\%wt_{Fe,\ K,\ Cu}$: are the desired weight percentage of iron, potassium and copper in the catalyst;

- $g_{Fe,\ K,\ Cu,\ SiO2}$: are the calculated weight of iron, potassium and copper in the catalyst.

In the equation reported above, the %wt of active metal and promoters are fixed numbers, 30 %wt for Fe, 2 %wt for K and 3.75 %wt of Cu, while g_{SiO2} is assumed to be equal to 5.

By setting a system with these three equations the right amounts of iron and promoters are easily calculable:

g_{Fe}= 2.335 g

g_K= 0.156 g

g_{Cu}= 0.292 g

Once that the exact amount of the three components is calculated, it is possible to calculate the number of moles of Fe, K and Cu.

$$moles_{Fe} = \frac{g_{Fe}}{PM_{Fe}} \quad \text{(Eq. 5.4)}$$

$$moles_K = \frac{g_K}{PM_K} \quad \text{(Eq. 5.5)}$$

$$moles_{Cu} = \frac{g_{Cu}}{PM_{Cu}} \quad \text{(Eq. 5.6)}$$

Where:

- $moles_{Fe,\ K,\ Cu}$: are the moles of active metal and promoters;

- $PM_{Fe,\ K,\ Cu}$: are the atomic weight of Fe (55.847 g·mol^{-1}), K (39.0983 g·mol^{-1}) and Cu (63.546 g·mol^{-1}).

The calculated moles for each component are:

$moles_{Fe}$= 0,0418 mol

$moles_K$= 0,00398 mol

$moles_{Cu}$= 0,0046 mol

Since the precursors molecules contain one atom of Fe, K and Cu respectively, it is possible to say that:

$$moles_{Fe} = moles_{Fe(NO3)3\cdot 9H2O} \quad \text{(Eq. 5.7)}$$

$$moles_{K} = moles_{KNO3} \quad \text{(Eq. 5.8)}$$

$$moles_{Cu} = moles_{Cu(CH3COO)2\cdot H2O} \quad \text{(Eq. 5.9)}$$

In this way, using the molecular weight of the molecules it is possible to calculate the correct weight of each precursors using the following Eq. 5.10- 5.12:

$$g_{Fe(NO3)3\cdot 9H2O} = moles_{Fe(NO3)3\cdot 9H2O} \cdot PM_{Fe(NO3)3\cdot 9H2O} \quad \text{(Eq. 5.10)}$$

$$g_{KNO3} = moles_{KNO3} \cdot PM_{KNO3} \quad \text{(Eq. 5.11)}$$

$$g_{Cu(CH3COO)2\cdot H2O} = moles_{Cu(CH3COO)2\cdot H2O} \cdot PM_{Cu(CH3COO)2\cdot H2O} \quad \text{(Eq. 5.12)}$$

The molecular weight of the promoters are:

$PM_{Fe(NO3)3\cdot 9H2O}$= 403,85 g·mol^{-1}

PM_{KNO3}= 101,11 g·mol^{-1}

$PM_{Cu(CH3COO)2\cdot H2O}$= 199,65 g·mol^{-1}

Using Eq. 5.10- 5.12 the calculated masses of promoters are:

$g_{Fe(NO3)3\cdot 9H2O}$= 16,882 g

g_{KNO3}= 0,4024 g

$g_{Cu(CH3COO)2\cdot H2O}$= 0,9168 g

5.2 Synthesis of 5Co, 10Co and 10Co-0.4Ru

The FSP technique allows to synthesize monometallic or bimetallic metal oxides which are characterized by an high surface area and great thermal stability. Usually, the precursors of the active metal and the support are in form of acetate or acetylacetonate and they are dissolved into an organic solvent. The organic solution chosen for the synthesis of 5Co, 10Co and 10Co-0.4Ru is a 1/1 mixture of propionic acid and p-xylene.

The final amount of active metal on the catalysts is easily changed by modifying the concentration of the Co precursor in the organic solution. The Ru-promoted catalyst was synthesized by adding an impregnation step after the FSP synthesis of 10Co using $Ru_3(CO)_{12}$ as a precursor.

The summary and the main characteristics of the support and active metal precursors are reported in Table 5.2.

	Reagents	Features
Support precursor	$Si(OC_2H_5)_4$	Company: Fluka Molecular weight: 208,33 g·mol^{-1} Purity: 99%
Active metal precursor	$Co(CH_3COO)_2{\cdot}4H_2O$	Company: Fluka Molecular weight: 249,09 g·mol^{-1} Purity: 99%
Promoter precursor	$Ru_3(CO)_{12}$	Company: Sigma Aldrich Molecular weight: 639.33 g·mol^{-1} Purity: 99%
Solvent	Decane	Company: Sigma Aldrich Molecular weight: 142.28 g·mol^{-1} Purity: > 99%
Solvent mixture	CH_3CH_2COOH	Company: Fluka Molecular weight: 74,08 g·mol^{-1} Purity: 99%
	C_8H_{10}	Company: Sigma Aldrich Molecular weight: 106,16 g·mol^{-1} Purity: 99%

Table 5.3: Features of the precursors of the support and active metals used for the synthesis of 5Co, 10Co and 10Co-0.4Ru.

5.2.1 Apparatus for FSP synthesis

The general scheme of the apparatus used for the flame spray pyrolysis synthesis is mainly showed in Figure 5.2:

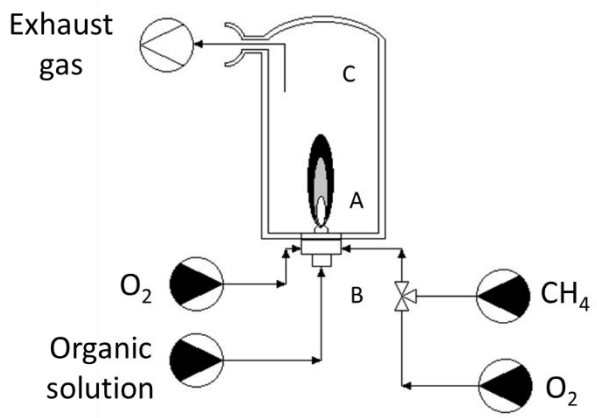

Figure 5.2: FSP apparatus.

It is mainly composed by three different parts:

- (A) The burner/flame: this part is the one in which the pyrolysis is achieved;

- (B) The injection system: is the system in which the organic solution is mixed with oxygen and then fed to the burner. In the injection system two different pipes are present too, in order to feed a CH_4/O_2 gaseous mixture used as combustible;

- (C): The powder collect system: this part is composed by a Pyrex glass column in which the fine powders synthesized are collected.

The organic solution is pumped with a syringe pump into the injection system and then mixed with O_2 which nebulizes the solution into very fine drops and acts as oxidizing agent. The organic/O_2 mixture passes through the burned and it is ignited by twelve external conical CH_4/O_2 flames. In the flame the instantaneous vaporization, dispersion and pyrolysis of the organic solution is achieved; in this way the first oxides nucleus are formed. These nucleus become bigger by coalescence and condensation among them by forming the desired powder.

There are several parameters that can influence the final characteristic of the material, for this reason it is important to optimize these parameters in order to synthesize a material with features that are as much uniform as possible. The parameters that can be modified are [72]:

- *The flowrate of the organic solution:*

The system productivity is highly influenced by the flowrate of the precursors solution. Usually quite high flowrates are preferred but it is important to keep the flowrate as much stable as possible and not too high because a great flowrate means to synthesize a great number of powder particles which can lead in an increase of sintering phenomena with a decrease in the surface area of the final product.

- *The type of the solvent mixture:*

The solvent mixture must be chosen in function of the type of precursors used. The organic solvents must dissolve the metallic and support precursors and it has to guarantee a good combustion enthalpy. Another crucial parameter that has to be taken into account is the vapor pressure of the solvent; an high vapor pressure (low boiling point) could result in sintering phenomena since a lot of powder particles are formed quickly.

- *The concentration of the precursors solution:*

High precursors concentration in the organic solution leads to a greater powder productivity which can cause sintering problems.

- *Burner combustion mixture:*

The components of the gaseous mixture used to ignites the organic solution are very important since they determine the flames temperature. Usually, an O_2/CH_4 mixture is preferred to an air/CH_4 one.

- *O_2 pressure before the nozzle:*

The O_2 relative pressure before the nozzle influences the residence time of the particles in the flames. In general, an high pressure leads to short residence times, thus the formation of small particles with an high surface area and less thermal stability is favored and vice versa. However, it is important to keep an optimized pressure value which allows enough residence time in order to decompose the precursors organic molecules.

5.2.2 Experimental preparation procedure

5.2.2.1 Preparation of the organic solution

The synthesis of the Co-based catalysts starts with the preparation of the organic solution. The methodology is composed by different steps, here described:

- Weigh the correct amount of metal and support precursors in order to reach the right loading of metal on the catalyst at the end of the procedure;

- Solubilize the metallic precursor ($Co(CH_3COO)_2{\cdot}4H_2O$) into 100 ml of propionic acid. It is advisable to keep the solution stirred in order to facilitate the dissolution;

- Insert into a 100 ml flask the calculated amount of tetraethyl orthosilicate ($Si(OC_2H_5)_4$) and fill the remaining part of the flask with p-xylene. Water and moisture must be avoided since this molecule is sensible to the presence of water and it begins decomposed with the reaction:

$$Si(OC_2H_5)_4 + 2\ H_2O \rightarrow SiO_2 + 4\ C_2H_5OH \qquad \text{(Eq. 5.13)}$$

- Mix the two solutions together;

At this point it is possible to continue the synthesis with the FSP step.

5.2.2.2 FSP step

The detailed preparation procedure steps adopted for the synthesis of 5Co, 10Co and 10Co-0.4Ru are reported hereinafter:

- Dry all the equipment used for the FSP synthesis into the oven at T= 120 °C overnight;

- Set up the FSP apparatus, open the CH_4 and O_2 cylinders and tur on the flames;

- Position the Pyrex manifold;

- Set up the pressure of the central oxygen line by using two manometers;

- Open and set up the air flowrate; the air will flow from the bottom to the top of the manifold and will carry all the solid particles to the top edge of the manifold;

- Withdraw the organic solution with a syringe, and place it into the pump system;

- Turn on the syringe pump till all the solution will flow through the burner;

- Repeat the last two step till the desired amount of catalyst is synthesized;

- Once the solution is finished, close the CH_4, air and O_2 lines and wait till the pyrex manifold cools down to room temperature.

- Collect all the powder and sieve the catalyst in the granulometry for the FT reactor.

The optimized parameters were:

- *Gases flowrates*: CH_4: 0.5 $NL \cdot min^{-1}$, O_2: 1 $NL \cdot min^{-1}$;

- *O_2 central flow:* 5,00 $NL \cdot min^{-1}$;

- *Syringe volume*: 50 ml;

- *Organic solution flowrate*: 5,5 $NmL \cdot min^{-1}$;

- *O_2 relative pressure before the nozzle*: 0,5- 0,8 bar.

Figure 5.3: Pyrex manifold during the FSP synthesis.

5.2.2.3 Synthesis of the Ru-promoted catalyst (10Co-0.4Ru)

The synthesis steps reported above allow the production of 5Co and/or 10Co. However the synthesis of the Ru-promoted samples involves a wetness impregnation step which follows the FSP one. This impregnation step is completely identical to the one used for the synthesis of $Fe_{30}K_2Cu_{3.75}$ reported in paragraph 5.1.1 except for some experimental conditions and reactants. The detailed procedure adopted for the synthesis of 10Co-0.4Ru is reported hereinafter:

- Drying step of 10Co catalyst into the oven at T= 120 °C overnight;

- Weigh of the exact amount of $Ru_3(CO)_{12}$;

- Dissolution of the precursor into a 250 ml flask by adding 100 ml of n-decane;

- Connect the flask to a rotary evaporator at 36 rpm, T= 40 °C, and atmospheric pressure for 24 hours;

- After the impregnation step, evaporation of the solvent at T= 80 °C under vacuum;

- Drying step of the catalyst powder into the oven at T= 120 °C for 48 hours;

- Calcination step at T= 200 °C in air for 4 hours, the calcination temperature must be not too high due to the great volatility of Ru carbonyl;

Once the calcination step is done; the catalyst is ready to be sieved and then used in the FT plant.

5.2.3 Calculation of the amount of active metal, support and promoter precursors

The equation used to calculate the amount of cobalt in the catalyst is the same of the one used for $Fe_{30}K_2Cu_{3.75}$:

$$\%wt_{Co} = \frac{g_{Co}}{g_{Co}+g_{SiO2}} \qquad \text{(Eq. 5.14)}$$

Where:

- $\%wt_{Co}$: is the desired weight percentage of Co in the catalyst;

- $g_{Co,\ SiO2}$: are the calculated weight of cobalt and silica in the catalyst.

Since in this equation there is only an unknown term (g_{Co}), it is easy to calculate the weight of the active metal just by fixing the total amount of catalyst desired.

If 5 g of catalyst have to be synthesized, the global efficiency of the process (60 %) must be taken into account:

$$g_{Catalyst} = \frac{Theoretical\ g_{Catalyst}}{process\ efficiency} = \frac{5\ g}{0.6} = 8.33\ g \quad \text{(Eq. 5.15)}$$

Where:

- $g_{Catalyst}$: is the total mass of catalyst;

- Theoretical $g_{Catalyst}$: is the theoretical amount of catalyst that has to be synthesized;

- process efficiency: is the typical efficiency of a FSP process.

This mass includes the weight of Co and SiO_2, if a catalysts with 10 %wt of Co have to be synthesized:

$$g_{Co} = g_{Catalyst} \cdot \%wt_{Co} = 8.33 \cdot 10\ \% = 0.833\ g \quad \text{(Eq. 5.16)}$$

Due to the stoichiometry:

$$moles_{Co} = moles_{Co(CH3COO)2\cdot4H2O} \quad \text{(Eq. 5.17)}$$

Once the moles of Co are calculated, it is possible to directly calculate the amount of the Co-precursor.

$$moles_{Co} = \frac{g_{Co}}{PM_{Co}} = \frac{0.833\ g}{58{,}93 g\cdot mol^{-1}} = 0.01413\ mol \quad \text{(Eq. 5.18)}$$

$$g_{Co(CH3COO)2\cdot4H2O} = moles_{Co(CH3COO)2\cdot2H2O} \cdot PM_{Co(CH3COO)2\cdot4H2O} \quad \text{(Eq. 5.19)}$$

Where:

- g_{Co}: is the mass of Co in the catalyst;

- $moles_{Co,\ Co(CH3COO)2\cdot4H2O}$: are the effective moles of Co and/or cobalt precursor in the catalyst.

- $g_{Co(CH3COO)2\cdot4H2O}$: is the mass of the precursor that has to be weigh in order to prepare the solution;

- $PM_{Co(CH3COO)2\cdot4H2O}$: is the atomic weight of the Co precursor, which is equal to 249.09 $g\cdot mol^{-1}$.

Using the above Eq. 5.19 the calculated amount of Co precursor is:

$g_{Co(CH3COO)2\cdot4H2O}$= 3.555 g

After that the amount of Co is determined, it is possible to determine the total amount of SiO_2:

$$g_{SiO2} = g_{Catalyst} - g_{Co} = 8.33 - 0.833 = 7.497\ g \quad \text{(Eq. 5.20)}$$

Where:

- g_{SiO2}: is the amount of SiO_2 in the catalyst.

Due to the stoichiometry:

$$moles_{SiO2} = moles_{Si(OC2H5)4} \quad \text{(Eq. 5.21)}$$

Once the moles of SiO_2 are calculated, it is possible to directly calculate the amount of the SiO_2-precursor.

$$moles_{SiO2} = \frac{g_{SiO2}}{PM_{SiO2}} = \frac{7.497\ g}{60.08\ g \cdot mol^{-1}} = 0.1247\ mol \quad \text{(Eq. 5.22)}$$

$$g_{Si(OC2H5)4} = moles_{Si(OC2H5)4} \cdot PM_{Si(OC2H5)4} \quad \text{(Eq. 5.23)}$$

Where:

- g_{SiO2}: is the mass of SiO_2 in the catalyst;

- $moles_{SiO2,\ Si(OC2H5)4}$: are the effective moles of SiO_2 and/or silica precursor in the catalyst.

- $g_{Si(OC2H5)4}$: is the mass of the silica precursor that has to be weigh in order to prepare the solution;

- $PM_{Si(OC2H5)4}$: is the atomic weight of the SiO_2 precursor, which is equal to 208.33 $g \cdot mol^{-1}$.

Using the above Eq. 5.23 the calculated amount of $Si(OC_2H_5)_4$ is:

$g_{Si(OC2H5)4}$= 25.98 g

Considering that $Si(OC_2H_5)_4$ is a liquid reactant, it is more convenient to calculate the volume instead of the mass, the volume of tetraethyl orthosilicate is given by:

$$volume_{Si(OC2H5)4} = \frac{g_{Si(OC2H5)4}}{density} = \frac{25{,}98\ g}{0{,}94\ g \cdot ml^{-1}} = 27.63\ ml \quad \text{(Eq. 5.24)}$$

5.3 Synthesis of $Fe_{10}US$, $Fe_{30}US$ and $Fe_{30}K_2Cu_{3.75}US$

The use of ultrasound finds its applications in a wide range of research and industrial processes. The main applications of US are the preparation of devices with special features, medicine, extraction and food processes and finally chemistry and catalysis.

US can be applied in both homogeneous and phase transfer catalysis and for the production of nanostructured heterogeneous catalysts that can be used in several industrial chemical reactions such as hydrogenation, hydrosilation, ammonia synthesis and then the FT process [80,85].

The power of ultrasound arises from cavitation. This process involves three steps, the nucleation of a gas bubble, the bubble growth and then, when the bubble reach a critical size, the implosive collapse occurs.

During the collapse process very high temperatures (T≈ 5000 K), pressures (P≈ 150 MPa) and cooling rates (10^9 K·s^{-1}) are locally reached [86].

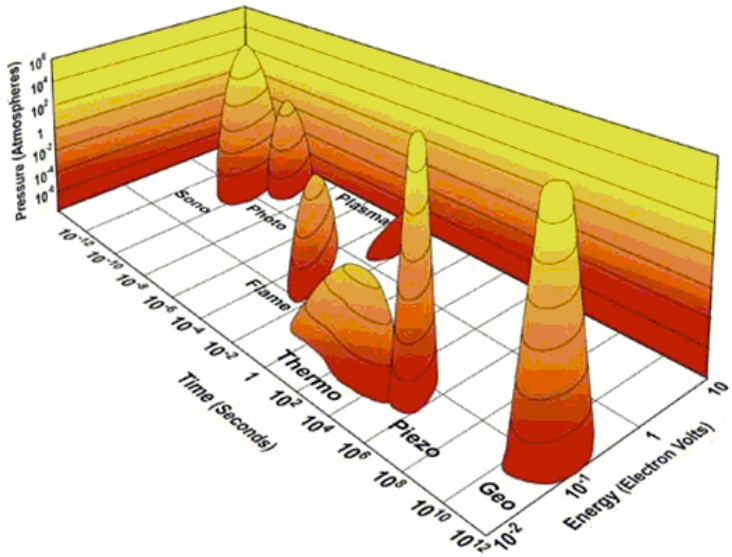

Figure 5.4: Lifetimes, pressures an energies of different types of waves.

Heterogeneous materials can be synthesized by ultrasonic synthesis of a volatile precursor, usually a carbonyl. The ultrasound decomposes the precursor into bulk metal and then, if an inorganic support is present, a nanophase supported material is synthesized.

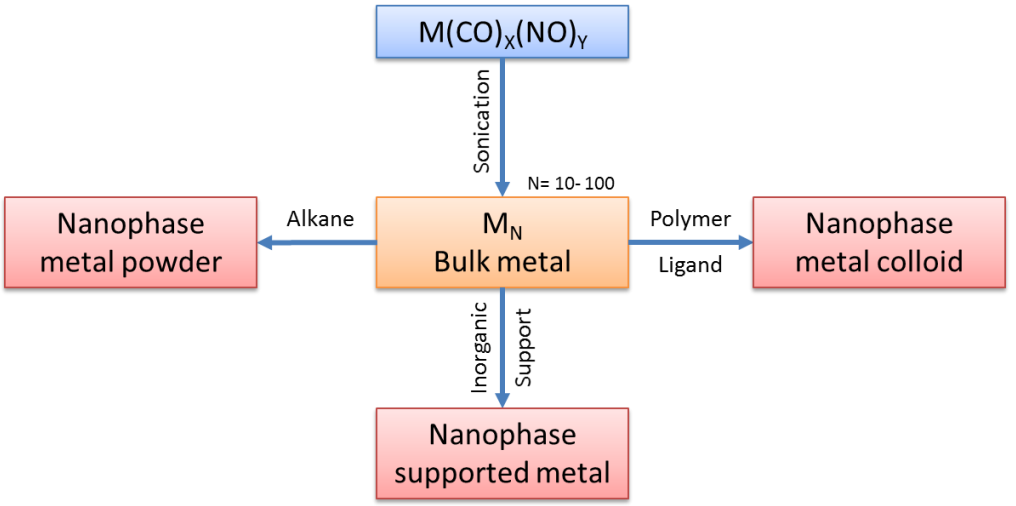

Figure 5.5: Ultrasonic synthetic approaches.

Three different iron based catalysts have been synthesized exploiting the effects of US, in particular $Fe_{10}US$ and $Fe_{30}US$ have been synthesized by ultrasonic decomposition of $Fe(CO)_5$ in presence of SiO_2 as a support into a glass made ultrasonic reactor filled with n-decane.

Moreover a K-Cu-promoted catalysts has been synthesized. The synthesis of the promoted catalysts starts with the impregnation of an aqueous solution of KNO_3 and $Cu(CH_3COO)_2{\cdot}H_2O$. This impregnation step is completely similar to the one adopted for the synthesis of $Fe_{30}K_2Cu_{3.75}$ reported in the previous paragraphs.

Once K and Cu are impregnated on the surface of the bare SiO_2, the active metal is added by the US decomposition of iron pentacarbonyl.

	Reagent	Features
Support	SiO_2	Company: Sigma Aldrich Molecular weight: 60,086 g·mol^{-1} Purity: > 99 % Superficial area: 515 m^2·g^{-1}
Precursors	$Fe(CO)_5$	Company: Sigma Aldrich Molecular weight: 195.9 g·mol^{-1} Purity: > 99.99 %
	KNO_3	Company: Merk Molecular weight: 101,11 g·mol^{-1} Purity: > 99 %
	$Cu(CH_3COO)_2{\cdot}H_2O$	Company: Fluka Molecular weight: 199,65 g·mol^{-1} Purity: 99 %
Solvent	Decane	Company**:** Sigma Aldrich Molecular weight: 142.28 g·mol^{-1} Purity: > 99%
	Pentane	Company**:** Sigma Aldrich Molecular weight: 72.5 g·mol^{-1} Purity: 98 %

Table 5.4: Features of the support and precursors used for the synthesis of $Fe_{10}US$, $Fe_{30}US$ and $Fe_{30}K_2Cu_{3.75}US$.

5.3.1 Apparatus for the ultrasonic synthesis

The US synthesis has been carried out using a VCX 500 (500 watts) & VCX 750 (750 watts) ultrasonic transductor horn equipped with titanium tip.

The sonochemical reaction has been conducted into a glass reactor with rounded bottom. During the US synthesis the distance from the tip and the bottom of the rector was around 10 mm. The reactor was equipped with three different in/out pipes which allowed the insertion of the solvent and reactant and the measurements of the temperature (TC) during the whole reaction cycle. Moreover the pipes allowed the insertion of an insert gas (argon). The US transductor and the sonochemical reactor are showed in Figure 5.6.

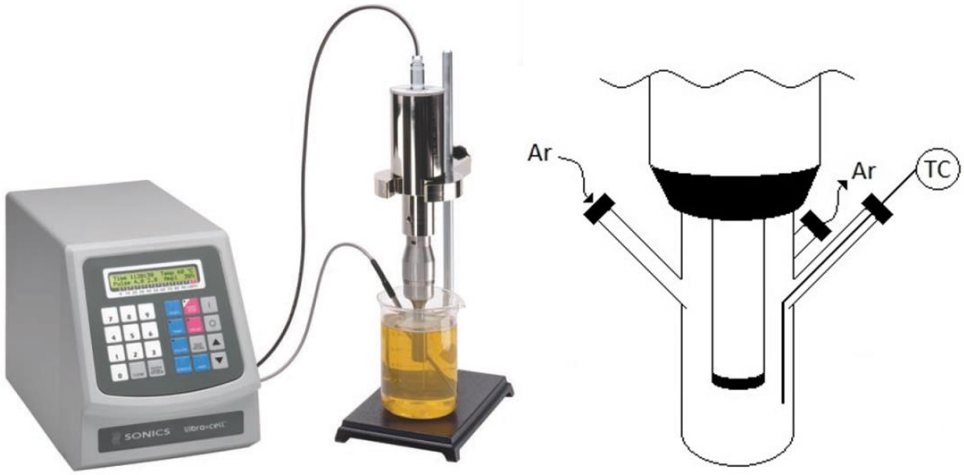

Figure 5.6: US transductor (left) and sonochemical reactor (right).

It is very important to evade the contact among the oxygen present in the air and the metal Fe^0 nanoparticles since they could be pyrophoric. Once atmospheric air was eliminated from the reactor the US step was carried out. At the end of the ultrasonic step the catalyst was oxidized by flowing air over the n-decane solution. **Hazard note: very fine powders of metallic iron are pyrophoric and can be a safety hazard when exposed to air.**

The ultrasonic process is affected by several variables, the most important are:

- *The frequency of the sound field*:

Cavitation phenomena can be observed in a range of frequency which varies from tens of Hz to few MHz. the frequency of the field directly influences the size of the cavitation effect. Usually, at very high frequencies (> 5 MHz) cavitation is not observed.

- *The acoustic intensity*:

This parameters has a strong effect on the cavitation phenomena, usually an increase in the amplitude results into an increase in the volume of the liquid which will

cavitate, thus it means a bigger reaction volume and greater reaction rates. On the other hand, high acoustic intensities can increase the temperature of the liquid bulk.

- *The bulk solution temperature*:

The temperature of the liquid where the sonochemical reaction occurs has a primary influence on the reaction rate. Usually sonochemical reaction are faster when the bulk temperature is low. The reason is findable in the vapor generated by the solvent: if the temperature is high, the solvent will evaporate into the bubble created by the acoustic field with the result to decrease the cavitation efficiency.

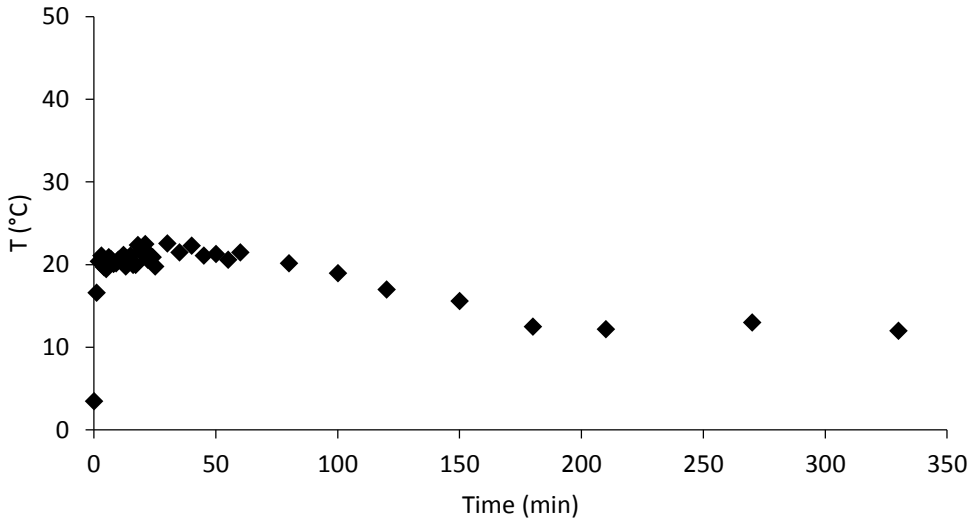

Figure 5.7: Temperature profile during the sonochemical synthesis of Fe_{30}US.

- *The type of the gas:*

Even this factor has a huge effect on the ultrasonic process efficiency. In general, it is preferable to choice monoatomic gases since they give more heating with respect to diatomic gases.

- *The type of the solvent:*

The choice of the solvent has a deep influence on the sonochemical reaction rate. The first effect is the vapor pressure of the solvent, which is conducible at the temperature effect: high vapor pressure leads to have a greater quantity of solvent vapors in the gas bubble thus reducing the cavitation phenomena. Other liquid properties such as viscosity or surface tension can alter the cavitation process, but they usually have less impact on it.

5.3.2 Experimental preparation procedure

5.3.2.1 Synthesis of $Fe_{10}US$ and $Fe_{30}US$

The synthesis of the sonochemical samples is a quick process which has a total duration that is usually shorter than one day. All the preparation steps are reported hereinafter:

- Dry the sonochemical reactor and the base SiO_2 in the oven (T= 120 °C) overnight;

- Weight the correct amount of SiO_2 and transfer it into the US reactor;

- Insert 10 mL of n-decane in the US reactor, turn on the cryostat (T= -5 °C) and cool down the sonochemical reactor;

- Open the Ar line and flow the inert gas through the solvent for 30 mins;

- Insert the correct amount of $Fe(CO)_5$ with a syringe into the US reactor;

- Flow Ar over the reactant mixture;

- Turn on the US transductor and start the sonochemical reaction, total US exposure time= 3 h, with a duty cycle of 5/4 seconds with an emitted power of 50 watts and a frequency equal to 20 kHz;

- At the end of the sonochemical reaction, close the Ar line and start to flux air over the n-decane (air flowrate= 0.5 $NL \cdot h^{-1}$) for 18 h;

- Recover the catalyst, wash it with pentane and filter it;

Once the washing/filter step is done; the catalyst is ready to be sieved and then used in the FT plant.

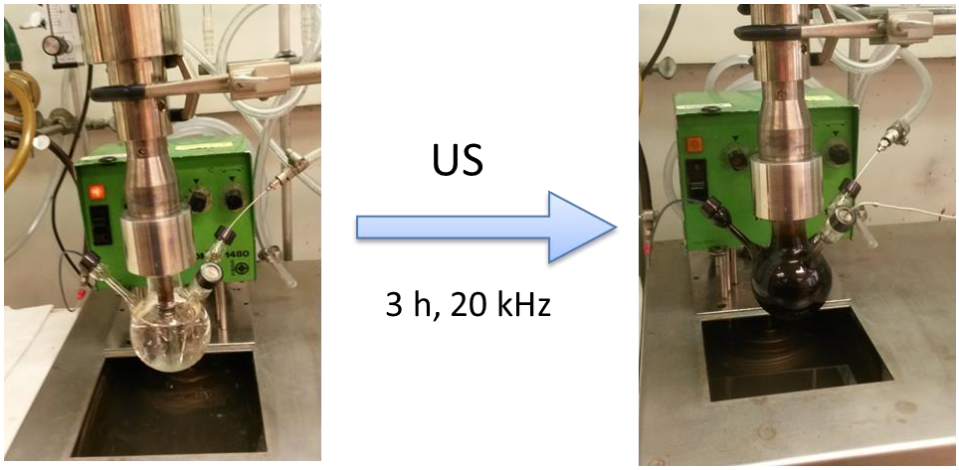

Figure 5.7: Ultrasonic $Fe(CO)_5$ decomposition.

5.3.2.2 Synthesis of $Fe_{30}K_2Cu_{3.75}US$

The synthesis of the K-Cu-promoted catalyst starts with an impregnation step. This impregnation step is carried out as the one for the synthesis of $Fe_{30}K_2Cu_{3.75}$. Even the calculation of the correct amounts of promoters in order to achieve the desired loading of potassium and copper is done identically.

When K and Cu are supported on SiO_2 it is possible to transfer the solid in the sonochemical reactor and carry out the US step reported in paragraph 5.3.2.1.

5.3.3 Calculation the amount of active metal precursor

The equation used to calculate the amount of cobalt in the catalyst is the same of the one used for $Fe_{30}K_2Cu_{3.75}$:

$$\%wt_{Fe} = \frac{g_{Fe}}{g_{Fe}+g_{SiO2}} \quad \text{(Eq. 5.25)}$$

Where:

- $\%wt_{Fe}$: is the desired weight percentage of Fe in the catalyst;

- $g_{Fe,\ SiO2}$: are the calculated weight of iron and silica in the catalyst.

Since in this equation there is only an unknown term (g_{Fe}), it is easy to calculate the weight of the active metal just by fixing the total amount of catalyst desired. If 0.5 g of catalyst have to be synthesized with a $\%wt_{Fe}$ equal to 10 %, the amount of iron will be:

$$g_{Fe} = g_{Catalyst} \cdot \%wt_{Fe} = 0.5 \cdot 10\ \% = 0.05\ g \quad \text{(Eq. 5.26)}$$

Due to the stoichiometry:

$$moles_{Fe} = moles_{Fe(CO)5} \quad \text{(Eq. 5.27)}$$

Once the moles of Fe are calculated, it is possible to directly calculate the amount of the Co-precursor.

$$moles_{Fe} = \frac{g_{Fe}}{PM_{Fe}} = \frac{0.05\ g}{55{,}845\ g \cdot mol^{-1}} = 0.00895\ mol \quad \text{(Eq. 5.28)}$$

$$g_{Fe(CO)5} = moles_{Fe(CO)5} \cdot PM_{Fe(CO)5} \quad \text{(Eq. 5.29)}$$

Where:

- g_{Fe}: is the mass of Fe in the catalyst;

- $moles_{Fe,\ Fe(CO)5}$: are the effective moles of Fe and/or iron precursor in the catalyst.

- $g_{Fe(CO)5}$: is the mass of the precursor that has to be weigh;

- $PM_{Fe(CO)5}$: is the atomic weight of the Fe precursor, which is equal to 195.9 $g \cdot mol^{-1}$.

Using the above Eq. 5.29, the calculated amount of Fe precursor is:

$g_{Fe(CO)5}$= 0.175 g

Considering that $Fe(CO)_5$ is a liquid reactant, it is more convenient to calculate the volume instead of the mass, the volume of iron pentacarbonyl is given by:

$$volume_{Fe(CO)5} = \frac{g_{Fe(CO)5}}{density} = \frac{0.175\ g}{1.45\ g{\cdot}ml^{-1}} = 0.12\ ml$$

6 Catalysts characterization: analyses techniques and experimental results

The catalysts characterization process can be divided into two different investigation areas, the first one deals with the study of the support material with analyses focused to find out the morphological properties such as surface area, pore volume and diameters and porosity distribution. The second is focused on the study of the chemical composition, and other chemical properties of the active species.

In general, a deep and detailed study of the physical and chemical properties of the samples is essential for a comparison and a correlation among different catalysts.

The catalytic systems synthesized and tested during the PhD research period have been characterized with several techniques such as BET (evaluation of the surface area), TEM (transmission electron microscopy), SEM-EDX (scanning electron microscopy), CHN/ICP (elementary analysis), XRD (X-ray powder diffraction) and TPR (temperature programmed reduction). Part of the characterization work was carried out in the Frederick Seitz Materials Research Laboratory Central Research Facilities, University of Illinois.

Catalyst	Characterization analyses							
	BET	TEM	SEM	EDX	CHN	ICP	XRD	TPR
$Fe_{30}K_2Cu_{3.75}$	X	X	X	X		X	X	X
5Co		X	X	X		X	X	X
10Co	X	X	X	X		X	X	X
10Co-0.4Ru	X	X	X	X		X	X	X
$Fe_{10}US$	X	X	X		X	X	X	X
$Fe_{30}US$	X	X	X		X	X	X	X
$Fe_{30}K_2Cu_{3.75}US$	X	X	X		X	X	X	X

Table 6.1: Characterization analyses made on the catalyst.

The characterization analyses have been carried out after the preparation procedure and before the activation step. In particular in the case of $Fe_{30}K_2Cu_{3.75}$ the analyses have been made after the calcination of the catalyst, while in the case on FSP and US synthesized catalyst the characterization analyses have been performed directly after the synthesis step since it did not involve any calcination procedure. However, in

some cases, several characterization analyses have been done after the activation step or even after the FT catalytic test in order to better understand the catalysts behaviors.

6.1 Characterization techniques: theory and fundamentals

6.1.1 BET

The surface area of a material can be measured by physical N_2 adsorption. The nitrogen will form a mono-layer of adsorbed molecules on the catalyst surface. If the surface of every molecule is known it is possible to calculate the total surface area of the sample, usually expressed in $m^2 \cdot g^{-1}$. It is also important that the gas used for the physical adsorption does not have big dimensions since they can constitute a problem during the adsorption process on the very fine sites of the solid material. Moreover, opportune procedures of calculation allow also to determine the distribution of the pores.

The BET technique took its acronym from the authors (Brunauer, Emmett and Teller) that elaborated this theory and the relative equation in 1938 [87]. The BET theory is an extension of the Langmuir one, with this additional assumptions:

- The gas molecules are physical adsorbed on the solid surface, forming an infinite series of layers one above to the other;

- There are not interactions among the different adsorbed layers;

- Every layer respects the Langmuir theory.

The BET equation is here reported in Eq. 6.1:

$$\frac{V}{Vm} = \frac{C \cdot \frac{P}{P^\circ}}{\left[1-\left(\frac{P}{P^\circ}\right)\right] \cdot \left[1+(C-1) \cdot \frac{P}{P^\circ}\right]} \qquad \text{(Eq. 6.1)}$$

Where:

- V: is the volume of adsorbed gas the pressure P;

- P°: is the saturation pressure, at the considered temperature;

- P/P°: is the relative pressure;

C: is the BET constant.

The BET constant C is expressed with the following Eq. 6.2:

$$C = e^{\frac{(q1-qL)}{RT}} \quad \text{(Eq. 6.2)}$$

Where:

- q_1: heat of adsorption of the first layer;

- q_L: heat of adsorption of the second and higher layers.

Eq. 6.2 can be linearized and can be used in a range of P/P° between 0.05- 0.3. The linearized equation is:

$$\frac{\frac{P}{P^\circ}}{V\cdot\left[1-\left(\frac{P}{P^\circ}\right)\right]} = \frac{1}{C\cdot Vm} + \frac{(C-1)\cdot\frac{P}{P^\circ}}{C\cdot Vm} \quad \text{(Eq. 6.3)}$$

This above equation represents an adsorption isotherm and it can be plotted with the left term on the Y axis and P/P° on the X axis. The experimental surface area is then determined with the equation related to Vm here presented in Eq. 6.4:

$$S.A. = \frac{Vm\cdot N_{AV}\cdot A_{MOL}}{V_{MOL}} \quad \text{(Eq. 6.4)}$$

Where:

- S. A: is the surface area value;

- N_{AV}: is the Avogadro's number;

A_{MOL}: adsorption cross section (for N_2 = 16.2 Å^2);

V_{MOL}= molar volume of a gas (22.414 L·mol^{-1});

Experimentally, the catalysts surface area has been determined using a Tristar II 3020 Micromeritics apparatus by low temperature (T= -196 °C) N_2 adsorption.

Before the measurement, catalysts have been outgassed at T= 200 °C for 1 hour and under inert gas (N_2) flux.

One the measurements were done, the surface area was calculated from nitrogen isotherms using BET theory from the instrumental software (Version 1.03).

6.1.2 TEM

TEM is the acronym of transmission electron microscope; this surface investigation technique allows to take images of a sample by using a beam of electrons transmitter through the sample which is anchored on a specimen.

The beam that is transmitted through it, forms an image that is focused and magnified by a series of lenses and at the end appears on a screen or is detected by a CCD camera. This particular analytical technique has been developed by Albert Prebus and James Hillier at the University of Toronto in 1938.

The resolution of the image that can be achieved is a function of the wavelength of the beam used. In traditional microscope techniques, it is limited by the wavelength of the photons. However, as photons, electrons possesses the characteristic of particles and electromagnetic radiation. Since electrons have smaller wavelength with respect to photons, greater magnifications can be achieved.

A field of electrons can be generated using different sources such as thermionic emission from a filament, usually tungsten, light bulb, or by field emission as wells. Once that the electron field is generated it is accelerated by applying an electrical potential and focused by a series of lenses and apertures.

TEM is a suitable technique for the imaging of supported catalysts with particles of 2-3 nm diameters. This technique can give information about the dimension of the active phase nanoparticles, their morphology and the disposition/dispersion over the bare support.

The TEM analysis have been carried out in collaboration with Perugia University (Dr. Alessandro Di Michele) using a Philips 208 transmission Electron Microscope and with a JEOL 2100 Cryo TEM (Frederick Seitz Materials Research Laboratory Central Research Facilities, University of Illinois). In both cases, the sample was prepared by deposing a small drop of micro-emulsion of the catalyst on a copper grid pre-coated with a Formvar film and then evaporated in air at room temperature.

6.1.3 SEM-EDX

The scanning electron microscopy, similarly with TEM technique, uses an electrons beam to obtain surface images of the sample. In this analytical technique, the electrons beams is not fixed and does not pass through the sample but it is scanned over the sample surface.

SEM involves not only primary electrons, but also secondary emitted electrons, characteristic x-rays, and back scattered electrons. For these reasons a wide range of detectors capable to catch these information have been developed.

SEM images have great depth of field yielding a characteristic three-dimensional appearance useful for understanding the surface structure of a sample. Moreover, with the study of the emitted x-ray (EDX technique) it is possible to carry out a

mapping for each element in order check the dispersion on the catalyst surface and its surface weight percentage.

SEM resolution does not allow to individuate single atoms as in TEM images but depending on the type of instrument, the resolution reach dimension from few nanometers to 20- 30 nm. Generally, SEM images are easier to interpret than TEM ones.

SEM analysis have been made in collaboration with Perugia University (Dr. Alessandro Di Michele) using a SEM Philips XL-30CP with RBS-EDX detector of back-scattered electrons and with a JEOL 7000F analytical SEM (Frederick Seitz Materials Research Laboratory Central Research Facilities, University of Illinois).

6.1.4 CHN and ICP

The CHN (carbon, hydrogen, nitrogen) analysis is another type of bulk elementary analysis which allow the determination of the content of carbon, hydrogen and nitrogen into a sample. From an analytical point of view, the CHN is a very simple instrument; the quantification of the elements is carried out by oxidizing the compounds in the samples and the combustion products are then quantified with a thermal conductivity detector (TCD) or infrared (IR) spectroscopy.

The inductively coupled plasma (ICP) analysis is bulk a characterization technique which allows the determination and the quantification of metal and some non-metal elements in the catalyst. As a function of the type of detector adopted in the instrument, ICP is a very sensible technique and it can reveal the presence of some elements even in concentrations that are lower of part per billion (ppb). Several detectors can be integrated with the ICP apparatus, the most common is the mass spectroscope (MS).

The catalyst sample is completely dissolved into a liquid matrix. This liquid solution is then fed through a nebulizer with a flow of an inert gas (usually argon). The catalyst atoms are ionized with the use of the plasma and then, the ionized sample is extracted from the plasma through a series of cones into a mass spectrometer; quadrupole MS are usually preferred. Once the ions reach the MS they are separated as a function of their mass/charge ratio and the intensity signal recorded by the detector is directly correlated to the concentration of the ion.

Experimentally, the samples have been analyzed with a PerkinElmer – SCIEX ELAN DRCe ICP-MS and a PerkinElmer 2400 Series II CHN/O (Frederick Seitz Materials Research Laboratory Central Research Facilities, University of Illinois).

6.1.5 XRD

The XRD (X-ray diffraction) is a non-destructive characterization technique which allows the qualitative and quantitative analysis of powder or solids crystalline materials. In the case of metal-based heterogeneous catalysis it is useful to identify the type of metal oxides (if crystalline) present on the support surface.

This technique is based on the reflection and diffraction of a monochromatic x-ray that comes from an x-ray emitter to different atomic (crystalline) parallel planes in the solid material. The crystalline atoms diffracts the incident x-rays into many specific directions. This diffraction process follows the Bragg law: when a x-ray beam with a wavelength equal to λ is incident on a reticular plane with an angle equal to θ, a diffraction is created if the optical path of the reflected x-ray in the other planes (which have a distance among themselves equal to d) is a multiple of the wavelength selected.

The Bragg equation is reported in the following Eq. 6.4:

$$2 \cdot d \cdot \sin\theta = n \cdot \lambda \qquad \text{(Eq. 6.4)}$$

Where:

- n*:* is a positive integer;

- λ: is the wavelength of the x-ray beam;

- d: is the distance between the crystallographic planes;

- θ: is the incident angle of the x-ray beam.

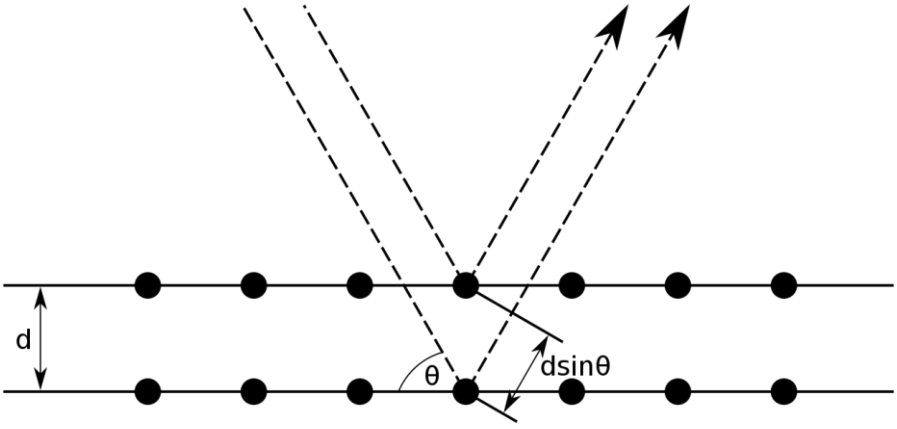

Figure 6.1: Graphical explanation of the Bragg law.

By analyzing and comparing with the literature the diffraction angles of a sample, it is possible to determine which type of phase, or phases are present.

The X-ray powder diffraction patterns of the catalysts were taken with a SIEMENS/BRUKER D-5000 using CuKα emission, operating at 40 kV and 20 mA, step scan 0.5 °·min^{-1}, and in the 5- 80 2θ range at room temperature (T= 25 °C) (Frederick Seitz Materials Research Laboratory Central Research Facilities, University of Illinois)

6.1.6 TPR

The TPR (temperature programmed reduction) characterization analysis is useful for three different reasons: the first one is to figure out the best reduction conditions (temperature, gas mixture) for a metal-based catalyst, the second reason is to identify the type of metal phases present on the catalyst and their interaction with the support while the third is to understand the role of the promoter and its interaction with the support and with the active metal of the catalyst.

TPR experiments are carried out by flowing a reducing gas mixture, usually H_2 or CO diluted into an inert gas, over a defined amount of oxidized sample while the temperature is raised with a constant rate.

TPR apparatus are usually capable to perform even TPO (temperature programmed oxidation) which is the inverse analysis of the TPR. In this case an oxidant gas mixture (O_2 and an inert gas) is flowed over the reduced catalyst.

By monitoring the outlet H_2 or O_2 with a TCD detector, it is possible to measure the gas consumption and to obtain a TPR/TPO profile.

TPR can be not only a qualitative, but even a quantitative technique where it is possible to measure the H_2 consumption for each reduction step. In order to carry out a quantitative analysis a calibration of the instrument must be done.

Experimentally, TPR analysis have been performed on the fresh catalyst (after the calcination or FSP/US step) using a TPR/D/O 1100 instrument (Thermoquest). Before the TPR run, the samples were pre-treated with a flow of Ar at T= 200 °C for 0.5 h in order to eliminate all the water present on the catalyst. After the pretreatment step, the samples were cooled down to T= 50 °C, and the H_2/Ar (5.1 %v/v) reducing mixture was flowed through the sample at 30 ml·min^{-1} while the temperature was raised from T= 50 °C to T= 900 °C at constant rate of 8 °C·min^{-1}.

6.1.6.1 TRP calibration

A calibration of the TPR instrument has been carried out in order to calculate the H_2 consumption for each reduction step of a sample.

TPR calibration is usually carried out using a sample of CuO, since it gives a very well defined TPR profile with one reduction peak. This peak is given by the reaction:

$CuO + H_2 \rightarrow Cu + H_2O$ (Eq. 6.5)

The TPR profile obtained during the calibration run is reported in Figure 6.2.

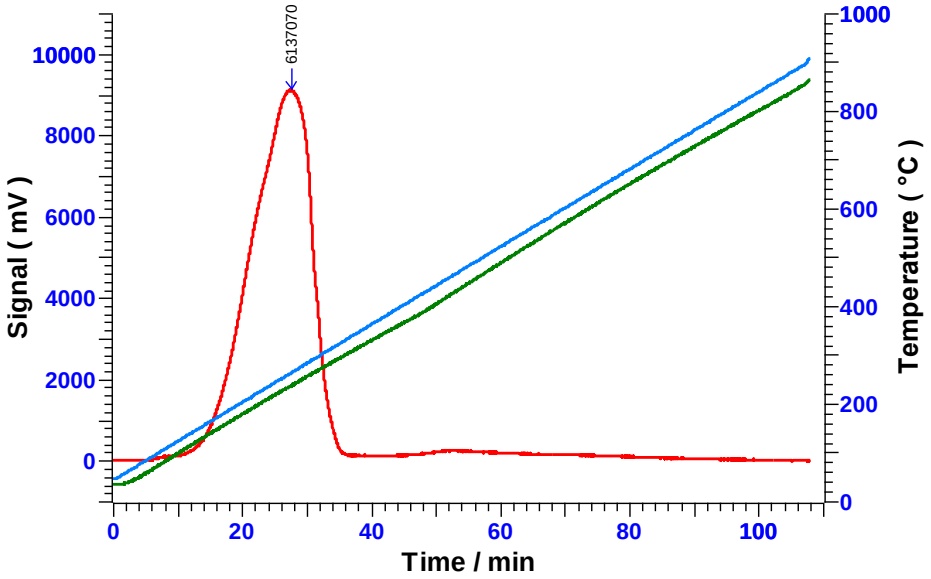

Figure 6.2: Calibration run with CuO. Red line: TPR profile; blue line: oven temperature; green line: sample temperature.

The calibration factor is calculated with the following Eq. 6.6:

$$TPR\ calibration\ factor = \frac{Sm \cdot 1000}{Fs \cdot PM \cdot \int Signal} \quad \text{(Eq. 6.6)}$$

Where:

- Sm: is the mass (g) of CuO used, which was equal to 0.026 g;

- 1000 is the conversion factor $mmol \cdot mol^{-1}$;

- Fs: is the stoichiometry factor, is CuO is used it is equal to 1;

- PM: is the molecular weight, with CuO it is equal to 79.54 $g \cdot mol^{-1}$;

- ∫Signal: is the area of the peak calculated by the instrument, which was equal to 6140900.5.

Using all the data and the results, the calculated calibration factor is:

TPR calibration factor: $5.32299061766867 \cdot 10^{-8}$

6.2 Characterization results

6.2.1 BET results

6.2.1.1 $Fe_{30}K_2Cu_{3.75}$

The study of the surface area and porosity distribution was focused on the investigation of the effect of the active metal on the bare silica and to highlight the differences in the pore area and volume between the support and $Fe_{30}K_2Cu_{3.75}$.

The results of the BET study are reported in Table 6.2:

Parameter	SiO_2	$Fe_{30}K_2Cu_{3,75}$
Specific Surface Area ($m^2 \cdot g^{-1}$)	305 ± 2	133 ± 1
C Constant	137	140
Micropores %	6.5	7.5

Table 6.2: BET results.

The insertion of 30 %wt of Fe and the promoters causes a decrease in the surface area from 305 $m^2 \cdot g^{-1}$ to 133 $m^2 \cdot g^{-1}$, this decrease can be due to the diluting effect of the metal, since Fe by itself has a very low surface area [69]. Moreover, both SiO_2 and $Fe_{30}K_2Cu_{3.75}$ isotherm showed in Figure 6.3 present the typical type IV shape which is attributable to the presence of inkbottle pores in the sample [88].

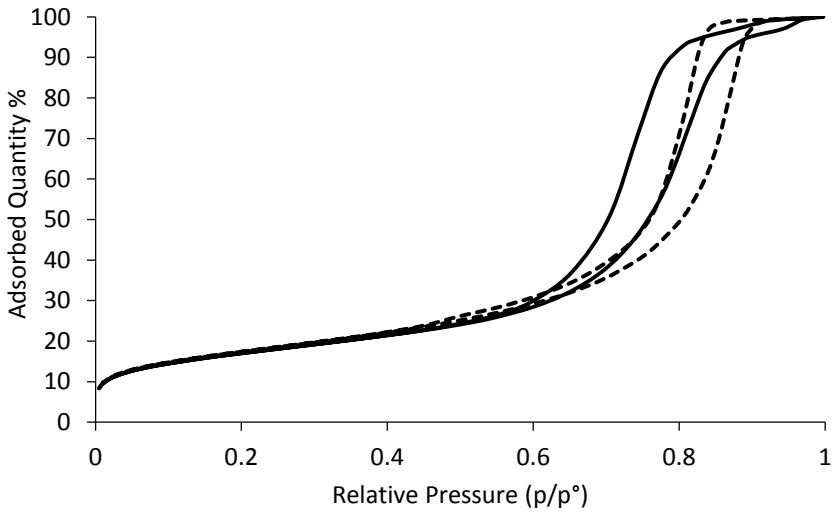

Figure 6.3: N_2 isotherms. Dashed line: SiO_2; continuous line: $Fe_{30}K_2Cu_{3.75}$.

If the incremental pore volume and pore area of the support and the catalyst are compared, it is possible to observe that the introduction of the active metal and the

promotes causes a decrease of all the mesoporous pores, except for the range of 5-10 nm which increases of 92 % for incremental pore volume 84 % in the case of incremental pore area. This great variation in the pore size distribution can be due to the fact that the addition of the metals may cause an occlusion of the pores with diameters bigger than 10 nm by a "lining" of internal pore with the result to form new pores in the range 5- 10 nm. The result concerning the pore size distribution are reported in Figure 6.4.

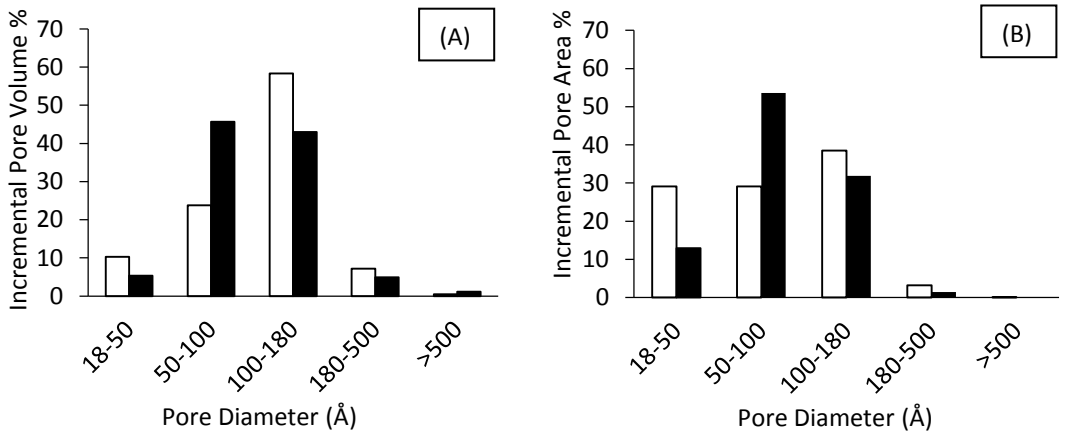

Figure 6.4: (A) incremental pore volume; (B) incremental pore area. White columns: SiO_2; black columns: $Fe_{30}K_2Cu_{3.75}$.

6.2.1.2 5Co, 10Co, 10Co-0.4Ru

The BET results of the Co-based catalysts made by FSP are reported in Table 6.3.

Sample	BET S. A. ($m^2 \cdot g^{-1}$)	Pore Volume ($cm^3 \cdot g^{-1}$)	Average Pore Size (Å)
10Co	159 ± 1	0.35	100.9
10Co-0.4Ru	145 ± 1	0.33	113.4

Table 6.3: BET results of 10Co and 10Co-0.4Ru.

The BET analysis of the sample 5Co is not reported in Table 6.3 because it is highly expectable that since both metal oxides particles and the support are formed at the same time in the FSP step, no differences in the surface area and pores size are expected.

Both 10Co and 10Co-0.4Ru present a quite high BET surface area. Moreover, the addition of Ru by wetness impregnation and the successive calcination step almost unaffected the surface area of the sample, and a decrease of only 14 $m^2 \cdot g^{-1}$ was recorded. The N_2 isotherms of the two samples with 10 %wt of Co are the ones

conducible to materials without an intrinsic mesoporosity (type II) in according with the results findable in the literature for what concern FSP-synthesized materials [72].

6.2.1.3 $Fe_{10}US$, $Fe_{30}US$, $Fe_{30}K_2Cu_{3.75}US$

The BET results of the sample sonochemically synthesized are reported in Table 6.4.

Sample	BET S. A. ($m^2 \cdot g^{-1}$)	Pore volume ($cm^3 \cdot g^{-1}$)	Pore diameter (nm)
$Fe_{10}US$	362 ± 2	0.63	5.6
$Fe_{30}US$	314 ± 1	0.54	5.7
$Fe_{30}K_2Cu_{3.75}US$	216 ± 1	0.5	6.8

Table 6.4: BET results of the US samples.

The results concerning the surface area of the catalysts highlighted that greater is the amount of the metals on the bare support, lower is the surface area of the catalysts, in fact a decrease from 515 $m^2 \cdot g^{-1}$ (SiO_2 surface area) to 216 $m^2 \cdot g^{-1}$ ($Fe_{30}K_2Cu_{3.75}US$ surface area) was recorded. As reported for the impregnated $Fe_{30}K_2Cu_{3.75}$ in paragraph 6.2.1.1, the decrease in the surface area is due to the diluting effect of the metals. Moreover, the BET results reported in Table 6.4 showed that there is a decrease of about 0.1 $cm^3 \cdot g^{-1}$ on the pore volume by increasing the loading of the metals; however, the average pore diameters of the catalysts are not strongly influenced by the %wt of the metals present on the catalysts surface.

A comparison among the BET surface area of the sonochemical samples (US) with respect to traditional impregnated samples (IMP) with the same amount of metal and synthesized with the same kind of SiO_2 is reported in Figure 6.5.

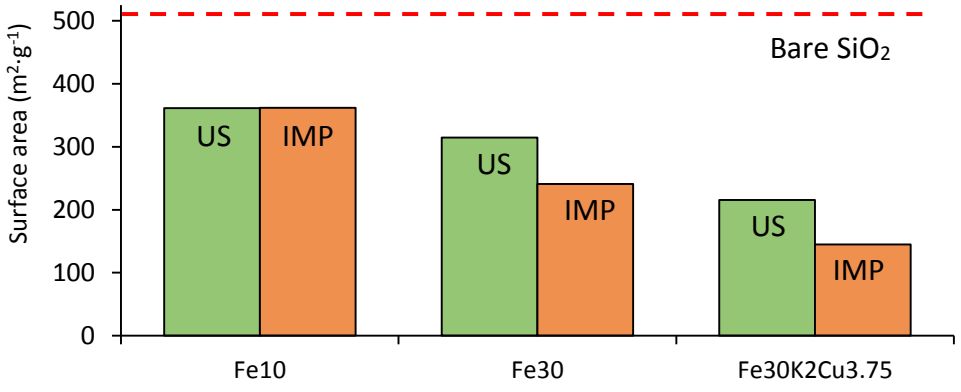

Figure 6.5: Comparison among the BET results of sonochemical and impregnated samples.

Both US samples with a loading of Fe equal to 30 %wt presented a bigger surface area if compared with the same kind of catalysts with the same metal loading but

synthesized with traditional impregnation (Fe_{30}IMP and $Fe_{30}K_2Cu_{3.75}$IMP). This fact is due to the ability of ultrasound to produce highly dispersed metal-based nanostructured materials [80].

Even if the samples with an high loading of active metals presented different results, Fe_{10}US and Fe_{10}IMP have the same surface area. This is because the benefits of the sonochemical synthesis are more visible when a big amount of metal needs to be disperse on the support surface since low metal/s loading, in this case 10 %wf of Fe, can be completely disperse even if traditional synthetic ways (impregnation techniques) are used to produce the catalysts.

6.2.2 TEM and SEM-EDX results

6.2.2.1 $Fe_{30}K_2Cu_{3.75}$

The TEM and SEM images taken on the catalyst $Fe_{30}K_2Cu_{3.75}$ are reported in Figure 6.6. and Figure 6.7.

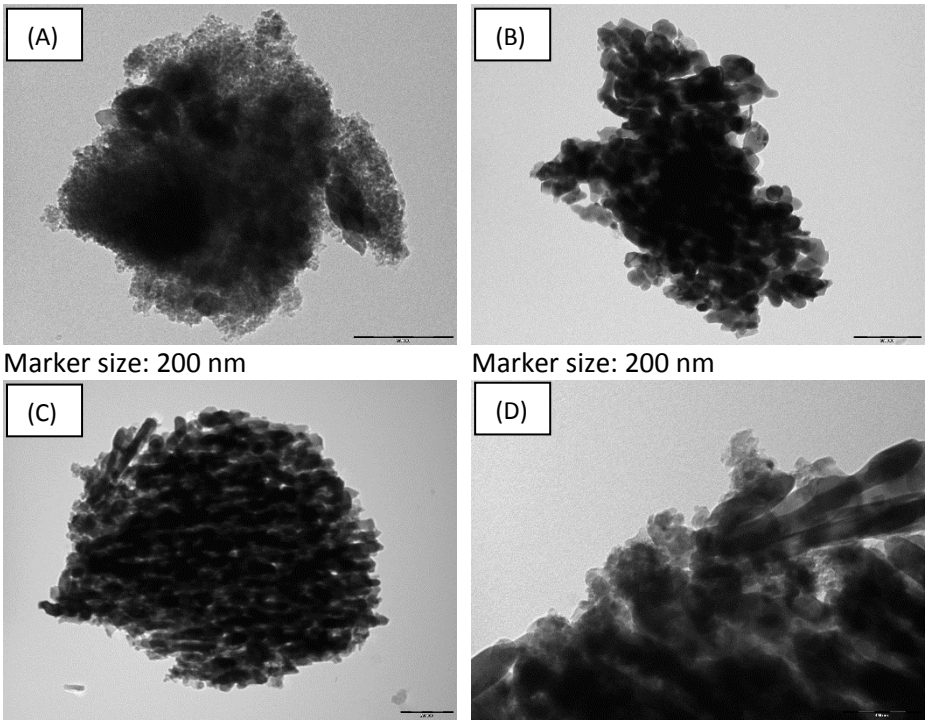

Figure 6.6: TEM images of $Fe_{30}K_2Cu_{3.75}$.

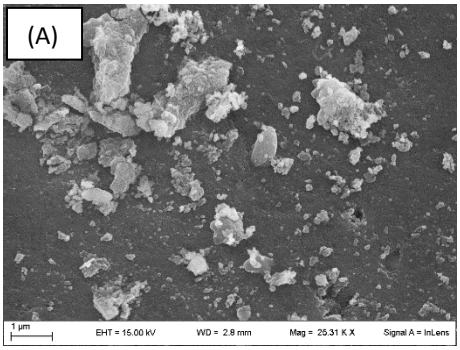

Marker size: 1 µm

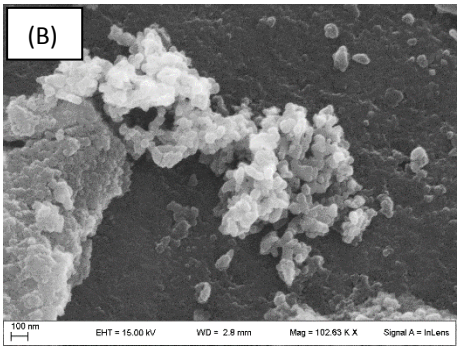

Marker size: 100 nm

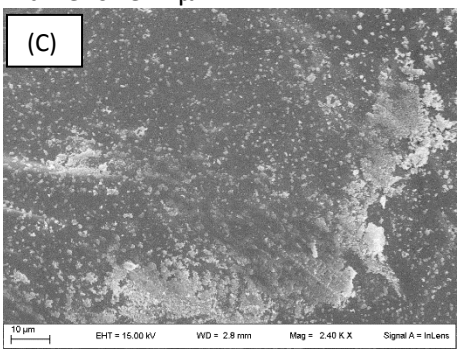

Marker size: 10 µm

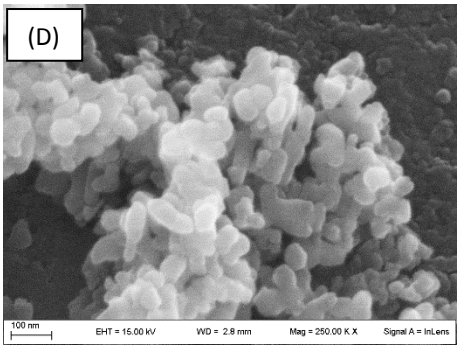

Marker size: 100 nm

Figure 6.7: SEM images of $Fe_{30}K_2Cu_{3.75}$.

The TEM and SEM captured at different magnifications help to evaluate the average dimension and the dispersion of the iron particles on the SiO_2 surface. It is possible to observe that iron is well dispersed on the support and the active metal aggregates have dimension in the range of 100- 150 nm. From Figure 6.6-(C), it is evident that as reported in the BET results, iron occludes pores with diameter bigger than 10 nm.

Another confirmation of the fact that iron, potassium and copper have a great dispersion of the support surface can be given by the EDX results.

As is possible to observe in the EDX analysis of a catalyst grain reported in Figure 6.8, the color given to Fe (red), K (yellow) and Cu (green) are completely uniform in the picture, suggesting that the metals are present in almost all the points of the bare SiO_2 support.

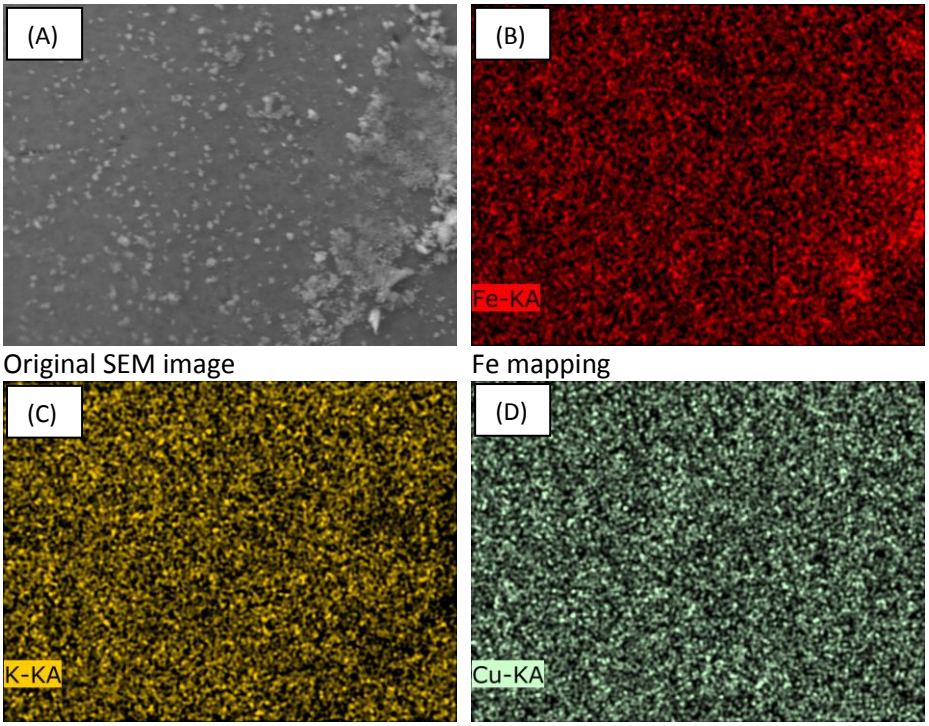

Original SEM image | Fe mapping

K mapping | Cu mapping

Figure 6.8: SEM-EDX image of $Fe_{30}K_2Cu_{3.75}$.

6.2.2.2 5Co, 10Co, 10Co-0.4Ru

The TEM images of 5Co, 10Co and 10Co-0.4Ru are reported in the following Figure 6.9- 6.11.

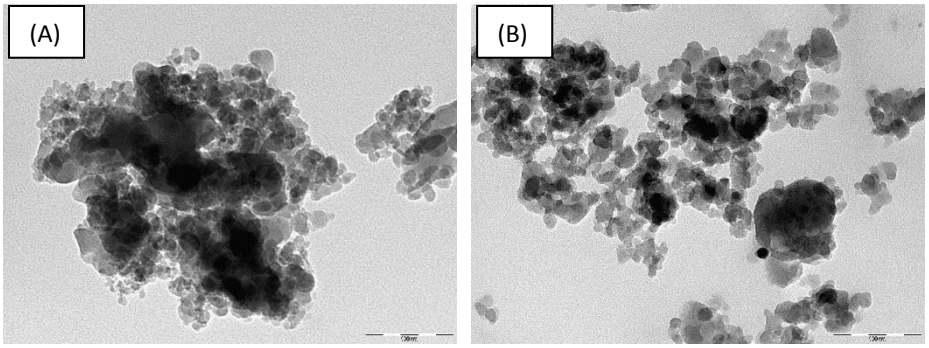

Marker size: 100 nm | Marker size: 100 nm

Figure 6.9: TEM images of 5Co.

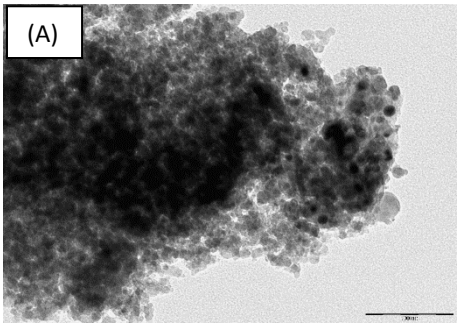

Marker size: 100 nm

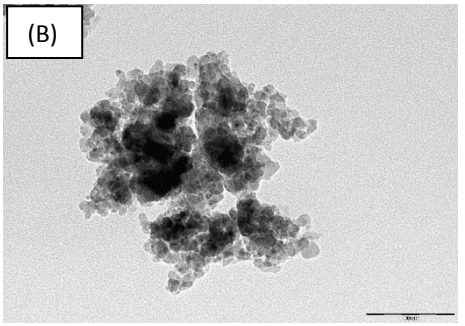

Marker size: 100 nm

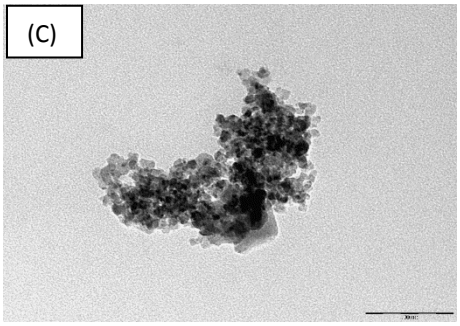

Marker size: 100 nm

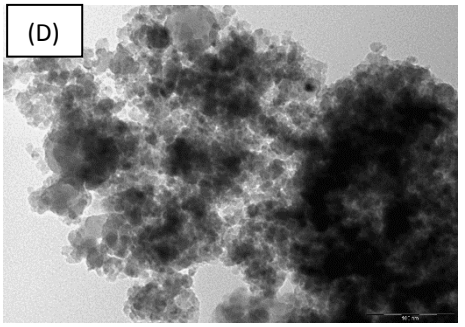

Marker size: 100 nm

Figure 6.10: TEM images of 10Co.

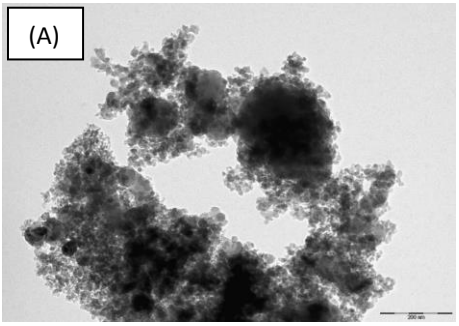

Marker size: 200 nm

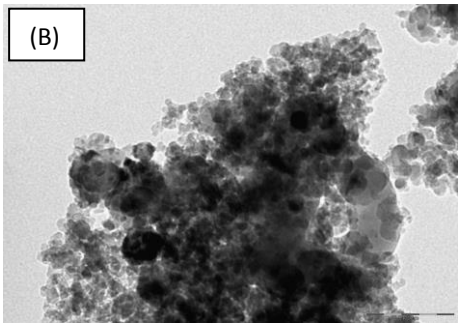

Marker size: 100 nm

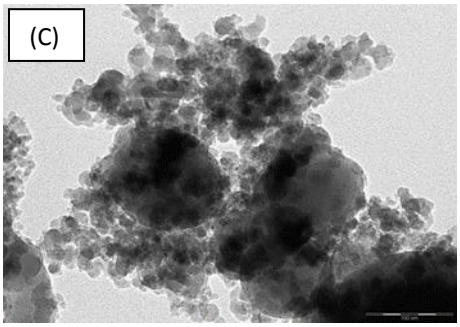

Marker size: 100 nm

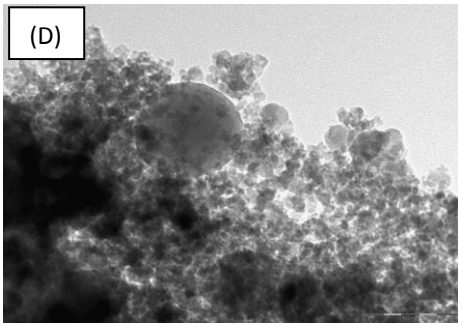

Marker size: 100 nm

Figure 6.11: TEM images of 10Co-0.4Ru.

The SEM pictures of the flame spray pyrolysis synthesized catalysts are reported hereinafter in Figure 6.11- 6.13.

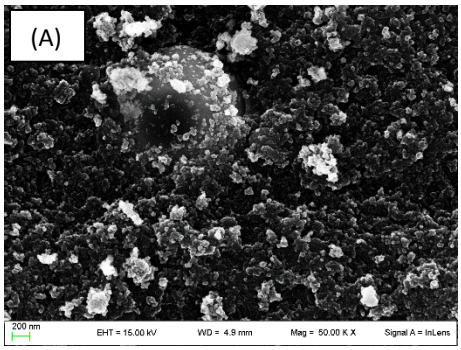

Marker size: 200 nm

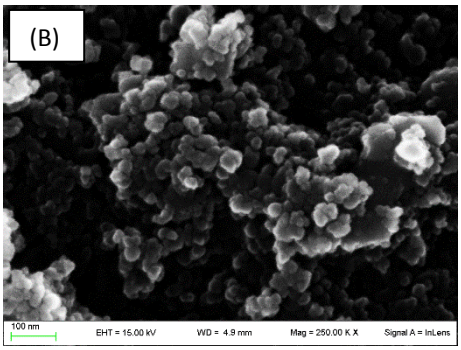

Marker size: 100 nm

Figure 6.12: SEM images of 5Co.

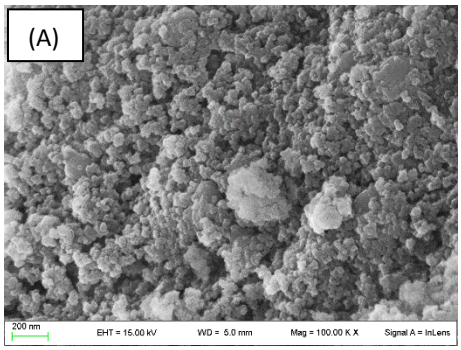

Marker size: 200 nm

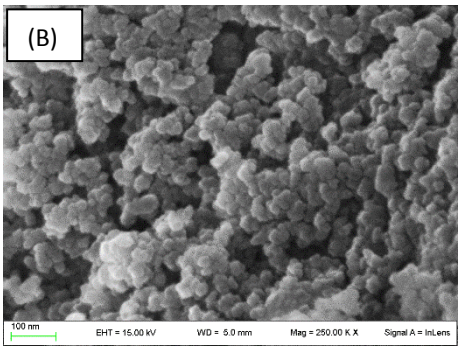

Marker size: 100 nm

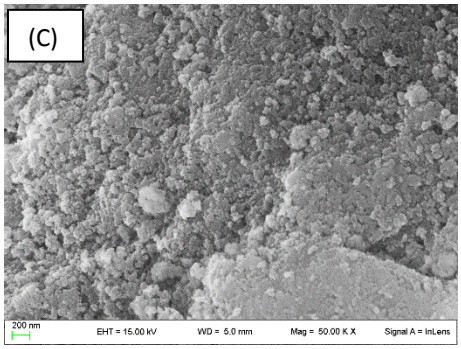

Marker size: 200 nm

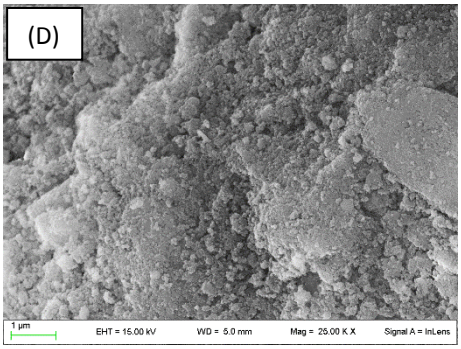

Marker size: 1 µm

Figure 6.13: SEM images of 10Co.

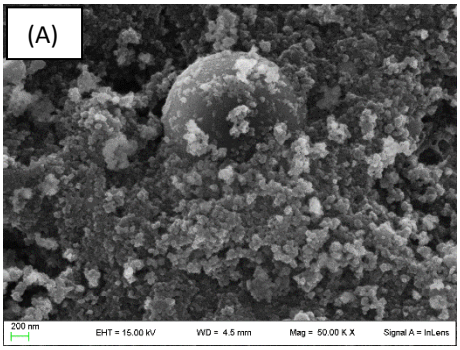

Marker size: 200 nm

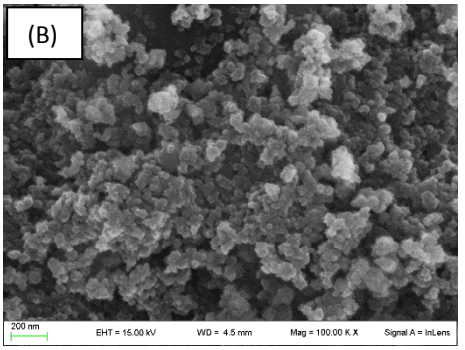

Marker size: 200 nm

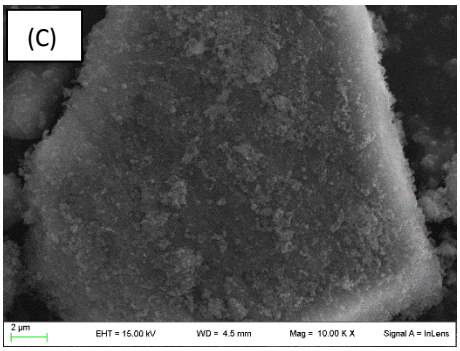

Marker size: 2 µm

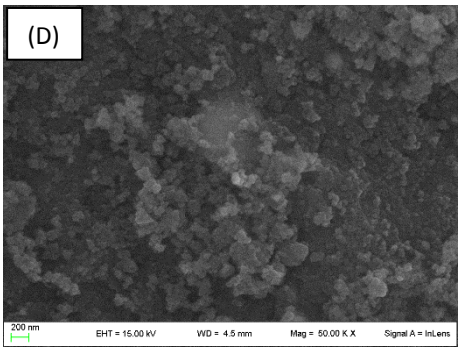

Marker size: 200 nm

Figure 6.14: SEM images of 10Co-0.4Ru.

The SEM and TEM images showed that the active metal in present on the support surface if form of quite uniform spherical particles, and these Co aggregates are uniformly distributed on the SiO_2 grain. From the TEM images of 5Co and 10Co samples it is possible to observe that the Co aggregates (dark areas) have dimensions in the range of 20- 40 nm.

The impregnation step, which involves a calcination at T= 200 °C, performed after the FSP synthesis of 10Co in order to add 0.4 %wt of Ru in the catalyst almost did not influence the dimension of Co aggregates, in fact the nanoparticles growth of about 1-5 nm. In all the sample synthesized by FSP are present bigger Co aggregates with dimensions equal to 45- 50 nm.

Moreover, SEM-EDX analyses have been performed on all the three FSP samples. The results of the SEM-EDX reported in Table 6.5 confirmed that both Co and Ru are well dispersed on the support surface and the desired amounts of active metals have been achieved on the catalyst surface.

Sample	Atom	EDX result (%wt)
5Co	Co	5.06
	Si	39.9
	O	58.9
10Co	Co	10.1
	Si	39.4
	O	50.4
10Co-0.4Ru	Co	8.56
	Ru	0.37
	Si	36.1
	O	54.6

Table 6.5: SEM-EDX results of FSP samples.

6.2.2.3 $Fe_{10}US$, $Fe_{30}US$, $Fe_{30}K_2Cu_{3.75}US$

The TEM images of the sonochemical catalysts and the SiO_2 used as support are reported in the following Figure 6.15- 6.18.

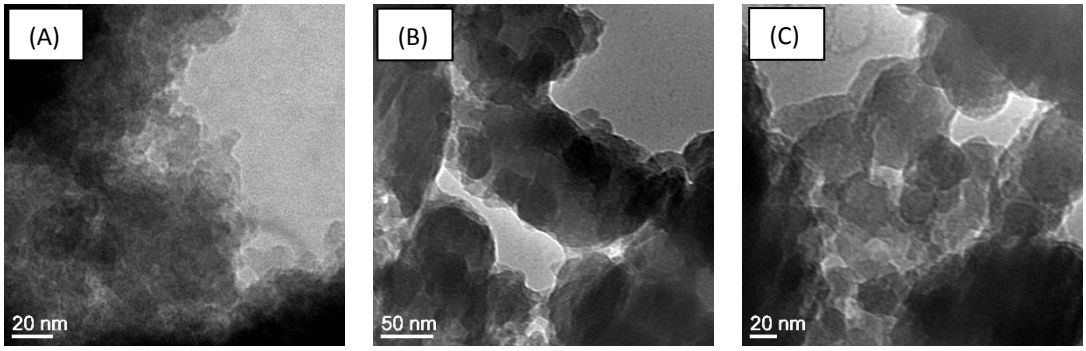

Figure 6.15: TEM images of SiO_2 support used for the synthesis of sonochemical catalysts.

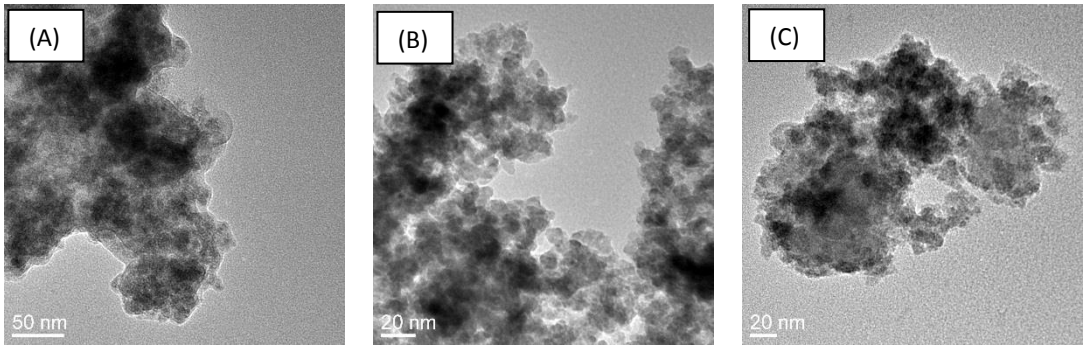

Figure 6.16: TEM images of $Fe_{10}US$.

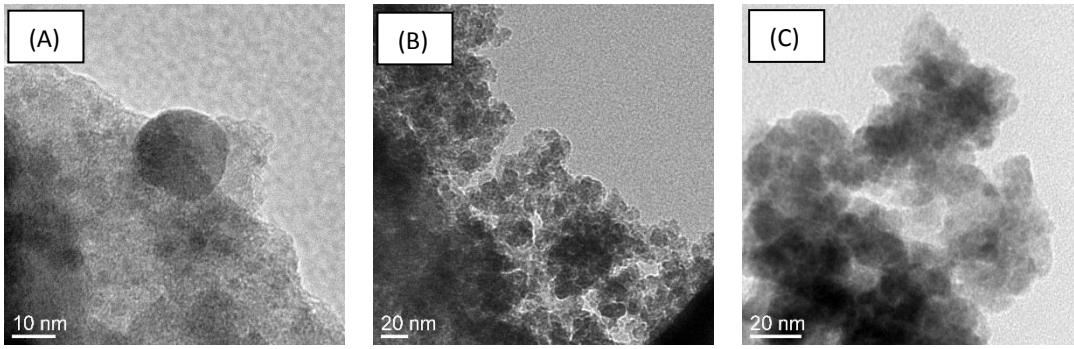

Figure 6.17: TEM images of $Fe_{30}US$.

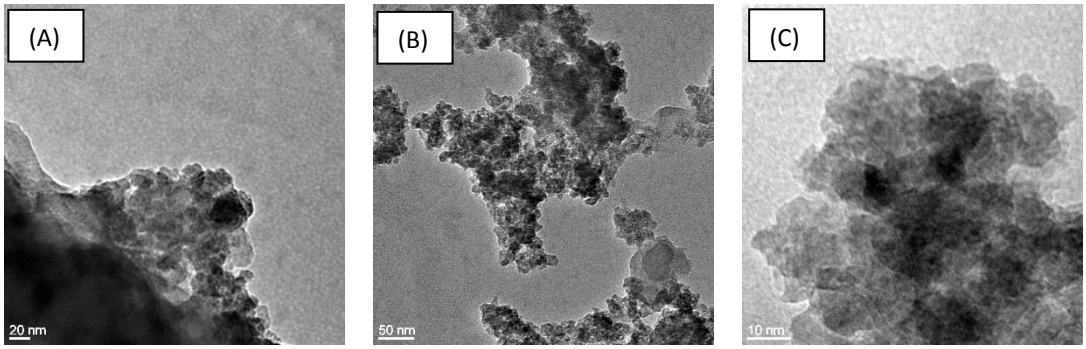

Figure 6.18: TEM images of $Fe_{30}K_2Cu_{3.75}US$.

The SEM pictures of the catalysts synthesized with the use of US are reported hereinafter in Figure 6.19- 6.22. Even in this case, the pictures of the bare support are showed.

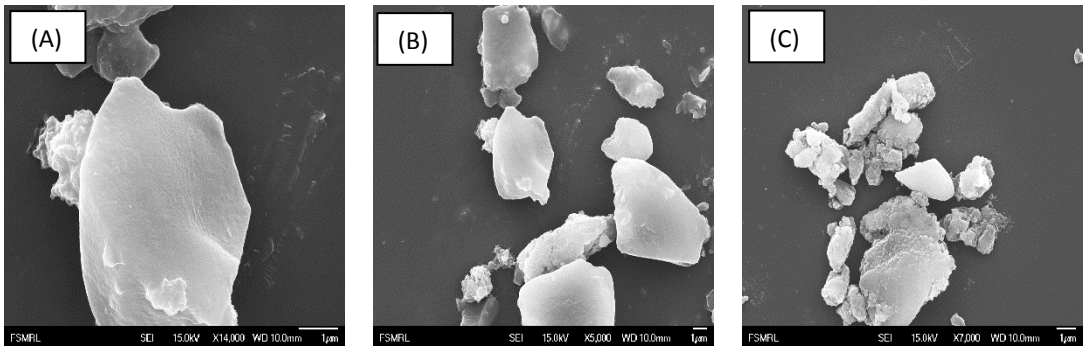

Marker size: 1 µm Marker size: 1 µm Marker size: 1 µm

Figure 6.19: SEM images of SiO_2 support used for the synthesis of sonochemical catalysts.

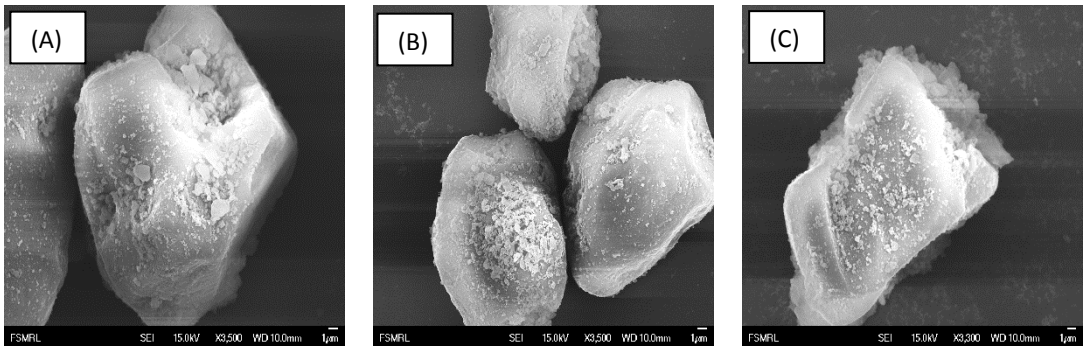

Marker size: 1 µm Marker size: 1 µm Marker size: 1 µm

Figure 6.20: SEM images of $Fe_{10}US$.

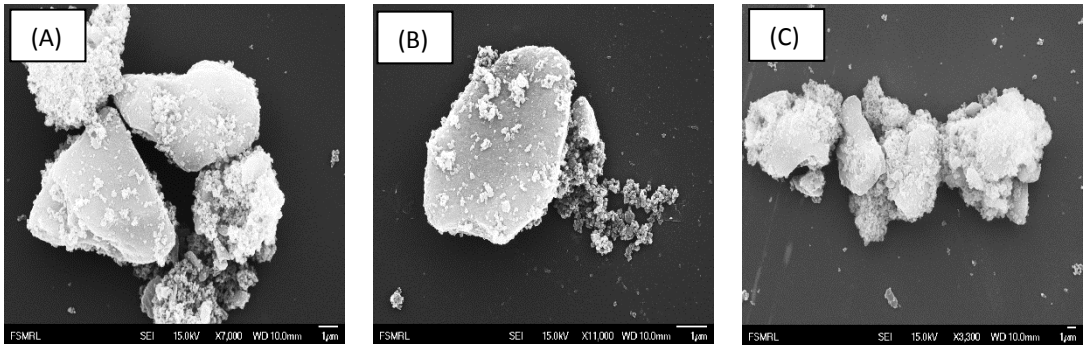

Marker size: 1 µm Marker size: 1 µm Marker size: 1 µm

Figure 6.21: SEM images of $Fe_{30}US$.

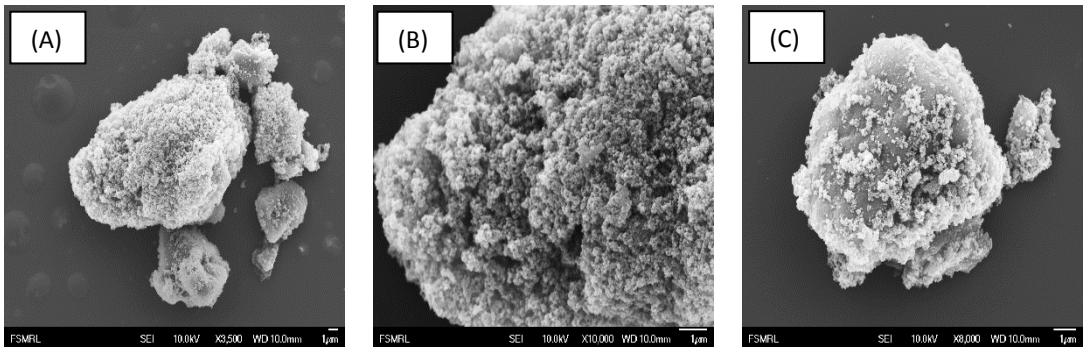

Marker size: 1 µm Marker size: 1 µm Marker size: 1 µm

Figure 6.22: SEM images of $Fe_{30}K_2Cu_{3.75}US$

Moreover additional TEM and SEM images have been taken of the sample $Fe_{10}US$ after the activation process carried out before the FT catalytic run in order to investigate the effect of the activation conditions on the morphological features of the catalyst.

The reduction has been carried out at T= 350 °C in a flow of syngas with a H_2/CO ratio equal to 2 for 4 h.

The TEM and SEM images of the sample $Fe_{10}US_{ACTIVATED}$ are reported in Figure 6.23-6.24.

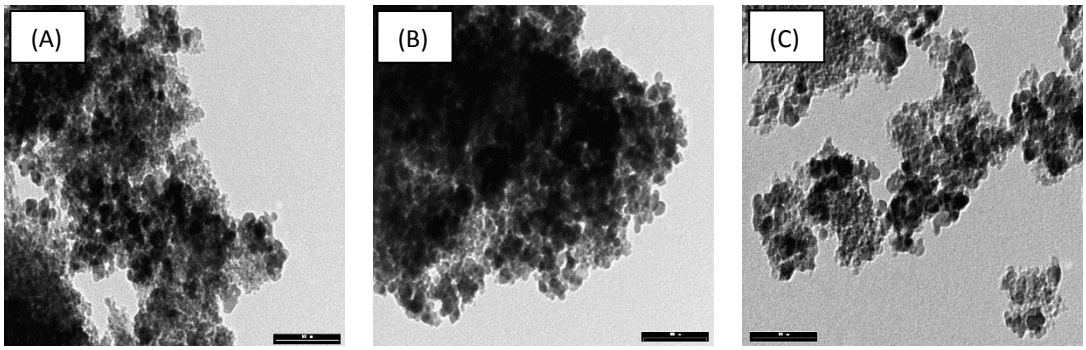

Marker size: 100 nm Marker size: 100 nm Marker size: 100 nm

Figure 6.23:TEM images of $Fe_{10}US_{ACTIVATED}$.

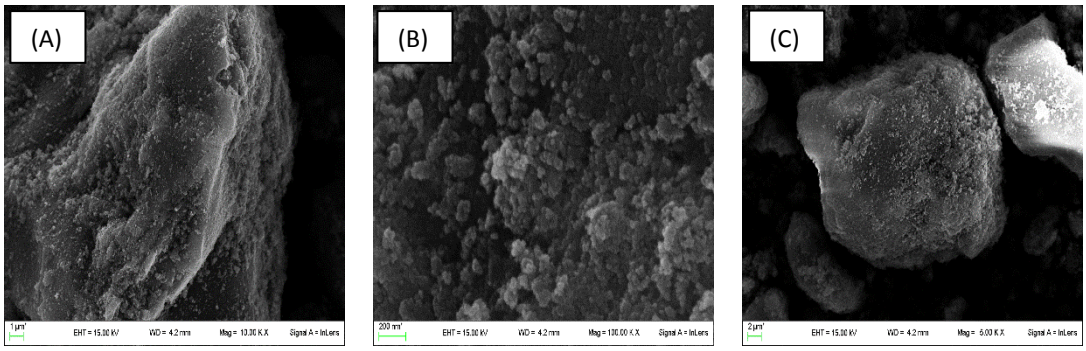

Marker size: 1 µm Marker size: 200 nm Marker size: 2 µm

Figure 6.24:SEM images of $Fe_{10}US_{ACTIVATED}$.

The TEM images of fresh catalysts showed that Fe is very well dispersed in the samples sonochemically synthesized. The black areas in the TEM images suggest that the iron nanoparticles have dimension in the range between few nanometers and 20 nm. SEM images show that the bare SiO_2 support is very smooth without the presence of the iron and the promoters, but with an increase in the metal loading the Fe-aggregates become bigger but well dispersed though.

The activation step does not influence the morphology of the sample $Fe_{10}US$ since even if it has been treated at T= 350 °C for 4 h, the dimension of the Fe-nanoparticles remained lower than 20 nm and the active metal was still well dispersed on the support surface.

6.2.3 CHN and ICP results

6.2.3.1 $Fe_{30}K_2Cu_{3.75}$

The elementary composition of the sample $Fe_{30}K_2Cu_{3.75}$ has been determined with the ICP analysis; the results are summarized in Table 6.6.

Sample	Atom	Theoretical metal loading (%wt)	Experimental metal loading (%wt)
$Fe_{30}K_2Cu_{3.75}$	Fe	30	29.73
	K	2	2.09
	Cu	3.75	3.79

Table 6.6: ICP results of the sample $Fe_{30}K_2Cu_{3.75}$.

The ICP results reported in Table 6.6 confirms that the experimental %wt of active metal and promoter are in a good agreement with the theoretical values expected.

6.2.3.2 5Co, 10Co, 10Co-0.4Ru

The ICP analysis has been carried out for all the three catalysts synthesized by flame spray pyrolysis. The main results are reported in Table 6.7.

Sample	Atom	Theoretical metal loading (%wt)	Experimental metal loading (%wt)
5Co	Co	5	4.97
10Co	Co	10	9.95
10Co-0.4Ru	Co	10	9.97
	Ru	0.4	0.41

Table 6.7: ICP results of the samples 5Co, 10Co and 10Co-0.4Ru.

The ICP analyses confirmed that all the precursors used for the synthesis of Co-based catalysts were completely decomposed in the catalyst by the flames in the FSP burner.

6.2.3.3 Fe_{10}US, Fe_{30}US, $Fe_{30}K_2Cu_{3.75}$US

The elementary composition of the catalysts synthesized with the use of US has been determined both with ICP and CHN. The first analytical technique is useful to verify if the desired amount of active metal promoters are present in the catalysts; moreover, specific ICP analyses have been carried out with all the ultrasonic catalysts in order to detect titanium contamination due to the use of a titanium-based US horn. The CHN analysis has been carried out in order to measure the amount of C in the samples.

The results of the ICP analyses on $Fe_{10}US$, $Fe_{30}US$ and $Fe_{30}K_2Cu_{3.75}US$ are reported in Table 6.8.

Sample	Atom	Theoretical metal loading (%wt)	Experimental metal loading (%wt)
$Fe_{10}US$	Fe	10	8.54
$Fe_{30}US$	Fe	30	29.66
	Fe	30	29.86
$Fe_{30}K_2Cu_{3.75}US$	K	2	1.82
	Cu	3.75	3.91

Table 6.8: ICP results of the samples $Fe_{10}US$, $Fe_{30}US$, $Fe_{30}K_2Cu_{3.75}US$.

The ICP results confirmed that the Fe precursor was almost completely decomposed under ultrasound irradiation. It is very important to optimize all the parameters and the reactor geometry in order to achieve a satisfactory decomposition of $Fe(CO)_5$. Moreover an amount of 0.009 ± 0.001 %wt of titanium was detected in all the US samples. The presence of Ti is due to the SiO_2-Ti_{TIP} interaction during the ultrasonic synthesis; however, as reported in the recent literature concerning the development and the study of the performances of Fischer-Tropsch catalysts, the presence of a little Ti contamination does not affect significantly the catalysts performances [62].

CHN highlighted the presence of 1.5 ± 0.05 %wt of carbon in each catalyst. The carbon can be formed for two different reasons: the first one is the decomposition of the n-decane solvent and the second one is the presence of carbon monoxide residue formed during ultrasonic irradiation [82]. Even though the C contamination is present in all the US samples, it is not a problem since iron carbides are active species for the FT synthesis [89].

6.2.4 XRD results

6.2.4.1 $Fe_{30}K_2Cu_{3.75}$

The XRD analysis of the sample $Fe_{30}K_2Cu_{3.75}$ which was carried out before the activation step is reported in Figure 6.25.

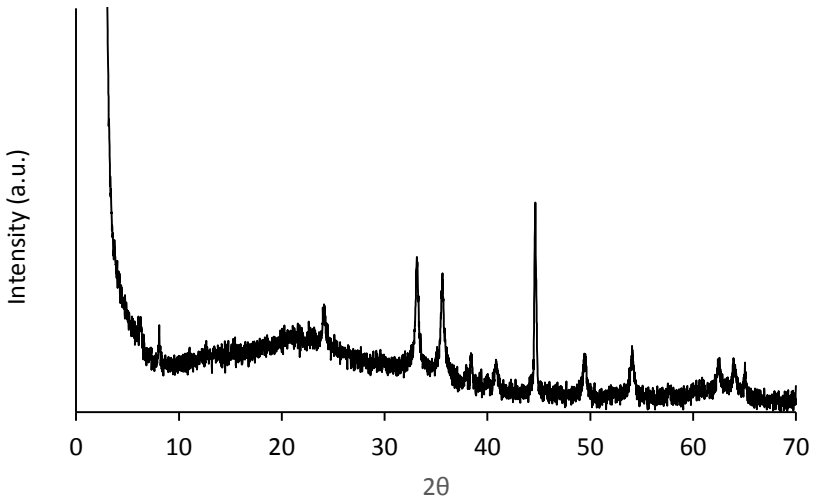

Figure 6.25: XRD pattern of $Fe_{30}K_2Cu_{3.75}$.

The XRD pattern showed the presence of hematite (Fe_2O_3) due to the presence of typical hematite peaks at 2θ= 33 °, 35 °, 41 °, 50 °, 54 °, 62 °, 64 °. This results suggests that after the impregnation synthesis Fe remains in the same oxidation state of its precursor (Fe^{3+}) [67].

6.2.4.2 5Co, 10Co and 10Co-0.4Ru

The XRD diffractograms of the FSP synthesized catalyst are reported in Figure 6.26-6.28.

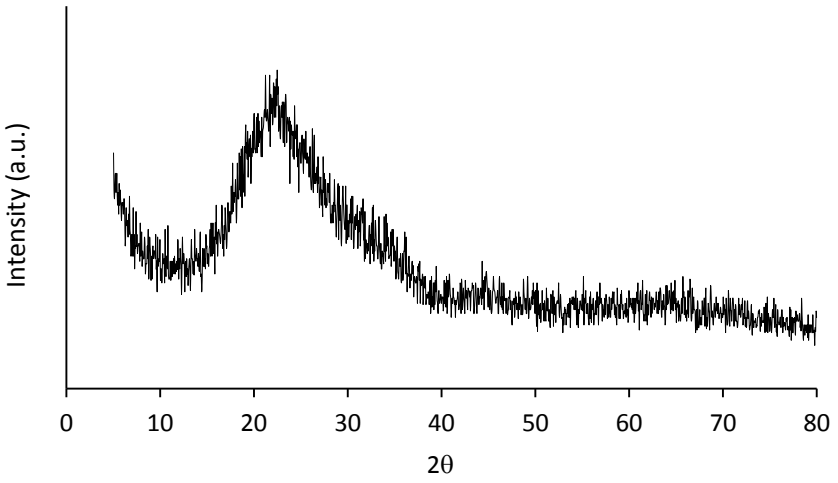

Figure 6.26: XRD pattern of 5Co.

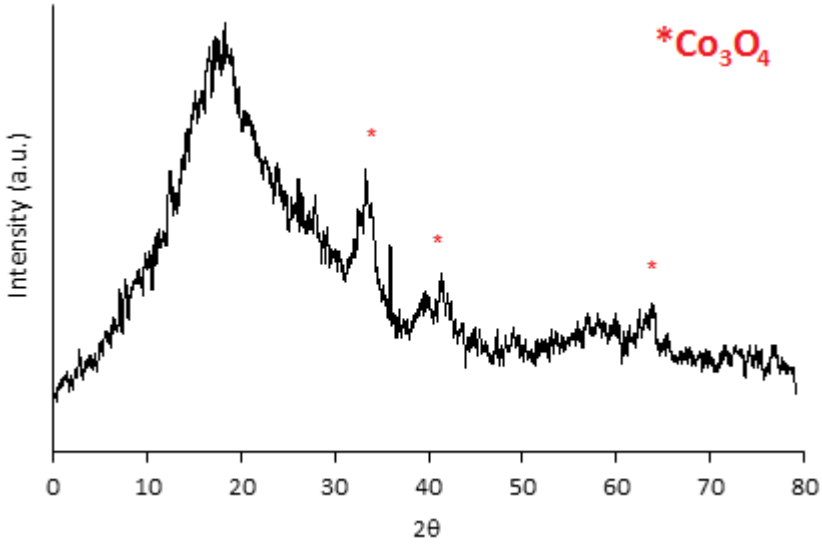

Figure 6.27: XRD pattern of 10Co.

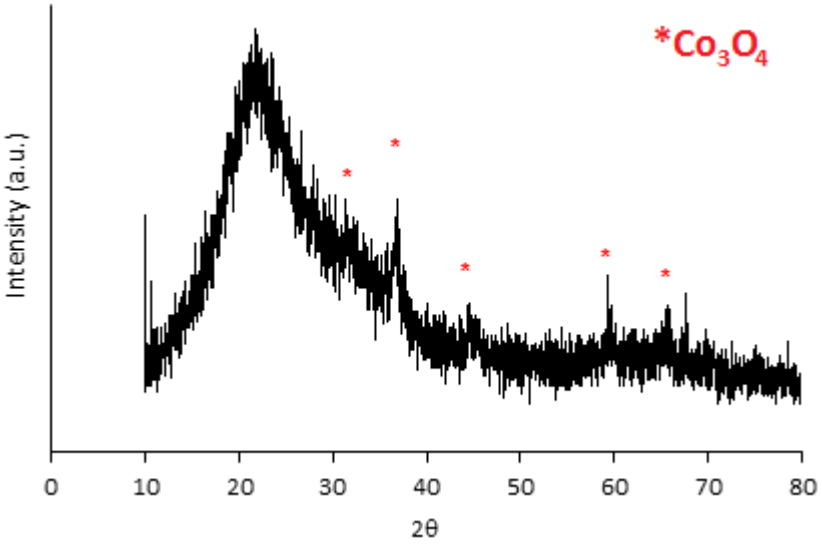

Figure 6.28: XRD pattern of 10Co-0.4Ru.

The XRD pattern of 5Co sample did not present any peak related to Co-oxides species; this because the small loading of active metal (5 %wt) is highly dispersed on the SiO_2 support; moreover highly oxidized Co-silicates could be formed during the FSP synthesis. This assumption is confirmed by the TPR profiles reported in the following paragraph.

When the load of active metal is raised to 10 %wt (10Co and 10Co-0.1Ru) some peaks related to the presence of Co_3O_4 oxide are present in both samples. Those peaks are highlighted with red stars in Figure 6.27- 6.28. Even though Co_3O_4 has been revealed, Co-silicates may be present in the catalysts.

6.2.4.3 $Fe_{10}US$, $Fe_{30}US$, $Fe_{30}K_2Cu_{3.75}US$

The XRD diffractograms of the catalysts synthesized with US are reported hereinafter in Figure 6.29- 6.32. A XRD pattern of the sample $Fe_{10}US$ after the activation step (called $Fe_{10}US_{ACTIVATED}$) is also reported.

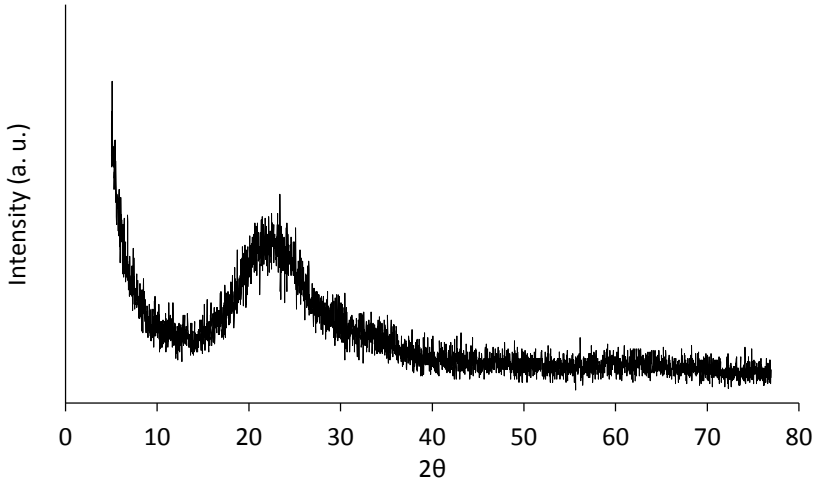

Figure 6.29: XRD diffractogram of sample $Fe_{10}US$.

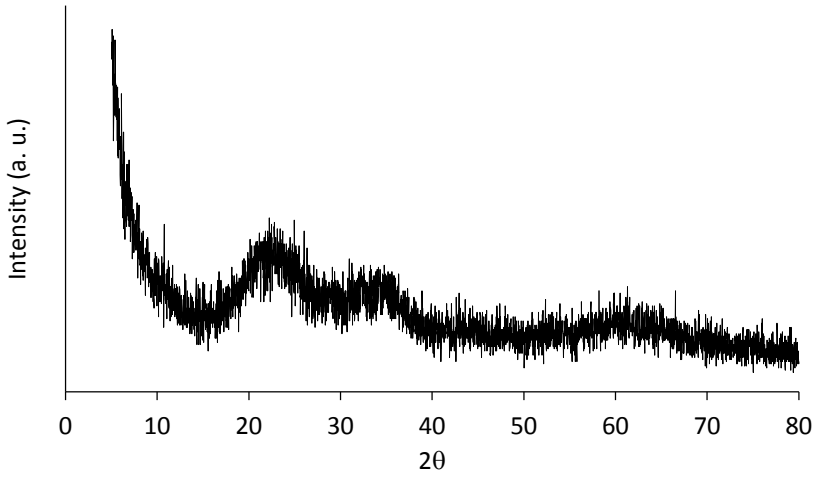

Figure 6.30: XRD diffractogram of sample $Fe_{30}US$.

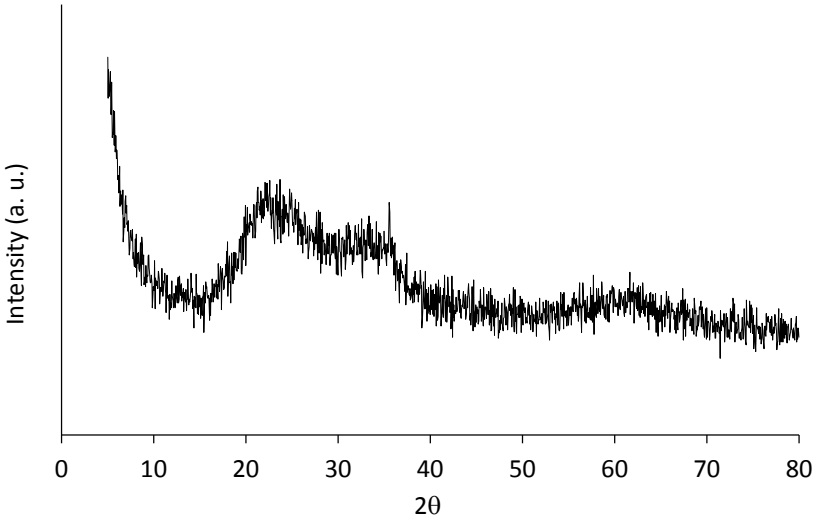

Figure 6.31: XRD diffractogram of $Fe_{30}K_2Cu_{3.75}US$.

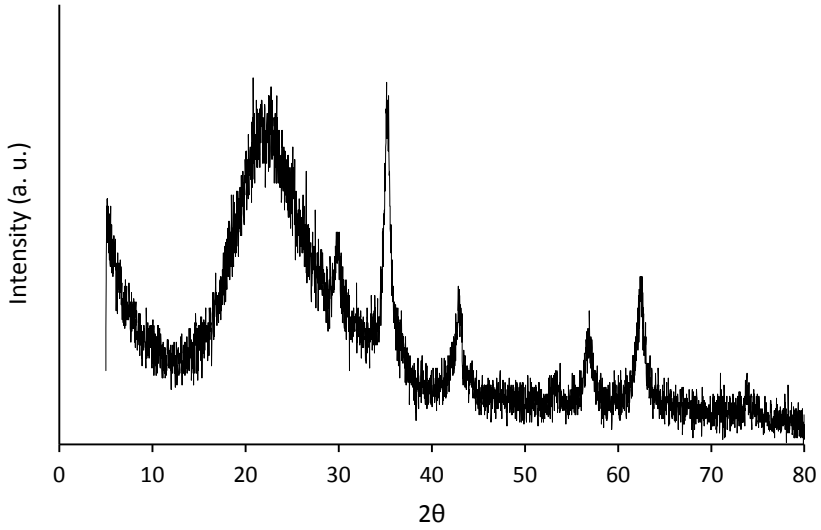

Figure 6.32: XRD diffractogram of $Fe_{10}US_{ACTIVATED}$.

The XRD patterns recorded with the fresh US catalysts do not reveal any peak related to crystalline iron oxides; this is justified to the fact, largely discussed in the literature, that during the sonochemical decomposition of a volatile metal precursor an amorphous bulk metal is formed and for this reason it is impossible to observe hematite or magnetite peaks [80,86].

However, after that $Fe_{10}US$ has been treated under activation conditions (T= 350 °C, H_2/CO= 2, t= 4 h) its XRD pattern (which is named as $Fe_{10}US_{ACTIVATED}$) is very similar to the XRD of the impregnated $Fe_{30}K_2Cu_{3.75}$ and presents peaks conducible to the presence of hematite. This behavior is normal and expected since in SiO_2 supported iron-based catalysts, the transition from amorphous solid to crystalline structure is usually obtained with a thermal treatment at T= 350 °C for 6 hours [85].

6.2.5 TPR results

6.2.5.1 $Fe_{30}K_2Cu_{3.75}$

The complete reduction process of Fe-based catalysts involves two steps, the first one from hematite to magnetite, and then at higher temperatures, from magnetite to metallic Fe. The two steps are reported hereinafter in Eqs. 6.7, 6.8 [67].

$$3\ Fe_2O_3 + H_2 \rightarrow 2\ Fe_3O_4 + H_2O \qquad \text{(Eq. 6.7)}$$

$$Fe_3O_4 + 4\ H_2 \rightarrow 3\ Fe + 4\ H_2O \qquad \text{(Eq. 6.8)}$$

If copper is present in the catalyst, the peak associated to its reduction is located at the same temperatures of the reduction of the hematite. The reduction reaction of copper oxide is reported in Eq. 6.9.

$$CuO + H_2 \rightarrow Cu + H_2O \qquad \text{(Eq. 6.9)}$$

The promotion effect of copper is to lower the temperature of the first reduction step of the iron phases transformation.

The TPR results of $Fe_{30}K_2Cu_{3.75}$ are reported in Figure 6.33 and Table 6.9.

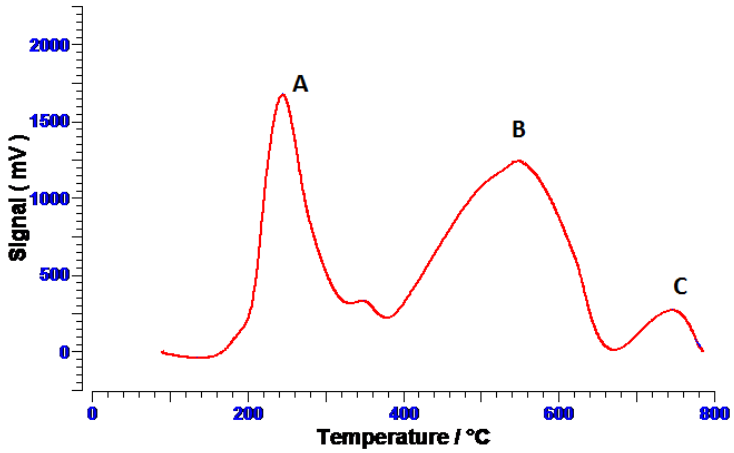

Figure 6.33: TPR profile of $Fe_{30}K_2Cu_{3.75}$

Catalyst	Peak	Reduction T (°C)
$Fe_{30}K_2Cu_{3.75}$	A	240
	B	540
	C	750

Table 6.9: TPR data of $Fe_{30}K_2Cu_{3.75}$

The TPR results of the Fe-based impregnated sample highlighted that three reduction peaks are present. Peak (A) can be associated with the reduction of hematite to magnetite and then peak (B) to the transition to metallic Fe. The presence of peak (C) can be attributable to the presence of Fe_3O_4 particles with different dimensions or stronger bounded with SiO_2 that causes the shift of the second reduction step to higher temperatures [51,90].

6.2.5.2 5Co, 10Co and 10Co-0.4Ru

The reduction path of Co-based catalysts is composed by two defined steps reported in Eqs. 6.10, 6.11.

$Co_2O_3 + H_2 \rightarrow 2\ CoO + H_2O$ (Eq. 6.10)

$2\ CoO + 2\ H_2 \rightarrow 2\ Co + H_2O$ (Eq. 6.11)

Therefore, these two reduction reactions result in the presence of two different peaks in the TPR profiles of the catalysts. By comparing the ratio between the first and the second peak it is possible to discover which type of Co oxides are present on the support surface. The first reduction steps involves the exchange of two electrons while in the second four electrons are transferred from hydrogen to two molecules of CoO thus means that the ration must be equal to 1/2.

If Co_3O_4 is present in the catalyst the ratio is decreased to 1/3 since Co_3O_4 is composed by a mole of Co_2O_3 and a mole of CoO. In this case in the second step three molecules of CoO have to be reduced, two of them derives from the reduction of Co_2O_3 while the third in the one present in Co_3O_4 specie.

Moreover, if Co-silicates are present in the catalyst, the second peak at higher temperature will become bigger due to the transfer of more electrons with the result to decrease the peaks ratio to values lower than 1/3. Obviously, if only Co-silicates or Co^{2+} species are present, no peaks related to the first reduction step are expected.

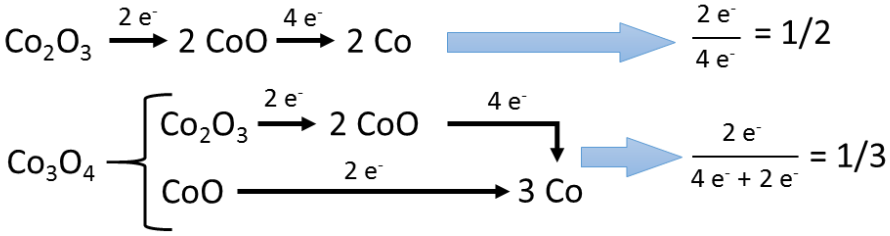

Figure 6.34: Co oxides reduction paths.

The TPR profiles of the FSP Co-based catalysts are shown in Figure 6.35- 6.37.

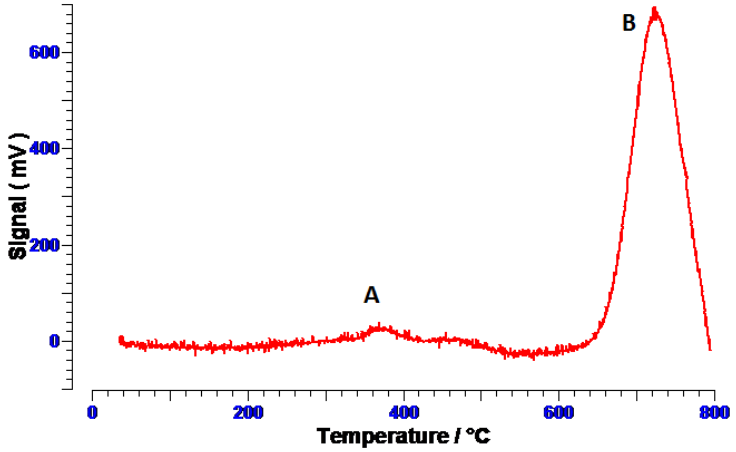

Figure 6.35: TPR profile of 5Co.

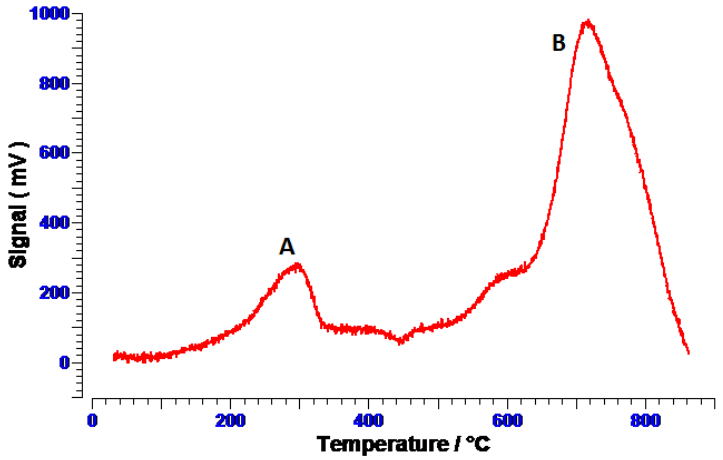

Figure 6.36: TPR profile of 10Co.

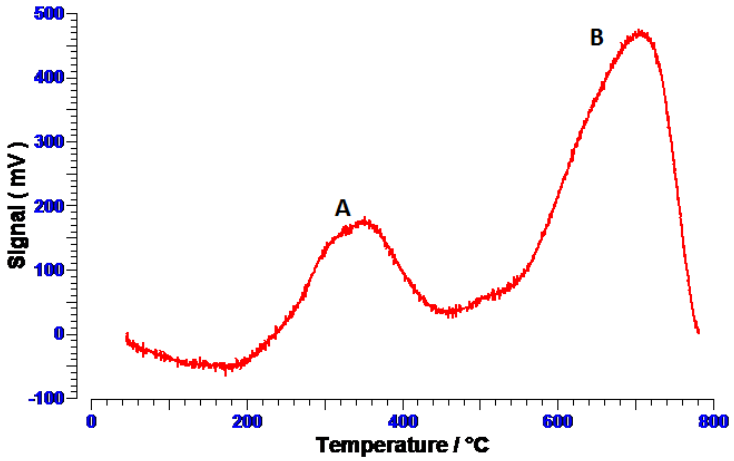

Figure 6.37: TPR profile of 10Co-0.4Ru.

Catalyst	Peak	Reduction T (°C)	A/B peaks areas ratio	peaks areas ratio/BET
5Co	A	360	0.067	//
	B	720		
10Co	A	300	0.221	$1.39 \cdot 10^{-3}$
	B	720		
10Co-0.4Ru	A	290	0.366	$2.52 \cdot 10^{-3}$
	B	690		

Table 6.10: TPR data of 5Co, 10Co and 10Co-0.4Ru.

The TPR profile of sample 5Co did not show any defined peak related to the first transition and only a faint bump (A) is present at temperatures around T= 360 °C. The lack of Co^{3+} species is due to the fact that the type cobalt oxides that are formed during the synthesis are determined by the loading of Co in the supported catalyst [91,92]. If low loadings of metal are presents (%wt< 7%) only CoO or Co-silicates are formed; for this reason the A/B peak ratio is much lower than 1/3. Moreover these species require very high temperatures (T≈ 700 °C) to be reduced.

Both TPRs of 10Co and 10Co-0.4Ru present two peaks attributable to the complete reduction process from Co^{3+} to metallic Co^0. In the case of 10Co, the A/B ratio is equal to 0.221 and still lower than 1/3; this result indicates that the active metal is present on the catalyst surface both in form of Co_3O_4 and CoO/Co-silicates. Moreover the peak (B) in Figure 6.36 is preceded by an another smaller peak which confirms the presence of different species of Co^{2+} particles and/or nanoparticles with different dimensions or differently bounded to the SiO_2 surface.

The addition of 0.4 %wt of Ru decreases both peaks reduction temperatures of about 10- 20 °C improving the catalyst reducibility. The A/B peak ratio of the promoted

sample is higher if compared with 10Co and it is almost equal to 1/3 suggesting that both Co_3O_4 and Co_2O_3 are present on the SiO_2 surface [93].

If the A/B peaks ratios of the two samples with 10 %wt of Co are divided by the BET surface area of the sample it if possible to confirm that the Ru-doped sample has a greater amount of Co^{3+} per m^2 of catalyst. Since the A/B peaks ratios of 10Co and 10Co-0.4Ru are different, some interactions between the promoter and the oxides particles of the active metal must have taken place during the Ru addition by post synthesis impregnation. The increase in the A/B ratio may be due to the calcination step carried out at T= 200 °C in air atmosphere that favoured the oxidation of Co^{2+} oxides or a part of Co-silicates into Co^{3+}. As reported in several TPO analyses of Co-based catalysts findable in the literature [94,95], depending of some factors such as the particles size, the synthesis procedure used, the metal/promoter loadings and the type of support, Co^{2+} can have different oxidation temperatures in the range T= 180-230 °C in fully accordance with the experimental results presented.

6.2.5.3 $Fe_{10}US$, $Fe_{30}US$, $Fe_{30}K_2Cu_{3.75}US$

The TPR profiles of $Fe_{10}US$, $Fe_{30}US$ and $Fe_{30}K_2Cu_{3.75}US$ are here reported in Figure 6.38-6.40. Moreover the TPRs of the catalysts with the same metal loadings and supported on SiO_2 but synthesized with traditional impregnation (IMP) are reported as well in Figure 6.41- 6.43 in order to compare the two different synthetic ways.

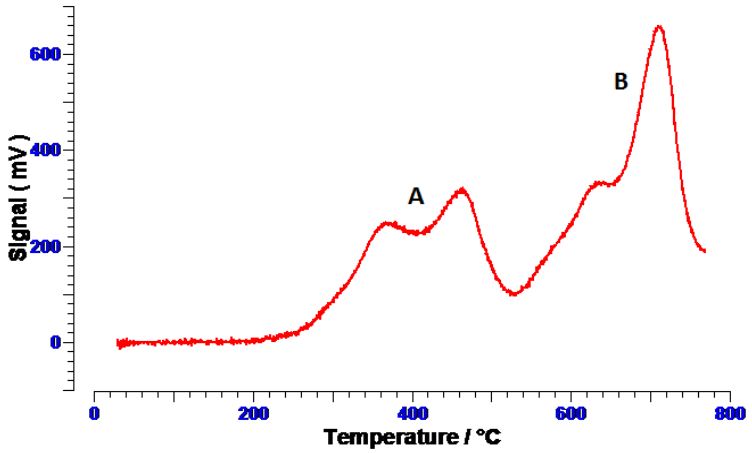

Figure 6.38: TPR profile of $Fe_{10}US$.

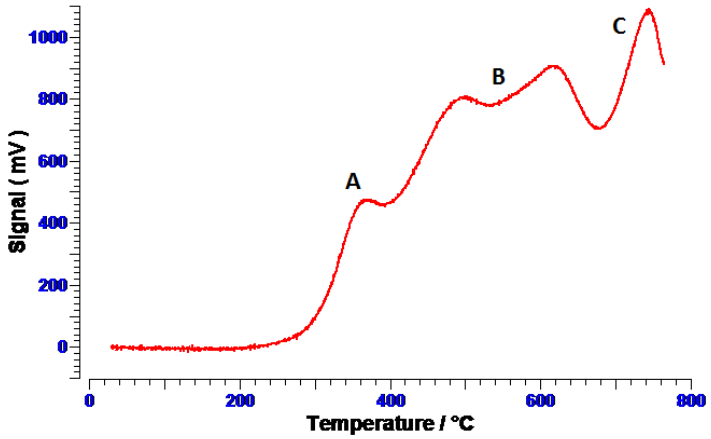

Figure 6.39: TPR profile of $Fe_{30}US$.

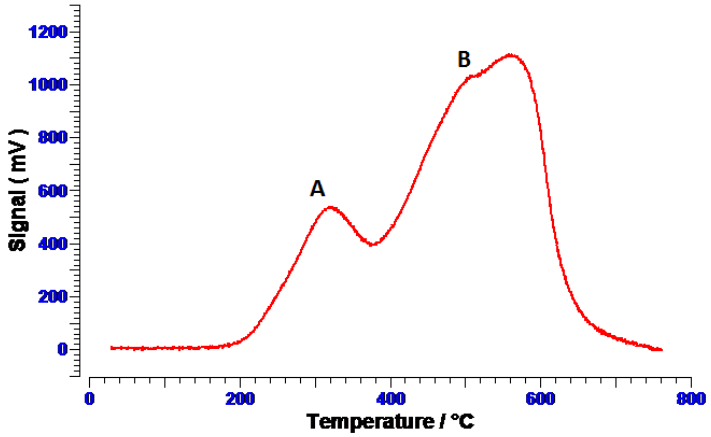

Figure 6.40: TPR profile of $Fe_{30}K_2Cu_{3.75}US$.

Catalyst	Peak	Reduction T (°C)
$Fe_{10}US$	A	350
	B	700
$Fe_{30}US$	A	350
	B	590
	C	760
$Fe_{30}K_2Cu_{3.75}US$	A	340
	B	580

Table 6.11: TPR data of $Fe_{10}US$, $Fe_{30}US$ and $Fe_{30}K_2Cu_{3.75}US$.

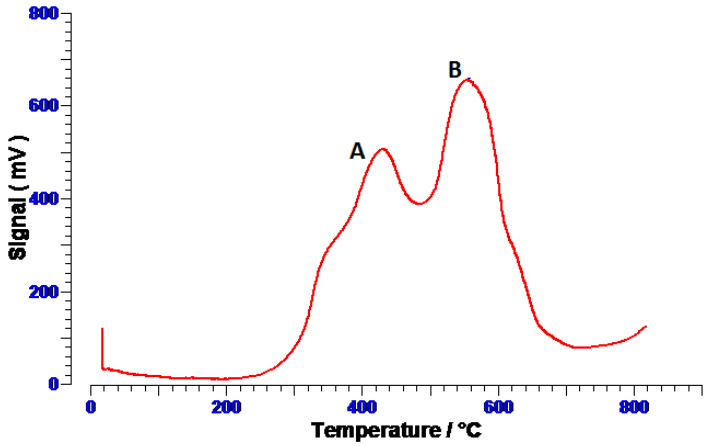

Figure 6.41: TPR profile of $Fe_{10}IMP$.

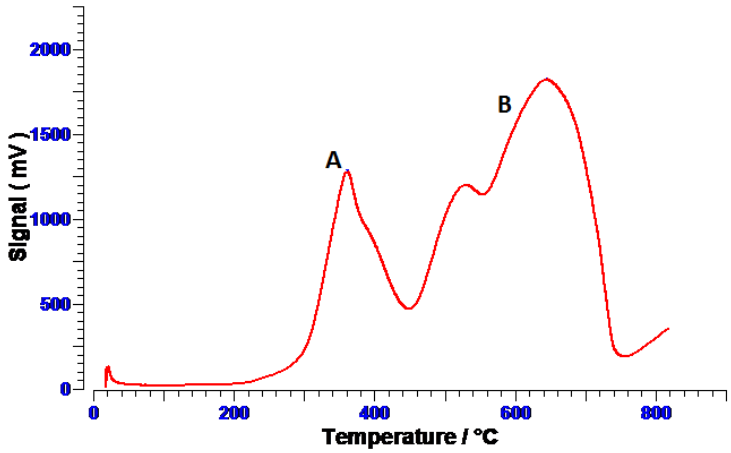

Figure 6.42: TPR profile of $Fe_{30}IMP$.

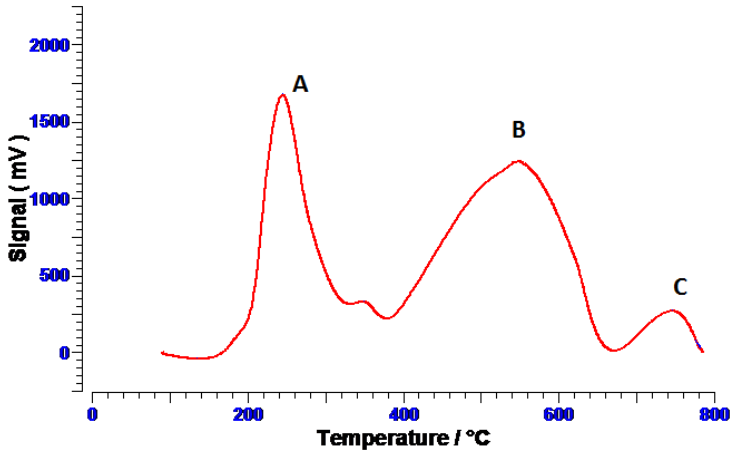

Figure 6.43: TPR profile of $Fe_{30}K_2Cu_{3.75}IMP$.

Catalyst	Peak	Reduction T (°C)
Fe_{10}IMP	A	400
	B	550
Fe_{10}IMP	A	370
	B	600
$Fe_{30}K_2Cu_{3.75}$IMP	A	220
	B	510
	C	750

Table 6.12: TPR data of Fe_{10}IMP, Fe_{30}IMP and $Fe_{30}K_2Cu_{3.75}$IMP.

The TPRs of Fe_{10}US and Fe_{30}US showed that both samples have the same reduction temperature associated to the first reduction step (A) which is equal to T= 350 °C. The insertion of the promoters decrease the hematite to magnetite transition temperature of about ≈ 10 °C. The US sample with 10 %wt of Fe has both peaks that are divided in two different parts suggesting that different species of Fe_2O_3 and Fe_3O_4 are present on the catalyst. The sample Fe_{30}US presents three different peaks, the most probable option is that what is defined as peak (B) is a fusion between a peak related to reduction of hematite which is strongly bounded with the support that is located at higher temperature than (A) and the peak due to the reduction of magnetite to metallic iron [51].

The ultrasonic synthesis proved to be a suitable preparation method to synthesizes Fe-based nanostructured supported catalysts that have lower reduction temperature with respect to traditional impregnated catalysts. In fact, Fe_{10}US and Fe_{30}Us have lower reduction temperatures related to the first step if compared with Fe_{10}IMP and Fe_{30}IMP samples. The increase in the temperature which is needed to reduce the hematite present on the catalyst can be due to the calcination step involved in the preparation of the impregnated sample; the high temperature (T= 500 °C) can oxidize part of the Fe present on the catalysts while forming Fe_2O_3 particles which have strong bound with the bare support. Only $Fe_{30}K_2Cu_{3.75}$IMP has lower reduction temperature if compared with the US synthesized catalyst. A possible reason is that in the K-Cu promoted catalyst synthesized by impregnation, copper and potassium are added in the same step, thus a better contact between iron oxides and Cu oxide particles on the SiO_2 surface can be achieved.

7 Catalytic results

The experimental results obtained with the catalysts in the FT rig are presented in this chapter. The catalytic activity is evaluated in term of CO conversion (%) or by calculating the rate of CO conversion which is expressed as $molCO_{CONV.} \cdot h^{-1} \cdot g_{CAT}^{-1}$. The catalysts selectivity are reported as molar percentage values toward CH_4 and CO_2 (byproducts of the FT reaction), light hydrocarbons (<C7, hydrocarbons with the number of carbon atoms between 2 and 6) and heavy hydrocarbons (>C7, hydrocarbons with 7 or more carbon atoms). The catalysts selectivity can be also evaluated with productivity values which are expressed as mol"i"$\cdot h^{-1} \cdot g_{CAT}^{-1}$, where "i" is CO_2, CH_4, <C7 or >C7. Moreover the total yield to C_{2+} is calculated without considering CO_2 and CH_4.

The rate of carbon monoxide conversion and the molar productivities are calculated as follows in Eqs. 7.1- 7.2:

$$molCO_{CONV.} \cdot h^{-1} \cdot g_{CAT}^{-1} = CO_{conversion} \cdot \frac{FCO_{IN} \cdot 60}{1000 \cdot 22.414} \quad \text{(Eq. 7.1)}$$

$$mol"i" \cdot h^{-1} \cdot g_{CAT}^{-1} = CO_{conversion} \cdot S"i" \quad \text{(Eq. 7.2)}$$

Where:

- $CO_{conv.}$: is the conversion (%) of carbon monoxide given by the catalyst;

- FCO_{IN}: is the inlet flow of CO;

- 1000: is the conversion factor from mL to L;

- 60: is the conversion factor from minutes to hours;

- 22.414: is the molar volume;

-S"i": is the selectivity value toward the generic compound "i".

When the results regarding the composition of the heavy organic phase measured with GC are reported, the molar fraction are usually divided into three different groups, for example $C_{7\text{-}9}$, $C_{10\text{-}15}$, $C_{16\text{-}30}$.

The experimental results of the three catalysts sets are presented in the following paragraphs.

7.1 $Fe_{30}K_2Cu_{3.75}$

The experimental tests carried out with the sample $Fe_{30}K_2Cu_{3.75}$ allowed the evaluation of the catalyst performances as a function of the experimental condition used, with a particular attention to the effect of the H_2/CO ratio fed. Moreover the catalyst stability versus the TOS using different experimental conditions is discussed.

A series of tests have been carried out to measure and discuss the species and the amount of light hydrocarbons dissolved in the heavy organic liquid fraction at different reaction temperatures and H_2/CO ratios.

Using all the collected data a regression of the kinetic parameters and the development of a suitable kinetic model have been carried out in collaboration with Ing. Flavio Manenti and Ing. Marco Gamilberti (Politecnico of Milan). The modeling work will be fully discussed in the next chapter of this thesis.

The sample $Fe_{30}K_2Cu_{3.75}$ has been activated and tested using the following conditions:

ACTIVATION STEP:

- reducing temperature: T= 350 °C;

- reducing gas: H_2/CO= 2/1, 46.8 NmL·min^{-1};

- reducing pressure: P= 4 bar;

- total activation time: t= 4 h;

CATALYTIC RUN:

- reaction temperature: T= 230- 260 °C;

- Syngas flow: 46.8 NmL·min^{-1} with H_2/CO= 2/1, 1.5/1, 1/1 and 5.02 NmL·min^{-1} of nitrogen;

- operative pressure: P= 20 bar

- total catalytic run time: TOS= 80 h

The experimental results obtained with $Fe_{30}K_2Cu_{3.75}$ at different H_2/CO ratios and different reaction temperatures are summarized in Table 7.1.

H_2/CO	T(°C)	$molCO_{CONV.} \cdot h^{-1} \cdot g_{CAT}^{-1}$	C_{2+} yield	$mol"i" \cdot h^{-1} \cdot g_{CAT}^{-1}$			
				CH_4	CO_2	<C7	>C7
2/1	220	0.0035	6.9	0.00028	0.00039	0.00078	0.00209
	235	0.0088	17.5	0.00053	0.00097	0.00176	0.00555
	250	0.021	39.3	0.00104	0.00333	0.00395	0.01248
	260	0.024	42.5	0.00142	0.0045	0.00474	0.01302
1.5/1	250	0.019	29.9	0.00097	0.0035	0.0033	0.01165
	260	0.023	33.8	0.00116	0.0051	0.00394	0.01298
1/1	250	0.014	18.2	0.00058	0.00246	0.00231	0.0091
	260	0.024	27.2	0.00098	0.00635	0.00391	0.0132

Table 7.1: Experimental results of $Fe_{30}K_2Cu_{3.75}$.

The rate of CO conversion increases with an increase in the reaction temperature and in the H_2/CO ratio fed to the reactor. The better catalytic results obtained with H_2/CO= 2 are due to the fact that an hydrogen/carbon monoxide ratio equal to 2 is the stoichiometry one required by the FT reaction.

The productivity of the reaction products is highly influenced by the reaction temperature. In particular, at a constant ratio of H_2/CO fed to the FT reactor, the productivity of CH_4 and CO_2 increased from 0.00028 $molCH_4 \cdot h^{-1} \cdot g_{CAT}^{-1}$ and 0.00039 $molCO_2 \cdot h^{-1} \cdot g_{CAT}^{-1}$ to 0.00142 $molCH_4 \cdot h^{-1} \cdot g_{CAT}^{-1}$ and 0.0045 $molCO_2 \cdot h^{-1} \cdot g_{CAT}^{-1}$ respectively. On the other hand the productivity is not strongly influenced by the syngas ratio fed. Productivity of CO_2, light and heavy hydrocarbons remains almost unchanged by raising the H_2/CO ratio from 1 to 2 while the CH_4 productivity falls from 0.00104 $molCH_4 \cdot h^{-1} \cdot g_{CAT}^{-1}$ at T= 250 °C and H_2/CO= 2 to 0.00058 $molCH_4 \cdot h^{-1} \cdot g_{CAT}^{-1}$ at T= 250 °C and H_2/CO= 1; this result is justified by the fact that a greater presence of H_2 in the reactant mixture means a bigger number of H_2 that will be dissociated on the catalyst surface leading to an increase in the number of termination mechanism that will increase the formation of short chain hydrocarbons, like methane.

In the following Figure 7.1- 7.4 the CO conversion rate and the products productivity as a function of TOS are presented.

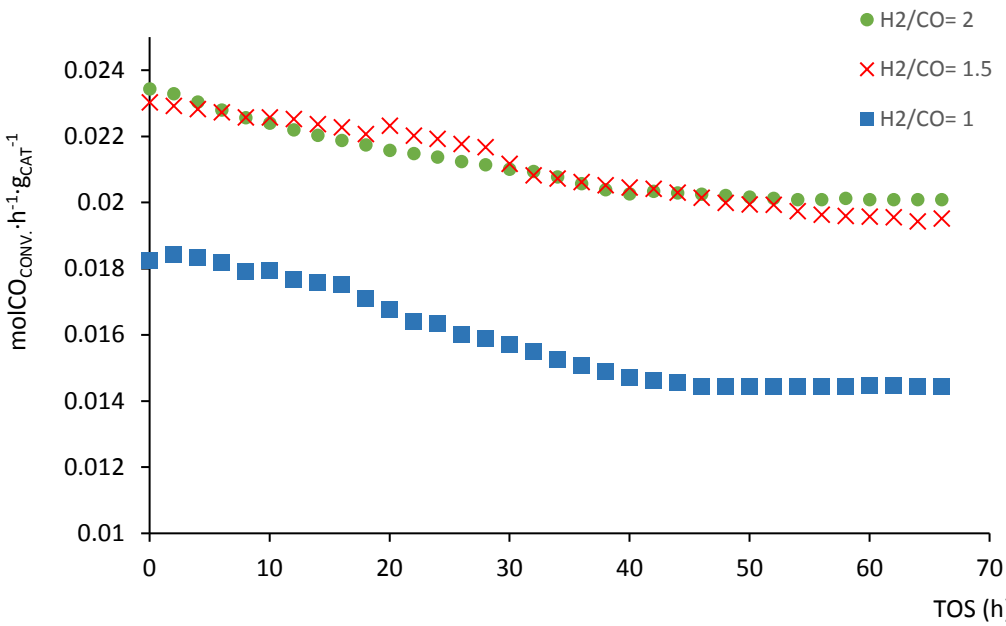

Figure 7.1: CO conversion rate of $Fe_{30}K_2Cu_{3.75}$ at T= 250 °C and different H_2/CO ratios as a function of TOS.

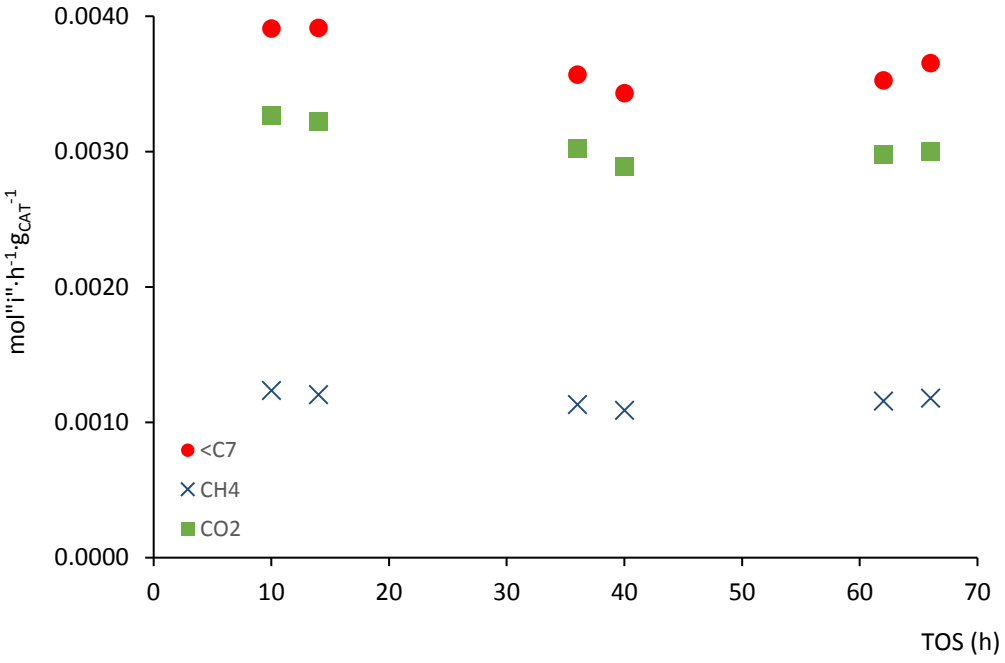

Figure 7.2: Molar productivities of <C7, CH_4 and CO_2 given by $Fe_{30}K_2Cu_{3.75}$ at T= 250 °C and H_2/CO= 2 as a function of TOS.

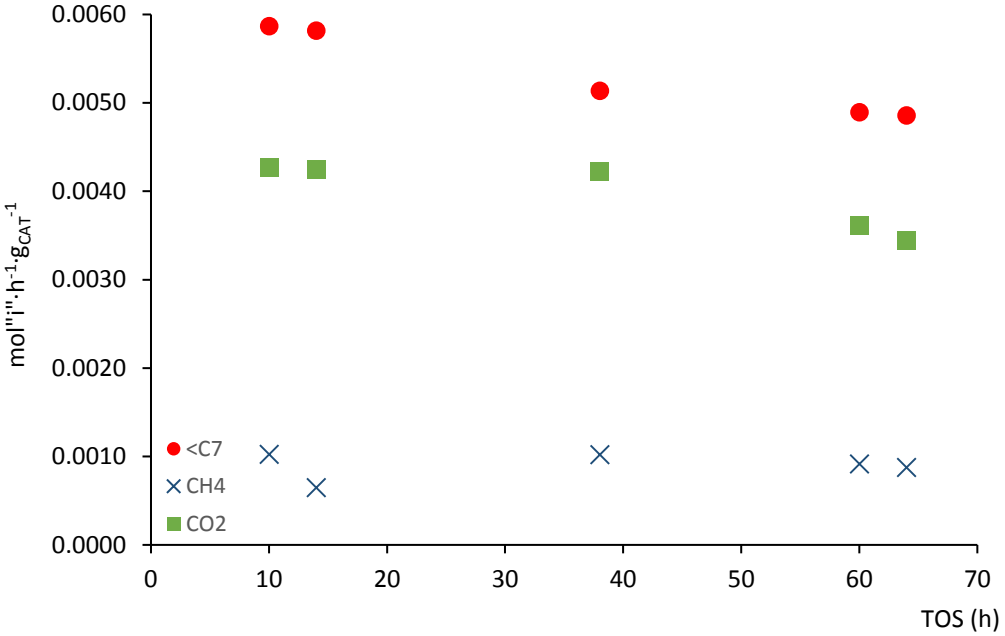

Figure 7.3: Molar productivities of <C7, CH_4 and CO_2 given by $Fe_{30}K_2Cu_{3.75}$ at T= 250 °C and H_2/CO= 1.5 as a function of TOS.

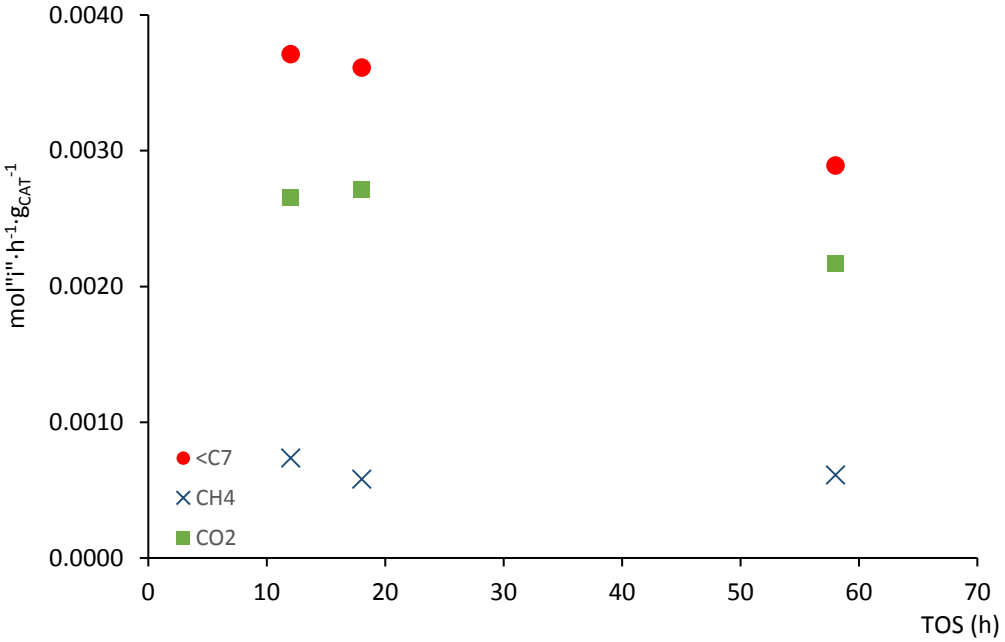

Figure 7.4: Molar productivities of <C7, CH_4 and CO_2 given by $Fe_{30}K_2Cu_{3.75}$ at T= 250 °C and H_2/CO= 1 as a function of TOS.

The CO conversion rate is not stable from the start of the FT kinetic test and it needs almost 40 h to reach the steady state value for all the three H_2/CO ratio tested. Once a constant value of $molCO_{CONV.} \cdot h^{-1} \cdot g_{CAT}^{-1}$ was reached it was constant for the remain duration of the test suggesting a good catalyst stability. The small decrease of the converted CO moles per hour, which is in the order of 0.004 $molCO_{CONV.} \cdot h^{-1} \cdot g_{CAT}^{-1}$ can be due to the formation of elementary carbon and/or waxes on the catalyst surface [42,96]. Differently, the molar productivities of CO_2, CH_4 and light hydrocarbons, are stable from the start of the experimental test and only small variations have been recorded.

In order to compare the catalyst performances under different reaction conditions, the total yield to C_{2+} of all the experimental test performed are reported in Figure 7.5.

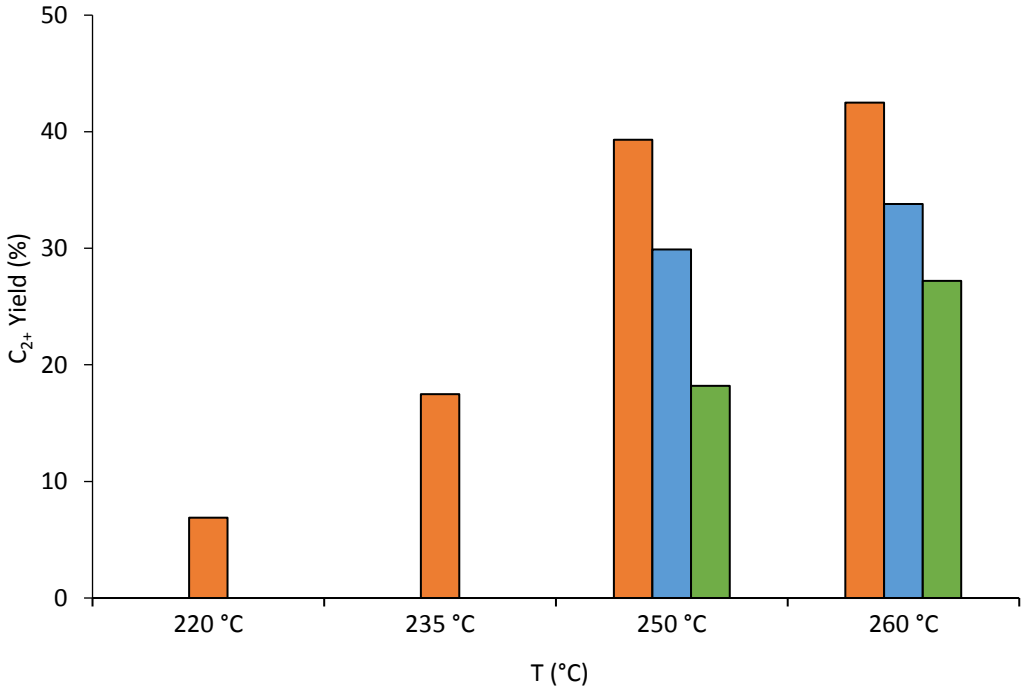

Figure 7.5: Total yield to C_{2+} of $Fe_{30}K_2Cu_{3.75}$ at different temperatures and H_2/CO ratios. Orange: H_2/CO= 2; blue: H_2/CO= 1.5; green: H_2/CO= 1.

As shown in Figure 7.5 the C_{2+} yield is highly influenced by the temperature and the H_2/CO ratio fed to the reactor. In particular, the yield to hydrocarbons increases with an increase in the reaction temperature and it presents higher values with hydrogen rich syngas due to the increase in the CO conversion since H_2/CO= 2 is the stoichiometry value required. Nevertheless, even if the yield to C_{2+} is lower with H_2/CO< 2, it still presents good and acceptable values to make $Fe_{30}K_2Cu_{3.75}$ a good

candidate as catalyst for FT reaction even in BTL-FT plant were poor hydrogen syngas are converted in the FT unit.

The results regarding the molar composition of the heavy organic phase are reported in Figure 7.6, the molar fractions have been grouped into three different groups: $C_{7\text{-}10}$, $C_{11\text{-}20}$ and $C_{21\text{-}30}$.

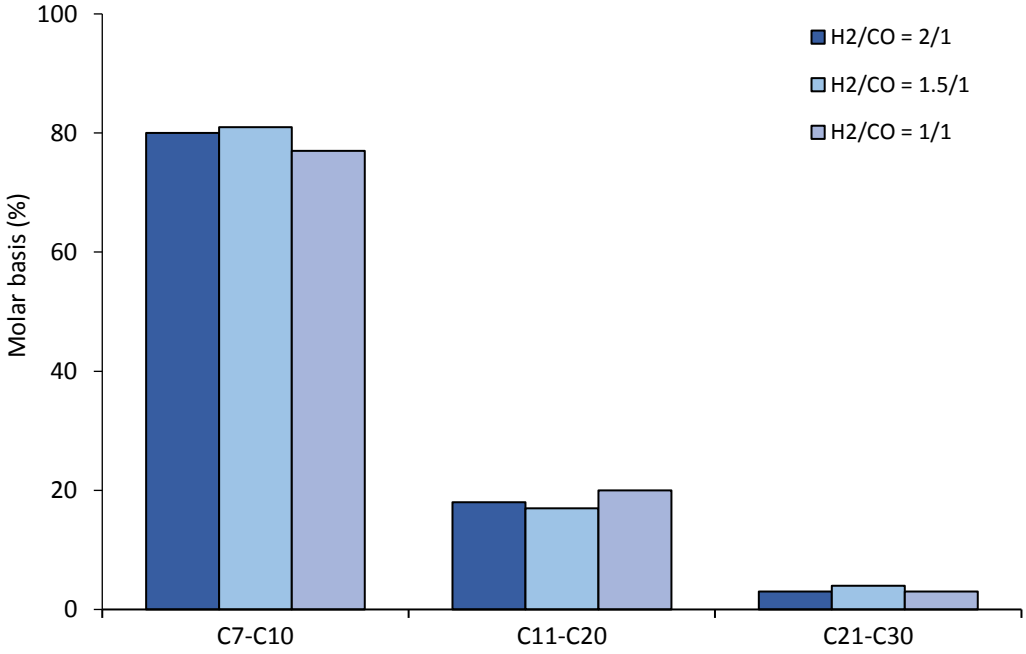

Figure 7.6: Molar composition of the heavy organic phase at different H_2/CO ratios and T= 250 °C.

The composition of the >C7 fraction is not strongly influenced by the inlet H_2/CO syngas ratio; a little increase of the $C_{11\text{-}20}$ fraction was recorded in the run performed at T= 250 °C and with a H_2/CO ratio equal to 1, due to the increase of the probability of chain growth which leads to the production of longer chain hydrocarbons. As already explained the presence of a lower amount of H_2 in the mixture (or bigger amount of CO) favors the production of heavy hydrocarbons since less termination reactions are present.

In the following Figure 7.7. The ASF diagrams obtained at different reaction conditions are reported.

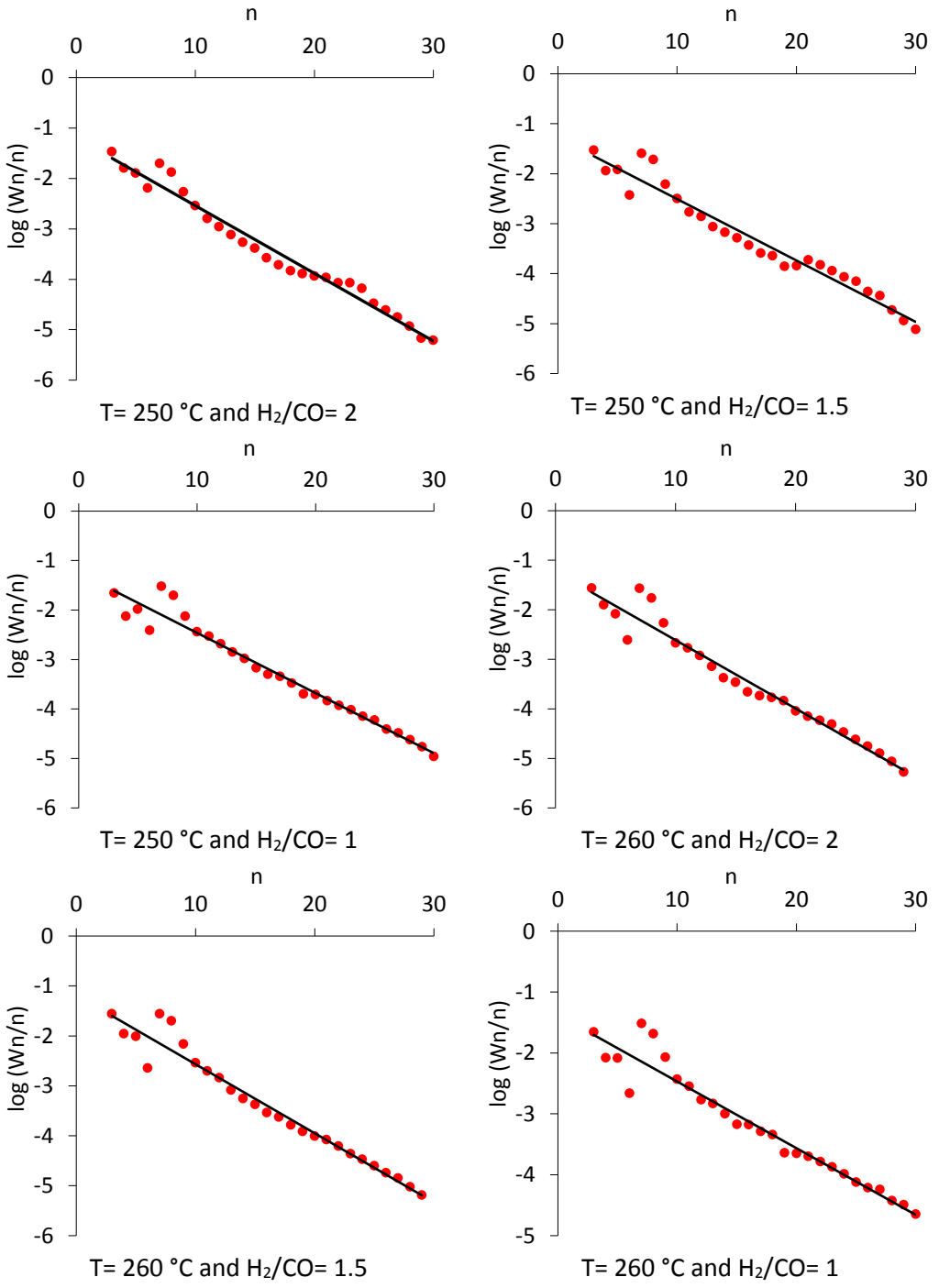

Figure 7.7: ASF diagrams of $Fe_{30}K_2Cu_{3.75}$ tested under different reaction temperatures and H_2/CO ratios.

With the reported ASF diagrams in Figure 7.7 is then possible to calculate the probability of chain growth for each run. The experimentally calculated α are reported in Table 7.2.

H_2/CO	α_{C1-C30} T=250°C	α_{C1-C30} T=260°C
2/1	0.74	0.73
1.5/1	0.76	0.73
1/1	0.76	0.74

Table 7.2: α values for the sample $Fe_{30}K_2Cu_{3,75}$ at T= 250- 260 °C.

The probability of chain growth is slightly influenced by the reaction temperature and the H_2/CO ratio fed to the reactor; the highest probability of chain growth values (α_{C1-C30}= 0.76) are the ones reached by the catalyst when tested at T= 250 °C and H_2/CO= 1.5- 1. This result is in fully agreement with other works present in the literature. Alpha is increased with low reaction temperature since high temperatures decrease the formation rate of long chain hydrocarbons.

For what concerns the study regarding the affinity of the light phase components for the heavy organic phase, the ratio of the molar composition of the single component desorbed from the heavy fraction, respect to the molar composition of the same component in the light fraction calculated at different T and H_2/CO ratios are reported in Figure 7.8- 7.9.

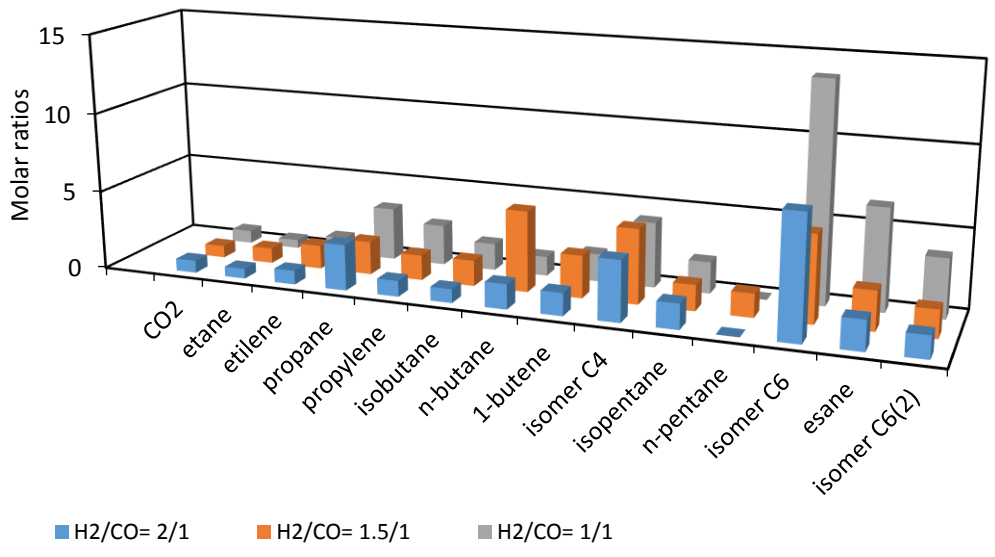

Figure 7.8: Molar ratios between the light products desorbed and the outlet light phase at T= 250 °C.

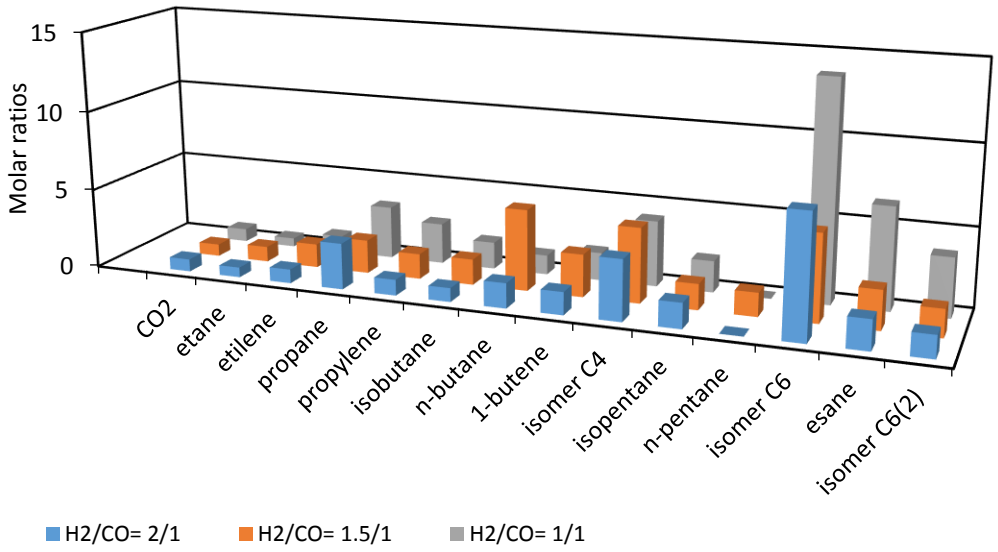

Figure 7.9: Molar ratios between the light products desorbed and the outlet light phase at T= 260 °C.

From the experimental results is evident that, as a general trend, higher is the number of carbon atoms in the molecule, higher is the ratio of the components. In particular, by increasing the reaction temperature this increase is more observable for runs performed with low H_2/CO ratio. These results confirm that since the heavy organic liquid phase is mainly composed by linear hydrocarbons, the light products with longer chain will have a greater solubility due to a better affinity and a lower volatility.

7.2 5Co, 10Co and 10Co-0.4Ru

The experimental work carried out with the catalysts synthesized by flame spray pyrolysis allowed the evaluation of the benefits of the FSP synthetic route with respect to the other Co-based traditionally synthesized catalysts. The catalytic tests allowed the estimation of the catalytic activity in terms of conversion of the reactant mixture and the productivities toward the reaction products. The experimental runs have been useful also for investigate the effect of Ru on the catalytic results. Moreover, a study regarding the stability of the sample 10Co over prolonged TOS has been carried out.

Even in this case the regression of the kinetic parameters and the development of a suitable kinetic model that can be used to simulate the catalysts performances in an

industrial FT reactor, have been carried out in collaboration with Ing. Flavio Manenti, Ing. Luca Vanalli and Ing. Marco Del Maso (Politecnico of Milan).

The samples 5Co, 10Co and 10Co-0.4Ru have been activated and tested using the following conditions:

ACTIVATION STEP:

- reducing temperature: T= 400 °C;

- reducing gas: H_2= 90 NmL·min^{-1};

- reducing pressure: P= 8 bar;

- total activation time: t= 4 h;

CATALYTIC RUN:

- reaction temperature: T= 220- 275 °C;

- Syngas flow: 46.8 NmL·min^{-1} with H_2/CO= 2/1 and 5.02 NmL·min^{-1} of nitrogen;

- operative pressure: P= 20 bar;

- total catalytic run time: TOS= 80 h, TOS= 200 h for the stability test made with 10Co.

The experimental results of the FSP catalysts obtained at different temperatures are reported in Table 7.3 and Figure 7.9- 7.10.

Sample	T (°C)	mol$CO_{CONV.}$·h^{-1}·g_{CAT}^{-1}	C_{2+} yield	mol"i"·h^{-1}·g_{CAT}^{-1}			
				CH_4	CO_2	<C7	>C7
10Co	245	0.00977	20.3	0.00117	0.00010	0.00098	0.00753
	250	0.03053	65.1	0.00306	0.00031	0.00397	0.02322
	255	0.03508	73.1	0.00386	0.00070	0.00456	0.02598
	260	0.04126	82	0.00454	0.00248	0.00413	0.03015
	275	0.04172	80,9	0.00501	0.00292	0.00334	0.03048
10Co-0.4Ru	220	0.01562	35,2	0.00094	0.00000	0.00234	0.01235
	225	0.02330	50,2	0.00210	0.00023	0.00420	0.01679
	230	0.03057	65,1	0.00275	0.00061	0.00520	0.02203
	245	0.03946	77,5	0.00474	0.00237	0.00553	0.02686

Table 7.3: Experimental results of FSP samples.

The experimental tests performed with these catalysts allowed the evaluation of the catalytic activity in function of the loadings of the active metal and the promoter. The results of 5Co are not reported in Table 7.3 because this sample did not show any catalytic activity toward the FT reaction and the carbon monoxide conversion was nix for the whole duration of all the runs performed at different temperatures. The TPR

of this sample can justify this inactivity, since in the catalyst there were a total lack of reducible species and the only Co-oxides presents were probably Co-silicates, due to the low loading of active metal which leads to the formation of only hard reducible species.

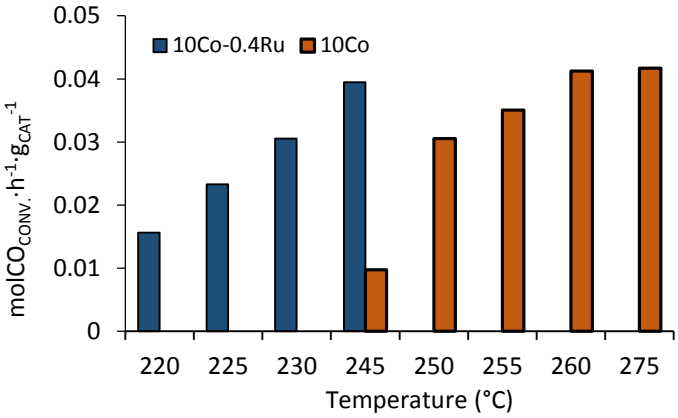

Figure7.9: Rate of CO conversion of 10Co and 10Co-0.4Ru at different temperatures.

However, for what concerns the catalytic results of 10Co and 10Co-0.4Ru, the CO conversion rate is influenced by the temperature, in particular it increases with an increase in the reaction temperature for both samples. On the other hand, the reaction temperature does not have a deep impact on products productivity expect for the >C7 production for both catalyst that increases of four times for 10Co and two times for the bimetallic catalyst with an increase in the reaction temperature of about 25 °C.

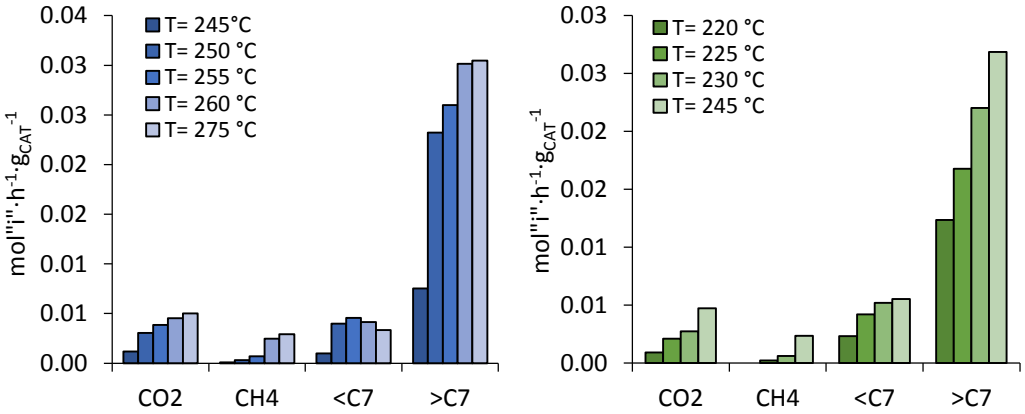

Figure7.10: Productivity of 10Co (left) and 10Co-0.4Ru (right) at different temperatures.

The addition of the promoter (0.4 %wt of Ru) highly influences the catalyst performances, the reactants conversion rate increases of about four times at the

same reaction temperature, in fact at T= 245 °C the rate of CO conversion is 0.0097 $molCO_{CONV.}\cdot h^{-1}\cdot g_{CAT}^{-1}$ for 10Co while it is equal to 0.03946 $molCO_{CONV.}\cdot h^{-1}\cdot g_{CAT}^{-1}$ for 10Co-0.4Ru. This achieved result if due to the greater reducibility of the Ru-doped catalyst.

Moreover, the promoted catalyst showed a greater C_{2+} yield with respect to 10CO sample, and lower productivity of FT byproducts (CO_2 and CH_4). Anyway, the monometallic sample did show satisfactory results and higher heavy products productivity.

The results concerning the stability test over long TOS performed with the sample 10Co at T= 250 °C are reported in Figure 7.11- 7.12.

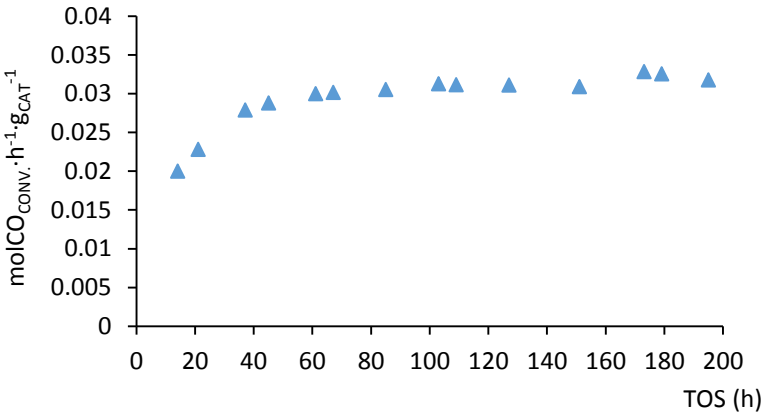

Figure 7.11: CO conversion rate with 10Co at T= 250 °C.

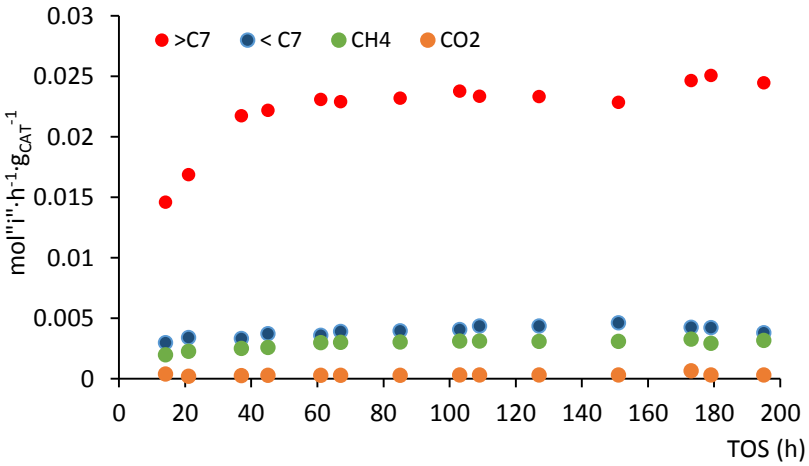

Figure 7.12: Products productivity with 10Co at T= 250 °C.

Figure 7.11- 7.12 highlight that the sample 10Co has a great stability over prolonged TOS both from CO conversion and products production rates point of views.

The carbon monoxide conversion and the productivity of >C7, <C7, CO_2 and CH_4 required almost 40 h from the start of the kinetic test in order to reach constant values. As findable in the literature, this behavior is normal for FT Co-based catalyst [97].

Figure 7.11- 7.12 suggest that FSP is a suitable technique in order to produce catalysts which are very stable even if they are treated with high temperatures for long time. This feature encourages the develop of FSP catalysts and their use into industrial heterogeneous catalytic process. If compared with several literature works, it is easily findable that traditional Co-based catalysts do not have this particular benefits. The performances over prolonged times are influenced by some factors, such as the synthetic method and the morphological properties, but in particular in the case of FT catalysts, the formation of elementary carbon via Boudouard reaction plays a key role in the determination of their durability in fact, that carbon negatively influences the lifetime of the sample [98]. This suggests that FSP synthesized 10Co and 10Co-0.4Ru present a very low activity toward the Boudouard equilibrium. The ASF diagram of 10Co and 10Co-0.4Ru are presented in Figure 7.13- 7.14.

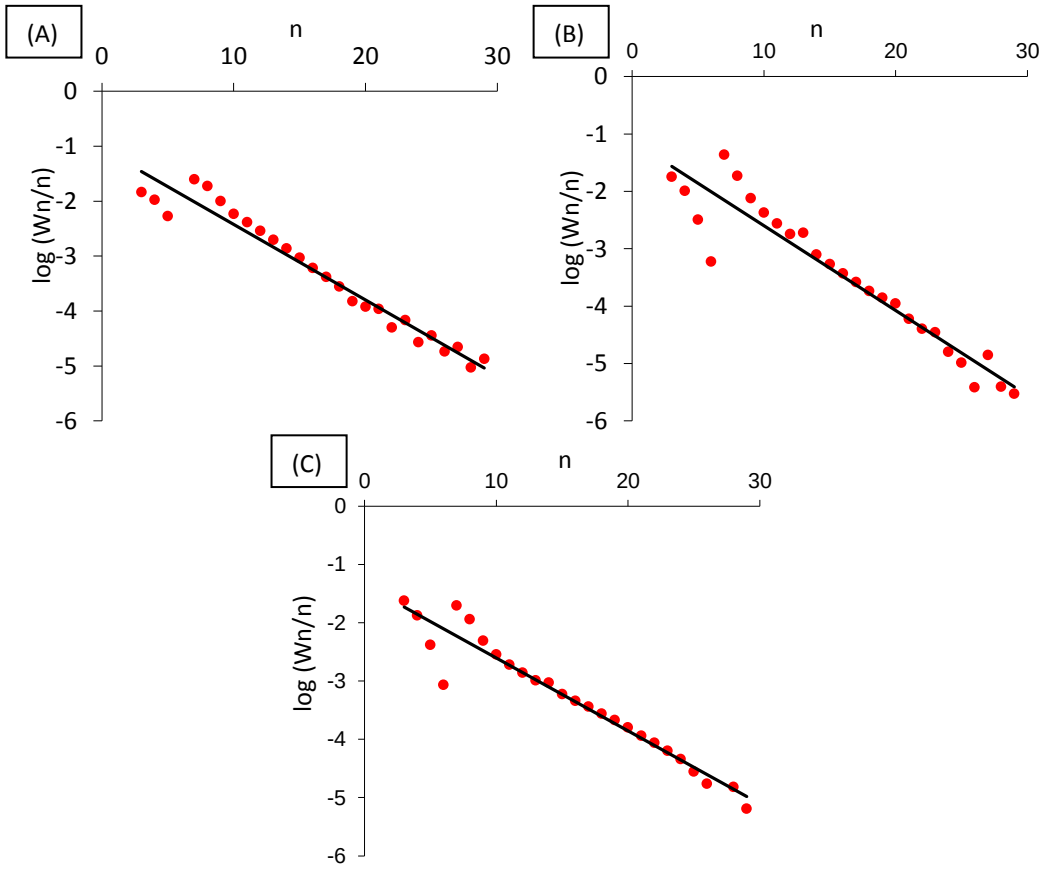

Figure 7.13: ASF diagrams of 10Co at T= 240 °C (A); T= 260 °C (B); T= 275 °C (C).

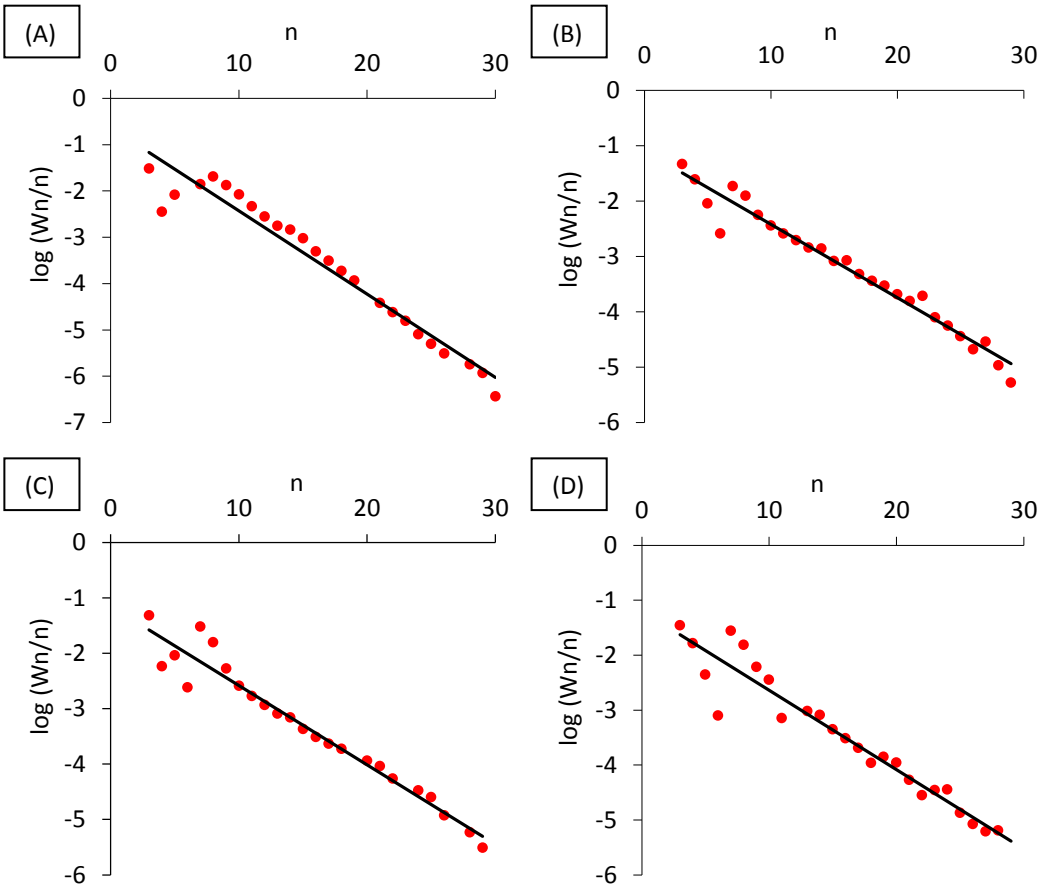

Figure 7.14: ASF diagrams of 10Co-0.4Ru at T= 220 °C (A); T= 225 °C (B); T= 230 °C (C); T= 245 °C (D).

The calculated probability of chain growth from the ASF diagrams are summarized in Table 7.4.

Sample	T (°C)	α_{C1-C30}
10Co	240	0.73
	260	0.72
	275	0.75
10Co-0.4Ru	220	0.66
	225	0.73
	230	0.72
	245	0.72

Table 7.4: α values for the samples 10Co and 10Co-0.4Ru at different temperatures.

The probability of chain growth follows the same trend of the heavy products productivity, in fact it increases by increasing the reaction temperature. This effect is

more visible with 10Co. Moreover the monometallic sample presents higher α with respect to the Ru-doped catalyst thanks to its great heavy product productivity.

The general trend confirmed for all the FT catalysts is that the heavy products selectivity is disadvantaged at high reaction temperatures. Nevertheless even if the reaction temperature is increased, the heavy fraction productivity can still be increased due to the increase in the CO conversion which is favored by higher reaction temperatures.

A detailed comparison among FSP samples and other FT catalysts is difficult due to the differences involved in the preparation methods, and then the intrinsic differences such as, morphological and structural ones (samples reducibility, the dispersion of the active metal, pores volumes and pore diameters, surface area, and the dimensions of the metal particles). Even though a deep comparison is hard do to, some catalytic results found in the recent literature concerning 10 %wt FT supported Co-based catalysts, and the experimental results reached with 10Co are reported in Table 7.5.

Catalyst	BET S.A. ($m^2 \cdot g^{-1}$)	dCo (nm)	T (°C)	$molCO_{CONV.} \cdot h^{-1} \cdot g_{CAT}^{-1}$	Selectivity (%)			
					CH_4	CO_2	<C7	>C7
10Co	159	20	250	0.0305	12	10	10	77
[78]	178	4- 40	230	0.1224	19.6	1	16	64
[97]			200	0.0015	9.6	0	22.8	67.5
[99]	60	10- 20	220	0.0031	80	0	9	11
[100]		5- 6	220	0.024	6.3	0	8.7	85
[101]	235	26.9	200	0.013	7	1	9	83
[102]			220	0.018	21.6	1.5	30.7	47.7

Table 7.5: Comparison among 10Co and other 10 %wt supported Co-based catalysts.

The dimension of the active metal on the support and the surface area properties are two parameters that are completely determined by the synthetic way adopted for the catalyst production. The BET result and the particles dimensions of 10Co are in fully agreement with the other 10 %wt FSP Al_2O_3 supported Co-based catalysts synthesized by Minnerman et al. [78] while the BET surface area of the catalysts prepared by Chaisku et at. [99] which is supported on ZrO_2 is much lower (60 $m^2 \cdot g^{-1}$).

Regarding the catalytic results, even if the literature is full of different examples of Co-based catalysts that depending of several parameters concerning the sample synthesis and the catalytic test (experimental conditions, type of reactor) they give

different catalytic results, the Co-based samples always follow the same trends. Qinghong et al. [39] and Gnanamani et al. [101] reported in their review that Fischer-Tropsch Cobalt catalysts are characterized by high CO conversion, low selectivity toward undesired products (CH_4 and CO_2) and high selectivity to linear hydrocarbons, especially for the heavier ones.

At the moment, except for the samples presented in this PhD research work, the only FSP 10 %wt catalyst active in the FT reaction is the one synthesized and tested by Minnerman et al. [78]

The results reported in Table 7.5 suggest that 10Co gives catalytic results that are fully comparable with the ones synthesized traditionally both from CO conversion rate and products selectivity point of view.

7.3 $Fe_{10}US$, $Fe_{30}US$ and $Fe_{30}K_2Cu_{3.75}US$

The use of irons SiO_2-supported catalysts have been deeply studied in previous works by Pirola et al. [81]. However, in this work only a primary and simple evaluation of the benefits of the ultrasonic synthesis was carried out.

The experimental work here reported concerning the Fe-based samples sonochemically synthesized allow the evaluation and the study of the catalysts performances in function of the loading of active metal and promoters. Moreover several test have been carried out using different experimental conditions (activation temperatures and reaction temperatures) in order to investigate the impact of these parameters on the CO conversion and the products productivity.

Finally, a deep comparison with the traditional impregnated catalyst is reported in order to evaluate the benefits on the US technique in the preparation of nanostructured supported heterogeneous catalysts.

The activation and catalytic tests conditions used in the experimental runs are reported hereinafter:

ACTIVATION STEP:

- reducing temperature: T= 350- 400 °C;

- reducing gas: H_2/CO= 2/1, 46.8 $NmL \cdot min^{-1}$;

- reducing pressure: P= 4 bar;

- total activation time: t= 4 h;

CATALYTIC RUN:

- reaction temperature: T= 250- 260 °C;

- Syngas flow: 46.8 NmL·min^{-1} with H_2/CO= 2/1 and 5.02 NmL·min^{-1} of nitrogen;

- operative pressure: P= 20 bar;

- total catalytic run time: TOS= 80 h.

The experimental results obtained at different reaction temperatures (Treac.) and activation temperatures (Tact.) are summarized in Table 7.6.

Sample	Tact. (°C)	Treac. (°C)	mol$CO_{CONV.}$·h^{-1}·g_{CAT}^{-1}	C_{2+} yield	mol"i"·h^{-1}·g_{CAT}^{-1}			
					CH_4	CO_2	<C7	>C7
$Fe_{10}US$	400	250	0.01403	30.2	0.00070	0.00070	0.00253	0.01010
		255	0.01708	36.4	0.00085	0.00102	0.00307	0.01213
		260	0.01850	39	0.00092	0.00129	0.00333	0.01295
	350	250	0.01282	27.6	0.00064	0.00064	0.00244	0.00910
		255	0.01545	32.9	0.00077	0.00093	0.00294	0.01082
		260	0.01720	36.3	0.00086	0.00120	0.00327	0.01187
$Fe_{30}US$	400	250	0.02606	54.3	0.00104	0.00235	0.00443	0.01824
		255	0.02685	54	0.00107	0.00322	0.00483	0.01772
		260	0.02723	54.8	0.00109	0.00327	0.00463	0.01824
	350	250	0.02009	42.8	0.00080	0.00141	0.00372	0.01416
		255	0.02088	44.0	0.00084	0.00167	0.00386	0.01451
		260	0.02063	43.0	0.00083	0.00186	0.00382	0.01413
$Fe_{30}K_2Cu_{3.75}$ US	350	250	0.02543	48.1	0.00076	0.00458	0.00356	0.01653
		255	0.02397	45.3	0.00072	0.00431	0.00336	0.01558
		260	0.02443	45.1	0.00073	0.00489	0.00342	0.01539

Table 7.6: Experimental results of $Fe_{10}US$, $Fe_{30}US$ and $Fe_{30}K_2Cu_{3.75}US$.

All the US samples have been activated at both Tact.= 350 °C and Tact.= 400 °C except the sample $Fe_{30}K_2Cu_{3.75}US$. During the run performed with $Fe_{30}K_2Cu_{3.75}US$ after an activation step performed at Tact.= 400 °C the CO conversion was nil since the start of the test. This result is justified by the fact that this sample presented a high activity to the Boudouard reaction which rapidly produces elementary carbon on the catalyst surface thus resulting in a complete deactivation of the sample. The presence of elementary carbon on the catalyst surface drammatically decreases the activity of the catalyst.

The productivity of the reaction products is not stronlgy influenced by the reaction temperature in the tested range (Treac.= 250- 260 °C) for all the samples except for $Fe_{10}US$ where all the productivities are increased with an increase in the Treac.; for example >C7 productivity growth from 0.0091 mol>C7·h^{-1}·g_{CAT}^{-1} to 0.01187 mol>C7·h^{-}

$^{1}\cdot g_{CAT}^{-1}$ at Treac.= 250 °C and Treac.= 260 °C respectively when the catalyst is activated at Tact.= 350 °C.

The activation temperature did not influence the results in terms of products productivity, in fact all the products formation rates remain steady at both activation temperatures tested.

The K-Cu promoted samples showed the greater production rate of CO_2 which is in the order of ≈ 0.0045 $molCO_2 \cdot h^{-1} \cdot g_{CAT}^{-1}$ for $Fe_{30}K_2Cu_{3.75}US$ while the highest one measured in the other runs with the other samples is 0.0033 $molCO_2 \cdot h^{-1} \cdot g_{CAT}^{-1}$ obtained with $Fe_{30}US$ at Treac.= 260 °C and Tact.= 400 °C.

The CO production rates of all the US samples at different Tact. and Treac. are shown in Figure 7.15.

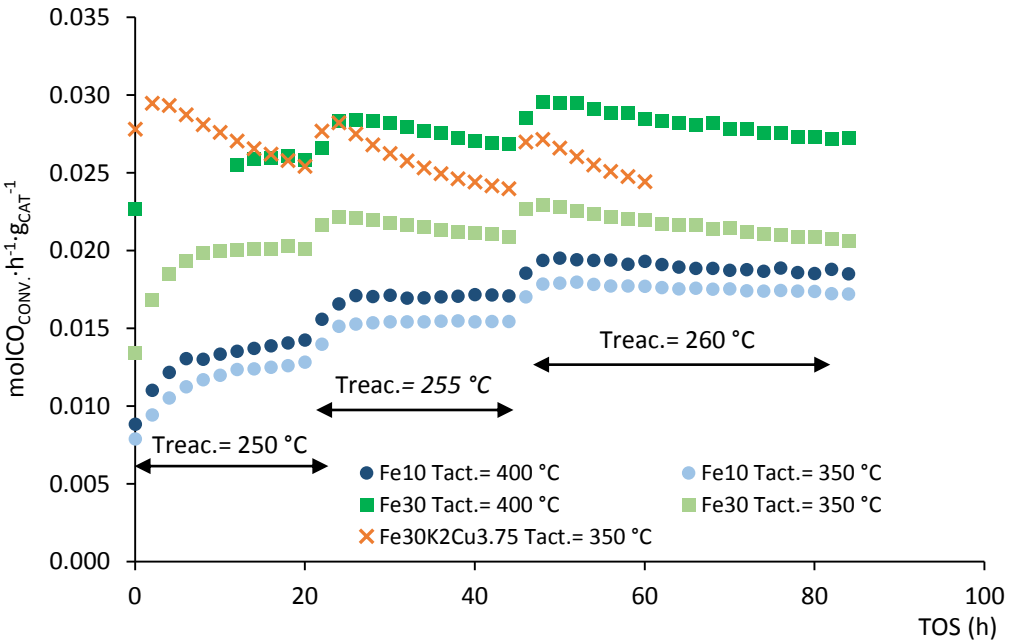

Figure 7.15: CO production rate of $Fe_{10}US$, $Fe_{30}US$ and $Fe_{30}K_2Cu_{3.75}US$ at different Tact. and Treac.

The reaction temperature increases the rate of CO conversion, in particular it slightly increases the moles of CO converted per hour for $Fe_{10}US$ sample of about ≈ 0.001 $molCO_{CONV.} \cdot h^{-1} \cdot g_{CAT}^{-1}$ by raising the activation temperature from Tact.= 350 °C to Tact.= 400 °C at in the range of reaction temperatures tested. The effect of the increase in the activation temperature on the rate of CO conversion is more visible for the sample $Fe_{30}US$ where the rate is increased of about 0.004 $molCO_{CONV.} \cdot h^{-1} \cdot g_{CAT}^{-1}$ with a

reaction temperature of Treac.= 250 °C and 0.007 $molCO_{CONV.} \cdot h^{-1} \cdot g_{CAT}^{-1}$ when the reaction tempoerature is equal to Treac.= 255- 260 °C.

Moreover, both $Fe_{10}US$ and $Fe_{30}US$ presented a good stability over TOS. The steady state CO conversion rate was reached since the first hours of the experimental tests at it remeined stable for the whole duration of the runs even when the reaction temperature was raised. This higlights that no carbonacaous residue were formed durinf the FT reaction. On the other hand $Fe_{30}K_2Cu_{3.75}US$ showed a decrease in the reactant conversion rate over small TOS even if activated at Tact.= 350 °C. This fact confirms that this sample is quite active towards the Boudouard equilibria.

In order to better understand the effect of the Tact. on the compositions of the heavy liquid organic fraction, the molar fractions have been combined into three different groups ($C_{7\text{-}9}$, $C_{10\text{-}15}$ and $C_{16\text{-}30}$). The >C7 phase composition results are shown in Figure 7.16.

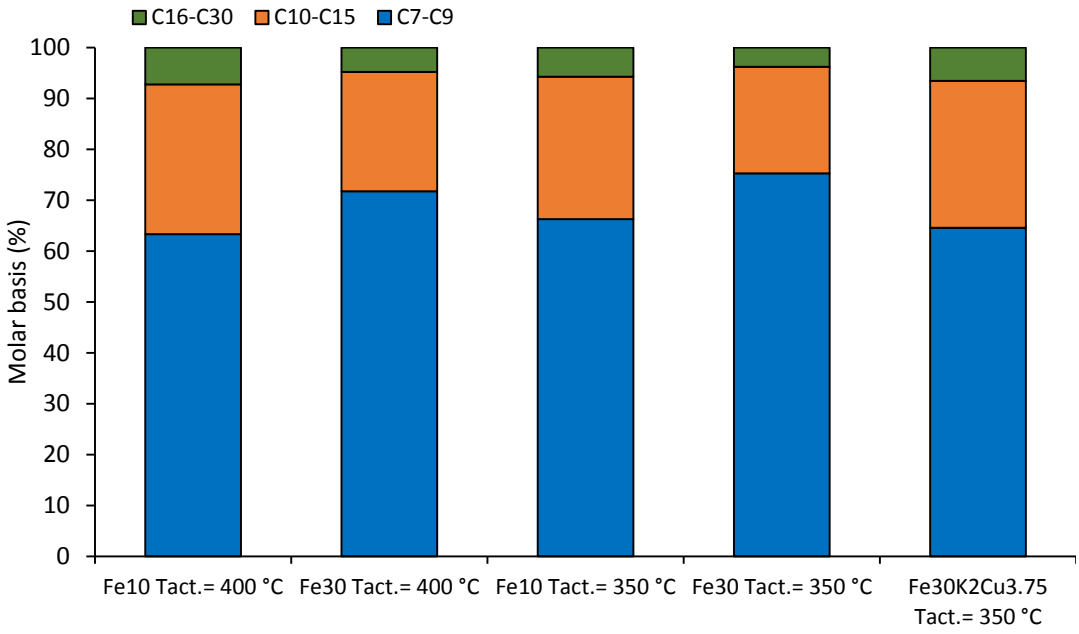

Figure 7.16: Composition of the heavy organic phase (>C7) for US samples activated at Tact.= 350- 400 °C and tested at Treac.= 255 °C.

The results of the GC analyses performed on the heavy fraction suggested that the composition of the C_7-C_{30} fraction is not strongly influenced by the temperature at which is performed the activation step. $Fe_{10}US$ activated both at Tact.= 350- 400 °C and $Fe_{30}K_2Cu_{3.75}$ presented almost the same composition of the heavy fraction while $Fe_{30}US$ showed a small increase in the $C_{7\text{-}9}$ fraction when reduced at Tact.= 350 °C.

However, the molar compositions of the heavy fraction measured with the US samples are in fully agreement with other literature works [96,103,104].

A comparison among the catalysts synthesized with US and traditional impregnation with the same amount of active metal and promoters and tested in the same experimental conditions is reported in Figure 7.17- 7.18.

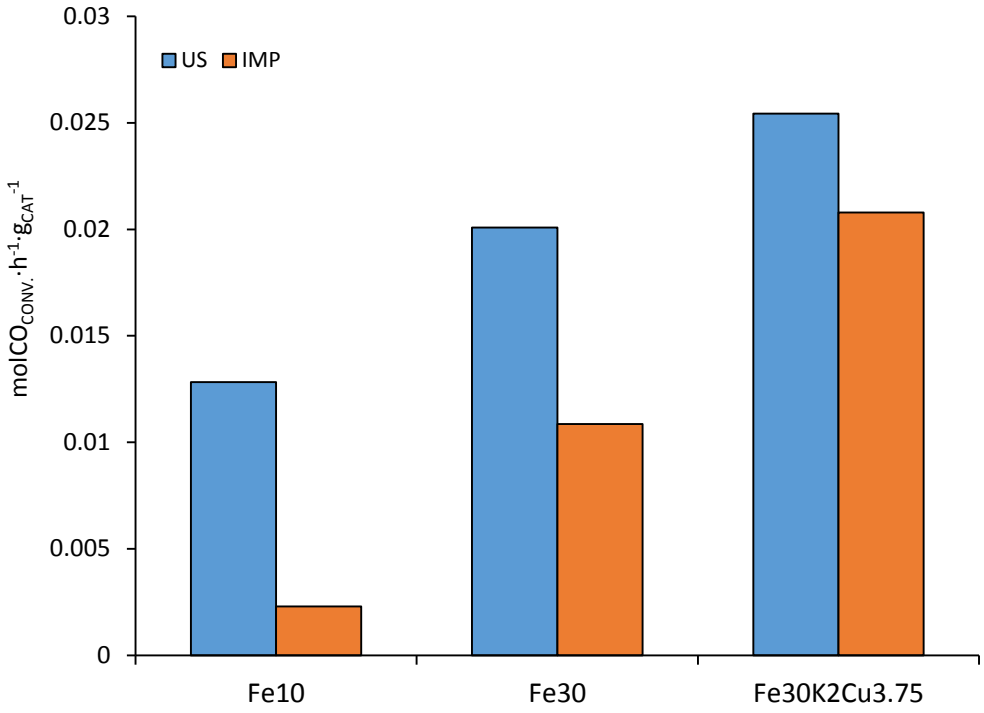

Figure 7.17: CO conversion rates of US and IMP catalysts tested at Treac.= 250 °C and reduced at Tact.= 350 °C.

The sample synthesized with the use of ultrasound proved to be more active than the same kind of samples synthesized with traditional wetness impregnation studied in previous works [81,84,88].

In particular US samples provided almost five times higher CO conversion rate in the case of Fe_{10}US while Fe_{30}US yielded a reactant conversion rate which is almost two time greater than the one achieved by Fe_{30}IMP. Moreover, even though $Fe_{30}K_2Cu_{3.75}$US is active to the Boudouard equilibria, the steady state CO conversion rate reached by the K-Cu promoted US sample is still higher than the one presented by the IMP sample.

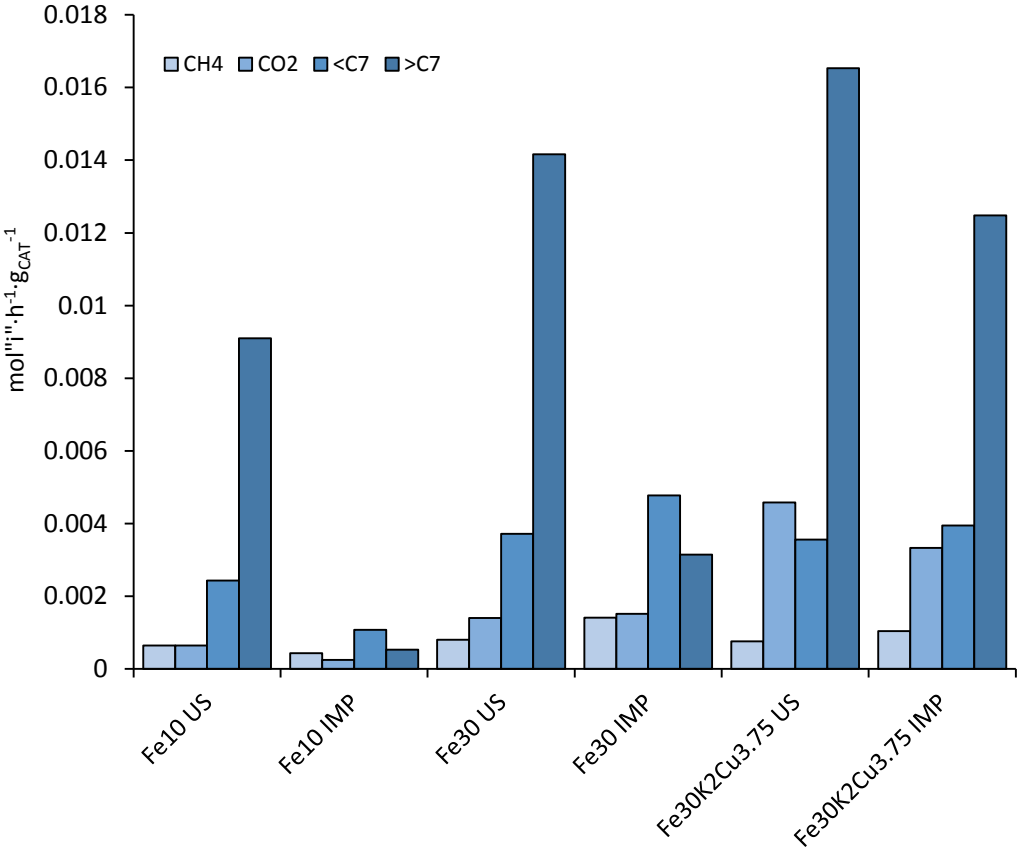

Figure 7.18: Reaction products productivity reached by US and IMP samples at Treac.= 250 °C and Tact.= 350 °C.

The US samples present almost the same productivity values for what concern FT undesired products CO_2 and CH_4. Only $Fe_{30}K_2Cu_{3.75}US$ showed a greater CO_2 productivity with respect to the IMP sample with the same active metal and promoters loadings.

Due to the higher CO conversion and the better selectivity values, the US samples present much greater productivities of the heavy >C7 fraction with respect to traditional impregnated catalysts. For example, $Fe_{10}US$ provided a >C7 productivity which is almost 17 times higher than the one reached by $Fe_{10}IMP$.

The improved activity and the better performances reached by the US samples can be attributed to the benefits of the US synthesis way. The use of ultrasound leads to the formation of nanostructured material which have greater surface area and better morphological properties with respect to the traditional synthesized catalyst. For example, the size of the active metal particles plays a key role in the FT catalytic

performances, since the dimensions of the metal particles will determine the amount of active metal which is available for the FT reaction [105]. The average dimension of the iron nanoparticles in impregnated samples is about 80- 100 nm while the dimension measured in the case of sonochemically synthesized catalyst is around 10 nm thus resulting in a better catalytic activity.

Moreover, the US samples showed quite big pore volumes which allows big metal loading avoiding the pores occlusion phenomena which has been observed in the BET characterization results of $Fe_{30}K_2Cu_{3.75}$ reported in the previous chapters and paragraphs. In addition, bigger pore sizes allow to reach a more uniform distribution of Fe and a greater accessibility of the active phase to the reactants.

8 Kinetic parameters regression and kinetic model development

8.1 Final aims of the modeling work

This part of the PhD research work has been focused on the kinetic parameters regression and the development of a suitable kinetic model in collaboration with Ing. Flavio Manenti, Ing. Marco Galimberti, Ing. Luca Vanalli and Ing. Riccardo Del Maso of the SuPER Team (Sustainable Process Engineering Research Team) from Politecnico di Milano.

The parameters regression and the simulation of the reactor behavior have been carried out with two catalysts set:

- $Fe_{30}K_2Cu_{3.75}$ synthesized by impregnation;

- 10Co-0.4Ru synthesized by FSP.

In the first case, both kinetic parameters of FT and WGS reactions have been regressed since Fe is a metal which is active to both of them, while in the second case only the FT reaction was considered active on the catalyst surface. Only 10Co-0.4Ru has been taken into account to perform a kinetic parameters regression since it presents better catalytic activity and performances if compared with the other FSP samples. Moreover the data available in the literature concerning the study of the kinetics of FT reaction with Co-based catalysts are referred to the same temperature at which 10Co-0.4Ru has been tested.

The regression procedure is based on the data collected in the laboratory FT rig, and the final aim of this work is to support and confirm the experimental data, to predict the reactor conversion, selectivity and productivity, to optimize the FT reactor conditions and moreover, in a further development of the work, a simulation of an entire industrial BTL-FT process from the conversion of the biomass feedstock to the production of hydrocarbons via FT synthesis.

Depending of the catalyst that it will be used in the BTL-FT two different configurations are possible. If $Fe_{30}K_2Cu_{3.75}$ is used in the FT reactor, it is possible to directly convert the bio-syngas ($H_2/CO< 2$) into hydrocarbons since the H_2/CO ratio is raised to the stoichiometry value required by via WGS. In the second case, if 10Co or

10Co-0.4Ru either are used, a WGS unit in between to the bio-syngas production step and the FT reactor, must be disposed in order to increase the H_2/CO ratio.

In this way, it will be possible to evaluate the performances of the catalysts not only on a laboratory scale, but even if used into an industrial volume plant.

The two possible configurations are shown in Figure 8.1.

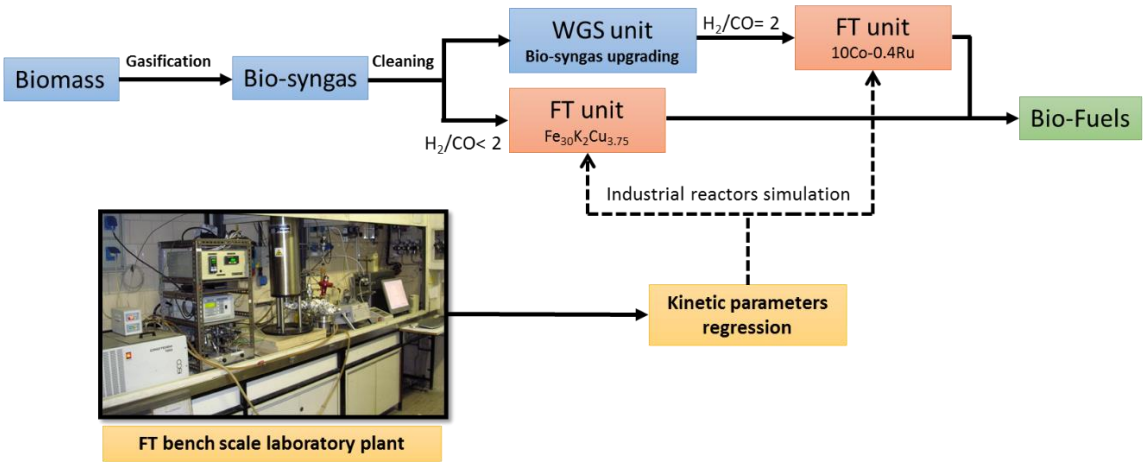

Figure 8.1: Possible configurations of the BTL-FT either with Fe or Co-based catalysts.

8.2 Laboratory reactor model

Since the laboratory FT reactor is a small volume fixed bed apparatus, some hypothesis can be made in order to simplify the system:

- The catalyst particles are small (105- 150 micrometers) and intra-porous resistances to mass transport are negligible, for these reasons the effectiveness factor for all the reactions is equal to one;

- The internal temperature over the whole catalytic bed can be considered constant since the catalyst reaction volume is very small ($6 \cdot 10^{-3}$ m^3) and the diluent material helps to avoid the formation of hot spots;

- The length of the catalytic bed is almost equal to 0.07 m, so even the pressure can be considered constant;

- The formation of a liquid phase over the catalysts particles is not taken into account.

Therefore, it is possible to reduce the system to a series of mass balances for each species. The general mass balance equation is reported hereinafter in Eq. 8.1:

$$\frac{dn_i}{dV} = \sum_{j=1}^{NR} v_{i,j} \cdot r_j \cdot \rho_{CAT} \cdot \varepsilon_2 \cdot (1 - \varepsilon) \qquad \text{(Eq. 8.1)}$$

Where:

- ni: is the molar flowrate of the generic "i" compound;

- V: is the volume of the catalytic bed and the diluent;

- vi,j: is the stoichiometry coefficient of the "i" specie in the "j" reaction;

- rj: is the rate of the "j" reaction;

- ρ_{CAT}: is the density of the catalytic bed;

- ε_2: is the fraction of the catalyst in the catalytic bed considered;

- ε: is the vacuum degree of the catalytic bed.

The FT reaction can be defined as follows in Eq. 8.2:

$$CO + U_{H2}H_2 \rightarrow \sum_{i=1}^{\infty} v_i C_i H_{2i+2} + H_2O \quad \text{(Eq. 8.2)}$$

Where the stoichiometry coefficient (ν_i) are function of the probability of chain growth (α) and defined as follows in Eq. 8.3:

$$\nu_i = (1-\alpha)^2 \alpha^{i-1} \quad \text{(Eq. 8.3)}$$

And the hydrogen consumption is calculated with Eq. 8.4:

$$U_{H2} = \frac{(3-\alpha)\,1}{1+\gamma} + ((1-\alpha)^2 + 2)\,\frac{\gamma}{1+\gamma} \quad \text{(Eq. 8.4)}$$

Where:

γ: is the olefin/paraffin ratio in the range equal to 0.35.

Even though the first part of the work, for both catalysts set, was the simulation of the results using parameters found in the literature, the second past has been focused on the regression of the kinetic parameters.

The nonlinear data regression consists in a minimization procedure where the objective function is the sum of the residuals squared. Residuals represent the difference between the experimental and simulated value. The minimization equation is reported hereinafter in Eq. 8.5:

$$\min_{xo} \; fobj(xo) = \sum_{i=1}^{Nobs} \sum_{j=1}^{Nc} (y_{i,j}^{exp} - y_{i,j}^{sim})^2 \quad \text{(Eq. 8.5)}$$

Where:

- $y_{i,j}^{exp}$: is the molar fraction of the "i" specie in the reaction "j" measured experimentally;

- $y_{i,j}^{sim}$: is the molar fraction of the "i" specie in the reaction "j" calculated by the model;

8.2.1 $Fe_{30}K_2Cu_{3.75}$

When $Fe_{30}K_2Cu_{3.75}$ is used to convert CO and H_2, both FT and WGS reactions are considered active on the catalyst surface.

The expressions for the reaction rates of both FTS and WGS are taken from the literature (Zimmerman et al.) [106]:

$$r_{FT} = k_{FT} \frac{P_{H_2} P_{CO}}{P_{CO} + a_{FT} P_{H_2O} + b_{FT} P_{CO_2}} \quad \text{(Eq. 8.6)}$$

$$r_{WGS} = k_{WGS} \frac{P_{CO} P_{H_2} - \frac{P_{H_2} P_{CO_2}}{K_P}}{P_{CO} + a_{WGS} P_{H_2O} + b_{WGS} P_{CO_2}} \quad \text{(Eq. 8.7)}$$

Where every kinetic constants is given by the Arrhenius formula:

$$k_i = k_{0,i} e^{-E_{act,i}/(RT)} \quad \text{(Eq. 8.8)}$$

And the equilibrium constant of the WGS reaction (K_P) is a function of the reaction temperature and it is calculated as:

$$K_p = e^{\left(\frac{4578}{T} - 4.33\right)} \quad \text{(Eq. 8.9)}$$

Usually, under the typical conditions adopted in FT reactors, the WGS equilibria is always shifted to the production of hydrogen and carbon dioxide.

The probability of chain growth (α) is calculated using the Lox and Forment [107] correlation:

$$\alpha = \frac{k_1 P_{CO}}{k_1 P_{CO} + k_5 P_{H_2} + k_6} \quad \text{(Eq. 8.10)}$$

And it can be rearranged as follows [107]:

$$\alpha = \frac{P_{CO}}{P_{CO} + k_A P_{H_2} + k_B} \quad \text{(Eq. 8.11)}$$

Where k_A and K_B are k_5 and k_6 divided by k_1 and each constant is given by:

$$k_i = k_{i,Ref} \exp\left(\frac{E_{act,i}}{R}\left(\frac{1}{T_{ref}} - \frac{1}{T}\right)\right) \quad \text{(Eq. 8.12)}$$

Where:

- $k_{i,Ref}$: is the constant at the reference temperature (T_{ref}) which is equal to T= 573 K.

All the FT and WGS reaction kinetic parameters reported in the works by Zimmerman et al. [106] and Lox and Forment [107] are listed in Table 8.1.- 8.2.

Reaction	k_i^0 ($mol \cdot kg_{CAT}^{-1} \cdot s^{-1} \cdot Pa^{-1}$)	$E_{act,i}$ ($kJ \cdot mol^{-1}$)	a,i	b,i
FT	8.58	86	4.8	0.33
WGS	$9.33 \cdot 10^{-6}$	132	21	0

Table 8.1: Literature kinetic parameters for WGS and FT reactions.

Constants at T_{ref} ($mol \cdot g^{-1} \cdot s^{-1} \cdot bar^{-1}$)	k_i	$E_{act,i}$ ($kJ \cdot mol^{-1}$)
k_1	$1.22 \cdot 10^{-5}$	0
k_5	$1.05 \cdot 10^{-6}$	94.5
k_6	$2.36 \cdot 10^{-6}$	132.3

Table 8.2: Literature kinetic parameters for α.

Using the data summarized in Table 8.1 and Table 8.2 and the experimental parameters adopted in the FT laboratory reactor, it is possible to carry out a first simulation and a comparison with the experimental results without setting a regression of the kinetic parameters.

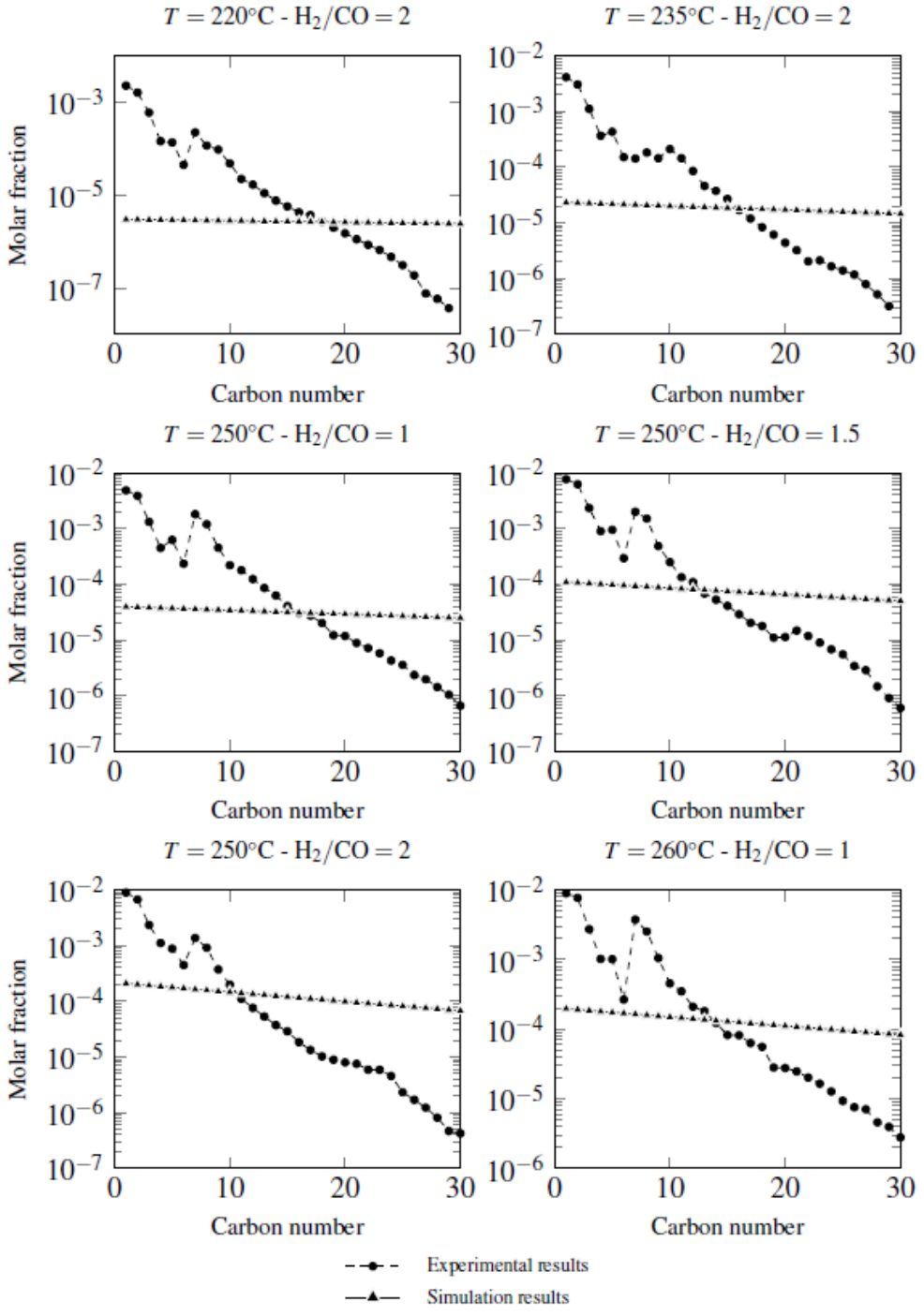

Figure 8.2: Comparison between experimental and simulated results before data regression.

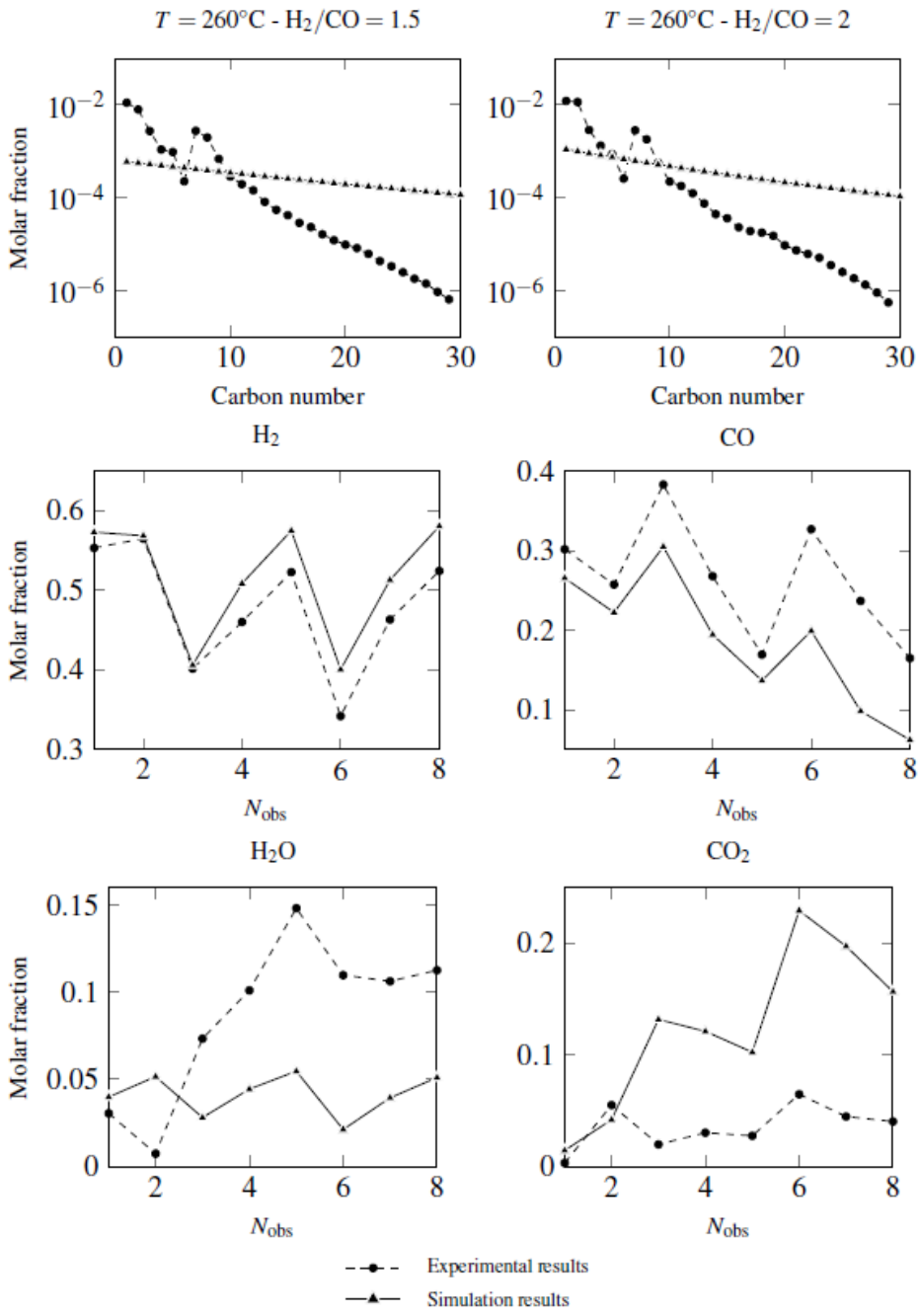

Figure 8.3: Comparison between experimental and simulated results before data regression.

As it is possible to observe in Figure 8.2 and Figure 8.3 the simulated values do not present a good fit with the one obtained in the FR reactor experimentally.

Two different problem could have affected the simulated data:

- the comparison between the experimental and simulated molar fractions (in semi-logarithmic scale) distributions of hydrocarbons (Figure 8.2) suggests that the chain growth probability evaluated in the case of simulated data is too high;

- the simulated CO_2 molar fractions in the outlet gaseous mixture are higher than the one measured during in the experimental tests in every runs performed. This result means that WGS reaction rate is overestimated.

In order to fix these issues and to obtain a better accuracy of the simulated values a nonlinear regression is therefore required.

The nonlinear regression was set by minimizing Eq. 8.5 without considering a_{FT}, b_{FT}, a_{WGS} and b_{WGS}, since they do not affect the simulated results in a significant way. The regression procedure should optimize as few parameters as possible, in order to allow an efficient convergence and to have a number of parameters that is lower than the number of experiments [43]. Moreover, since the probability of chain growth values calculated experimentally showed that this parameter is not highly influenced by the temperature in the range of reaction temperature tested, the activation energies in the Lox and Froment model are set to zero.

Initially, the nonlinear regression has been performed using MATLAB® 2014b, but an acceptable solution was not figured out since the simulated hydrocarbons molar fractions were always overestimated by the model and the outlet gas phase molar composition was not satisfactorily approximated.

This problem is due to the fact that the set objective function (Eq. 8.5) presents a quite high number of local minimums therefore the final solution is strongly dependent by the parameters given for the first attempt.

In order to avoid this problem, and to improve the minimization process, BzzMath libraries and, in particular, the BzzNonLinearRegression class with a developed C++ procedure have been used [108].

The regressed parameters are presented in Table 8.3 [43].

Model	Parameter	Unit of measure	Regressed value
α	$k_{A,\,Ref}$	//	$1.45\cdot10^{-5}$
	$k_{B,\,Ref}$	bar	2.078
FT	k_{FT}^0	$mol\cdot g^{-1}\cdot s^{-1}\cdot bar^{-1}$	$3.365\cdot10^{3}$
	$E_{act,FT}$	$kJ\cdot mol^{-1}$	113.7
WGS	k_{wgs}^0	$mol\cdot g^{-1}\cdot s^{-1}\cdot bar^{-1}$	19.03
	$E_{act,WGS}$	$kJ\cdot mol^{-1}$	80.26

Table 8.3: Regressed kinetic parameter for $Fe_{30}K_2Cu_{3.75}$.

The simulated results after the kinetic parameters nonlinear regression are shown in Figure 8.4- 8.5.

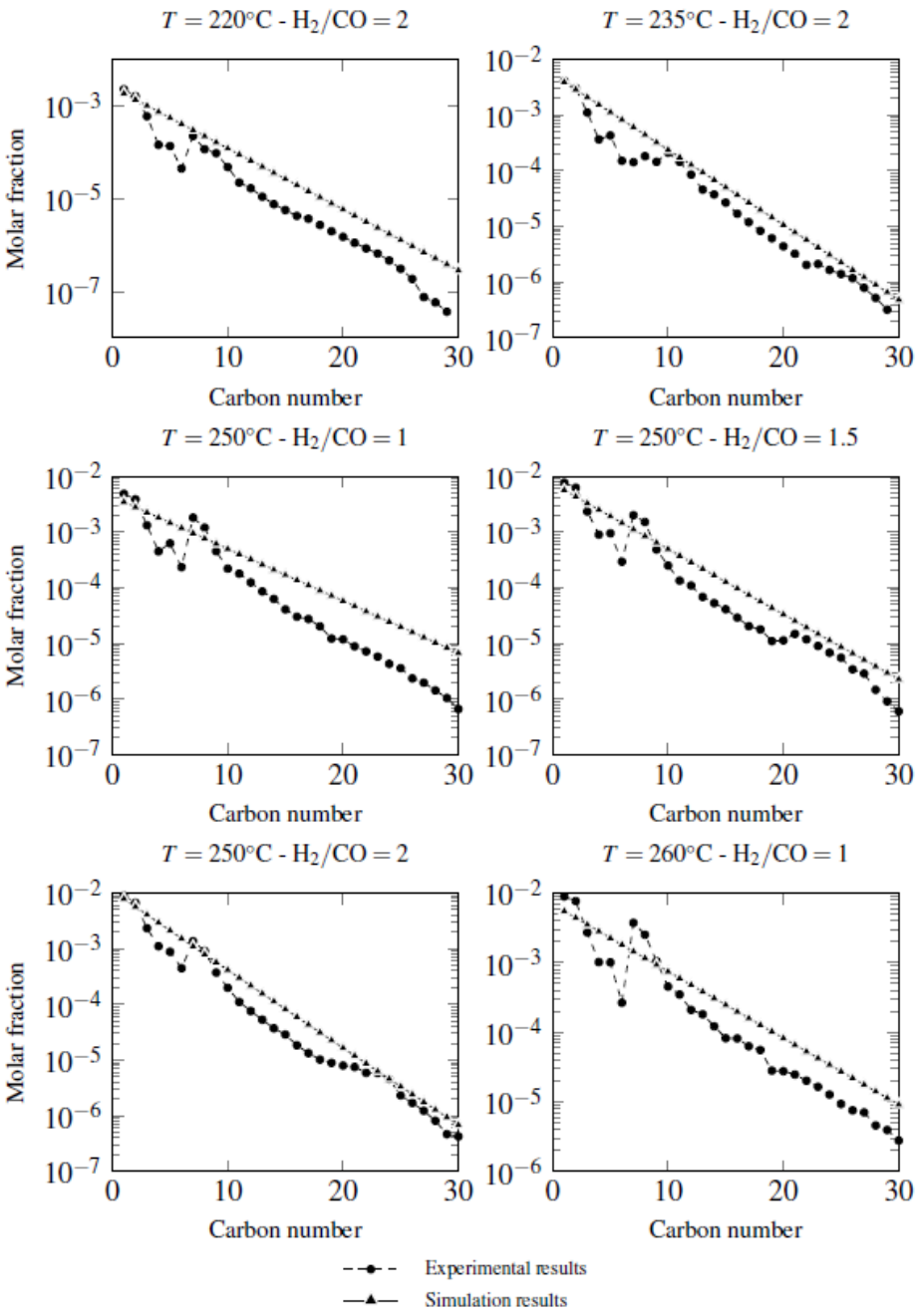

Figure 8.4: Comparison between experimental and simulated results after the data nonlinear regression.

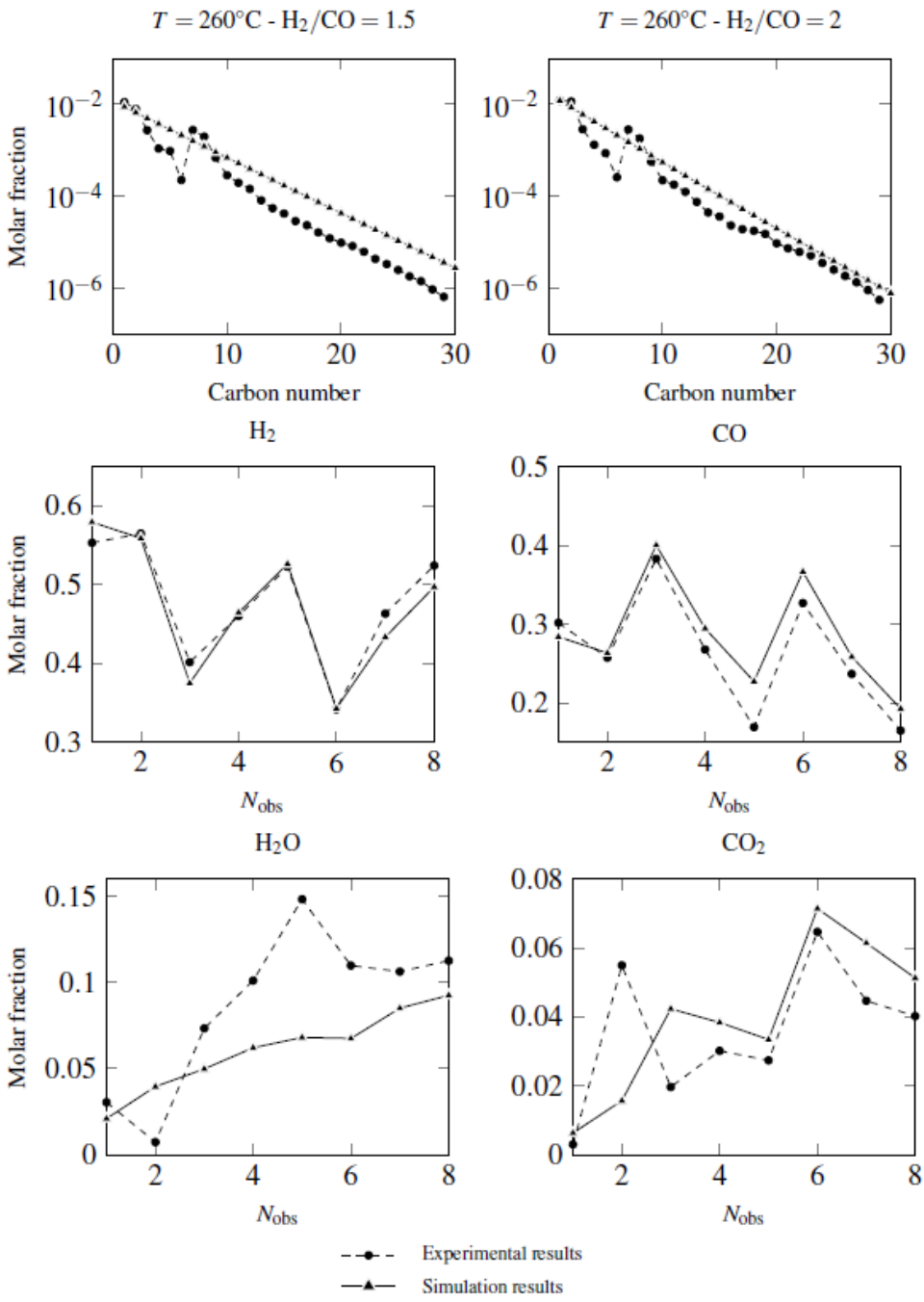

Figure 8.5: Comparison between experimental and simulated results after the data nonlinear regression.

With the comparison reported in Figure 8.4 and Figure 8.5 it is possible to observe that the developed C++ procedure and the use of BzzMath libraries allow a good prediction of the experimental data obtained in the laboratory FT reactor.

The elaborated model it is capable to follow the hydrocarbons distribution as reported in the ASF diagrams at different temperatures and different H_2/CO fed to the reactor.

Moreover, a satisfactory prediction of the outlet gas molar fractions has been achieved.

8.2.2 10Co-0.4Ru

In the case of Co-based catalyst, the FT reaction is the only one which is active on the catalyst surface.

The equation which express the FT reaction rate (Yates et al.) [109] is here reported in Eq. 8.13:

$$rFT = \frac{aP_{CO}P_{H2}}{(1+bP_{CO})^2} \quad \text{(Eq. 8.13)}$$

Where every kinetic constants is given by the Arrhenius formula as already reported in Eq. 8.8.

While the probability of chain growth reported in Eq. 8.14 is given by (Vervloet et al.) [110]:

$$\alpha = \frac{k_p}{k_p+\left(\frac{C_{H2}}{C_{CO}}\right)^{\beta} k_t} \quad \text{(Eq. 8.14)}$$

Where each constant ki, is calculated with Eq. 8.15:

$$k_i = k_{i,Ref}^0 \exp\left(\frac{E_{act,i}}{R}\left(\frac{1}{T_{ref}} - \frac{1}{T}\right)\right) \quad \text{(Eq. 8.15)}$$

Where:

- $k_{i,Ref}$: is the constant at the reference temperature (T_{ref}) which is equal to T= 493.15 K.

In order to reduce the parameters that have to be minimized, Eq. 8.14 can be rearranged as follows in Eq. 8.16:

$$\alpha = \frac{1}{1+k_\alpha\left(\frac{C_{H2}}{C_{CO}}\right)^{\beta} \exp\left(\frac{\Delta E_\alpha}{R}\left(\frac{1}{493.15}-\frac{1}{T}\right)\right)} \quad \text{(Eq. 8.16)}$$

Where:

k_α: is the ratio between k_T^0 and k_P^0;

ΔE_α: is equal to $E_t - E_p$.

The literature parameters for the FT reaction at two different temperature reported by Yates et al. [109] are summarized in Table 8.4.

T (°C)	parameter	
	a ($mmol \cdot min^{-1} \cdot g_{CAT}^{-1} \cdot MPa^{-2}$)	b (MPa^{-1})
240	75.76	11.61
220	53.11	22.26

Table 8.4: Literature kinetic parameters for FT reaction.

While the literature parameters for the probability of chain growth are reported in Table 8.5.

kα (-)	β (-)	ΔE_α ($kJ \cdot mol^{-1}$)
$56.7 \cdot 10^{-3}$	1.76	120.4

Table 8.5: Literature kinetic parameters for the probability of chain growth.

Even in this case, the simulation work has been initially performed by comparing the experimental results and the one given by the model using only the literature parameters, and then by setting a nonlinear regression.

The nonlinear regression procedure is divided in two parts. In the first one seven parameters are regressed, and in the second one only four parameters are taken into account for the regression.

The regression is achieved by minimizing Eq. 8.5 using BzzMath libraries with MATLAB® 2014b.

In the following Table 8.6 the parameter that need to be regressed are reported.

Type of regression	Model	Parameter
7 parameters	FT	k_a^0
		Ea
		k_b^0
		Eb
	α	kα
		β
		ΔE_α

Type of regression	Model	Parameter
4 parameters	FT	k_a^0
		Ea
		k_b^0
		Eb

Table 8.6: Regressed parameters in the 7-data and 4-data regression.

When the four parameter regression is carried out, only the kinetic parameters that regard the FT reaction are taken into account, while the ones related to the probability of chain growth are considered constant and equal to the ones that have been found in the literature.

The first data presented are the comparison between the experimental results and the simulated data obtained with the literature parameters, while in the second and third case the experimental results are compared with the simulated ones obtained with 4-data or 7-data nonlinear regression.

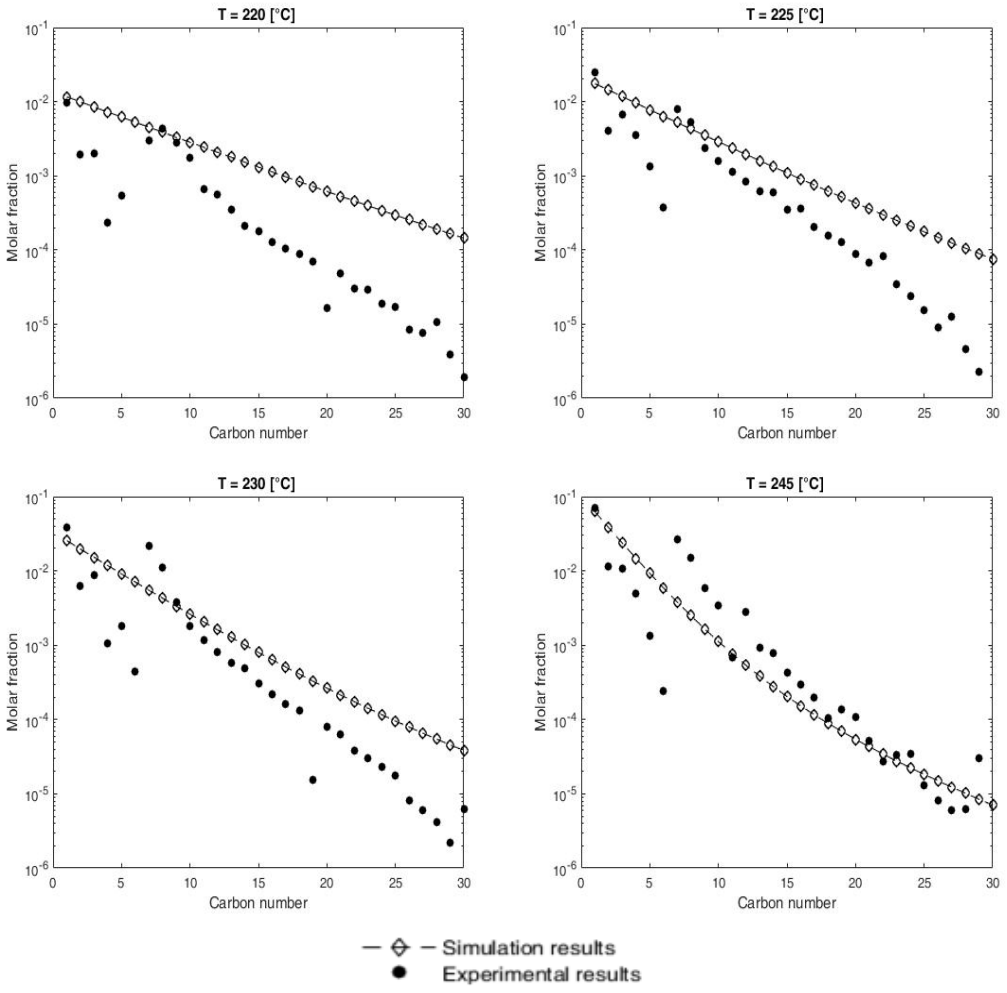

Figure 8.6: Comparison between experimental and simulated results before data regression.

Even though the simulated results presents the right trend if compared with the experimental ones, a nonlinear regression is required in order to minimize the

differences and make the simulated data as much equal as possible with the experimental ones.

In the following Figure 8.7- 8.8 is reported the comparison between the experimental data obtained in the FT reactor and the results calculated by the model with the four data parameters regression.

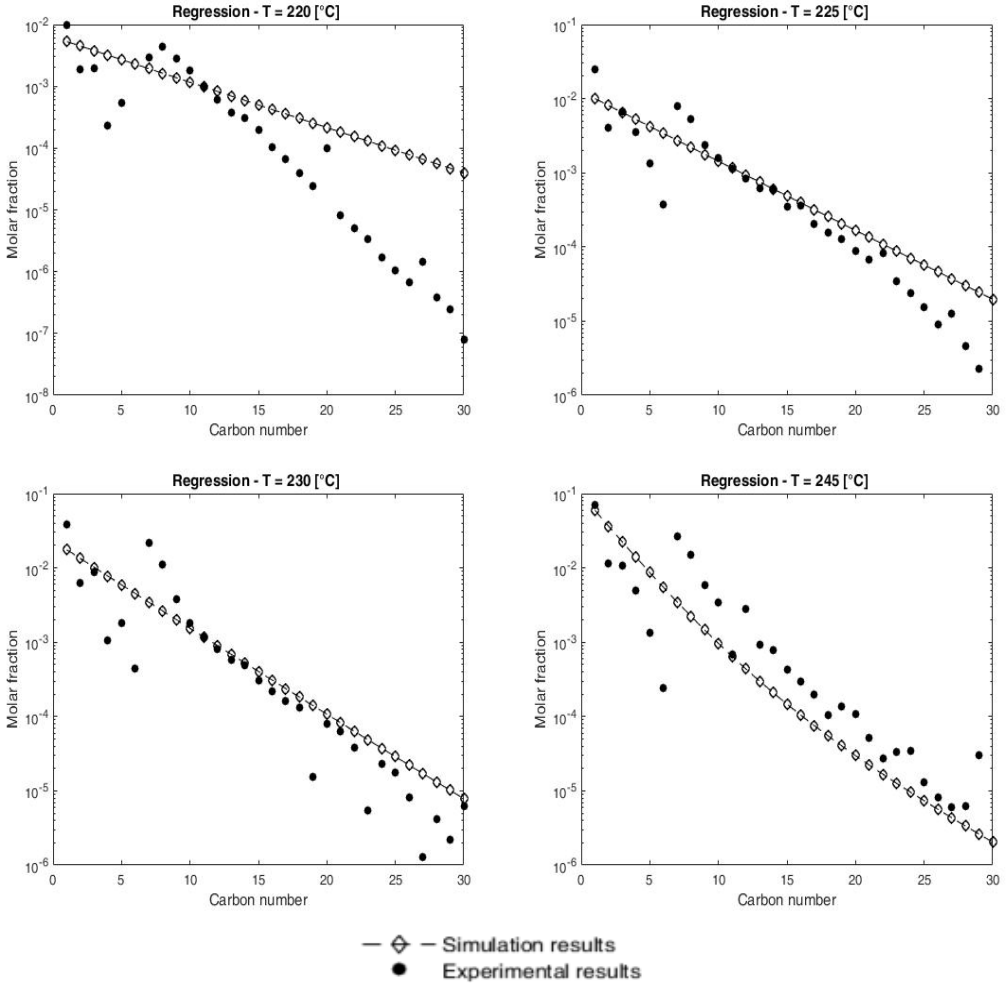

Figure 8.7: Comparison between experimental and simulated results after 4-data regression.

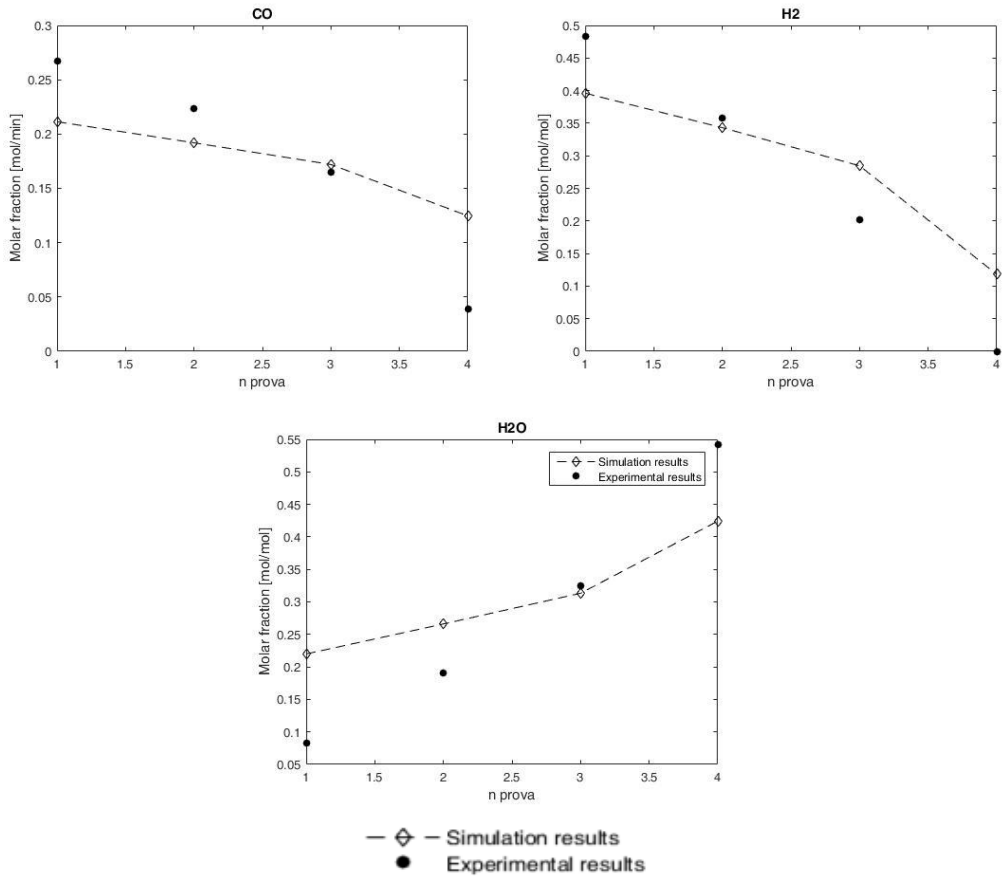

Figure 8.8: Comparison between experimental and simulated results after 4-data regression.

The results achieved with the four data regression present a better fit of the one obtained with the literature parameters. However, the hydrocarbons distribution and the molar fraction of CO, H_2 and H_2O are not in good agreement with the experimental values in the simulations at low temperatures.

The regressed parameters are reported in Table 8.7.

Type of regression	Model	Parameter	Unit of measure	Value
4 parameters	FT	k_a^0	(-)	$4.378 \cdot 10^9$
		Ea	$J \cdot mol^{-1}$	$9.24 \cdot 10^4$
		k_b^0	(-)	$1.66 \cdot 10^8$
		Eb	$J \cdot mol^{-1}$	$1.721 \cdot 10^5$

Table 8.7: Regressed kinetic parameters in the 4-data regression

In the following Figure 8.9- 8.10 are reported the results obtained with the 7-data regression.

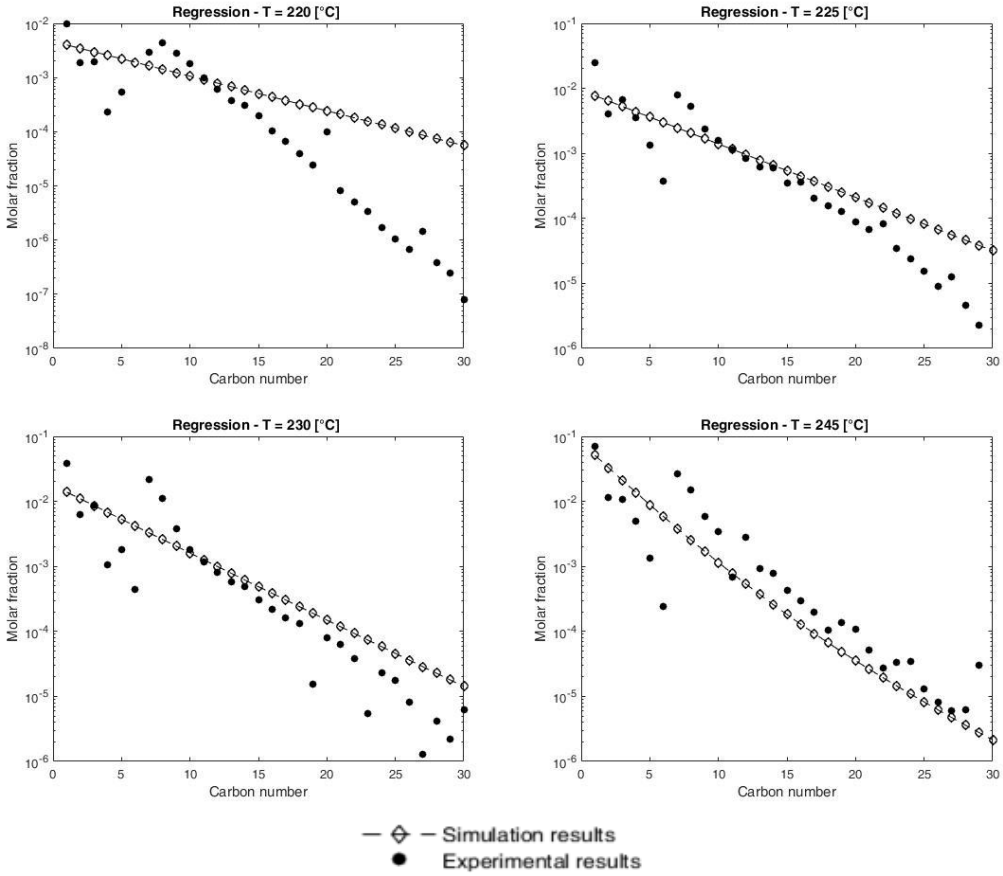

Figure 8.9: Comparison between experimental and simulated results after 7-data regression.

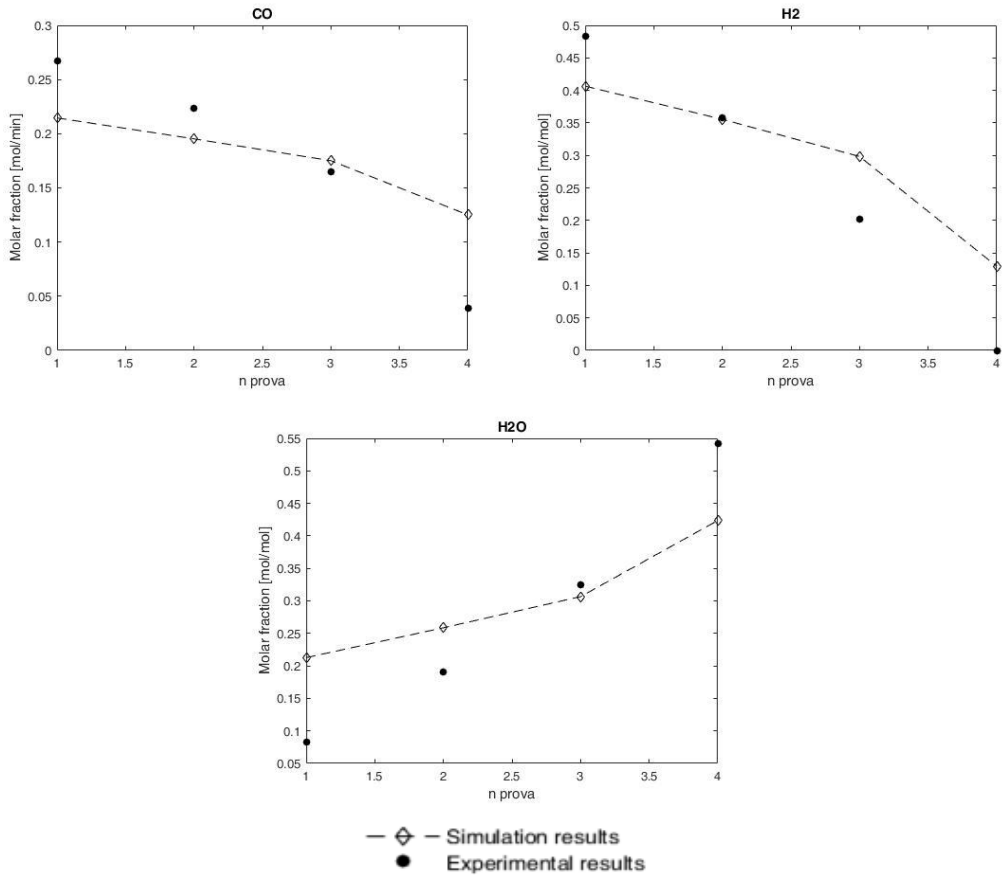

Figure 8.10: Comparison between experimental and simulated results after 7-data regression.

The seven parameters regression allows to reach better results than the two previous simulation results presented. Nevertheless, the model still present a quite high difference in the experimental results and the simulated one when the catalyst is tested at low temperature (T= 220 °C). The regressed values are summarized in Table 8.8.

Type of regression	Model	Parameter	Unit of measure	Value
7 parameters	FT	k_a^0	(-)	$4.378 \cdot 10^9$
		Ea	$J \cdot mol^{-1}$	$9.22 \cdot 10^4$
		k_b^0	(-)	$1.66 \cdot 10^8$
		Eb	$J \cdot mol^{-1}$	$1.712 \cdot 10^5$
	α	kα	(-)	0.051
		β	(-)	1.683
		ΔE_α	$J \cdot mol^{-1}$	$1.204 \cdot 10^5$

Table 8.8: Regressed kinetic parameters in the 7-data regression

Since the simulated results with the 7-data regression are good, but not still in fully agreement with the experimental ones measured in the laboratory reactor, it has been decide to vary the equation which express the rate of FT reaction with Co-base catalyst.

The proposed equation is the following Eq. 8.17 [109]:

$$rFT = \frac{aP_{CO}^{0.65}P_{H2}^{0.6}}{(1+bP_{CO})} \quad \text{(Eq. 8.17)}$$

Moreover, the olefin/paraffin ratio that has been used in the previous simulations was kept equal to 0.35 that is a typical value for FT iron based catalysts. In this case γ has been calculated by Eq. 8.18:

$$\gamma = e^{-cn} \quad \text{(Eq. 8.18)}$$

Where:

- c: is equal to 0.1- 0.49;

- n: number of carbon atoms.

In order to better the fitting of the simulated data with the experimental ones, the objective function has been varied as is reported in Eq. 8.19:

$$fobj = \sum_{i=1}^{Nobs}\sum_{j=1}^{N_C^{Light}}\left(P_L \cdot \left(y_{i,j}^{exp} - y_{i,j}^{sim}\right)^2\right) + \sum_{i=1}^{Nobs}\sum_{j=1}^{N_C^{Heavy}}\left(P_H \cdot \left(y_{i,j}^{exp} - y_{i,j}^{sim}\right)^2\right) \quad \text{(Eq. 8.19)}$$

Where:

P_H: is a correction factor for the heavy fraction and it is equal to 1;

P_L: is a correction factor for the heavy fraction and it is equal to 0.5.

These correction fraction have been estimated experimentally by taking into account the error of the analytical apparatus in the detection of the C_5-C_9 fraction.

The comparison of the experimental results and the data given by the model with the new kinetic equation and the new set objective function are reported in Figure 8.11.

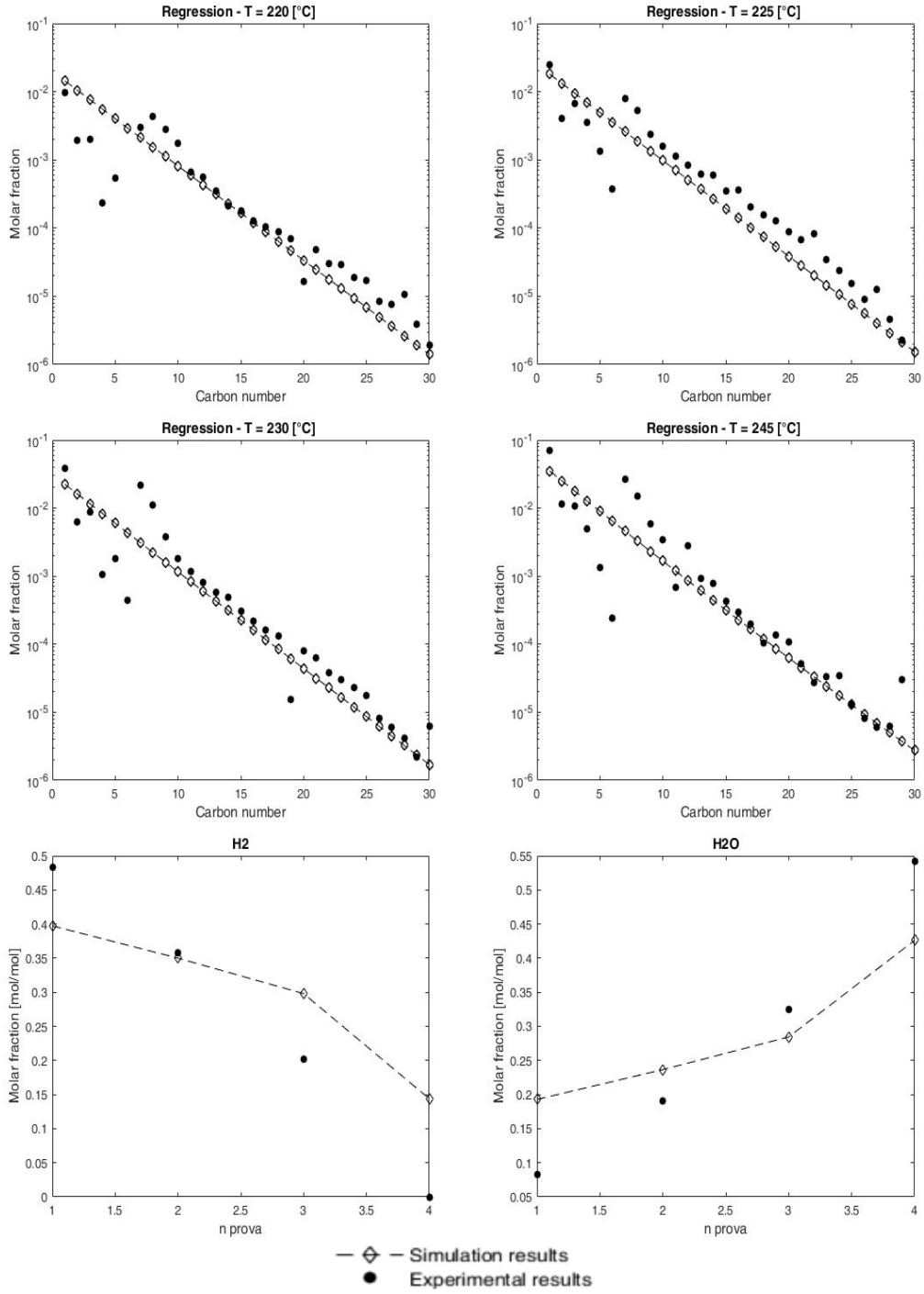

Figure 8.10: Comparison between experimental and simulated results after the modified data regression.

The regressed constant with the modified data regression are summarized in Table 8.9.

Type of regression	Model	Parameter	Unit of measure	Value
Modified data regression	FT	k_a^0	(-)	$4.378 \cdot 10^9$
		Ea	$J \cdot mol^{-1}$	$9.28 \cdot 10^4$
		k_b^0	(-)	$1.66 \cdot 10^8$
		Eb	$J \cdot mol^{-1}$	$1.712 \cdot 10^5$
	α	kα	(-)	0.216
		β	(-)	0.8564
		ΔE_α	$J \cdot mol^{-1}$	$1.249 \cdot 10^5$

Table 8.9: Regressed kinetic parameters in the modified data regression.

The modified data regression allows a great and satisfactory fitting between the model data and the experimental results at all the reaction temperature tested. From a comparison among the regressed parameters of the 7-data regression and the modified one, it is clear that the data that have been affected by a great variation are the one regarding the probability of chain growth. However, the regressed values show a good agreement with the one reported in the literature.

9 Conclusions and final remarks

Three different catalysts sets active in the Fischer-Tropsch (FT) reaction have been synthesized using different preparation methods. The complete list of the catalysts is reported hereinafter:

- $Fe_{30}K_2Cu_{3.75}$: (30 %wt of Fe, 2 %wt of K and 3.75 %wt of Cu) synthesized by traditional wetness impregnation;
- 5Co, 10Co, 10Co-0.4Ru (5 %wt of Co; 10 %wt of Co; 10 %wt of Co and 0.4 %wt of Ru) synthesized by flame spray pyrolysis (FSP);
- Fe_{10}US, Fe_{30}US, $Fe_{30}K_2Cu_{3.75}$US: (10 %wt of Fe; 30 %wt of Fe; 30 %wt of Fe, 2 %wt of K and 3.75 %wt of Cu) prepared with the use of ultrasound (US).

After the synthesis, all the catalysts have been characterized and then tested in a suitable laboratory FT rig equipped with a fixed bed reactor.

The main conclusions for each type of catalyst set are reported in the following paragraphs.

9.1 Catalysts characterization

9.1.1 $Fe_{30}K_2Cu_{3.75}$

The ICP analysis highlights that the desired amount of active metal and promoters was present in the catalyst.

The insertion of 30 %wt of Fe and the promoters on the bare support, causes a decrease in the surface area from 305 $m^2 \cdot g^{-1}$ to 133 $m^2 \cdot g^{-1}$, due to the diluting effect of the metal. Moreover, Fe, K and Cu cause the occlusion of the pores with diameters bigger than 10 nm by a “lining” of internal pore which induces a decrease of all the mesoporous pores, with the result to form new pores in the range 5- 10 nm.

The TEM and SEM-EDX analyses suggest that iron is well dispersed on the support and the active metal aggregates have dimension in the range of 100- 150 nm.

The XRD pattern showed the presence of hematite (Fe_2O_3) suggesting that after the impregnation synthesis Fe remains in the same oxidation state of its precursor (Fe^{3+}).

The TPR results highlight that two reduction steps are present, the first one can be associated with the reduction of hematite to magnetite and then the second one to the transition from magnetite to metallic iron.

9.1.2 5Co, 10Co and 10Co-0.4Ru

The elementary analysis confirmed that all the precursors used for the synthesis of Co-based catalysts were completely decomposed in the catalyst by the pyrolysis process.

Both 10Co and 10Co-0.4Ru present a quite high BET surface area. Moreover, the addition of Ru by wetness impregnation and the successive calcination step almost unaffected the surface area of the sample, and a decrease of only 14 $m^2 \cdot g^{-1}$ was recorded.

The morphological evaluation of the samples performed by TEM and SEM highlights that the Co aggregates in 5Co and 10Co have dimensions in the range of 20- 40 nm. The addition of Ru by impregnation almost do not affect the dimension of Co aggregates, in fact the nanoparticles growth of about 1- 5 nm. In all the samples synthesized by FSP bigger Co aggregates with dimensions equal to 45- 50 nm are present.

The XRD pattern of 5Co sample did not present any peak related to Co-oxides species while in 10Co and 10Co-0.4Ru some peaks related to the presence of Co_3O_4 oxide are present.

The TPR profile of sample 5Co did not show any defined peak related to the transition from Co^{3+} to Co^{2+} suggesting that only CoO or Co-silicates are formed during the FSP synthesis. Both TPRs of 10Co and 10Co-0.4Ru present two peak attributable to the complete reduction process from Co^{3+} to Co^0, The addition of 0.4 %wt of Ru decreases both peaks reduction temperatures of about 10- 20 °C improving the catalyst reducibility.

9.1.3 Fe_{10}US, Fe_{30}US, $Fe_{30}K_2Cu_{3.75}$US

The quantification of the elements performed with ICP confirmed that the experimentally determined loadings of Fe and when present, promoters, were in a good agreement with the theoretical expected. Moreover an amount of 0.009 ± 0.001 %wt of titanium was detected in all the US sample due to the SiO_2-Ti_{TIP} interaction and the presence of 1.5 ± 0.05 %wt of carbon was measured in each catalysts due to the decomposition of the n-decane solvent and/or the presence of carbon monoxide residue.

According with the previous BET results, greater is the amount of the metals on the bare support, lower is the surface of the catalysts, in fact a decrease from 515 $m^2 \cdot g^{-1}$ (SiO_2 surface area) to 216 $m^2 \cdot g^{-1}$ ($Fe_{30}K_2Cu_{3.75}US$ surface area) was recorded. US samples present surface area that is equal (in the case of $Fe_{10}US$) or higher (in the case of $Fe_{30}US$ $Fe_{30}K_2Cu_{3.75}US$) with respect to the same kind of catalysts with the same metal loading but synthesized with traditional impregnation.

TEM and SEM images showed that Fe is very well dispersed in all the sonochemical samples, with dimensions in the range between few nanometers and 20 nm. The activation step does not influence the morphology of the sample $Fe_{10}US$ since even if it has been treated at T= 350 °C for 4 h, the dimension of the Fe-nanoparticles remained lower than 20 nm and the active metal was still well dispersed on the support surface.

The XRD patterns recorded with the fresh US catalysts do not reveal any peak related to crystalline iron oxides since amorphous bulk metal is formed during the US synthesis. However, a transition from amorphous to crystalline structure was confirmed by XRD analysis performed on $Fe_{10}US$ after the activation treatment.

The TPR profiles of $Fe_{10}US$ and $Fe_{30}US$ showed that both samples have the same reduction temperature associated to the first reduction step which is equal to T= 350 °C. The insertion of the promoters decreases the hematite to magnetite transition temperature of about ≈ 10 °C. Moreover, $Fe_{10}US$ and $Fe_{30}US$ have lower reduction temperatures related to the first step if compared with the same impregnated catalysts.

9.2 Catalytic results

9.2.1 $Fe_{30}K_2Cu_{3.75}$

The rate of CO conversion increases with an increase in the reaction temperature and in the H_2/CO ratio fed to the reactor. The better catalytic results obtained with H_2/CO= 2 are due to the fact that an hydrogen/carbon monoxide ratio equal to 2 is the stoichiometry one required by the FT reaction.

The productivity of the reaction products is highly influenced by the reaction temperature. In particular, at a constant ratio of H_2/CO fed to the FT reactor, the productivity of CH_4 and CO_2 increased. On the other hand the productivity and the composition of the >C7 fraction are not strongly influenced by the syngas ratio fed.

$Fe_{30}K_2Cu_{3.75}$ proved to be a stable catalysts over TOS; the CO conversion rate needs almost 40 h from the start of the tests to reach the steady state value for all the three

H_2/CO ratios tested while the molar productivities of CO_2, CH_4 and light hydrocarbons, are stable from the start of the experimental tests.

The probability of chain growth is slightly influenced by the reaction temperature and the H_2/CO ratio fed to the reactor; the highest probability of chain growth values are the ones reached by the catalyst when tested at T= 250 °C and H_2/CO= 1.5- 1.

For what concerns the study regarding the affinity of the light phase components for the heavy organic phase, from the experimental results is evident that, as a general trend, higher is the number of carbon atoms in the molecule, greater is the presence of the components dissolved in the heavy liquid fraction.

The developed kinetic model allows a good prediction of the experimental data obtained in the laboratory FT reactor.

9.2.2 5Co, 10Co and 10Co-0.4Ru

5Co did not show any catalytic activity toward the FT reaction due to the total lack of reducible species on the catalyst.

CO conversion rate reached by 10Co and 10Co-0.4Ru increases with an increase in the reaction temperature while the productivity towards the reaction products is not highly influenced by the temperature. Only >C7 production is increased with an increase in the reaction temperature.

The addition of the promoter increases of about four times the CO conversion rate at the same reaction temperature.

The durability test highlighted that the sample 10Co has a really good stability over prolonged TOS both from CO conversion and products production rates points of view.

The probability of chain growth follows the same trend of the heavy products productivity, in fact it increases by increasing the reaction temperature.

The different kinetic parameters regression performed with 10Co-0.4Ru allowed to identify the best kinetic equation for the rate expression of the FT synthesis. Moreover with a 7-data regression a satisfactory fitting between the model data and the experimental results has been achieved.

9.2.3 Fe_{10}US, Fe_{30}US, $Fe_{30}K_2Cu_{3.75}$US

All the US samples have been activated at both at Tact.= 350 °C and Tact.= 400 °C except the sample $Fe_{30}K_2Cu_{3.75}$US since at Tact.= 400 °C the high activity to the

Boudouard equilibria leads to the formation of elementary carbon on the catalyst surface which drammatically decreases the activity of the catalyst.

The increase in the reaction and the activation temperatures increases the rate of CO conversion for all the samples, but they do not stronlgy influence the results in terms of products productivity.

Both Fe_{10}US and Fe_{30}US presented a good stability over TOS. The steady state CO conversion rate was reached since the first hours of the experimental test and it remained stable for the whole duration of the test even when the reaction temperature was raised.

A comparison between the samples synthesized with the use of ultrasound and the impregnated catalysts suggests that US samples proved to be more active to the FT reaction. In particular, US samples provided almost five times higher CO conversion rate in the case of Fe_{10}US. Moreover, due to the higher CO conversion and the better selectivity value of the US samples, they present much greater productivities of the heavy >C7 fraction with respect to traditional impregnated catalysts.

References

[1] M.M. Farid, A.M. Khudhair, S.A.K. Razack, S. Al-Hallaj, A review on phase change energy storage: Materials and applications, Energy Convers. Manag. 45 (2004) 1597–1615. doi:10.1016/j.enconman.2003.09.015.

[2] EIA, Annual Energy Outlook 2015, (2015) 154. doi:DOE/EIA-0383(2013).

[3] M.E. Dry, The Fischer-Tropsch process: 1950-2000, Catal. Today. 71 (2002) 227–241. doi:10.1016/S0920-5861(01)00453-9.

[4] L. Krishnamurthy, R. Purushothaman, M.I. Ahmed, V. Vadez, Plant Biomass Productivity Under Abiotic Stresses in SAT Agriculture, (2006).

[5] H. Boerrigter, H. Den Uil, H.-P. Calis, Green Diesel from Biomass via Fischer-Tropsch synthesis: New Insights in Gas Cleaning and Process Design, Pyrolysis Gasif. Biomass Waste, Expert Meet. (2002) 1–13.

[6] G.P. Van Der Laan, A.A.C.M. Beenackers, Kinetics and Selectivity of the Fischer–Tropsch Synthesis: A Literature Review, Catal. Rev. Sci. Eng. 41 (1999) 255–318. doi:10.1016/j.apcata.2013.10.061.

[7] W. Ma, G. Jacobs, D.E. Sparks, J.L.S. Klettlinger, C.H. Yen, B.H. Davis, Fischer–Tropsch synthesis and water gas shift kinetics for a precipitated iron catalyst, Catal. Today. (2016) -. doi:http://dx.doi.org/10.1016/j.cattod.2016.01.006.

[8] R.S. Dhillon, G. von Wuehlisch, Mitigation of global warming through renewable biomass, Biomass and Bioenergy. 48 (2013) 75–89. doi:10.1016/j.biombioe.2012.11.005.

[9] C.N. Hamelinck, A.P.C. Faaij, Outlook for advanced biofuels, Energy Policy. 34 (2006) 3268–3283. doi:10.1016/j.enpol.2005.06.012.

[10] P. Ruiz, A. Sgobbi, W. Nijs, F.D. Longa, T. Kober, The JRC-EU-TIMES model . Bioenergy potentials for EU and neighbouring countries ., 2015. doi:10.2790/39014.

[11] A. V. Bridgwater, Review of fast pyrolysis of biomass and product upgrading, Biomass and Bioenergy. 38 (2012) 68–94. doi:10.1016/j.biombioe.2011.01.048.

[12] D.S. Scott, P. Majerski, J. Piskorz, D. Radlein, A second look at fast pyrolysis of biomass—the RTI process, J. Anal. Appl. Pyrolysis. 51 (1999) 23–37. doi:10.1016/S0165-2370(99)00006-6.

[13] H.B. Goyal, D. Seal, R.C. Saxena, Bio-fuels from thermochemical conversion of renewable resources: A review, Renew. Sustain. Energy Rev. 12 (2008) 504–

517. doi:10.1016/j.rser.2006.07.014.

[14] A. Sharma, V. Pareek, D. Zhang, Biomass pyrolysis - A review of modelling, process parameters and catalytic studies, Renew. Sustain. Energy Rev. 50 (2015) 1081–1096. doi:10.1016/j.rser.2015.04.193.

[15] F. Behrendt, Y. Neubauer, M. Oevermann, B. Wilmes, N. Zobel, Direct liquefaction of biomass, Chem. Eng. Technol. 31 (2008) 667–677. doi:10.1002/ceat.200800077.

[16] S.S. Toor, L. Rosendahl, A. Rudolf, Hydrothermal liquefaction of biomass: A review of subcritical water technologies, Energy. 36 (2011) 2328–2342. doi:10.1016/j.energy.2011.03.013.

[17] H.J. Kim, B.S. Kang, M.J. Kim, Y.M. Park, D.K. Kim, J.S. Lee, et al., Transesterification of vegetable oil to biodiesel using heterogeneous base catalyst, Catal. Today. 93-95 (2004) 315–320. doi:10.1016/j.cattod.2004.06.007.

[18] C. Pirola, F. Galli, C.L. Bianchi, D.C. Bo, A. Comazzi, D. Chimica, Vegetable Oil Deacidi fi cation by Methanol Heterogeneously Catalyzed Esteri fi cation in (Monophasic Liquid)/ Solid Batch and Continuous Reactors, (2014). doi:10.1021/ef501397h.

[19] Y. Chisti, Biodiesel from microalgae beats bioethanol, Trends Biotechnol. 26 (2008) 126–131. doi:10.1016/j.tibtech.2007.12.002.

[20] Y. Chisti, Constraints to commercialization of algal fuels, J. Biotechnol. 167 (2013) 201–214. doi:10.1016/j.jbiotec.2013.07.020.

[21] A. Demirbas, Progress and recent trends in biofuels, Prog. Energy Combust. Sci. 33 (2007) 1–18. doi:10.1016/j.pecs.2006.06.001.

[22] J. Hu, F. Yu, Y. Lu, Application of Fischer–Tropsch Synthesis in Biomass to Liquid Conversion, Catalysts. 2 (2012) 303–326. doi:10.3390/catal2020303.

[23] K. Raveendran, A. Ganesh, K.C. Khilar, Influence of mineral matter on biomass pyrolysis characteristics, Fuel. 74 (1995) 1812–1822. doi:10.1016/0016-2361(95)80013-8.

[24] P. McKendry, Energy production from biomass (part 3): Gasification technologies, Bioresour. Technol. 83 (2002) 55–63. doi:10.1016/S0960-8524(01)00120-1.

[25] R. Warnecke, Gasification of biomass: Comparison of fixed bed and fluidized bed gasifier, Biomass and Bioenergy. 18 (2000) 489–497. doi:10.1016/S0961-9534(00)00009-X.

[26] H. Boerrigter, Economy of Biomass-to-Liquids (BTL) plants An engineering assessment, (2006) 29. www.ecn.nl/biomass.

[27] B. Dawoud, E. Amer, D. Gross, Experimental investigation of an adsorptive thermal energy storage, Int. J. Energy Res. 31 (2007) 135–147. doi:10.1002/er.

[28] X. Lu, Z. Yu, L. Wu, J. Yu, G. Chen, M. Fan, Policy study on development and utilization of clean coal technology in China, Fuel Process. Technol. 89 (2008) 475–484. doi:10.1016/j.fuproc.2007.11.017.

[29] A.G. Collot, Matching gasification technologies to coal properties, Int. J. Coal Geol. 65 (2006) 191–212. doi:10.1016/j.coal.2005.05.003.

[30] M. Höök, K. Aleklett, A review on coal to liquid fuels and its coal consumption, Int. J. Energy Res. 34 (2010) 848–864. doi:10.1002/er.1596.

[31] F.N. Cayan, M. Zhi, S.R. Pakalapati, I. Celik, N. Wu, R. Gemmen, Effects of coal syngas impurities on anodes of solid oxide fuel cells, J. Power Sources. 185 (2008) 595–602. doi:10.1016/j.jpowsour.2008.06.058.

[32] E.D. Larson, R. Tingjin, Synthetic fuel production by indirect coal liquefaction, Energy Sustain. Dev. 7 (2003) 79–102. doi:10.1016/S0973-0826(08)60381-6.

[33] R.H. Williams, E.D. Larson, A comparison of direct and indirect liquefaction technologies for making fluid fuels from coal, Energy Sustain. Dev. 7 (2003) 103–129. doi:10.1016/S0973-0826(08)60382-8.

[34] D.A. Wood, C. Nwaoha, B.F. Towler, Gas-to-liquids (GTL): A review of an industry offering several routes for monetizing natural gas, J. Nat. Gas Sci. Eng. 9 (2012) 196–208. doi:10.1016/j.jngse.2012.07.001.

[35] T.H. Fleisch, 03/01654 Emergence of the gas-to-liquids industry: a review of global GTL developments, Fuel Energy Abstr. 44 (2003) 290. doi:10.1016/S0140-6701(03)91770-X.

[36] O. Glebova, Gas to Liquids : Historical Development and Future Prospects, 2013. http://www.oxfordenergy.org/wpcms/wp-content/uploads/2013/12/NG-80.pdf.

[37] C. Dillerop, H. Van Den Berg, A.G.J. Van Der Ham, Novel syngas production techniques for GTL-FT synthesis of gasoline using reverse flow catalytic membrane reactors, Ind. Eng. Chem. Res. 49 (2010) 12529–12537. doi:10.1021/ie1007568.

[38] H. Schulz, Short history and present trends of Fischer – Tropsch synthesis, 186 (1999) 3–12.

[39] Q. Zhang, W. Deng, Y. Wang, Recent advances in understanding the key catalyst factors for Fischer-Tropsch synthesis, J. Energy Chem. 22 (2013) 27–38. doi:10.1016/S2095-4956(13)60003-0.

[40] Y. Liu, O. Ersen, C. Meny, F. Luck, C. Pham-Huu, Fischer-Tropsch reaction on a thermally conductive and reusable silicon carbide support, ChemSusChem. 7

(2014) 1218–1239. doi:10.1002/cssc.201300921.

[41] R. Luque, A.R. de la Osa, J.M. Campelo, A.A. Romero, J.L. Valverde, P. Sanchez, Design and development of catalysts for Biomass-To-Liquid-Fischer–Tropsch (BTL-FT) processes for biofuels production, Energy Environ. Sci. 5 (2012) 5186. doi:10.1039/c1ee02238e.

[42] B. Todic, L. Nowicki, N. Nikacevic, D.B. Bukur, Fischer-Tropsch synthesis product selectivity over an industrial iron-based catalyst: Effect of process conditions, Catal. Today. 261 (2016) 28–39. doi:10.1016/j.cattod.2015.09.005.

[43] M. Galimberti, Multi-Scale Modelling and Optimization of a Biomass To Liquid Plant, (2015).

[44] R.M. de Deugd, Fischer-Tropsch Synthesis Revisited; Efficiency and Selectivity Benefits from Imposing Temporal and/or Spatial Structure in the Reactor, 2004.

[45] Liu, Li, Zhou, Zhang, Intrinsic kinetics of Fischer-Tropsch synthesis over temperature sensitive iron catalyst, Huagong Xuebao/Journal Chem. Ind. Eng. 46 (1995) 137–143.

[46] R.A. Friedel, R.B. Anderson, Composition of Synthetic Liquid Fuels. Product Distribution and Analysis of C5-C8 Paraffin Isomers from Cobalt Catalyst, 6 (1960) 1212–1215.

[47] J. Flory, Molecular Size Distribution in Three Dimensional Polymers. I. Gelation, J. Am. Chem. Soc. 63 (1941) 3083–3090. doi:10.1021/ja01856a061.

[48] H. Schulz, M. Claeys, Kinetic modelling of Fischer–Tropsch product distributions, Appl. Catal. A Gen. 186 (1999) 91–107. doi:10.1016/S0926-860X(99)00166-0.

[49] B. Sarup, B.W. Wojciechowski, Studies of the fischer-tropsch synthesis on a cobalt catalyst I. evaluation of product distribution parameters from experimental data, Can. J. Chem. Eng. 66 (1988) 831–842. doi:10.1002/cjce.5450660518.

[50] T. Ngwenya, D. Glasser, D. Hildebrandt, N. Coville, P. Mukoma, Fischer - Tropsch Results and Their Analysis for Reactor Synthesis, (2005) 5987–5994.

[51] D.B. Bukur, M.P. Rosynek, E.B. Yeh, C. Lil, Activation Studies with a Promoted Precipitated Iron Fischer-Tropsch Catalyst, Ind. Eng. Chem. Process Des. Dev. 28 (1989) 1130–1140. doi:10.1021/ie00092a003.

[52] A. Mohajeri, Y. Zamani, L. Shirazi, Investigation of Products Distribution In Fischer-Tropsch Synthesis By Nano-sized Iron-based Catalyst, (n.d.) 1–7.

[53] R. Guettel, U. Kunz, T. Turek, Reactors for Fischer-Tropsch synthesis, Chem. Eng. Technol. 31 (2008) 746–754. doi:10.1002/ceat.200800023.

[54] D.M. Alonso, J.Q. Bond, J. a Dumesic, Catalytic conversion of biomass to biofuels, Green Chem. 12 (2010) 1493–1513. doi:10.1039/c004654j.

[55] A. Di Michele, P. Sassi, A. Comazzi, F. Galli, C. Pirola, C.L. Bianchi, Co- and Co(Ru)-Based Catalysts for Fischer-Tropsch Synthesis Prepared by High Power Ultrasound, Mater. Focus. 4 (2015) 295–301. doi:10.1166/mat.2015.1273.

[56] O. Kitakami, H. Sato, Y. Shimada, F. Sato, M. Tanaka, Size effect on the crystal phase of cobalt fine particles, Phys. Rev. B. 56 (1997) 13849–13854. doi:10.1103/PhysRevB.56.13849.

[57] Y. Pei, Y. Ding, H. Zhu, J. Zang, X. Song, W. Dong, et al., Effect of Al2O3 promoter on a performance of C 1-C14 α-alcohols direct synthesis over Co/AC catalysts via fischer-tropsch synthesis, Catal. Letters. 144 (2014) 1433–1442. doi:10.1007/s10562-014-1283-8.

[58] S. Janbroers, J.N. Louwen, H.W. Zandbergen, P.J. Kooyman, Insights into the nature of iron-based Fischer-Tropsch catalysts from quasi in situ TEM-EELS and XRD, J. Catal. 268 (2009) 235–242. doi:10.1016/j.jcat.2009.09.021.

[59] G.L. Bezemer, J.H. Bitter, H.P.C.E. Kuipers, H. Oosterbeek, J.E. Holewijn, X. Xu, et al., Cobalt Particle Size Effects in the Fischer − Tropsch Reaction Studied with Carbon Nanofiber Supported Catalysts, Am. Chem. Soc. 128 (2006) 3956–3964. doi:10.1021/ja058282w.

[60] J.-Y. Park, Y.-J. Lee, P.K. Khanna, K.-W. Jun, J.W. Bae, Y.H. Kim, Alumina-supported iron oxide nanoparticles as Fischer–Tropsch catalysts: Effect of particle size of iron oxide, J. Mol. Catal. A Chem. 323 (2010) 84–90. doi:10.1016/j.molcata.2010.03.025.

[61] Z. Sun, B. Sun, M. Qiao, J. Wei, Q. Yue, C. Wang, et al., A general chelate-assisted co-assembly to metallic nanoparticles-incorporated ordered mesoporous carbon catalysts for Fischer-Tropsch synthesis., J. Am. Chem. Soc. 134 (2012) 17653–60. doi:10.1021/ja306913x.

[62] K. Shimura, T. Miyazawa, T. Hanaoka, S. Hirata, Fischer-Tropsch synthesis over alumina supported cobalt catalyst: Effect of promoter addition, Appl. Catal. A Gen. 494 (2015) 1–11. doi:10.1016/j.apcata.2015.01.017.

[63] M.C. Ribeiro, G. Jacobs, B.H. Davis, D.C. Cronauer, A.J. Kropf, C.L. Marshall, Fischer-tropsch synthesis: An in-situ TPR-EXAFS/XANES investigation of the influence of group i alkali promoters on the local atomic and electronic structure of carburized iron/silica catalysts, J. Phys. Chem. C. 114 (2010) 7895–7903. doi:10.1021/jp911856q.

[64] S. Li, S. Krishnamoorthy, A. Li, G.D. Meitzner, E. Iglesia, Promoted Iron-Based Catalysts for the Fischer–Tropsch Synthesis: Design, Synthesis, Site Densities, and Catalytic Properties, J. Catal. 206 (2002) 202–217.

doi:10.1006/jcat.2001.3506.

[65] R.C. Reuel, C.H. Bartholomew, Effects of support and dispersion on the CO hydrogenation activity/selectivity properties of cobalt, J. Catal. 85 (1984) 78–88. doi:10.1016/0021-9517(84)90111-8.

[66] E. Iglesia, S.L. Soled, R.A. Fiato, Fischer-Tropsch synthesis on cobalt and ruthenium. Metal dispersion and support effects on reaction rate and selectivity, J. Catal. 137 (1992) 212–224. doi:10.1016/0021-9517(92)90150-G.

[67] C. Pirola, A. Di Fronzo, F. Galli, C.L. Bianchi, A. Comazzi, F. Manenti, Biosyngas conversion by Fischer-Tropsch synthesis: Experimental results and multi-scale simulation of a pbr with high Fe loaded supported catalysts, Chem. Eng. Trans. 37 (2014) 595–600.

[68] A. Comazzi, C. Pirola, A. Di Michele, M. Compagnoni, F. Galli, I. Rossetti, et al., Flame Spray Pyrolysis as fine preparation technique for stable Co and Co/Ru based catalysts for FT process, Appl. Catal. A Gen. 520 (2016) 92–98. doi:10.1016/j.apcata.2016.04.010.

[69] C. Pirola C, L. Bianchi, A. Di Michele, P. Diodati, S. Vitali, V. Ragaini, High loading Fe-supported fischer-tropsch catalysts: Optimization of the catalyst performance, Catal. Letters. 131 (2009) 294–304. doi:10.1007/s10562-009-0060-6.

[70] A. Di Fronzo, Biomass to Liquid Process: new kind of cobalt and iron based catalysts for the Fischer-Tropsch Synthesis, (2013). https://air.unimi.it/retrieve/handle/2434/229549/297889/phd_unimi_R09037.pdf.

[71] A.M. Beale, S.D.M. Jacques, J.A. Bergwerff, P. Barnes, B.M. Weckhuysen, Tomographic energy dispersive diffraction imaging as a tool to profile in three dimensions the distribution and composition of metal oxide species in catalyst bodies, Angew. Chemie - Int. Ed. 46 (2007) 8832–8835. doi:10.1002/anie.200703673.

[72] R. Strobel, S.E. Pratsinis, Flame aerosol synthesis of smart nanostructured materials, J. Mater. Chem. 17 (2007) 4743–4756. doi:10.1039/b711652g.

[73] I. Rossetti, A. Gallo, V. DalSanto, C.L. Bianchi, V. Nichele, M. Signoretto, et al., Nickel Catalysts Supported Over TiO2, SiO2 and ZrO2 for the Steam Reforming of Glycerol, ChemCatChem. 5 (2013) 294–306. doi:10.1002/cctc.201200481.

[74] I. Rossetti, G.F. Mancini, P. Ghigna, M. Scavini, M. Piumetti, B. Bonelli, et al., Spectroscopic enlightening of the local structure of VO X active sites in catalysts for the Odh of propane, J. Phys. Chem. C. 116 (2012) 22386–22398. doi:10.1021/jp307031b.

[75] I. Rossetti, J. Lasso, V. Nichele, M. Signoretto, E. Finocchio, G. Ramis, et al.,

Silica and zirconia supported catalysts for the low-temperature ethanol steam reforming, Appl. Catal. B Environ. 150-151 (2014) 257–267. doi:10.1016/j.apcatb.2013.12.012.

[76] S.E. Pratsinis, Flame aerosol synthesis of ceramic powders, Prog. Energy Combust. Sci. 24 (1998) 197–219. doi:10.1016/S0360-1285(97)00028-2.

[77] R. Maric, J. Roller, R. Neagu, Flame-Based Technologies and Reactive Spray Deposition Technology for Low-Temperature Solid Oxide Fuel Cells: Technical and Economic Aspects, J. Therm. Spray Technol. 20 (2011) 696–718. doi:10.1007/s11666-011-9645-x.

[78] M. Minnermann, H.K. Grossmann, S. Pokhrel, K. Thiel, H. Hagelin-Weaver, M. Bäumer, et al., Double flame spray pyrolysis as a novel technique to synthesize alumina-supported cobalt Fischer-Tropsch catalysts, Catal. Today. 214 (2013) 90–99. doi:10.1016/j.cattod.2013.04.001.

[79] V. Safarifard, A. Morsali, Applications of ultrasound to the synthesis of nanoscale metal-organic coordination polymers, Coord. Chem. Rev. 292 (2015) 1–14. doi:10.1016/j.ccr.2015.02.014.

[80] K.S. Suslick, T. Hyeon, M. Fang, Nanostructured Materials Generated by High-Intensity Ultrasound: Sonochemical Synthesis and Catalytic Studies, Chem. Mater. 8 (1996) 2172–2179. doi:10.1021/cm960056l.

[81] C. Pirola, C.L. Bianchi, A. Di Michele, P. Diodati, D. Boffito, V. Ragaini, Ultrasound and microwave assisted synthesis of high loading Fe-supported Fischer-Tropsch catalysts, Ultrason. Sonochem. 17 (2010) 610–616. doi:10.1016/j.ultsonch.2009.11.004.

[82] K.S. Suslick, T. Hyeon, M. Fang, A.A. Cichowlas, Sonochemical synthesis of nanostructured catalysts, Mater. Sci. Eng. A. 204 (1995) 186 – 192.

[83] C.L. Bianchi, C. Pirola, V. Ragaini, Choosing the best diluent for a fixed catalytic bed: The case of CO hydrogenation, Catal. Commun. 7 (2006) 669–672. doi:10.1016/j.catcom.2006.02.004.

[84] C. Pirola, NOVEL SUPPORTED IRON BASED FISCHER-TROPSCH CATALYSTS: PREPARATION, CHARACTERIZATION AND APPLICATIONS, Università degli Studi di Milano, 2008.

[85] J.H. Bang, K.S. Suslick, Applications of ultrasound to the synthesis of nanostructured materials, Adv. Mater. 22 (2010) 1039–1059. doi:10.1002/adma.200904093.

[86] H. Xu, B.W. Zeiger, K.S. Suslick, Sonochemical synthesis of nanomaterials., Chem. Soc. Rev. 42 (2013) 2555–67. doi:10.1039/c2cs35282f.

[87] R.P. Ahlquist, Citation Classics, J. Biol. Chem. (1978) 1978.

doi:10.1016/j.ajog.2010.07.025.

[88] A. Comazzi, C. Pirola, C.L. Bianchi, F. Galli, M. Longhi, F. Manenti, High-loaded Fe-supported catalyst for the thermochemical BTL-FT process: Experimental results and modelling, Can. J. Chem. Eng. 94 (2016) 696–702. doi:10.1002/cjce.22357.

[89] M.K. Gnanamani, G. Jacobs, U.M. Graham, M.C. Ribeiro, F.B. Noronha, W.D. Shafer, et al., Influence of carbide formation on oxygenates selectivity during Fischer-Tropsch synthesis over Ce-containing Co catalysts, Catal. Today. 261 (2016) 40–47. doi:10.1016/j.cattod.2015.08.047.

[90] K.R.P. D. Bukur, K. Okabe, M. P. Rosynek, C. Li, D. Wang, G.P.H. M. Rao, Activation Studies with a Precipitated Iron Catalyst for Fischer-Tropsch Synthesis: I. Characterization Studies, (1995) 353–365.

[91] M. Høj, D.K. Pham, M. Brorson, L. Mädler, A.D. Jensen, J.D. Grunwaldt, Two-Nozzle Flame Spray Pyrolysis (FSP) Synthesis of CoMo/Al2O3 Hydrotreating Catalysts, Catal. Letters. (2013) 1–9. doi:10.1007/s10562-013-0990-x.

[92] M. Høj, K. Linde, T.K. Hansen, M. Brorson, A.D. Jensen, J.D. Grunwaldt, Flame spray synthesis of CoMo/Al2O3 hydrotreating catalysts, Appl. Catal. A Gen. 397 (2011) 201–208. doi:10.1016/j.apcata.2011.02.034.

[93] H.Y. Lin, Y.W. Chen, The mechanism of reduction of cobalt by hydrogen, Mater. Chem. Phys. 85 (2004) 171–175. doi:10.1016/j.matchemphys.2003.12.028.

[94] G. Bagnasco, C. Cammarano, M. Turco, S. Esposito, A. Aronne, P. Pernice, TPR/TPO characterization of cobalt-silicon mixed oxide nanocomposites prepared by sol-gel, Thermochim. Acta. 471 (2008) 51–54. doi:10.1016/j.tca.2008.02.019.

[95] H. Al-Megren, H. Chen, Y. Huang, M. AlKinany, P.P. Edwards, T. Xiao, et al., TPO/TPD study on the activation of silica supported cobalt catalyst, Appl. Petrochemical Res. 3 (2013) 25–34. doi:10.1007/s13203-013-0026-x.

[96] S. Abelló, D. Montané, Exploring iron-based multifunctional catalysts for Fischer-Tropsch synthesis: A review, ChemSusChem. 4 (2011) 1538–1556. doi:10.1002/cssc.201100189.

[97] M. Kraum, M. Baerns, Fischer–Tropsch synthesis: the influence of various cobalt compounds applied in the preparation of supported cobalt catalysts on their performance, Appl. Catal. A Gen. 186 (1999) 189–200. doi:10.1016/S0926-860X(99)00172-6.

[98] J. van de Loosdrecht, B. Balzhinimaev, J.A. Dalmon, J.W. Niemantsverdriet, S. V. Tsybulya, A.M. Saib, et al., Cobalt Fischer-Tropsch synthesis: Deactivation by oxidation?, Catal. Today. 123 (2007) 293–302. doi:10.1016/j.cattod.2007.02.032.

[99] C. Chaisuk, P. Boonpitak, J. Panpranot, O. Mekasuwandumrong, Effects of Co dopants and flame conditions on the formation of Co/ZrO 2 nanoparticles by flame spray pyrolysis and their catalytic properties in CO hydrogenation, Catal. Commun. 12 (2011) 917–923. doi:10.1016/j.catcom.2011.01.016.

[100] T.O. Eschemann, J. Oenema, K.P. De Jong, Effects of noble metal promotion for Co/TiO2 Fischer-Tropsch catalysts, Catal. Today. 261 (2016) 60–66. doi:10.1016/j.cattod.2015.06.016.

[101] M.K. Gnanamani, G. Jacobs, W.D. Shafer, B.H. Davis, Fischer-Tropsch synthesis: Activity of metallic phases of cobalt supported on silica, Catal. Today. 215 (2013) 13–17. doi:10.1016/j.cattod.2013.03.004.

[102] G. Jacobs, W. Ma, B. Davis, Influence of Reduction Promoters on Stability of Cobalt/g-Alumina Fischer-Tropsch Synthesis Catalysts, Catalysts. 4 (2014) 49–76. doi:10.3390/catal4010049.

[103] A.N. Pour, Y. Zamani, A. Tavasoli, S.M. Kamali Shahri, S.A. Taheri, Study on products distribution of iron and iron-zeolite catalysts in Fischer-Tropsch synthesis, Fuel. 87 (2008) 2004–2012. doi:10.1016/j.fuel.2007.10.014.

[104] Y. Zamani, Fischer-Tropsch Synthesis Over Nano-Sized Iron-Based Catalysts: Investigation of Promoter and Temperature Effects on Products Distribution, Pet. Coal. 57 (2015) 71–75.

[105] K. Cheng, V.V. Ordomsky, M. Virginie, B. Legras, P. a. Chernavskii, V.O. Kazak, et al., Support effects in high temperature Fischer-Tropsch synthesis on iron catalysts, Appl. Catal. A Gen. 488 (2014) 66–77. doi:10.1016/j.apcata.2014.09.033.

[106] Zimmerman, Bukur, Reaction kinetics over iron catalysts used for the Fischer-Tropsch synthesis, Can. J. Chem. Eng. 68 (1990) 292–301. doi:10.1002/cjce.5450680215.

[107] E.S. Lox, G.F. Froment, Kinetics of the Fischer-Tropsch reaction on a precipitated promoted iron catalyst. 2. Kinetic modeling, Ind. Eng. Chem. Res. 32 (1993) 71–82. doi:10.1021/ie00013a010.

[108] G. Buzzi-Ferraris, F. Manenti, Improving the selection of interior points for one-dimensional finite element methods, Comput. Chem. Eng. 40 (2012) 41–44. doi:10.1016/j.compchemeng.2012.02.004.

[109] I.C. Yates, C.N. Satterfield, Intrinsic Kinetics of the Fischer-Tropsch Synthesis on a Cobalt Catalyst, Energy & Fuels. 5 (1991) 168–173. doi:10.1021/ef00025a029.

[110] D. Vervloet, F. Kapteijn, J. Nijenhuis, J.R. van Ommen, Fischer–Tropsch reaction–diffusion in a cobalt catalyst particle: aspects of activity and selectivity for a variable chain growth probability, Catal. Sci. Technol. 2 (2012)

1221. doi:10.1039/c2cy20060k.

List of publications and conferences communications

Contribution to the drafting of a book chapter:

[1] A. Iulianelli, C. Pirola, **A. Comazzi**, F. Galli, F. Manenti, A. Basile. "*Water gas shift membrane reactors*". Chapter 1, (2015) 1-27, in the book "Membrane Reactors for Energy Applications and Basic Chemical Production" edited by A. Basile, L. Di Paola, F.I. Hai and V. Piemonte.

Scientific publications on journals:

[1] A. Di Fronzo, C. Pirola, **A. Comazzi**, C.L. Bianchi, A. Di Michele, R. Viviani, M. Nocchetti, M. Bastianini, D.C. Boffito, F. Galli. "*Co-based Hydrotalcites as new Catalysts for the Fischer-Tropsch Synthesis Process*". Fuel, 119 (2014) 62-69. DOI: 0.1016/j.fuel.2013.11.014.

[2] C. Pirola, M. Scavini, P. Ghigna, S. Vitali, F. Galli, **A. Comazzi**. "*EXAFS study of Ru and Pt bimetallic Co based catalysts for Fischer-Tropsch synthesis*". Fuel, 132 (2014) 62-70. DOI: 10.1016/j.fuel.2014.04.063.

[3] C. Pirola, C.L. Bianchi, A. Di Fronzo, **A. Comazzi**, F. Manenti. "*Biosyngas Conversion by Fischer–Tropsch Synthesis: Experimental Results and Multi-scale Simulation of a PBR with High Fe Loaded Supported Catalysts*". Chemical Engineering Transactions, 37 (2014) 595-600. DOI: 10.3303/CET1437100.

[4] C. Pirola, F. Galli, C.L. Bianchi, D.C. Boffito, **A. Comazzi**, F. Manenti. *"Vegetable Oil Deacidification by Methanol Heterogeneously Catalyzed Esterification in (Monophasic Liquid)/Solid Batch and Continuous Reactors"*. Energy & Fuels, 28 (2014) 5236-5240. DOI: 10.1021/ef501397h.

[5] C. Pirola, F. Galli, **A. Comazzi**, F. Manenti, C.L. Bianchi. *"Preservation of carotenes in the deacidification of crude palm oil"*. RSC Advances, 4 (2014) 46922–46925. DOI: 10.1039/c4ra09575h.

[6] A. Di Michele, P. Sassi, **A. Comazzi**, F. Galli, C. Pirola, C.L. Bianchi. "*Co- and Co(Ru)-based catalysts for Fischer-Tropsch synthesis prepared by high power ultrasound*". Material Focus, 4 (2015) 295-301 DOI: 10.1166/mat.2015.1273.

[7] **A. Comazzi**, C. Pirola, C.L. Bianchi, F. Galli, M. Longhi, F. Manenti. *"High loaded Fe supported catalyst for the thermochemical BTL-FT process: experimental results and modeling"*. The Canadian Journal of Chemical Engineering, 94 (2016) 696–702. DOI: 10.1002/cjce.22357.

[8] **A. Comazzi**, C. Pirola, A. Di Michele, M. Compagnoni, F. Galli, I. Rossetti, F. Manenti, C.L. Bianchi. *"Flame Spray Pyrolysis as fine preparation technique for stable Co and Co/Ru based catalysts for FT process"*. Applied Catalysis A: General, 520 (2016) 92-98. DOI: 10.1016/j.apcata.2016.04.010.

[9] **A. Comazzi**, C. Pirola, M. Longhi, C.L. Bianchi, K.S. Suslick. *"Fe-based Heterogeneous Catalysts for the Fischer-Tropsch Reaction: Sonochemical Synthesis and Bench-Scale Experimental Tests"*. Ultrasonics Sonochemistry, 34 (2017) 774-780. DOI: 10.1016/j.ultsonch.2016.07.012.

[10] F. Galli, **A. Comazzi**, D. Previtali, F. Manenti, G. Bozzano, C.L. Bianchi, C. Pirola. *"Production of oxygen-enriched air via desorption from water: experimental data, simulations and economic assessment"*. Computers & Chemical Engineering, in press. DOI: dx.doi.org/10.1016/j.compchemeng.2016.07.031.

[11] R. Lahti, D. Bergna, H. Romar, T. Hu, **A. Comazzi**, C. Pirola, C.L. Bianchi, U. Lassi. "*Characterization of cobalt catalysts on biomass-derived carbon supports*". Topics in Catalysis, in press.

Contributions to conferences (oral and poster communications):

[1] A. Di Michele, C. Pirola, A. Di Fronzo, **A. Comazzi**, F. Galli, C.L. Bianchi. "*Co based bimetallic catalysts* for *Fischer-Tropsch synthesis prepared by high-power ultrasound*" at "XI European Congress on Catalysis" Lyon, France 1st-6th September 2013, poster communication.

[2] A. Di Michele, C. Pirola, A. Di Fronzo, **A. Comazzi**, C.L. Bianchi. "*Co based bimetallic catalysts for Fischer-Tropsch synthesis prepared by high power ultrasound*" at "1st Asia-Oceania Sonochemical Society Meeting" Melbourne, Australia 10th-12th July 2013, oral communication.

[3] A. Di Michele, C. Pirola, A. Di Fronzo, **A. Comazzi**, F. Galli, C.L. Bianchi. "*Sonochemical synthesis of Co based bimetallic catalyst for Fischer-Tropsch synthesis*" at "XVII Congresso Nazionale di Catalisi e XI Congresso Nazionale di Scienza e Tecnologia delle Zeoliti" Riccione, Italy 15th-18th September 2013, poster communication.

[4] C. Pirola, C.L. Bianchi, A. Di Fronzo, **A. Comazzi**, F. Manenti. "*Biosyngas Conversion by Fischer-Tropsch Synthesis: Experimental Results and Multi-scale Simulation of a PBR with High Fe Loaded Supported Catalysts*" at "iconBM: international conference on BioMass" Florence, Italy 4th-7th May 2014, poster communication.

[5] **A. Comazzi**, C. Pirola, F. Manenti, A. Di Fronzo, A. Di Michele, C.L. Bianchi. "*Co and Co-Ru based catalysts prepared by high power ultrasound for the Fischer-Tropsch synthesis*" at "14th Meeting of the European Society of Sonochemistry" Avignon, France 2nd-6th June 2014, poster communication.

[6] **A. Comazzi**, C. Pirola, C.L. Bianchi, F. Galli, F. Manenti. ***"****Biosyngas Conversion by Fischer-Tropsch Synthesis: Experimental Results and Multi-scale Simulation of a PBR with High Fe Loaded Supported Catalysts"* at "5th International Symposium on energy from biomass and waste" Venice, Italy 17th-20th November 2014, oral communication.

[7] **A. Comazzi**, C. Pirola, C.L. Bianchi, F. Galli, F. Manenti. "*Low Temperature and Pressure Biogas Upgrading by Water Washing: Experimental Data in a Micro-Pilot Absorption Column*" at "5th International Symposium on energy from biomass and waste" Venice, Italy 17th-20th November 2014, poster communication.

[8] C. Pirola, **A. Comazzi**, F. Galli, C.L. Bianchi, F. Rossi, F. Manenti. "*Production of enriched air by water degassing for process intensification: experimental results and relative modeling*" at "12th PSE and 25th ESCAPE" Copenhagen, Denmark 31st-4th May/June 2015, poster communication.

[9] **A. Comazzi**, C. Pirola, A. Di Michele, M. Compagnoni, F. Galli, S. Cane, F. Manenti, I. Rossetti, C.L. Bianchi. "*Flame Spray Pyrolysis Synthesized Co and Co/Ru Based Catalysts for the Thermochemical GTL – Fischer Tropsch Process*" at "Synthesis Gas Chemistry, DGMK Conference" Dresden, Germany 7th-9th October 2015, poster communication.

[10] **A. Comazzi**, F. Galli, C.L. Bianchi, I. Rossetti, F. Manenti, C. Pirola, A. Di Michele. "*Co and Co/Ru based catalysts synthesized by FSP for the industrial Gas-to-Liquid Fischer-Tropsch process*" at "Congresso della Divisione di Chimica Industriale" Salerno, Italy 14th-16th September 2015, poster communication.

[11] C. Pirola, **A. Comazzi**, F. Galli, C.L. Bianchi, F. Manenti, F. Rossi. "*Experimental results and dynamic simulation of enriched air production by water degassing for process intensification*" at "Congresso della Divisione di Chimica Industriale" Salerno, Italy 14th-16th September 2015, poster communication.

[12] **A. Comazzi**, F. Galli, M. Galimberti, F. Manenti, C.L. Bianchi, C. Pirola. "*Bio-syngas Conversion by FT Synthesis with High Loaded Fe-based Catalysts: Kinetic Parameters*

Regression" at "26th European Symposium on Computer-Aided Process Engineering, ESCAPE 26th" Portorož, Slovenia 12th-15th June 2016, oral communication.

[13] **A. Comazzi**, C. Pirola, C.L. Bianchi, K.S. Suslick. "*Ultrasonic Synthesis and Bench Scale Experimental Tests of Fe-Based Catalysts for the Fischer-Tropsch Process*" at "15th Meeting of the European Society of Sonochemistry" Istanbul, Turkey 27th-1st June/July 2016, oral communication.

[14] R. Lahti, H. Romar, D. Bergna, H. Tao, U. Lassi1, **A. Comazzi**, C. Pirola, C.L. Bianchi. "*Characterization and properties of biomass-derived carbon-supported metal catalysts active in the Fischer-Tropsch process*" at "17th Nordic Symposium on Catalysis 2016" Lund, Sweden 14th-16th June 2016, poster communication.

[15] F. Galli, **A. Comazzi**, F. Manenti, G. Bozzano, C.L. Bianchi, C. Pirola. "*Produzione di aria arricchita in ossigeno tramite degasaggio da acqua in continuo per intensificazione di processo*" at "Convegno GRICU 2016, gli orizzonti 2020 dell'Ingegneria Chimica" Anacapri, Italy 12th-14th September 2016, poster communication.

[16] **A. Comazzi**, N. Livraghi, C. Pirola, C.L. Bianchi, A. Di Michele, F. Demartin, K.S. Suslick. "*Ultrasonic Synthesis and Bench Scale Experimental Tests of Fe-Based Catalysts for the Fischer-Tropsch Reaction*" al "Catalysis – Novel Aspects in Petrochemistry and Refining, DGMK Conference" Berlin, Germany 26th-28th September 2016, oral communication.

[17] C. Pirola, I. Rossetti, A. Di Michele, C.L. Bianchi, **A. Comazzi**. "*Co and Co-Ru based catalysts active in the Fischer-Tropsch reaction synthesized by flame spray pyrolysis*" al "XIX Congresso Nazionale di Catalisi, GIC 2016" Bressanone, Italy 11th-14th September 2016, poster communication.